FINAL REPORT

Corrosion Protection Mechanisms of Rare-Earth Compounds Based on Cerium and Praseodymium

SERDP Project WP-1618

APRIL 2012

William Fahrenholtz
Missouri University of Science and Technology

SERDP
DOD ▪ EPA ▪ DOE

REPORT DOCUMENTATION PAGE

Form Approved
OMB No. 0704-0188

PLEASE DO NOT RETURN YOUR FORM TO THE ABOVE ORGANIZATION.

1. REPORT DATE *(DD-MM-YYYY)*	2. REPORT TYPE	3. DATES COVERED *(From - To)*
05-04-2012	Final	March 2008 to March 2012

4. TITLE AND SUBTITLE

Corrosion Protection Mechanisms of Rare-Earth Compounds Based on Cerium and Praseodymium

5a. CONTRACT NUMBER

W912HQ-08-C-0008

5b. GRANT NUMBER

5c. PROGRAM ELEMENT NUMBER

6. AUTHOR(S)

William G. Fahrenholtz, Matthew J. O'Keefe, and Eric L. Morris

5d. PROJECT NUMBER

WP-1618

5e. TASK NUMBER

5f. WORK UNIT NUMBER

7. PERFORMING ORGANIZATION NAME(S) AND ADDRESS(ES)

Missouri University of Science and Technology
Materials Science and Engineering Department, 222 McNutt Hall
Rolla, MO 65409

8. PERFORMING ORGANIZATION REPORT NUMBER

9. SPONSORING/MONITORING AGENCY NAME(S) AND ADDRESS(ES)

Strategic Environmental Research and Development Program
901 North Stuart Street, Suite 303
Arlington, VA 22203

10. SPONSOR/MONITOR'S ACRONYM(S)

SERDP

11. SPONSOR/MONITOR'S REPORT NUMBER(S)

12. DISTRIBUTION/AVAILABILITY STATEMENT

This report is approved for public release; distribution is unlimited

13. SUPPLEMENTARY NOTES

14. ABSTRACT

The mechanisms by which rare-earth compounds provide corrosion protection were investigated. A variety of environmentally benign corrosion inhibitors, including rare-earth compounds, are potential replacements for carcinogenic chromate-based inhibitors in conversion coatings and primers. Chromates are robust inhibitors that provide protection to a multitude of metal alloys from a variety of different types of coatings, whereas most alternative inhibitors only protect a limited number of alloys or can only be used in a specific type of coating. Understanding protection mechanisms could allow for extension of protection to other alloys or coating types. For cerium-based conversion coatings, protection was accompanied by the formation of an interfacial reaction layer between the coating and the substrate. Praseodymium-based inhibitors in epoxy-polyamide primers provided protection by dissolving from the primer and forming precipitates in damaged areas. Both inhibitors are capable of providing corrosion protection on high strength aluminum alloys that is comparable to chromates when a suitable phase is incorporated into an appropriate coating.

15. SUBJECT TERMS

Corrosion protection mechanisms; non-chromate corrosion inhibitors; cerium; praseodymium; cerium-based conversion coatings, epoxy-polyamide primers;

16. SECURITY CLASSIFICATION OF:			17. LIMITATION OF ABSTRACT	18. NUMBER OF PAGES	19a. NAME OF RESPONSIBLE PERSON
a. REPORT	b. ABSTRACT	c. THIS PAGE			K. Krishnamurthy
U	U	U	UU	247	19b. TELEPHONE NUMBER *(Include area code)* 573-341-4154

Reset

Table of Contents

List of Acronyms

A–Hexagonal crystal structure
AA–Aluminum alloy
AES—Auger Electron Spectroscopy
ASTM—American Society for Testing and Materials
B–Monoclinic crystal structure
BET– Brunauer, Emmett, and Teller
C–Cubic crystal structure
CAA—Clean Air Act
CeCC—Cerium-based Conversion Coatings
CERCLA—Comprehensive Environmental Response Compensation and Liability Act
CPDS—Cyclic potentiodynamic spectroscopy
CrCC—Chromate Conversion Coatings
CWA—Clean Water Act
DI–Deionized
DoD—Department of Defense
EDCeCC—Electrodeposited cerium-based conversion coating
EDS—Energy Dispersive X-ray Spectroscopy
EIS—Electrochemical Impedance Spectroscopy
EPA—Environmental Protection Agency
FIB–Focused Ion Beam
FTIR—Fouier Transform Infrared Spectroscopy
H–high temperature hexagonal crystal structure
HAADF—High Angle Annular Dark Field
IMC–Intermetallic compound
LA-ICP-MS Laser Ablation Inductively Coupled Plasma Mass Spectrometry
MPY—Mils per year (a measure of corrosion rate)
OCP–Open Circuit Potential
OLI—
OSHA—Occupational Safety and Health Administration
PEL—Permissible Exposure Limit
RCRA—Resource Conservation and Recovery Act
RE—Rare Earth
SARA—Superfund Amendments and Reauthorization Act
SCE–Saturated Calomel Electrode
SEM-Scanning Electron Microscopy
SERDP—Strategic Environmental Research and Development Program
SPCeCC—Spray deposited cerium-based conversion coating
STEM–Scanning Transmission Electron Microscopy
TCP—Trivalent chromium passivation
TEM—Transmission Electron Microscopy
TGA/DTA—Thermal Gravimetric Analysis/Differential Thermal Analysis
TSCA—Toxic Substances Control Act
TRI—Toxic Release Inventory
UV-VIS-NIR—Ultraviolet Visible Near Infrared

X–High temperature cubic crystal structure
XRD-–X-ray Diffraction
XPS–X-ray photoelectron spectroscopy

List of Figures

List of Tables

Acknowledgements

A number of people have made significant contributions to the efforts documented in this report. The project was a collaborative effort between Missouri S&T and Deft. The original Missouri S&T team included Bill Fahrenholtz, Matt O'Keefe, Tom O'Keefe, and Paul Yu. Unfortunately, both Tom O'Keefe and Paul Hu passed away between the time that the proposal was written and the project started. From Deft, Dr. Eric Morris and Mr. Rich Albers participated in the research.

During the course of the project, the research was performed by four graduate students, two post-doctoral fellows, and one temporary technician. Graduate students Daimon Heller, Will Pinc, Simon Joshi, and Ci Lin were supported by the project for at least part of their graduate studies. Among the graduate students, Will and Simon were supported during the majority of their PhD studies and made major contributions to the understanding of the protection mechanisms of cerium-based conversion coatings. Post-doctoral fellows Dr. Becky Treu and Dr. Elizabeth Kulp also contributed to the project. In particular, Becky was responsible for research on the protection mechanisms of the praseodymium-based inhibitor. She also had primary responsibility for supervising day-to-day activities in the laboratory, interacting with Deft, and preparing project reports. The contributions of the support of the staff at the Graduate Center for Materials Research Center at Missouri S&T is gratefully acknowledged.

Finally, the project team would like to acknowledge the support of SERDP. We would like to thank Bruce Sartwell for his guidance and encouragement during the course of the project. In addition, the entire SERDP staff has been very supportive and helpful. We had great interactions with Jeff Houff, Caitlin Rohan, and the others throughout the project.

Executive Summary

This project focused on determining corrosion protection mechanisms for coatings that contain rare-earth (RE) compounds. The participants were the Missouri University of Science and Technology (Missouri S&T), which served as the lead organization, and Deft, Inc., which was a sub-contractor. Two specific coating systems were examined; cerium-based conversion coatings (CeCCs) and epoxy polyamide primers containing praseodymium-based inhibitors. Prior to the start of the project, both coating systems had demonstrated corrosion protection that could meet current U.S. military requirements for aircraft. The current chromated coatings that are widely used in U.S. military systems, including corrosion protection coatings for the high strength aluminum alloys used to construct military aircraft, present acute health and environmental hazards. Understanding the mechanisms by which RE compounds inhibit corrosion would reduce the risk of implementing environmentally friendly coating systems as chromate replacements.

The approach taken in the current project assumed that RE compounds are not inherently protective. Instead, the appropriate phase of a RE compound has to be incorporated into the proper type of coating to provide corrosion protection in specific environments. As part of the project, mechanistic models for corrosion protection were devised by fully characterizing the phases that were present in as-deposited coatings, the transport processes that occurred during corrosive attack, and the species that formed to passivate the substrates.

Discovery of sub-surface crevices in substrates with CeCCs during Year 1 led to a significant change in the emphasis of the project during that year. The initial concept for the model was that CeCCs were primarily barriers between the corrosive species (i.e., chloride ions) and the underlying high strength aluminum alloys. After the discovery of the sub-surface crevices, more research was required to develop and validate models that explained how CeCCs could not only protect the substrate directly beneath the coating, but also inhibit corrosion in sub-surface crevices that were connected to the surface through large (>1 μm wide) cracks visible through the coating surface. The final models identified an altered layer between the coating and the substrate that inhibited corrosion through the coating and showed how growth of a hydrated aluminum oxide layer inhibited corrosion in the crevices.

For epoxy-polyamide primers containing a praseodymium-based inhibitor package, elucidation of a corrosion protection mechanism first required investigation of the phase stability of praseodymium species in aqueous and ambient air environments. At the beginning of the project, very little was known about the phase stability of praseodymium species compared to cerium species. After the initial phase stability studies, the emphasis switched to examining the corrosion response of model primers that were formulated with specific praseodymium compounds or other components of the inhibitor package to isolate and identify the corrosion response of each component as a function of exposure time and exposure conditions (e.g., pH). At the same time, characterization studies provided evidence of the precipitation of praseodymium-rich crystallites in areas of exposed substrate during corrosive attack. Through the understanding of praseodymium phase stability and studying the corrosion response as a function of pH, a model for the corrosion protection provided by the praseodymium-based

inhibitor package was developed. Protection relies on the dissolution of praseodymium species from the primer matrix that occurs at a relatively low pH, which is promoted by the incorporation of an acid extender into the primer. The dissolved praseodymium species then transport to the site of attack and precipitate due to a rise in local pH, which is promoted by the cathodic response of intermetallic particles in the alloy matrix near the site of corrosive attack.

This report describes the results and analysis from SERDP project number WP-1618. Significant progress was made in all technical areas, which were reviewing the technical literature (Task 1), studying the phase stability of Pr compounds (Task 2), coating deposition (Task 3), characterization of coatings (Task 4), corrosion mechanism analysis (Task 5), and final model development and validation (Task 6). Some of the significant accomplishments of the project are:

1. Surveyed the technical literature, which revealed that Pr_2O_3 is susceptible to hydration and/or carbonation by reaction with atmospheric H_2O vapor and CO_2. The cubic forms of the oxide are more stable than the other structural variants. Consequently, Pr_6O_{11} does not react with the ambient atmosphere to form hydroxides, carbonates, or hydroxycarbonates (Task 1)
2. Characterized the decomposition sequence and phase stability of praseodymium oxides, hydroxides, and hydroxycarbonates (Task 2)
3. Performed precipitation studies on Pr^{3+} species. The effects of temperature and dissolved gas composition were evaluated (Task 2)
4. Analyzed the effect of alkaline surface activations on the composition and structure of the native oxide layer on Al 7075-T6 (Task 3)
5. Deposited cerium-based conversion coatings that could provide corrosion protection using process parameters that either promoted the formation of sub-surface crevices or resulted in coatings on substrates with no crevice formation (Task 3)
6. Formulated and deposited model primers with Pr-species or other additives to isolate and characterize the function of different components (Task 3)
7. Developed a process for deposition of cerium-based conversion coatings on aluminum alloys used for casting including Al 380 and Al 413 (Task 3)
8. Identified surface activation conditions for Al 7075-T6 that provide a balance between removing the native oxide and providing a uniform surface for deposition of cerium-based conversion coatings with optimal corrosion protection (Task 4)
9. Separated the effect of humidity and temperature from the presence of chloride ions on changes in the corrosion response of cerium-based conversion coatings (Task 4)
10. Developed microelectrochemical tools to probe the electrochemical response of specific regions of coatings and substrates (Task 4)
11. Identified species migrating to damages areas of primers containing Pr-based inhibitor packages using a combination of analytical and electrochemical tools (Task 4)
12. Identified Pr-rich species in scribes of Al 2024-T3 test panels with chromate conversion coatings and Pr-rich primers after exposure to salt spray (Task 4)
13. Analyzed changes in the concentrations of inhibitor species in primers containing Pr-based corrosion inhibitors as a function of time in salt spray testing (Task 4)
14. Characterized the effect of pH on passivation of exposed areas of panels of Al 2024-T3 coated with primers containing Pr-based corrosion inhibitors using electrochemical testing (Task 4)

15. Identified an interfacial layer that develops between cerium-based conversion coatings and Al 2024-T3 substrates during exposure to corrosive environments that appears to play a critical role in corrosion protection (Task 5)
16. Developed solubility plots to support experimental studies that show that cerium dissolution from a cerium-based conversion coatings role plays a minimal role in corrosion protection of cerium-based conversion coatings (Task 5)
17. Characterized the electrochemical response and corrosion protection provided by primers with Pr-based inhibitors on Al 2024-T3 with different surface treatments including chromate conversion coatings, cerium-based conversion coatings, and trivalent chromium passivation (Task 5)
18. Investigated the effect of non-chromate conversion coatings on the corrosion protection of primers containing Pr-based corrosion inhibitors (Task 5)
19. Devised two models to explain the corrosion protection provided by cerium-based conversion coatings; one to explain the protection provided by the coating in contact with a high strength aluminum alloy surface and a second to describe the inhibition of corrosion in sub-surface crevices (Task 6)
20. Proposed a mechanism by which Pr-based inhibitors inhibit corrosion of high strength aluminum alloys (Task 6)

The overall project met the original statement of need by developing models that describe the corrosion protection mechanisms for cerium-based conversion coatings and a praseodymium-based inhibitor package that is used in epoxy-polyamide primers.

Objective

The objective of this project was to investigate the corrosion protection mechanisms of rare earth (RE)-based non-chromate corrosion inhibitors. As outlined in SERDP Statement of Need WPSON-08-02, a scientific understanding of the protection mechanisms offered by non-chromate corrosion inhibitors would reduce the risk of implementing environmentally friendly coating systems. Missouri S&T and Deft Inc. collaborated to investigate the corrosion protection mechanisms of coatings with RE inhibitors, specifically cerium (Ce) and praseodymium (Pr) compounds. For Ce compounds, the initial research focused on cerium-based conversion coatings (CeCCs) on aluminum alloy 2024-T3. At the beginning of the project, the influence of process parameters and deposition conditions on the morphology and crystal structure of coatings was understood, but little was known about why different conversion coatings had drastically different corrosion performance. Likewise, primers containing RE compounds had been shown to provide corrosion protection to Al alloys, but the mechanism of the protection had not been investigated. Based on previous studies, RE compounds are not inherently protective. Instead, protection requires that the proper phase be present in the right type of coating. The ultimate goal of the project was to devise parallel but separate models for the protection mechanisms of RE inhibitors in conversion coatings and primers. The research included identification of compounds present in the coatings and that dissolve during exposure to corrosive species, characterization of transport processes and rates, and determination of specific reactions that lead to passivation (Figure 1). Practical protection mechanisms were deduced by understanding the phase stability of the RE compounds and the crystal structure, morphology, and distribution of the phases in as-deposited coatings as well as during and after corrosion. For RE inhibitors, a combination of analytical tools, electrochemical testing, and performance evaluation was employed to characterize coatings. Electrochemical techniques were investigated as rapid methods of correlating coating characteristics to corrosion performance in salt spray performance.

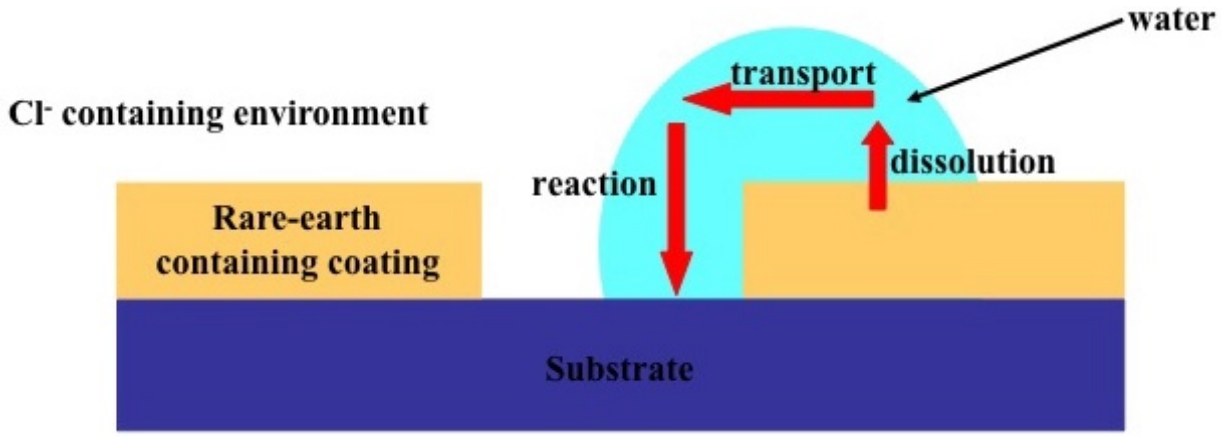

Figure 1. Illustration of the steps thought to be involved in corrosion protection mechanisms for rare-earth based coatings, which consist of dissolution of species from the coating, transport to the site of attack, and reaction to passivate the substrate.

Background

Currently, chromate conversion coatings (CrCCs) and chromated primers are used to provide corrosion protection for metallic components in DoD systems such as the high strength aluminum alloys used in military aircraft. Although chromates are highly effective corrosion inhibitors, these compounds are toxic and carcinogenic [1]. Based on their negative environmental and health impacts, chromium compounds are listed on the Toxic Release Inventory (TRI), making their use subject to regulation by the Environmental Protection Agency (EPA) under the Clean Air Act (CAA), Clean Water Act (CWA), Comprehensive Environmental Response Compensation and Liability Act (CERCLA), Resource Conservation and Recovery Act (RCRA), Superfund Amendments and Reauthorization Act (SARA), and Toxic Substances Control Act (TSCA). In May 2006, the Occupational Safety and Health Administration (OSHA) implemented new, stricter regulations regarding workplace exposure to chromates [2]. The permissible exposure limit (PEL) issued by OSHA for hexavalent chromium and for all Cr(VI) compounds in general industry were reduced from the previous 52 $\mu g/m^3$ to 5 $\mu g/m^3$ in an eight hour time-weighted average [2]. These regulations resulted in significant increases to the life cycle costs associated with chromate-containing coatings due to increased costs of controlling exposure, respiratory protection, protective work clothing and equipment, hygiene areas and practices, medical surveillance, hazard communication, record keeping, and waste stream disposal. Both the costs and time associated with this increased level of regulation affect military readiness. Increased scientific understanding of the protection mechanisms of chromate alternatives would reduce the risk associated with implementing new technologies by identifying and correcting potential shortcomings prior to extensive field-testing.

Non-Chromate Inhibitors

A variety of non-chromate corrosion inhibitors have been developed as environmentally friendly alternatives to chromates [3]. Among the possible alternatives to chromates, RE compounds have proven to be effective corrosion inhibitors when the proper RE phase is incorporated into the appropriate type of coating. Select RE-based compounds are currently being used to replace toxic, carcinogenic chromates in certain military applications. Little is known about how RE compounds provide corrosion protection. For this project, the corrosion protection mechanisms of two proven non-chromate corrosion-inhibiting coatings are being investigated: 1) Ce-based conversion coatings; and 2) RE compounds in epoxy-polyamide primers.

Cerium-Based Conversion Coatings

Ce compounds have proven to be effective corrosion inhibitors in CeCCs on high strength aluminum alloys. CeCCs are capable of inhibiting the corrosion of aluminum alloys for 336 hours in ASTM B117 salt spray as specified in MIL-DTL-81706. The solutions used to deposit CeCCs contain aqueous Ce^{3+} ions, which are precipitated as hydrated CeO_2 during coating deposition. CeCCs developed at Missouri S&T can be deposited using electrolytic, immersion, or spray processes. The corrosion protection afforded by CeCCs is more sensitive to substrate preparation, coating deposition parameters, and post-treatment than CrCCs.

Sub-Surface Void Formation

The mechanism by which voids are formed in the substrate during deposition is likely related to the coating deposition mechanism of CeCCs. It has been shown that sub-surface damage in both Al 2024-T3 and Al 7075-T6 substrates was due to the combined effects of chloride ions and H_2O_2, which were present in the coating spray solution. The continuous breakdown of oxide by chloride and oxidation of aluminum in localized areas, likely around intermetallic compounds, results in the formation of subsurface voids in ~10% of the area beneath CeCCs surface.

Praseodymium Inhibitors

Previous research at Missouri S&T showed that Pr compounds in combination with other additives are effective corrosion inhibitors in epoxy polyamide primers. These primers have been commercialized by Deft, Inc. and have been qualified to DoD requirements [4]. The Pr-based inhibitors are highly effective in epoxy-polyamide primer systems when the primer is deposited onto high strength aluminum alloys with CrCCs. The primers do not perform as well when they are applied on non-chromate conversion coatings or bare Al alloys. The phase of the Pr compound and the solubility of other additives affect corrosion protection, but corrosion protection mechanisms have not been fully investigated.

Materials and Methods

The technical approach employed for this project required collaboration between Missouri S&T and Deft Inc. The team members from each organization had key roles in the progress described in the rest of the report. Tasks were distributed according to areas of expertise and capabilities in each area. Missouri S&T was the lead organization for the CeCC and primer mechanistic studies as well as other fundamental aspects of the research. Deft Inc. was responsible for the formulation and application of the primer test panels. Both Missouri S&T and Deft, Inc. participated in analysis of data and collaborate to devise protection mechanisms and transition the results to interested customers. With respect to the project tasks and subtasks, Missouri S&T had primary responsibility for Task 1 (Literature Review), Task 2 (Phase Stability of Pr Compounds), Task 3 (CeCC Deposition), and Task 4 (Characterization of Corrosion Behavior). Deft, Inc. had primary responsibility for Task 3 (Primer Formulation and Deposition). The responsibilities for Task 5 (Protection Mechanism Analysis), Task 6 (Final Model Development and Application), Task 7 (Attend SERDP Symposium and in Progress Review Meeting), and Task 8 (Presentations, Publications, Quarterly and Final Reports) were shared between Deft Inc. and Missouri S&T.

Phase Stability Studies

Commercially available Pr_2O_3, Pr_6O_{11}, $Pr(OH)_3$ and $Pr_2(CO_3)_3 \bullet xH_2O$ were used as starting materials. Each material was subjected to thermal treatment then analyzed using thermal gravimetric analysis (TGA) and differential thermal analysis (DTA). The functionality of each compound was studied using Fourier-transform infrared spectroscopy (FT-IR). Scanning electron microscopy (SEM) was used to characterize particle morphology and x-ray diffraction (XRD) analysis was used to determine the crystalline phase present. Surface area and the

calculated equivalent radius of each particle was determined using the Brunauer, Emmett, and Teller (BET) method and a nitrogen adsorption Surface Area Analyzer.[5]

Phase stability studies focusing on the effects of $Ca_2SO_4 \bullet 2H_2O/Ca_2SO_4$, solvent, temperature, and time on the disproportionation of Pr_6O_{11} were performed. Samples were prepared under static conditions consisting of 1g Pr_6O_{11}, 3 g $Ca_2SO_4 \bullet 2H_2O$ or Ca_2SO_4, and 10 mL H_2O or oxall (parachlorobenzotrifluoride) at time increments ranging from 3 hours to 2 days and at temperatures of 20°C, 85°C, and 100°C. The final products were analyzed using XRD to determine the crystalline phase present.

Precipitation studies were performed by dissolving 10 g of Pr_2O_3 into 25% tricholoroacetic acid and diluting this stock solution to 300 mL with DI water. For each experiment, 100 mL of stock solution was used and 1 M NaOH was added stepwise to increase the pH and induce precipitation. The pH of the solution was recorded under various conditions/combinations including: room temperature or heated to 85°C; bubbling Ar, O_2, or CO_2 through the Pr solution. The resulting precipitates (green powders) were collected by filtration, rinsed, and dried prior to characterization. SEM was used to characterize particle morphology and XRD was used to determine the crystalline phase(s) present. Surface area and the calculated equivalent radius of each particle were determined using the BET method. Gravimetric analysis was also performed in order to determine the solubility of each precipitated species. Each powder was ground into fine particulates with a mortar and pestle prior to weighing out to the nearest 1.000 ± 0.005g. Each powder was allowed to stir for 1 hr in 1000 mL of DI water at room temperature. The resultant slurries were then vacuum filtered and the powder collected was weighed and subtracted from the original starting amount to determine the amount of Pr-powder that had dissolved. Experiments were done in triplicate.

CeCC Deposition

To determine the role of a specific processing parameter or coating solution component in the corrosion protection mechanism of CeCCs, panels were treated in such a way as to isolate certain process parameters in various experiments. Panels were examined after surface preparation to identify if the acid/alkaline activation or other cleaning steps were the cause of subsurface voids. The next processing parameter that was examined was the coating method, as subsurface voids may be formed during coating deposition. Lastly, as-deposited coatings versus post-treated coatings were studied.

Surface Preparation

Aluminum 2024-T3 panels were 0.08 cm thick and sheared to 2.5 cm by 7.6 cm in size before undergoing a multistep surface preparation process prior to coating deposition. First, panels were degreased with a laboratory wiper saturated with isopropyl alcohol. Next, panels were immersed in a 55°C alkaline cleaning solution (5 wt% Turco 4215 NC LT) for 5 minutes. Then, panels were activated by immersion in a 50 ºC, 1 wt% sulfuric acid solution for 10 minutes. Between each step of the surface preparation process and prior to coating, the panels were rinsed with deionized water.

Similarly, aluminum 7075-T6 sheets that were 0.08 cm thick were cut into 2.5 cm by 7.6 cm panels. First, the panels were rinsed with acetone followed by degreasing in an aqueous solution of a commercial alkaline cleaner (5 wt% Turco 4215 NC-LT) for 5 minutes at 55° C. After degreasing, the panels were activated by immersion in one of three different alkaline solutions at room temperature: 1) 20 sec immersion in a solution containing 1 wt% NaOH in deionized water (pH of the solution 12.9), which is referred to as 1NaOH; 2) 20 sec immersion in a solution containing 2 wt% NaOH in deionized water (pH of the solution 13.1), which is referred to as 2NaOH; and 3) 30 sec immersion in an aqueous solution containing 5 wt% $Na_2CO_3 \cdot H_2O$ in deionized water (pH of the solution 11.5), which is referred to as $5Na_2CO_3$. Between each step of the surface preparation process and prior to coating, the panels were rinsed with deionized water.

Spray Deposition of CeCCs

Previous research has resulted in significant progress in understanding the phase stability of Ce compounds and the deposition process for CeCCs. Methods for deposition of CeCCs that meet military performance requirements have been identified and CeCCs can be reproducibly deposited using several different processes. For standard coatings, CeCCs are spray deposited on Al 2024-T3 and 7075-T6 panels using established procedures. The substrate is kept wet throughout the coating process and the coating is deposited using a commercially available air powered spray gun. The CeCC deposition solution was prepared from a stock solution consisting of 40 g $CeCl_3 \bullet xH_2O$, 780 g of de-ionized water, pH adjusted to 2.07 with HCl. For the deposition solution, 205 g of the stock solution was mixed with 0.8 g of a water soluble gelatin dissolved in 25 g of de-ionized water, and 20 mL of H_2O_2 (Fisher Chemical, 30 wt.%). Coatings were deposited using a detail spray gun held at a distance of about 25 cm from the panels. Activated panels were sprayed for ~5 seconds and then allowed to drain for ~35 seconds. Multiple spray-drain cycles were used to achieve the desired coating thickness and uniformity. Following deposition, the panels are post-treated (sealed) in a phosphate-based solution at pH 4.5 to convert the as-deposited hydrated cerium oxide coating to a hydrated cerium phosphate ($CePO_4 \bullet H_2O$) coating. The phosphate post-treatment reduces cracking and makes the coating more protective against corrosion. A representative schematic of the process can be seen in Figure 2.

Direct Deposition of Cerium Phosphate Coatings

The solution used to prepare directly deposited $CePO_4$ coatings consisted of two precursor solutions that were chilled to ≤ 5 °C before being mixed immediately prior to coating deposition. The first solution was comprised of a mixture of $Ce(NO_3)_3 \cdot 6H_2O$ and citric acid, forming a cerium citrate complex, and the second was an aqueous solution of H_3PO_4. The concentrations and ratios of individual species were varied experimentally to optimize the morphology and corrosion performance of the coatings. Precursor concentrations designed to yield 60 g/L $CePO_4$ were chosen for these experiments because the thickness of the resulting coating was 400 – 450 nm and most closely matched thicknesses of spontaneously spray deposited CeCCs. The direct deposition process consisted of mixing equal parts of the precursors solutions, distributing a continuous film of coating solution across the substrate with a transfer pipette, and immersing the panel in a 50 °C water bath for ≈10 sec. Following deposition, coated surfaces were gently wiped to remove loosely bound precipitates and rinsed with deionized water. This process was repeated five times, after which specimens were allowed to dry in the ambient prior to analysis.

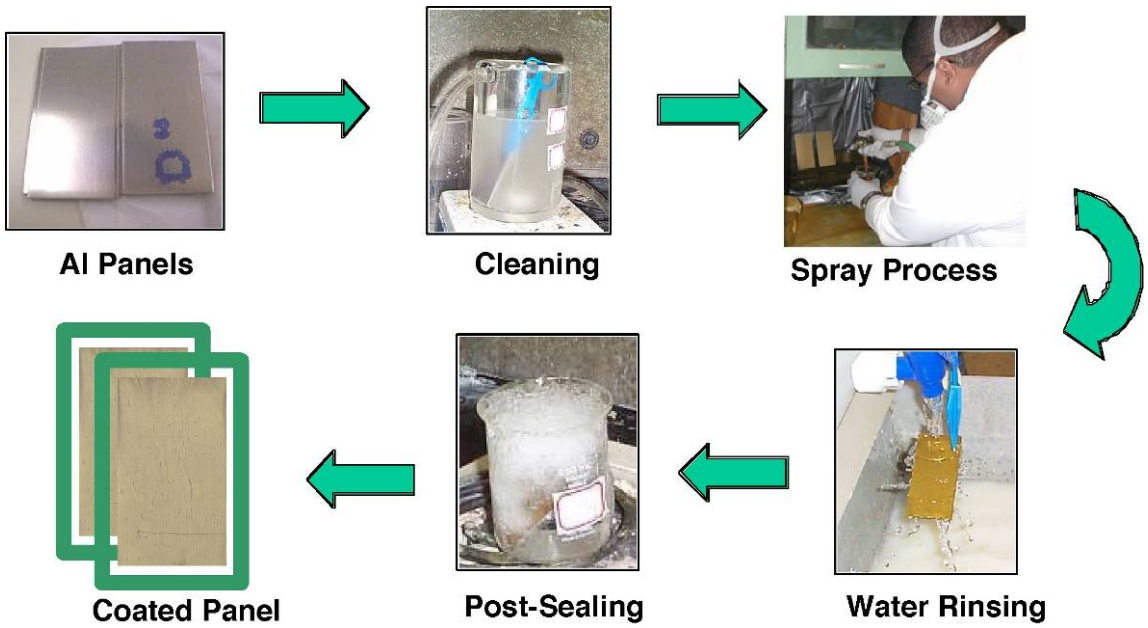

Figure 2. Illustration of the steps in the spray deposition process for the preparation of CeCCs on Al 2024-T3 and Al 7075-T6.

Electrodeposition of CeCCs

Coatings were electrodeposited from solutions consisting of 0.007 M $Ce(NO_3)_3 \cdot xH_2O$, 0.5 M H_2O_2, and 2.4 g/L gelatin. The pH of the coating solution was adjusted with nitric acid prior to the addition of hydrogen peroxide such that the pH of the final solution was ~2.3. Electrodeposition was carried out at a current density of 5 mA/cm^2 for 200 seconds using a potentiostat (EG&G Princeton Applied Research Model 273A) and a platinum mesh counter electrode. After deposition, the coated panels were post-treated by immersion in an 85 ºC, 2.5 wt% NaH_2PO_4 solution for 5 minutes. After post-treatment, coatings were either dried overnight under ambient laboratory conditions or underwent further processing. The coatings that did not undergo further processing are thought to be crevice-free coatings because no subsurface crevices would be expected since the coatings were electrodeposited from nitrate solutions (i.e., the combination of chloride ions and H_2O_2 thought to be responsible for crevice formation was not present). The remaining coatings underwent a spray process designed to introduce subsurface crevices into the panels. Immediately after electrodeposition and post-treatment, these coatings were treated with an aqueous solution of 0.32 M NaCl, 1 M H_2O_2, and 2.4 g/L gelatin with a final pH adjusted to ~2.3 using HCl. Panels were treated by spraying to form a continuous layer of solution followed by draining for ~30 seconds. The spray-drain treatment was repeated five times. After treatment, panels were rinsed with DI water. Then, the treated panels were either left to dry under ambient laboratory conditions or post-treated a second time in the 85 ºC, 2.5 wt% NaH_2PO_4 solution for 5 minutes. The coatings that underwent the spray process after electrodeposition are referred to as crevice-containing coatings as exposure to solutions containing chloride ions and hydrogen peroxide would be expected to produce subsurface crevices.

CeCC Characterization

Corrosion Testing and Surface Characterization

A cyclic corrosion tester (Q-FOG, Q-Panel Lab Products) was used to evaluate the performance of the coatings according to ASTM B117. Based on military performance requirements for conversion coatings such as those described in MIL-DTL-81706, the goal for the CeCCs is to prevent the formation of corrosion pits and salt tails for 2 weeks (336 hours) of salt spray exposure. Coating surface morphology was examined using SEM. Energy dispersive x-ray spectroscopy (EDS) was used to characterize chemical compositions in the SEM. Cross-sections of coated panels were prepared and imaged using a dual beam system focused ion beam (FIB) SEM. Transmission electron microscopy (TEM) analysis was performed on certain coating cross-sections and electron diffraction ring patters were collected in order to identify the phase/chemical composition of specific interfaces. Coating thicknesses and composition depth profiles were characterized using Auger electron spectrometry (AES). X-ray photoelectron spectroscopy (XPS) was performed using a monochromatic aluminum source to analyze the chemical state of the surface.

Electrochemical Testing

The panels were characterized electrochemically using a Princeton Applied Research potentiostat. The test sequence was done by first measuring the open circuit potential (OCP) for 1500-5000 seconds followed by electrochemical impedance spectroscopy (EIS) with the final measurement being potentiodynamic polarization scans. EIS was conducted at OCP with a frequency of 100,000-0.01 Hz. Ten points were taken per decade. A potentiodynamic scan was performed from -0.3 to 1.4 V_{SCE} versus OCP with a scan rate of 1mV/sec. The electrolyte consisted of 0.35 wt% NaCl and 0.70 wt% $(NH_4)_2SO_4$ in deionized water. A saturated calomel electrode (SCE) was used as the reference electrode. The impedance data were analyzed using ZSimpWin 3.21 software from Princeton Applied Research.

Microelectrochemical Testing

Microelectrochemical testing has the potential to isolate and probe specific surface features, which could provide insight into corrosion mechanisms as well as identifying specific locations where corrosion is likely to initiate. It is a small area technique that can isolate and test sections less than 100 μm in diameter. The principles behind microelectrochemical testing are identical to traditional electrochemical testing that utilizes a three electrode configuration. Microelectrochemical testing requires a more deliberate and delicate operation than traditional electrochemical testing due to the difficulty in pinpointing the desired test areas and the use of a fragile glass capillary probe.

A cell was custom-built (Figure 3) specifically for this project in order to do microelectrochemical testing of areas of CeCCs that were ~50 μm in diameter. The cell is attached to the optical microscope so that the capillary can be positioned on the desired test area. The system was sealed and the syringe was used to inject electrolyte as well as to apply pressure to the system to counter the surface forces inside the capillary. A small conduit was made to join the reference electrode chamber with the cell such that the opening of the conduit in the cell would be as close as possible to the working electrode. A platinum wire was inserted inside the conduit to reduce solution resistance. Platinum mesh was used as the counter electrode and was wrapped around the reference electrode conduit providing a more uniform electric field between

the working electrode and the counter electrode. The capillary was made by heating, pulling, and polishing borosilicate glass Pasteur pipettes until the desired size was attained (internal diameters between 40 and 60 µm). Then, the capillary was embedded in silicone to prevent leakage.

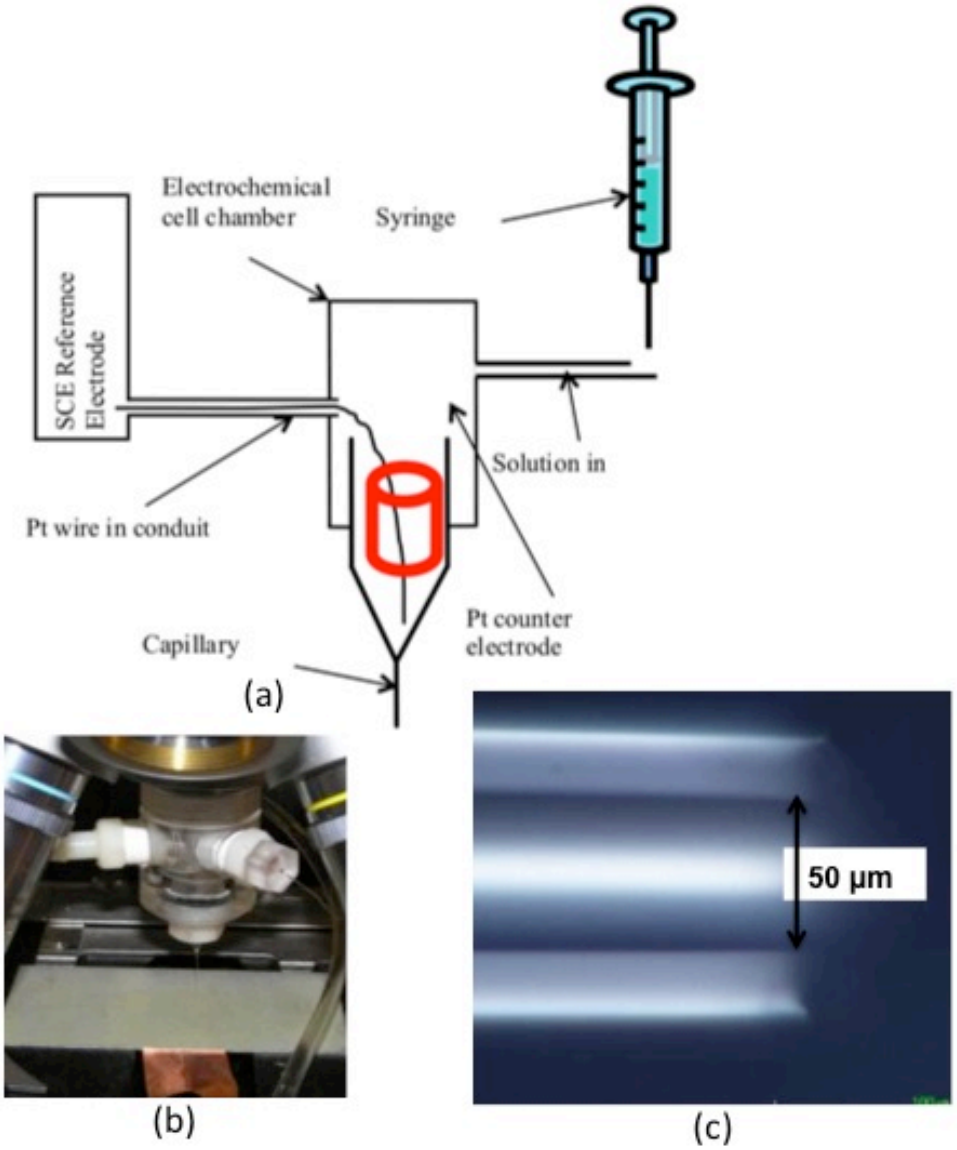

Figure 3. **(a) Schematic of the electrochemical cell used for microelectrochemical testing, (b) a microelectrochemical cell attached to the objective lens of an optical microscope, and (c) a side view of a capillary used for microelectrochemical testing.**

CeCCs on Al 7075-T6 were first rinsed with DI water then fixed to the stage of an optical microscope, scanned to find the desired test area, and imaged. After determining the position for the test, the cell was attached to the objective lens support. The overall success of positioning the capillary on the desired spot depended on the straightness of the capillary, the stability of the microscope during attachment of the cell, and adjusting the difference in coordinates between the actual test area and the desired test area, which was based on an initial test. The process of

applying/releasing pressure and raising the sample platform was repeated several times until the potential did not shift sharply with time. During the 1500 second stabilization period the OCP was monitored to see if the potential drifted above -0.40 V vs. SCE (saturated calomel electrode) or below -0.85 V vs. SCE. Values outside this range were an indication the capillary was not positioned correctly or that it was broken. After testing was completed, the sample stage was lowered and checked to determine if any solution was visible, an indication that the electrolyte had leaked and the test was invalid. After locating the test area, the sample was removed, rinsed with DI water, and again observed under an optical microscope.

Cerium Solubility Studies

Immediately after coating deposition, the panels were fully immersed in 0.1 M NaCl solution at pH values of 2.0. 3.0, 4.0, 5.0, and the natural solution pH of 5.7. The first set of experiments was performed using 0.1 M NaCl solution at pH 2.0 and 5.7. The second set of experiments used 0.1 M NaCl solutions ranging from pH 2.0 to 5.7. After soaking, about 5 ml of solution from each beaker was drawn and examined using a UV-VIS-NIR spectrophotometer at fixed intervals. After measurements, the solution was returned to the appropriate beaker. Standard solution of $CeCl_3$ (1 mM) and $Ce(ClO_4)_4$ (1 mM) that were dissolved in 0.1 M NaCl solution were also made. The reference solution used during UV-vis analysis was 0.1 M NaCl solution at pH 2.0, 3.0, 4.0, 5.0, and 5.7. MathCad software (version 14) was used to construct the solubility diagrams. FactSage software version 5 was used to construct E-pH diagrams.

Coatings with Pr-Based Corrosion Inhibitors

As part of this project, the corrosion protection offered by Pr-based inhibitors in epoxy-polyamide primers was studied. Two commercial primers (Deft products 02GN084, which is solvent-borne, and 44GN098, which is water-borne) that have been approved for use on military aircraft were examined along with model primers. Primers were formulated using standard procedures established for the commercial products and spray-applied by Deft.

The Deft epoxy-polyamide primers with Pr-based inhibitors have the best performance on CrCCs and can inhibit corrosion of high strength Al alloy panels scribed to bare metal for at least 3000 hours in ASTM B117 salt spray. Primer formulation and deposition was performed by Deft. Both standard solvent-based formulations and model primers were formulated to current production standards for deposition and subsequent analysis. A commercial fluorinated, military aerospace grade top coat was applied to some specimens. Efforts remained focused on primers deposited onto Al alloys 2024-T3 with CrCC pre-treatments. The set of samples discussed in this report consisted of Deft formulated test coatings in which the standard inhibitor package was replaced by Pr-phases (Pr_2O_3 and Pr_6O_{11}), acid extenders ($Ca_2SO_4 \bullet 2H_2O$/gypsum), or an inert filler ($Mg_3Si_4O_{10}(OH)_2$/talc). The standard 084 solvent-based primer, which contains both Pr_2O_3 and gypsum, was the control composition. These samples were subjected salt spray exposure similar to the standard formulations and characterized to pinpoint key components in the coating and their relationship to the overall corrosion protection mechanism. Panels were characterized before salt spray testing and after various intervals in salt spray using both electrochemical and analytical techniques.

Characterization of Primers

Panels prepared by Deft were characterized using both electrochemical and surface techniques. Coating surface morphology was examined using SEM. EDS was used to characterize chemical compositions in the SEM. Cross-sections of coated panels were prepared and imaged using a dual beam system focused ion beam (FIB) SEM. The phases and relative amounts of crystalline species present were identified by XRD. Corrosion performance was evaluated by salt spray testing using a cyclic corrosion tester according to the specifications in ASTM B117. Electrochemical impedance spectroscopy (EIS) and potentiodynamic testing were also used to characterize the relative corrosion resistance of coatings with artificial defects prepared by milling an area to expose the underlying substrate.

Corrosion Response Following Salt Spray Testing

Panels were machined scribed and then subjected to salt spray testing using a cyclic corrosion tester (Q-Fog, Q-Panel Lab Products) according to the specifications in ASTM B117. The phases and relative amounts of crystalline species present were identified by x-ray diffraction (XRD). Diffraction patterns were collected from the field region (1cm^2 sample size of non-scribed area) of as-received panels and panels following up to 500 hours of salt spray exposure. Coating field and scribed-area morphologies were examined in as-received coatings and coatings following 500 hours of salt spray exposure using SEM and EDS was used to characterize chemical compositions in the SEM. The chemical composition of corrosion products in scribed panels were analyzed in-situ using Laser Ablation-Inductively Coupled Plasma-Mass Spectrometry (LA-ICP-MS). The goal was to quantify trace amounts of Pr, S, and Ca in the scribes of Al 2024-T3 panels that were coated with CrCCs and standard 084 primers. Panels were examined prior to and following ASTM B117 salt spray exposure.

Electrochemical Measurements

As-received test panels (0 hours salt spray exposure) were characterized using electrochemical methods. Artificial defects (~1.6 mm i.d.) were machined into field areas of panels to provide a controlled test area. The experimental set-up consisted of a Princeton Applied Research model K0235 Flat Cell with an exposed working electrode area of 1 cm^2, a platinum mesh counter electrode, and a saturated calomel reference electrode (SCE). Potentiodynamic scans were performed (scan rate 1mV/s) in electrolyte consisting of 0.35 wt. % NaCl and 0.70 wt. % $(NH_4)_2SO_4$ with the pH adjusted to 5, 6, 7, or 8 with HCl or NaOH as needed. For each experiment, the OCP values were measured after 1500 seconds of immersion in the test electrolyte, which allowed the panel to equilibrate with the electrolyte to obtain a stable OCP value. Each experiment was performed in triplicate. Corrware (Scribner Associates) data acquisition software was used to control the electrochemical tests and data fitting was performed using CView. The calculated corrosion potential (E_{corr}) and corrosion current (i_{corr}), were obtained by a Tafel fit. The pitting potential (E_{pit}) was estimated from the anodic sweep of the potentiodynamic curve. The passive region is defined as the area of the curve on the anodic sweep extending between E_{corr} and E_{pit}.

Colormetric Detection of Pr

Colormetric UV-VIS assays were performed to study the role of pH and phase on Pr^{3+} solubility within the primer matrix. Test panels were prepared using Al 2024-T3 with CrCCs followed by: 1) the Deft 084 solvent-borne primer with the standard inhibitor package (Pr_2O_3 and gypsum); 2)

a primer in which the standard corrosion inhibitor package was replaced by only Pr_2O_3; and 3) a primer in which the standard corrosion inhibitor package was replaced by only Pr_6O_{11}. Small samples (~1 cm^2) were cut from larger test panels and soaked for 2 weeks in ~10 mL of electrolyte (0.35 wt. % NaCl and 0.7 wt. % $(NH_4)_2SO_4$ with the pH values of 5, 6, 7, and 8. The colormetric reaction mixture consisted of 1 mL of solution from each soaked panel, 0.05 wt% Arsenazo III, and 1 wt% ascorbic acid in a formate buffer with the pH adjusted to ~2.6. The absorbance of the solution from each sample was recorded at 650 nm and the concentration of Pr^{3+} leached from the panels was calculated from a calibration curve.

Results and Accomplishments

The sections that follow describe data that were collected, analysis that was performed, conclusions that were reached, and accomplishments that were achieved during the course of this project. During the first year of the project, the primary focus areas included characterization of as-deposited CeCCs and primer coatings along with studying the precipitation behavior and phase stability of Ce and Pr species alone and in coating systems. During the second year, the Pr phase stability studies were concluded and the research emphasis shifted to the corrosion protection mechanisms of CeCCs and primers containing Pr-based inhibitors. During this year, the formation of sub-surface crevices was discovered and the emphasis of the CeCC effort shifted to understanding the formation of the crevices and their effect on the corrosion protection of CeCCs. The Pr inhibitor studies were initiated by formulating a number of model primers and studying their corrosion response. During the third year, emphasis was on finalizing the corrosion protection models for CeCCs and characterizing the corrosion response of primers with Pr-based inhibitors. For the final year of the project, research emphasized development of a model for the mechanism of corrosion protection for Pr-based inhibitors in epoxy-polamide primers.

Task 1: Review of Literature

Rare-Earth Toxicology

The use of rare-earth elements is continually increasing as new materials are developed and applications utilizing their properties are explored. These elements are commonly used in superconductors, lasers, catalysts, magnets, ceramics, and abrasives. As the use of rare earth elements increases, so does the need to understand their toxicological effect on living organisms.

The absorption of rare earth elements, including cerium, into the body through the skin is negligible, except when abrasions are present. In this case, increased absorption may occur, but the dominate response is irritation and scarring caused by reaction with tissue constituents (e.g., phosphates) [6]. Intradermal injection of rare earth chlorides or nitrates can produce granulomas or lesions at the injection site and moderate adsorption. Intravenous injection causes rapid absorption of rare earth elements, which are removed from the bloodstream within 24 hours. The absorption and clearance of rare earth elements depends on their stability in the bloodstream. More stable chelated forms, such as citrate complexes, are quickly removed through the body's waste stream, whereas ionic forms are absorbed into the body. Rare earth elements are primarily transported to the liver, spleen, and bone where the half-life of removal is between 150 – 250 days for most rare earth elements [6-7]. Removal time varies with organ, as half-life for removal

from the liver is approximately 15 days. However, 66 % of the rare earth concentration in bone remained eight months after initial exposure, with heavier rare earth elements having a larger propensity to be incorporated into bone compared to light rare earths. Once transported to the organs, rare earth elements can cause development of a fatty liver and premature death of liver or spleen tissue [6-8]. Because of the similar ionic radii, many rare earth elements exhibit a propensity to remove Ca^{2+} and deposit in bone, resulting in increased calcium concentration in other organs [8]. Eye exposure and inhalation generally leads to irritation of the affected tissue, but longterm exposure to rare earth dust can cause pneumoconiosis (restricted lung capacity) caused by fibrosis [6,9]. Rare earth elements are poorly absorbed through the intestinal tract and no toxic side effects were observed after longterm ingestion. Exposure to rare earth elements is not highly toxic, with lethal dose in 50% of test animals (LD_{50}) values from 10 – 100 mg/kg when intravenously injected and generally from 250 – 1000 mg/kg for intraperitoneal (i.e., into a body cavity) injections [7]. The development of carcinomas was not reported after exposure to rare earth elements.

Pr Phase Stability

Pr (III) oxide (Pr_2O_3) is the RE compound introduced into the epoxy-polyamide primer matrix to inhibit corrosion. The majority of fundamental research on Pr-O containing species (praseodymium (III/IV) oxides, hydroxides, carbonates, oxyhydroxides, oxycarbonates, hydroxycarbonates etc.) was performed in the 1950s-1980s with a later resurgence of interest for catalyst applications.[10] Early work (1950s-1960s) focused mainly on the various phases possible for complexes formed at low/high pressures, low/high temperatures, and various oxygen concentrations.[11-12] The two most commonly found Pr oxides found at atmospheric conditions are Pr_6O_{11} and Pr_2O_3 but, there are a variety of Pr-O species that can be produced at non-atmospheric conditions and have been studied.[13] Phase diagrams, thermal analysis, XRD patterns, and thermodynamic data can be found for select Pr-O species in various phases described in this early literature.[10,14,15]

The most stable Pr-O species at ambient atmospheric conditions (i.e., near room temperature in humid laboratory air) is Pr_6O_{11}, which has a cubic crystal structure.[13] Cubic Pr_6O_{11} is thermally stable and is resistant to hydration and carbonation in the presence of atmospheric H_2O vapor and CO_2.[16,17] The Pr-O species used to formulate the corrosion inhibitor for the commercial Deft primers, Pr_2O_3, is known to be reactive in atmospheric conditions, which is termed aging in the literature. Previous studies have shown that Pr_2O_3 is reactive towards H_2O vapor and atmospheric CO_2. The effects of aging (phases/states present at atmospheric conditions) of rare earth compounds were studied during the 1970s-1980s using thermal analysis, XRD, and infrared (IR) spectroscopy.[10,18-20] Researchers have generalized previous results for all light lanthanide (Ln) series oxides (elements La-Sm) due to similar trends found within the series. Most literature has focused on Ce-O, La-O, Nd-O, and Sm-O, which has left an opportunity to study Pr-O complexes in more detail.[10,18-20]

Previous studies describe the tendency of light Ln-oxides, and specifically Pr_2O_3, to form various hydroxides, hydrated oxides, hydroxycarbonates, and hydrated carbonates when exposed to H_2O and CO_2.[10,18-20] The tendency for complete hydration decreases as atomic number increases through the lanthanide series.

The interactions with H_2O and CO_2 can be bulk or surface processes, depending on how the materials are prepared.[13,20] The aging process varies for each RE oxide and both structure and reactivity are related to atmospheric conditions. Previous studies have described trends in the reactivity of the oxides of lanthanide compounds (designated Ln_2O_3 here) toward H_2O vapor. The conversion of Ln_2O_3 compounds is much faster for hexagonal species (which are the common commercially available variety) compared to cubic forms (can be synthesized, but are not commercially available).[13,20] In addition, during the conversion of Ln_2O_3 to $Ln(OH)_3$, the affinity of Ln_2O_3 for H_2O vapor leads to preferential formation of hydroxide species instead of surface carbonation.[20] The aging reactions tend to reach a stable state (oxide converted to a mixed hydroxide/hydroxycarbonate) after about 24 hours in atmospheric conditions. However, samples placed in water are resistant to further uptake of CO_2.[17] During thermal decomposition, surface adsorbed H_2O is driven off first, followed by bulk chemically combined H_2O, then chemically combined CO_2, which requires a higher temperature.[19,20] A representative schematic for the thermal evolution of Ln_2O_3 following the uptake of H_2O and CO_2 can be seen in Figure 4.[10,15] Based on the literature review that was conducted, aging studies (and other phase stability experiments) were performed at Missouri S&T for both Pr_2O_3 and Pr_6O_{11} as part of Task 2.

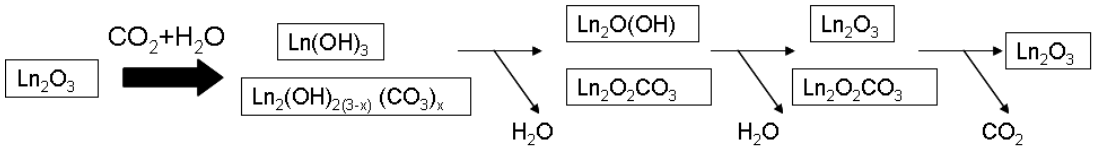

Figure 4. The thermal evolution of oxides belonging to the light Ln-series.

Phase Stability and Precipitation Studies in the System Pr-H_2O-CO_2

Rare earth compounds have an unusual combination of thermal stability and chemical activity [21,22]. Recent interest in rare earth oxides is due in part to their potential chemical applications [23]. Several review articles dealing with fundamentals and applications of these materials have been published since 1990. Eyring reviewed preparation, crystal structures, and phase transformations of rare earth oxides in 1991[24]. Schweda focused on structures and transformations of rare earth oxides in 1992 [25]. Finally, Morss reviewed thermodynamic properties of rare earth oxides in 1994 [21]. A member of the light-lanthanide series of oxides (Ln_2O_3; Ln=elements La-Sm), praseodymium oxides (PrO_x) are important materials for catalysis applications, oxygen-storage components, and highly conductive materials because the oxides exhibit multiple phases with unique structures and stoichiometries [10,24,25]. Early fundamental research on Pr-O based species focused mainly on the various phases possible for complexes formed at low/high pressures, low/high temperatures, and various oxygen concentrations [11,12,26]. The recent resurgence in interest is due to potential catalyst [27-29] and sensor applications [30-31]. The two most common PrO_x species found under ambient condition are Pr_6O_{11} and Pr_2O_3, but a variety of other oxides can be produced at non-atmospheric conditions [32]. Heating Pr(III) salts or Pr_2O_3 in air results in the formation of Pr_6O_{11}. This oxide is thermally stable and is the final decomposition product when Pr species are heated in the presence of oxygen. The final stoichiometry depends the temperature and the oxygen partial pressure in the ambient atmosphere [21,33]. Phase diagrams, thermal analysis, x-ray diffraction

patterns, and thermodynamic data can be found for several Pr-O species and various crystalline phases [11,12,26,34-36].

At moderate temperature, compounds of oxygen and rare earth elements are solids and have melting points ranging from 2300°C to 2500°C [23]. All the rare earth elements, including praseodymium, form a sesquioxide and are polymorphic. Sesquioxides have three polymorphic phases A (hexagonal), B (monoclinic), and C (cubic). For praseodymium, only two structures, C-Pr_2O_3 (body centered cubic) and A-Pr_2O_3 (hexagonal) have been observed in bulk specimens produced under ambient pressure. The B-Pr_2O_3 form (monoclinic) is only stabilized under hydrothermal conditions (i.e., high temperature and pressure) [32]. At normal atmospheric conditions at temperatures lower than 2000°C, the A form (hexagonal) is present for Pr_2O_3 and the C form (cubic) is present for Pr_6O_{11}. Above 2000°C the H type (high temperature hexagonal) forms for Pr_2O_3 and the X type (high temperature cubic) forms for Pr_6O_{11} [23]. The A to H transition is accompanied by a lattice expansion, while the H to X transition results in the lattice contraction [37-38].

Ternary sesquioxide systems that contain water and carbon dioxide can exhibit numerous solid phases, complex ions in solution, and metastable equilibria [10]. Cubic Pr_6O_{11} is thermally stable, but under exposure to ambient conditions, will undergo disproportionation into PrO_2 and $Pr(OH)_3$ in the presence of H_2O. However, the cubic structure is more resistant to hydration and carbonation under atmospheric conditions compared to hexagonal forms [36,39]. In contrast, Pr_2O_3, which has hexagonal reported crystal structures, is reactive towards H_2O vapor and atmospheric CO_2 [10,36,40-48]. Previous studies describe the tendency of light Ln_2O_3 species, and specifically Pr_2O_3, to form various hydroxides, hydrated oxides, hydroxycarbonates, and hydrated carbonates when exposed to H_2O and CO_2 [10,40-42]. Hydration and/or carbonation can modify the properties of the oxide and can be bulk and/or surface processes, depending on how the materials are prepared [32,40,42,48,49].

Preferential formation of hydroxide species over surface carbonation occurs for light Ln_2O_3 species due to their basic nature and high affinity for H_2O vapor [42]. Reactions tend to reach a steady state (oxide converted to a mixed hydroxide/hydroxycarbonate) after about 24 hours in atmospheric conditions. However, samples placed in liquid are labile against further uptake of CO_2 [42]. The bulk hydration of rare earth oxides on exposure to air is thermodynamically favored. Further, a relationship exists between the preparation of the oxide and degree of hydration [48-49]. Accordingly, the degree of hydration is controlled by kinetic factors and is a function of time, precursor material, and activation temperature of the precursor [50]. The effects of aging (phases/states present at atmospheric conditions) of all light Ln_2O_3 species follow similar trends and have been previously studied using thermal analysis, XRD, and infrared (FT-IR) spectroscopy [10,40-42].

Research has shown highly coordinated, layered solid compounds are produced when CO_2 is present in the Ln_2O_3 system [51]. The slight substitution of CO_3^{2-} for OH^- occurs with extremely low CO_2 concentration and the species present has an x-ray diffraction pattern similar to pure $Ln(OH)_3$[23]. In the Pr_2O_3-H_2O phase, the nucleation of a hydroxycarbonate phase occurs on the outer layers of a bulk hydroxide and consists of a nucleus of $Pr(OH)_3$ overcoated by the

carbonate phase [42,52]. Therefore, a precipitated hydroxide, or one which has been prepared under conditions with CO_2 present, will be slightly carbonated.

Surface Activation of Aluminum Alloys 2024-T3 and 7075-T6

Studies have shown that if aluminum alloy surfaces are properly cleaned and activated, the deposition of CeCCs can be completed in less than 5 minutes [53-62]. In the original research reported by Hinton et al., [63] CeCC deposition required deposition time of about 200 hours. The more rapidly deposited coatings developed at Missouri S&T can meet military corrosion testing specifications by protecting substrates for up to 336 hours in ASTM B117 salt spray testing [64]. The role of the surface activation process is to reduce the thickness of the native oxide layer, exposing intermetallic compounds and allowing the constituents in the coating solution to react directly with the alloy surface. Because of the amphoteric nature of aluminum, a wide variety of processes can be used to activate 2024 or 7075 substrates, such as immersion in solutions comprised of NaOH, H_2SO_4, Na_2CO_3, HBF_4, HF, H_3PO_4, or HNO_3. The strength and duration of the surface activation will affect the resulting chemistry of the sample surface and, in turn, can modify the deposition and properties of CeCCs [54,56,69].In some cases a combination of activation solutions is used to remove the surface oxide and then desmut the resulting surface.

Decroly et al. [65] have shown during strong alkaline activation, a smut layer (non-insulating alumina gel) is formed and this layer was identified as necessary for the rapid deposition of CeCCs in copper containing aluminum alloys. Frutos et al. [69] have shown in the case of copper containing aluminum alloys such as 2024 and 7075, a thick, but non-adherent, cerium (III) hydroxide layer quickly forms due to the re-deposition of copper during alkaline etching. Pinc et al. [54] have shown that 40 spray cycles were needed to deposit a coating that was approximately 275 nm thick on Al 2024-T3 with only using degreasing as surface cleaning step, whereas surface activation with sulfuric acid after degreasing resulted in a coating thickness of about 200 nm after only one spray cycle. Previous research [66] characterized the effect of degreasing and alkaline activation solutions on the surface oxide composition of Al 7075-T6. Degreasing only removed the upper ~20 nm magnesium-rich oxide layer and did not alter the thickness or composition of the more robust aluminum-rich oxide layer in direct contact with the metal that was ~10 nm thick. Degreasing and alkaline activation aqueous solutions containing 5 wt% Na_2CO_3, 1 wt% NaOH, or 2 wt% NaOH were shown to thicken the surface oxide to ~20-60 nm. The outer ~10-50 nm of the surface oxide was a magnesium-rich corrosion product, while the aluminum-rich oxide layer near the underlying substrate provided passivation. After degreasing and alkaline activation deposition led to the formation of CeCCs that were ~100 nm to ~250 nm thick and the surface of the aluminum alloy quickly changed to yellow color during the first spray cycle. Thus, different surface activations are needed for different type of alloys so that rapid deposition of conversion coatings can take place.

Deposition of Cerium-Based Conversion Coatings

Since the initial research by Hinton [63], numerous studies have focused on various aspects of CeCCs such as the deposition mechanism [55,67-68] and impact of processing parameters (surface preparation [54,69], coating solution composition [70,71], post treatment, etc.) on corrosion resistance. One aspect of CeCCs that has not been adequately studied is the mechanism by which these coatings provide corrosion protection. Several studies have reported a decrease in the corrosion potential and a cathodic shift of the corrosion current for panels with CeCCs

compared to bare aluminum alloy substrates [72,82]. This indicates that coatings may prevent corrosion by inhibiting the oxygen reduction reaction at cathodic sites, which could be due to the coatings acting as a barrier to transport of either oxygen or electrons involved in corrosion reactions [72,82]. Experimental studies performed as part of this project focus on comparing changes observed in CeCCs with good corrosion resistance (post-treated) to those in poor performing coatings (as-deposited CeCCs) upon exposure to salt spray corrosion testing. Corrosion protection mechanisms of CeCCs deposited using process parameters developed by Missouri S&T are discussed in the section designated for Task 3.

Hinton originally showed that CeCCs could be deposited onto AA 2024-T3 and provide significant corrosion protection; however, deposition times approached 200 hours [45]. Modifications to the coating solution and surface activation of the alloy were able to decrease deposition times significantly to where a ~400 nm CeCC could be deposited in minutes [47,53]. Coating solutions used in the deposition of CeCCs typically contain a cerium salt ($CeCl_3$, $Ce(NO_3)_3$)[61,73] an oxidizing agent (H_2O_2) [55], and various additives (gelatin, NaF, etc.) [70,74]. Coatings can be deposited by immersion, spraying, or electrodeposition processes [75]. Surface preparation of the aluminum alloy substrates prior to deposition can vary; however, most processes involve degreasing, deoxidization/activation, and sometimes desmutting of the panels [54,74,76]. Table 1 outlines the deposition parameters used by groups currently researching CeCCs on AA 2024-T3.

SEM has been used extensively to characterize the surface morphology of CeCCs [53,75]. SEM analysis alone is unable to examine the cross sectional structure of these coatings and examine how the aluminum alloy substrate may be affected by the application of the coating. Analysis of CeCCs (using Missouri S&T's processing parameters) using a FIB/SEM system revealed the presence of large sub-surface voids in the substrate underneath the coating. The study at Missouri S&T is identifying which processing parameters, such as surface preparation and coating solution composition, are the causes of the sub-surface voids identified by FIB/SEM analysis. Results are discussed in the section designated Task 4.

Table 1. Deposition parameters of groups currently researching CeCCs.

Group	Surface Preparation	Coating Application	Coating Soln. Composition
Missouri S&T [70]	Acetone rinse, commercial alkaline cleaner, H_2SO_4 acid etch	Spray applied for 3-4 sec, then 35 sec. delay, repeated 5 times.	0.162 M $CeCl_3$, 1 M H_2O_2, 2.4 g/L gelatin, pH to 2.3 w/ HCl
H. Zhang [74]	Alcohol rinse, Na_2CO_3 + Na_3PO_4 degreasing, NaOH etch, HNO_3 etch	Electrodeposited (0.75 mA/cm^2, 40-60 min), 50º C	0.031 M $Ce(NO_3)_3$, 0.39 – 0.62 M H_2O_2, 0.0012 M NaF, pH 3-5
A.E. Hughes [76]	Acetone rinse, silicated alkaline cleaner, $(NH_4)Ce(SO_4)_4$ + H_2SO_4 deoxidizer	Immersion, 45º C, 2-5 min	0.035 M $CeCl_3$, 0.105 M H_2O_2, pH to 1.9 w/ HCl
de Frutos [69]	Ethanol degreasing, NaOH etch, de-smutted w/ HNO_3	Immersion, 85º C, 5 min.	0.016 M $Ce(NO_3)_3$, 0.13 M H_2O_2, pH unreported
C.M. Rangel [61]	Polished, ethanol rinse, NaOH and HNO_3 etches	Immersion, 20ºC	0.002 M $Ce(NO_3)_3$, 0.1 M Na_2SO_4, up to 0.05 M H_2O_2, pH unreported

Microelectrochemical Cell Design and Testing

Electrochemical testing has been used to investigate the corrosion performance of coatings. In addition, results have been correlated to coating corrosion performance in salt spray testing. In general, higher total impedance measured by EIS, lower current density (i_{corr}) at open circuit potential (OCP), and higher anodic pitting potentials measured by potentiodynamic tests indicate better coating performance during salt spray testing [77]. Most of the electrochemical tests performed on coatings such as CeCCs have been on a macroscale, with the test area typically 1 cm^2 or greater [71,77] compared to the size of corrosion pits ~10^{-3} cm^2 that result in failure per MIL-DTL-5541F standards. Traditional testing provides average corrosion performance across a variety of surface features and phases and is unable to determine differences among specific surface features. In contrast, microelectrochemical techniques have been developed to probe coatings on a smaller scale of around 10^{-5} cm^2 or smaller in an effort to understand how specific features affect corrosion performance.

Microelectrochemical corrosion testing using a microcapillary is a relatively new method that was developed in the mid-1990s to probe surfaces without requiring that surfaces be perfectly flat [78-80]. It is a small area technique that can isolate and test sections less than 100 µm in diameter. The principles behind microelectrochemical testing are identical to traditional electrochemical testing that utilizes a three electrode configuration. The main requirement for microelectrochemical testing is that the potentiostat have electrical current resolution of 10 fA or lower because of the size of the area being probed [79,81]. Microelectrochemical testing also requires more deliberate and delicate operation than traditional electrochemical testing due to the difficulty in pinpointing desired test areas and the use of a fragile glass capillary probe. Microelectrochemical test methods were developed at Missouri S&T to characterize CeCCs.

Different areas were probed to understand the effect of surface morphology on localized corrosion behavior and are discussed in the section designated for Task 4

CeCC Protection Mechanism

Despite the promising corrosion protection of CeCCs, only limited studies have been conducted on the corrosion protection mechanisms of these coatings. Several papers, including Hinton's original study on CeCCs, have observed that the potentiodynamic curves of a coated panel compared to a bare alloy exhibited a shift in the cathodic side of the curve to lower current densities and a decrease in the open circuit potential (Figure 5). These shifts were interpreted to mean that the CeCC acted as a cathodic protector by inhibiting the reduction of water and oxygen at cathodic sites (intermetallics) by limiting transport of oxygen and/or electrons at these sites [63-66,72,82,83].

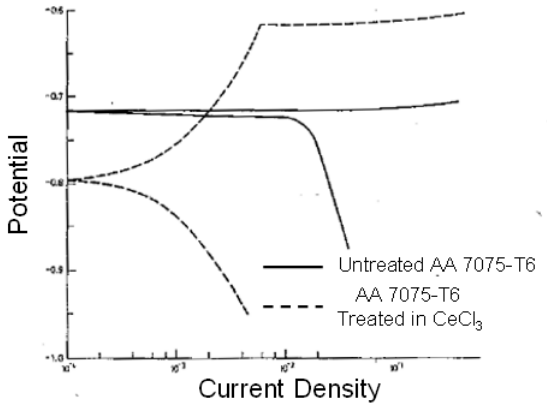

Figure 5. Potentiodynamic curve of bare AA 7075-T6 and AA 7075-T6 coated from a $CeCl_3$ solution [82].

This proposed protection mechanism surmise that CeCCs act only as barriers to corrosion and must cover an area in order to protect. These studies have not observed any potential active protection that CeCCs may exhibit such as throwing power, the ability to heal after pit formation, or form other protective features after corrosion initiation. Better understanding of this, through study of the factors that affect the degree in which these coating can protect, will allow for improvements of properties and, should the technology be deployed into the field, make implementation and troubleshooting easier. Corrosion protection mechanisms of CeCCs deposited using process parameters developed by Missouri S&T have been completed and are discussed in the section designated for Task 4 and 5.

Task 2: Phase Stability of Praseodymium Compounds

As part of Task 2, the fundamental precipitation behavior and phase stability was investigated for Pr oxides, hydroxides, hydroxycarbonates, and/or carbonates. The results are needed to understand the corrosion response of the inhibitors. Simultaneous TGA/DTA is being used to determine the state of hydration/carbonation and other thermochemical characteristics of Pr_2O_3, Pr_6O_{11}, $Pr(OH)_3$ and $Pr_2(CO_3)_3 \bullet 8H_2O$ standards as well as precipitated materials and thermally treated samples. Precipitation studies are being conducted by first solvating and then inducing

precipitation at various temperatures and in the presence of a variety of chemical species such as dissolved gases (e.g., CO_2 and O_2) and different temperatures. Using commercial powders including Pr_2O_3, Pr_6O_{11}, $Pr(OH)_3$, and $Pr_2(CO_3)_3 \bullet 8H_2O$ as standards, precipitation products are currently being characterized to determine the crystalline phases (XRD analysis) and the particle morphology (SEM). Because other XRD cannot always distinguish carbonate and hydroxide species, FT-IR is also being employed as a spectroscopic characterization tool.

Hydration and Carbonation of Praseodymium Compounds

Characterization using TGA/DTA, FT-IR, and XRD was performed on Pr_2O_3, Pr_6O_{11}, $Pr(OH)_3$ and $Pr_2(CO_3)_3 \bullet 8H_2O$ powders to compare and contrast the thermal decomposition mechanisms and gain insight into the aging processes of both Pr_2O_3 and Pr_6O_{11}. As discussed in literature reports, Pr_2O_3 readily adsorbs H_2O and/or CO_2 to form hydroxide, carbonate, or hydroxycarbonate phases. It is of interest to compare the hydration/carbonation effects of Pr_6O_{11} (more stable cubic form of Pr-O) to Pr_2O_3 (less stable hexagonal form). Commercially available Pr_2O_3 and Pr_6O_{11} were analyzed by XRD at several intervals over an 8 hour period of exposure to the ambient atmosphere. Visually, it is apparent that Pr_2O_3 had a much greater affinity towards the uptake of H_2O and CO_2 compared to Pr_6O_{11}. Figure 6 shows Pr_2O_3 expanding over the edge of the XRD sample holder while Pr_6O_{11} remained intact unaffected by the presence of H_2O vapor and CO_2 during the aging study. Analysis by XRD confirmed that aged Pr_2O_3 contained large amounts of $Pr(OH)_3$ in addition to hexagonal Pr_2O_3. In contrast, Pr_6O_{11} that contained only trace amounts of $Pr(OH)_3$ and was largely unaffected by exposure to atmospheric conditions. Analysis of $Pr(OH)_3$ and $Pr_2(CO_3)_3 \bullet 8H_2O$ was also performed to confirm the compositions of the commercial Pr-O compounds following exposure to the ambient atmosphere. While $Pr(OH)_3$ was not affected by exposure, $Pr_2(CO_3)_3 \bullet 8H_2O$ partially converted to $Pr(CO_3)OH$. The studies have provided insight into the rate at which Pr-O compounds will or will not convert to other species when exposed to atmospheric conditions. Unlike Pr_2O_3 and $Pr_2(CO_3)_3 \bullet 8H_2O$, $Pr(OH)_3$ was not affected by exposure to H_2O or CO_2. So, once Pr species are in the hydroxide phase, they will not adsorb CO_2. Likewise, Pr_6O_{11} is stable and did not react with ambient H_2O or CO_2.

Pr_2O_3 `

, Pr_6O_{11}

Figure 6. Pr_2O_3 and Pr_6O_{11} following eight hours of XRD analysis exposed to ambient H_2O and CO_2, showing that the Pr_2O_3 reacted with the atmosphere to form species with a higher specific volume.

Pr-O species including Pr_2O_3, Pr_6O_{11}, $Pr(OH)_3$ and $Pr_2(CO_3)_3 \bullet 8H_2O$ undergo a multiple step thermal decomposition process dictated by the state in which each became hydrated and/or carbonated. The weight loss as a function of temperature was determined in air and argon for Pr_2O_3, Pr_6O_{11}, $Pr(OH)_3$ and $Pr_2(CO_3)_3 \bullet 8H_2O$ (Figure 7 shows data for decomposition in air). Each compound displayed at least four stages during thermal decomposition regardless of the test atmosphere (air or Ar). Weight loss during Stage 1 was due to the loss of surface H_2O species. Bulk chemically combined H_2O (i.e., hydroxide species) were driven off beginning in Stage 2, but chemically combined CO_2 was not driven off until Stage 3. Stages 2 through 4 were steps in which phase transitions began to take place in the bulk of the powders and intermediate phases were formed. Stage 4 denotes formation of the final and most stable phase for each compound. Additional stages in the decomposition of $Pr_2(CO_3)_3 \bullet 8H_2O$ and $Pr(OH)_3$ may occur due to the presence of different types of –OH bonds in these two compounds. Characterization by DTA (not shown) also varied for each species (temperature and number of peaks), but was not affected by atmosphere in which the experiments were run. Only endothermic peaks were detected, which correlated well with evidence of mass loss for each compound. Each mass loss between Steps 1 and 3 can be attributed to H_2O/-OH and/or CO_2 being driven off which was consistent with FT-IR characterization. Analysis by XRD did not detect the presence of carbonate species in the starting Pr_2O_3 nor did XRD detect hydroxide in Pr_6O_{11}. However, carbonate (C-O stretch) and/or water (-OH bend) could be identified by FT-IR analysis (Figure 8). During the final stages of thermal decomposition (Stage 4), there is an overall change in the oxygen stoichiometry for each species examined. Stoichiometric oxygen to Pr ratios (x=1.5 for Pr_2O_3, and x=3 for $Pr(OH)_3$, and x= 8.5 for $Pr_2(CO_3)_3 \bullet 8H_2O$) are converted to a non-stoichiometric ratio (x=1.83 for Pr_6O_{11}). The phase transformation of Pr_2O_3, $Pr(OH)_3$ and $Pr_2(CO_3)_3 \bullet 8H_2O$ to cubic Pr_6O_{11} with a non-stoichiometric oxygen to Pr ratio is also attributed to the resultant mass loss.

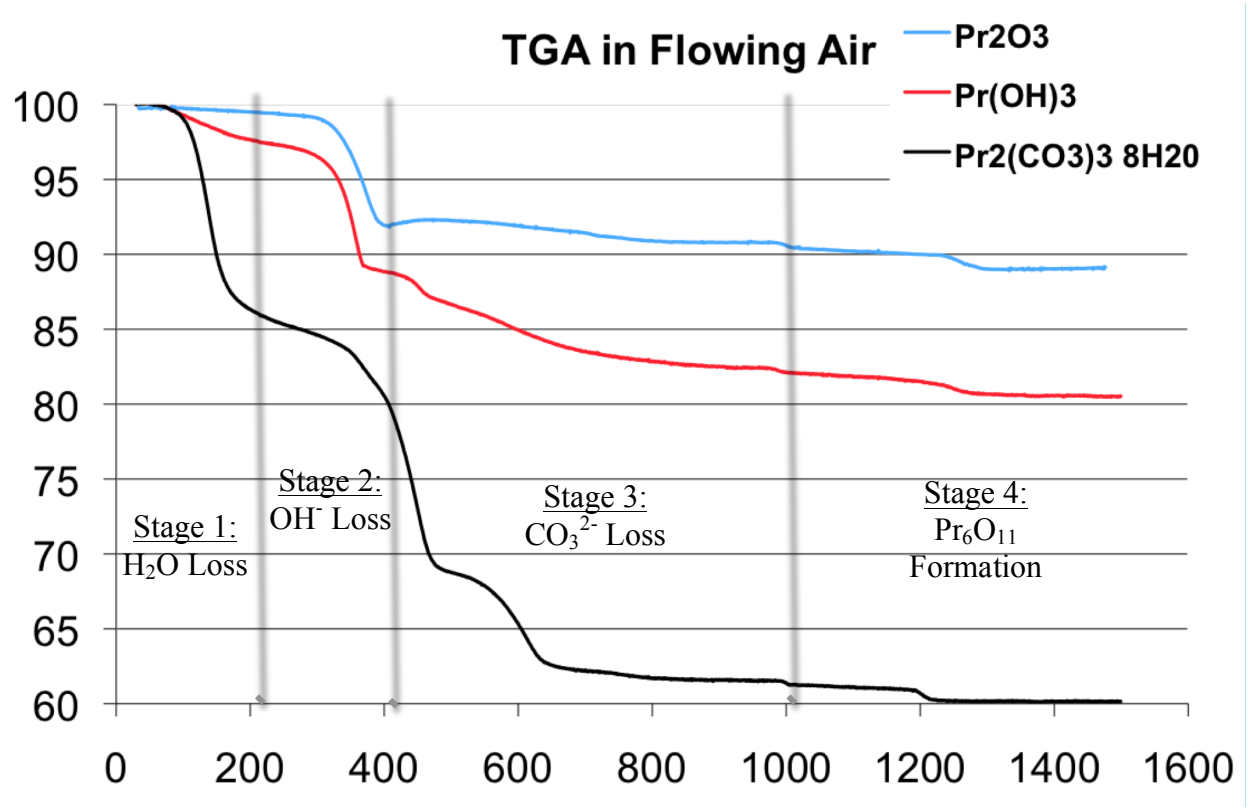

Figure 7. **Weight loss as a function of temperature by for Pr_2O_3, Pr_6O_{11}, and $Pr_2(CO_3)_3 \bullet 8H_2O$ in both air and Ar atmospheres.**

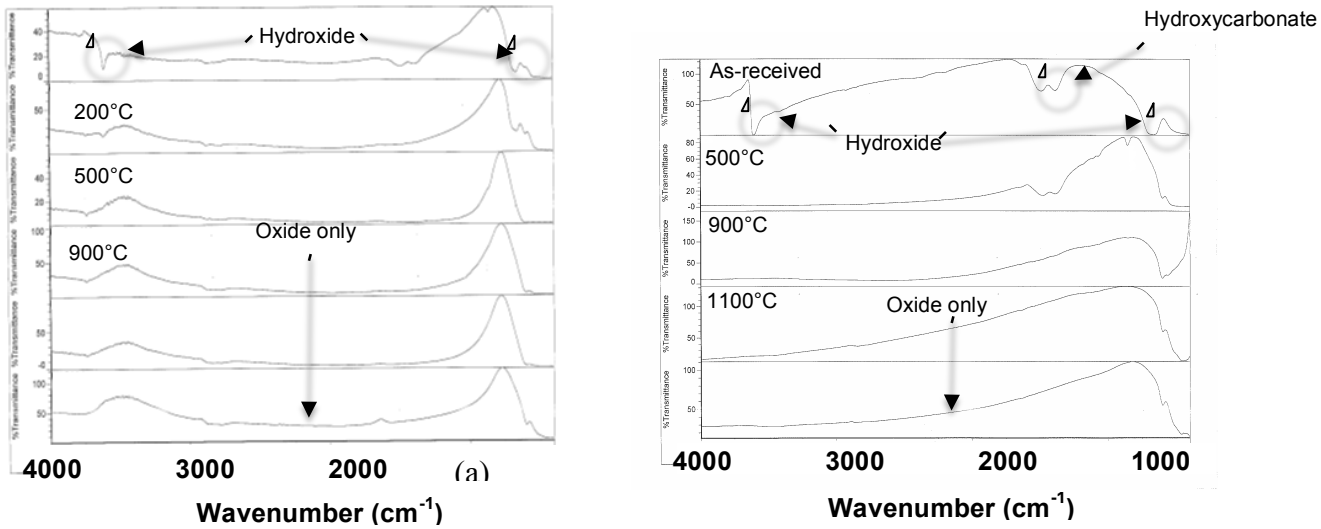

Figure 8. **Comparison of FT-IR spectra for Pr_6O_{11} (A) and Pr_2O_3 (B) after heating to various temperatures.**

For each material, the most significant mass losses were due to the loss of H_2O and/or CO_2, which also correlates to the intensity of peaks visible in the FR-IR spectra. Surface adsorbed H_2O was driven off at lower temperatures followed by bulk chemical H_2O then CO_2. Chemically combined CO_2 was not completely driven off until temperatures greater than 500°C, which correlates to FT-IR data. Also, both TGA and FT-IR results agree with previous reports that indicated that Pr_6O_{11} is more stable at elevated temperatures and more resistant to reaction with atmospheric H_2O and CO_2 under ambient conditions compared to Pr_2O_3. Characterization by XRD of both Pr_2O_3 and Pr_6O_{11} thermally treated at 1400°C indicated that the final thermal decomposition product was Pr_6O_{11} for both starting materials, further confirming the stability of Pr_6O_{11} compared to Pr_2O_3. A proposed schematic for the thermal decomposition of Pr_2O_3 based species ($Pr(OH_3)$ and $Pr_2(OH)_4(CO_3)•XH_2O$) is shown as Figure 9. The textural, structural, and chemical properties of Pr-O compounds are modified by their interaction with atmospheric H_2O and CO_2. Conditions which affect the rate and temperature at which H_2O and CO_2 are driven off during the thermal decomposition of Pr-O species include the presence of two structurally distinct hydroxyl species, and the formation of highly disordered layered CO_2/OH phases. Work will continue to confirm this model.

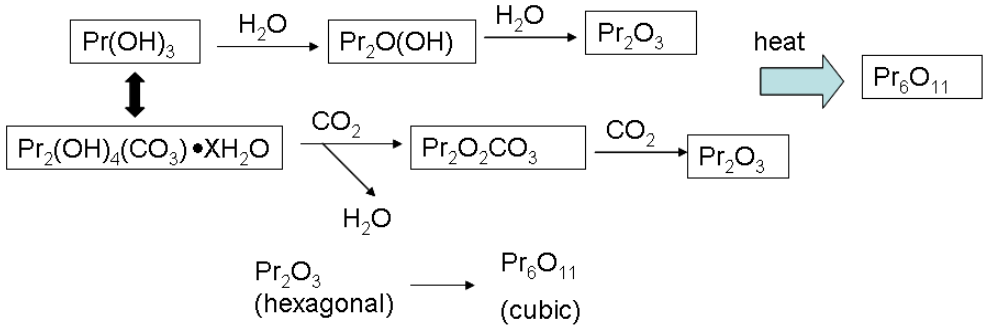

Figure 9. Proposed thermal decomposition and aging steps for Pr_2O_3 based hydroxide and hydroxycarbonate species.

To characterize evolution of structure and particle morphology during thermal decomposition, SEM images were taken of Pr_2O_3 and Pr_6O_{11} following heat treatment (Figure 10 and Figure 11). In general, both powders appeared agglomerated in the as-received condition. As Pr_2O_3 was heated, it appeared to break into finer particles at temperatures of 1100°C and above. In contrast, the Pr_6O_{11} powder appeared to remain as agglomerated particles as it was heated. At 1400°C, the Pr_6O_{11} appears to have undergone some sintering as indicated by the rounded morphology.

Initial Precipitation Studies

Precipitation studies were performed using Pr_2O_3 that was dissolved in trichloroacetic acid. Precipitation was induced by adding 1 M NaOH to solutions at room temperature or 85°C. The control sample was precipitated at room temperature from an as-prepared solution. In addition to the control material, different gases were bubbled through the Pr solution to further control the precipitation environment. Argon was bubbled through some solutions to remove other dissolved gases. Other solutions were bubbled with oxygen or CO_2 to saturate them with those

gases. In all cases, green powders precipitated at the point where the pH began to increase rapidly as NaOH was added (denoted by circles in Figure 12).

The time required for the initial formation of precipitate was dependent upon the amount of solution chemistry and the temperature of the solution. Precipitation could not proceed until acidic species were decomposed by NaOH addition. Heating the solution should increase the kinetics of the decomposition of the trichloroacetic acid, which should, in turn, require less NaOH to neutralize the solution. As shown in Figure 12, heating to 85°C resulted in precipitation with lower NaOH additions for all of the conditions. A correlation was also found between the presence of dissolved CO_2 and the solubility of the Pr species. Analysis showed that the presence of dissolved CO_2 led to precipitation at lower NaOH additions compared to samples where O_2 or argon had been bubbled through the solution. The addition of CO_2 should lead to the formation of carbonates at room temperature and hydroxycarbonates at higher temperatures, which apparently have different solubilities than species formed in CO_2 deficient conditions. Further research will be required to correlate the solubility of each precipitate to the conditions in which precipitation was induced.

Each precipitate was analyzed using XRD and SEM (Figure 13 and Figure 14). Analysis by XRD was consistent with the formation of $Pr(OH)_3$ from the as-prepared solution as well as cases where O_2 or argon were bubbled through the solutions. When CO_2 was bubbled through the solution, the precipitate was nanocrystalline, which prevented unambiguous identification of the crystalline phases by this method. Further analysis is underway to determine if the precipitate from the CO_2 saturated solution is a hydroxycarbonate species or some other material. Observation using SEM revealed that the commercial powder and the precipitates from the solutions saturated with O_2 and argon were angular crystallites that were several tens of micrometers in size. The precipitate from the CO_2 saturated solution appeared to contain a large fraction of much finer crystallites. Further analysis is planned to characterize the phases that are precipitated including FT-IR analysis, which has proven useful for identifying the presence of hydroxide and hydroxycarbonate species. In addition, precipitated powders will be characterized using DTA/TGA to evaluate their thermal stability and the steps in the decomposition to Pr_2O_3 and/or Pr_6O_{11}.

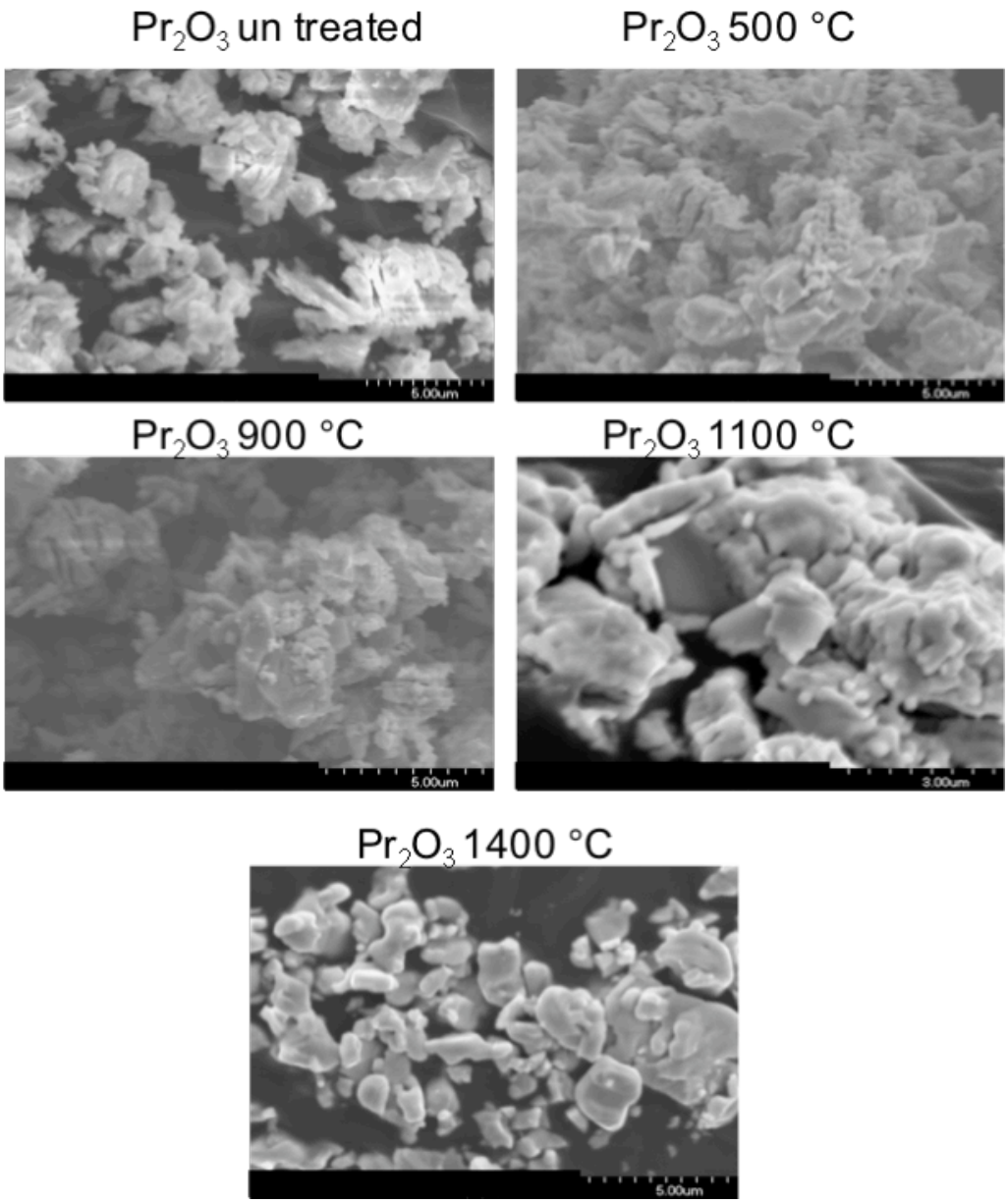

Figure 10. Micrographs of thermally treated Pr_2O_3 showing the evolution of particle morphology with temperature. Note that the magnification varies among the images.

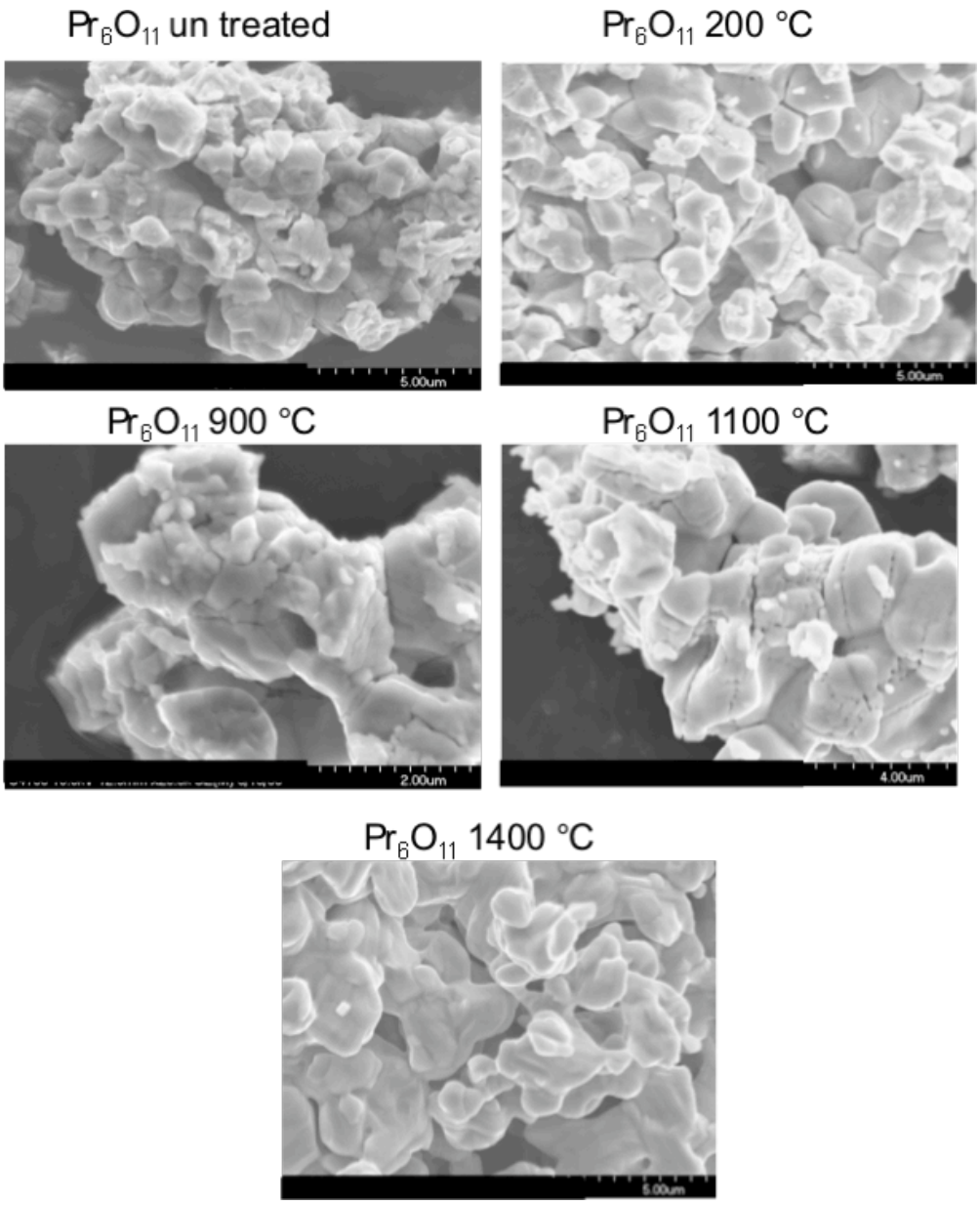

Figure 11. Micrographs of thermally treated Pr_6O_{11} showing the evolution of particle morphology with temperature. Note that the magnification varies among the images.

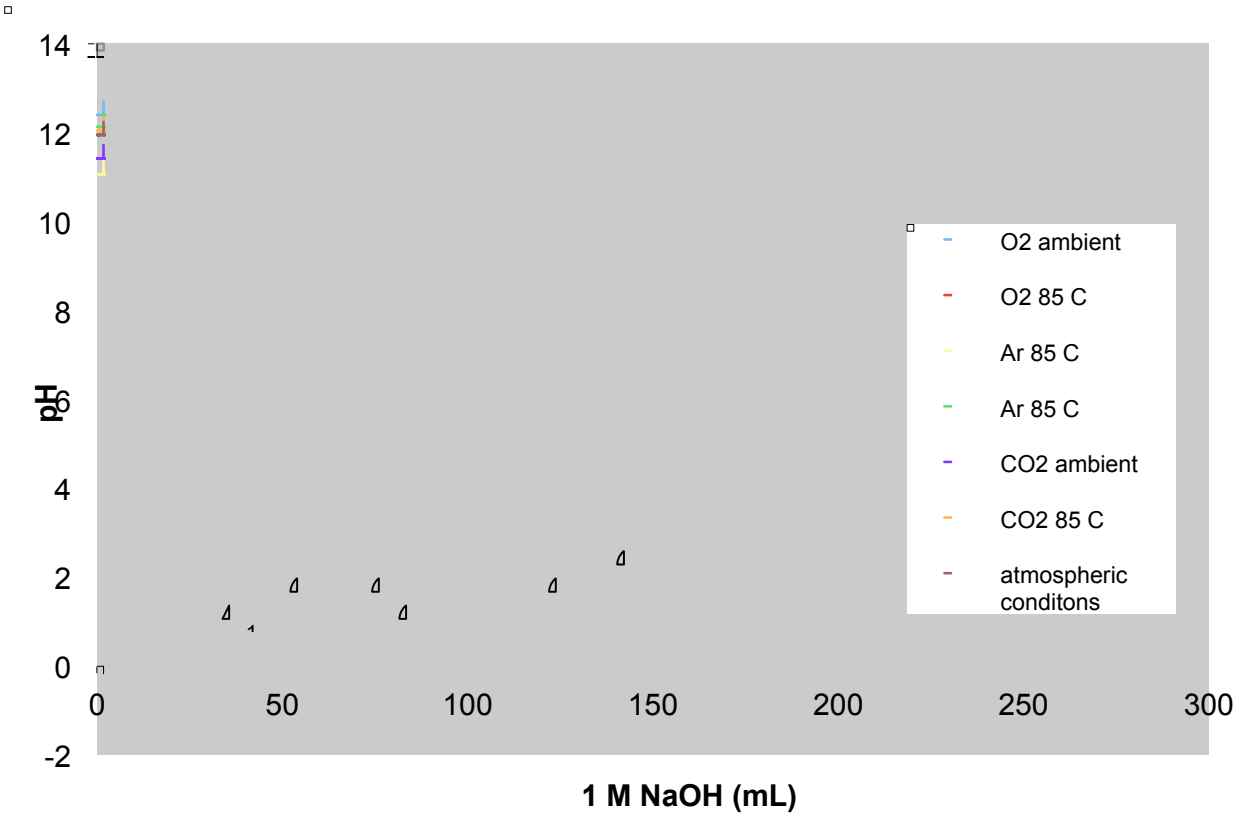

Figure 12. Precipitation curves for solvated Pr^{3+} at room temperature (nominally 25°C) or 85°C after saturating the solution with various gases.

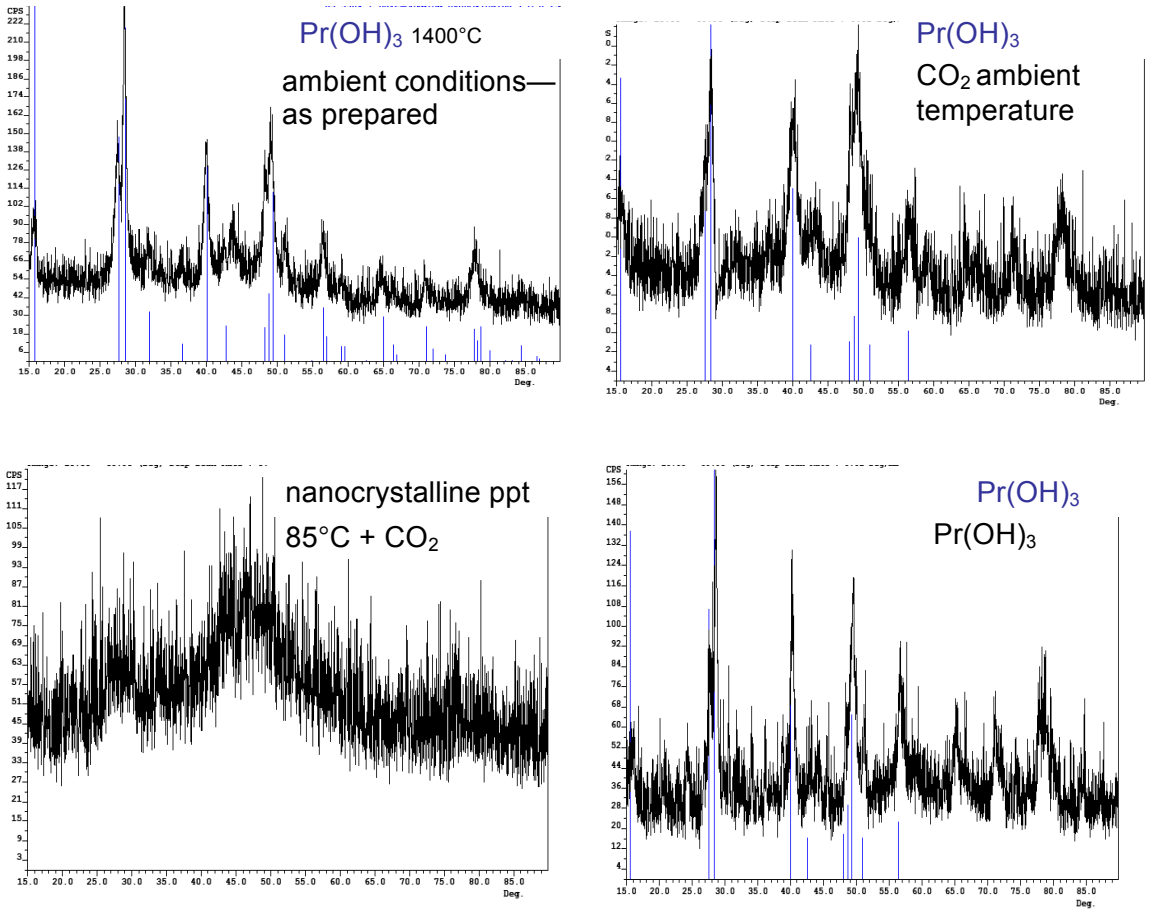

Figure 13. Representative XRD patterns for powders precipitated species from various solutions showing that $Pr(OH)_3$ formed for precipitation at room temperature and 85°C under most conditions. A nanocrystalline precipitate formed at 85°C from the solution saturated with CO_2.

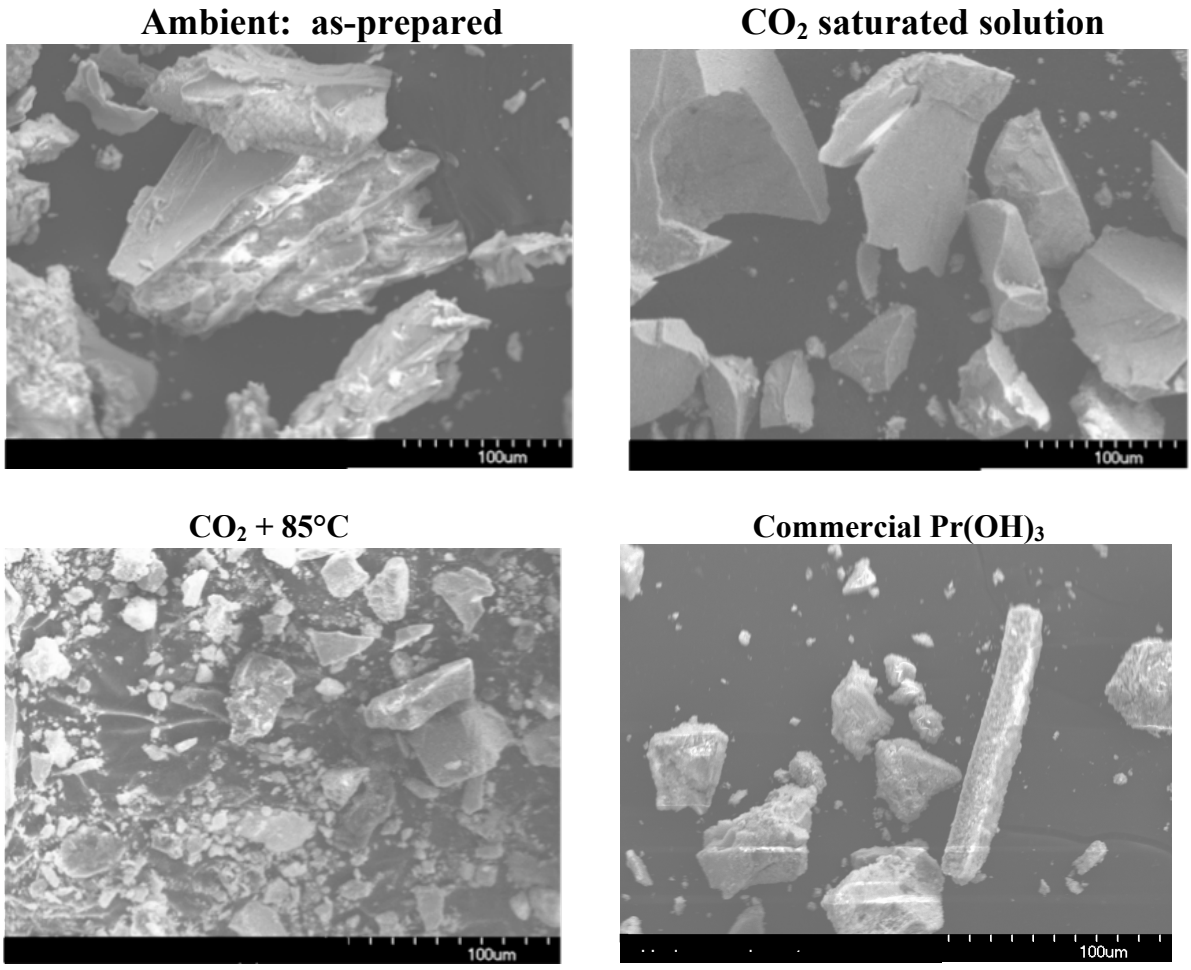

Figure 14. SEM images of powders precipitated under various conditions compared to commercial $Pr(OH)_3$.

Thermal Decomposition Behavior of Praseodymium Oxides, Hydroxides, and Carbonates
The thermal decomposition behaviors of Pr_6O_{11}, Pr_2O_3, $Pr(OH)_3$, and $Pr_2(CO_3)_3 \bullet xH_2O$ were systematically investigated by TGA/DTA, FT-IR spectroscopy, and powder XRD. In addition, morphological changes for each species were also characterized using scanning electron microscopy and surface area analysis. Pr_6O_{11}, Pr_2O_3, $Pr(OH)_3$, and $Pr_2(CO_3)_3 \bullet xH_2O$ undergo multiple step thermal decomposition processes as shown by the TGA and DTA plots in Figure 15. Each compound displayed up to six stages during thermal decomposition, which occurred between 20° C to 200 °C –Stage I, 200°C to 400°C —Stage II, 400°C to 600°C—Stage III, 600°C to 800°C—Stage IV, 800 °C to 1100°C—Stage V, and 1100°C to 1400°C—Stage VI regardless of the test atmosphere (air or Ar). Table 2 summarizes the mass loss for each compound during each decomposition stage.

Pr_2O_3 and Pr_6O_{11} that were nominally not hydrated or carbonated showed multiple stages of weight loss and reaction similar to $Pr(OH)_3$ and $Pr_2(CO_3)_3 \bullet xH_2O$. The representative peaks in the DTA up to ~1000°C were all endothermic. In addition, the peak temperatures were not affected

by whether the experiments were run in air or argon, which is consistent with the loss of adsorbed water/hydroxyl groups (-OH), or carbonate groups ($-CO_3$). These reactions are endothermic processes that should not be affected by the presence or absence of oxygen in the reaction atmosphere. Each material contained between 0.233 and 13.7 wt % surface adsorbed water that was driven off below 200°C, which accounted for the mass loss during Stage I. During Stages II and III, remaining surface water was removed and bulk chemically combined hydroxyl groups began to decompose, resulting in the largest mass loss for any thermal decomposition stage for Pr_6O_{11}, Pr_2O_3, $Pr(OH)_3$ and $Pr_2(CO_3)_3 \bullet xH_2O$.

Table 2. Mass percent losses during various ranges of thermal treatment for Pr_6O_{11}, Pr_2O_3, $Pr(OH_3)$, and $Pr_2(CO_3)_3 \bullet xH_2O$.

Temperature Range (°C)	Mass % Loss			
	Pr_6O_{11}	Pr_2O_3	$Pr(OH)_3$	$Pr_2(CO_3)_3 \bullet xH_2O$
0-200	0.233	0.492	2.35	13.7
200-400	3.24	7.57	8.81	5.76
400-600	0.335	0.0249	3.89	15.5
600-800	0.819	1.0073	2.071	3.60
800-1100	0.253	0.315	0.781	0.352
1000-1200	0.612	0.602	0.573	0.680
1200-1400	0.933	0.935	0.955	0.537
Total Mass % Loss	6.43	11.0	19.4	40.1

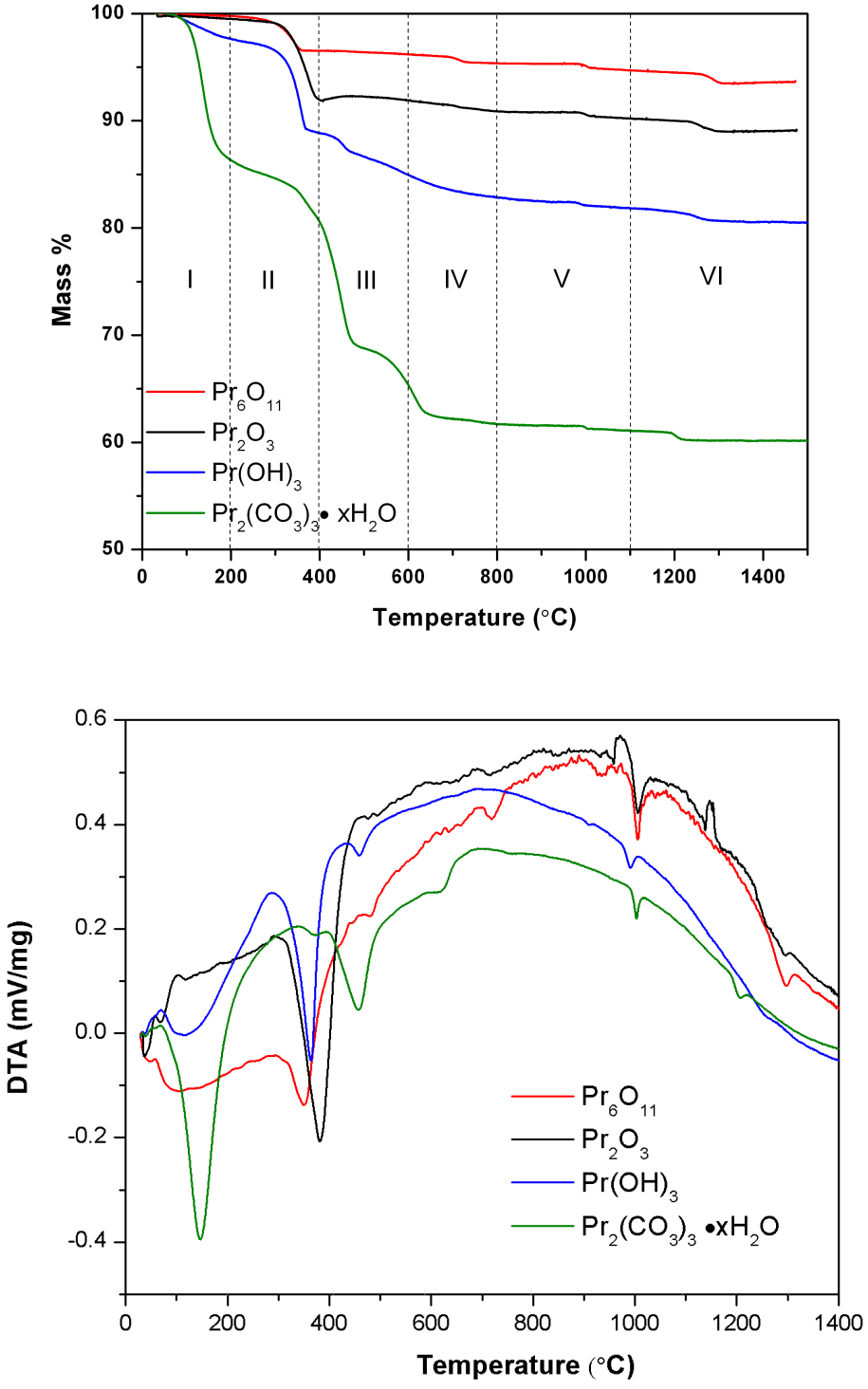

(A) (B)

Figure 15. TGA (A) and DTA (B) plots for Pr_6O_{11}, Pr_2O_3, $Pr(OH)_3$, and $Pr_2(CO_3)_3 \bullet H_2O$ heated at 20°C/min in flowing air.

Pr_2O_3, $Pr(OH_3)$ and $Pr_2(CO_3)_3 \bullet xH_2O$ experienced greater mass losses during Stages I-III than Pr_6O_{11} indicating that those materials were more readily hydrated than Pr_6O_{11}. The combined mass loss during Stages I—III quantitatively showed that Pr_6O_{11} was less reactive in the presence of atmospheric conditions, adsorbing the least amount of water among the Pr compounds. In contrast, $Pr_2(CO_3)_3 \bullet xH_2O$, had the highest content of hydrated species. The additional stage in the decomposition observed for $Pr_2(CO_3)_3 \bullet xH_2O$ and $Pr(OH)_3$, during Stage III, were most likely due to the presence of two different types of O-H bonds in these two compounds. During Stages IV-VI remaining hydroxyl groups were driven off and carbonate groups began to decompose. $Pr_2(CO_3)_3 \bullet xH_2O$ and $Pr(OH)_3$ experienced greater percent mass losses during this stage compared to Pr_2O_3 and Pr_6O_{11}, indicating the presence of carbonate species in $Pr_2(CO_3)_3 \bullet xH_2O$ and $Pr(OH)_3$. In addition, $Pr(OH)_3$ appears to have a higher reactivity towards CO_2 than Pr_2O_3 and Pr_6O_{11}.

During thermal decomposition, $Pr_2(CO_3)_3 \bullet xH_2O$ experienced the largest total mass loss at 40.1%, followed by $Pr(OH)_3$ at 19.4%, and Pr_2O_3 at 11.0%. By comparison, Pr_6O_{11} had the smallest mass loss at 6.4%. This trend in mass loss was expected as both hydroxyl groups and carbonate groups were present in bulk $Pr_2(CO_3)_3 \bullet xH_2O$ in the as-received form. $Pr(OH)_3$ was hydroxide rich, but reactive toward CO_2. As a result, it became partially carbonated, which resulted in the second greatest mass loss among the Pr compounds. Although Pr_6O_{11} was nominally a phase-pure oxide, TGA data showed that it became hydrated and/or carbonated during exposure to the ambient based on 6.4% mass loss observed by TGA. Likewise, Pr_2O_3 also reacted with the ambient and had a higher mass loss than Pr_6O_{11} during thermal decomposition. As discussed previously, Pr_6O_{11} has a cubic crystal structure whereas Pr_2O_3 has a hexagonal crystal structure, which makes Pr_2O_3 more likely to combine with both H_2O and CO_2. The thermal decomposition of Pr_6O_{11}, Pr_2O_3, $Pr(OH)_3$ and $Pr_2(CO_3)_3 \bullet xH_2O$ were all dictated by the state of hydration and/or carbonation.

FT-IR analysis was employed to confirm the changes in hydroxyl and/or carbonate losses as a function of thermal treatment temperature in air. Other techniques such as XRD were not sensitive to the presence/absence of what were presumed to be primarily surface species. Spectra were taken for powders that had been heated to specific temperatures near which mass losses were observed by TGA. The spectra are shown in Figure 16. According to Bernal et al., Rosynek et al., Caro et al., and Zubova et al., the sharp band at ~3600 cm^{-1} is due to O-H stretching in surface adsorbed/chemically combined H_2O for light Ln_2O_3 species [18-20,43,51,84,85]. According to Bernal et al., Dextpert et al, and Rosynek et al., the broad band observed in the range of ~1300-1500 cm^{-1} is due to the C=O stretch and can be assigned to hydroxycarbonate-like phases ($PrOHCO_3$), which result from chemically combined CO_2 [20,43,84]. Based on these assignments, each mass loss between Stages I-VI can be attributed to H_2O/-OH and/or CO_2 being driven off. During thermal decomposition, surface adsorbed H_2O was driven off first (~300°C), followed by bulk chemically combined H_2O. Chemically combined CO_2 required higher temperatures (~700°C-800 °C) for removal [86]. Following thermal treatment up to 800°C (Stages I-VI) H_2O and/or CO_2 were removed from each material, which accounted for the mass loss observed by TGA and disappearance of bands at ~3600 cm^{-1} and ~1300-1500 cm^{-1} observed in FT-IR spectra. Stage VI was the final stable stage for each compound and no further reactions or weight losses were observed after thermal treatment to 1300 °C.

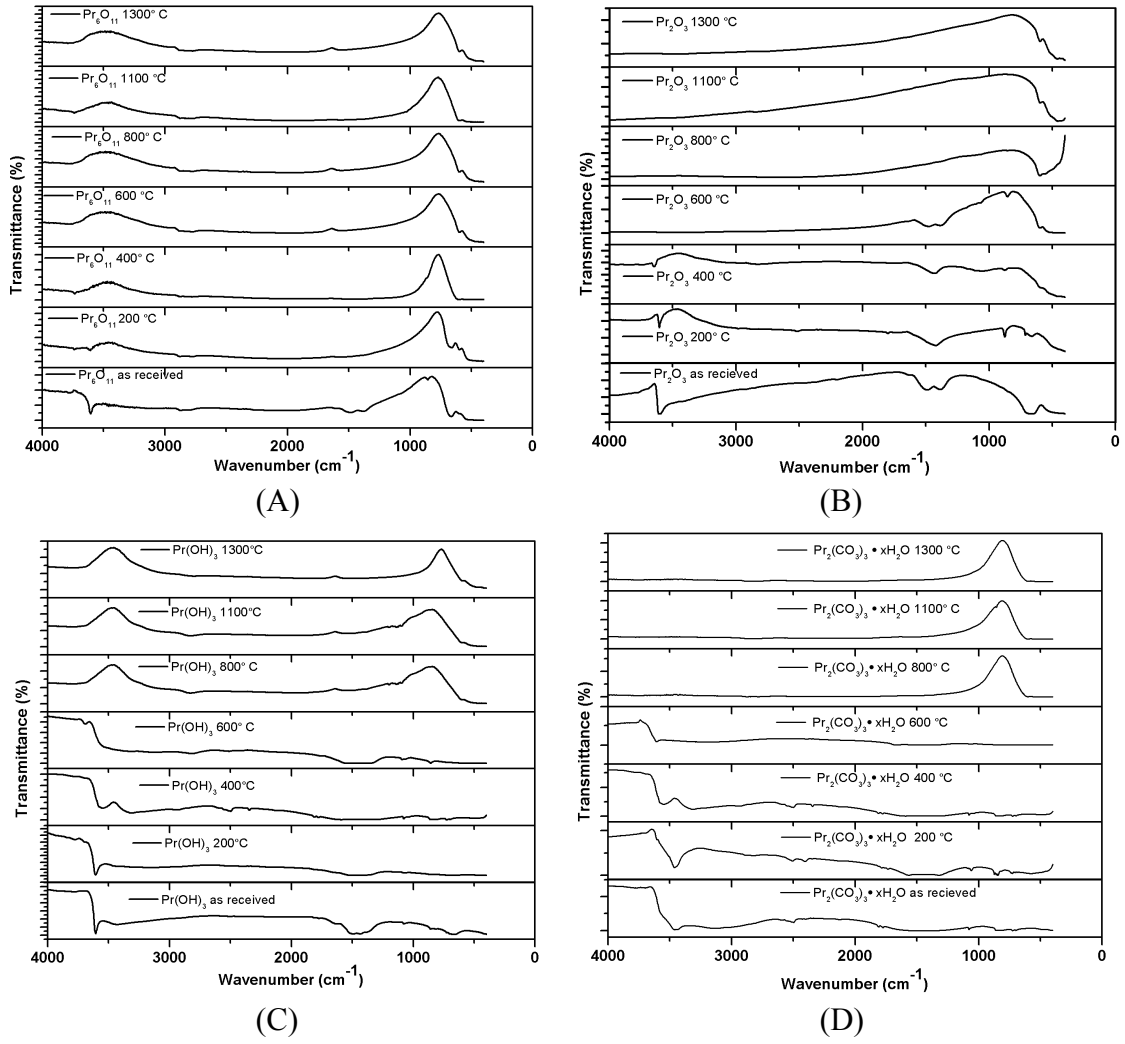

Figure 16. FT-IR spectra of Pr_6O_{11} (A), Pr_2O_3 (B), $Pr(OH_3)$ (C), and $Pr_2(CO_3)_3 \bullet xH_2O$ (D) prior to thermal treatment and after heating in air to temperatures ranging from 200°C to 1300°C.

In addition to FT-IR characterization, Pr_6O_{11}, Pr_2O_3, $Pr(OH)_3$, and $Pr_2(CO_3)_3 \bullet xH_2O$ powders were also characterized using powder XRD in the as- received condition and after thermal treatments (Table 3 and Figure 17).

Table 3. Summary of intermediate and final phases as determined by XRD for the as-received compounds and after heat treatment to various temperatures.

Phase	As Received	200 C	400 C	600 C	800 C	1100 C	1300 C
Pr_2O_3	Pr_2O_3 $Pr(OH)_3$	Pr_2O_3 $Pr(OH)_3$	Pr_2O_3 $Pr(OH)_3$ Pr_6O_{11}	Pr_6O_{11}	Pr_6O_{11}	Pr_6O_{11}	Pr_6O_{11}
Pr_6O_{11}	Pr_6O_{11} PrO_2	Pr_6O_{11} PrO_2	Pr_6O_{11}	Pr_6O_{11}	Pr_6O_{11}	Pr_6O_{11}	Pr_6O_{11}
$Pr(OH)_3$	$Pr(OH)_3$	$Pr(OH)_3$	$Pr(OH)_3$	Pr_6O_{11}	Pr_6O_{11}	Pr_6O_{11}	Pr_6O_{11}
$Pr_2(CO_3)_3 \bullet xH_2O$	$Pr(CO_3)OH$	$Pr(CO_3)OH$	$Pr(CO_3)OH$	$Pr_2O_2CO_3$	Pr_6O_{11}	Pr_6O_{11}	Pr_6O_{11}

XRD did not detect crystalline hydroxide or carbonate containing species in Pr_6O_{11}. Likewise, TGA data showed that Pr_6O_{11} experienced about half the weight loss of Pr_2O_3. In addition, FT-IR analysis indicated a decreased presence of carbonate and hydroxide groups of Pr_6O_{11} compared to Pr_2O_3. When exposed to room temperature air, Pr_6O_{11} reacted to form PrO_2 and $Pr(OH)_3$. The reaction was slow at 20°C, but rapid at 100° C [23]. As part of the present study, diffraction patterns were collected at ambient temperature (~20 °C) for each powder, which likely limited the extent of hydration or disproportionation of Pr_6O_{11}. As reported by others, the cubic form of Pr_6O_{11} appeared to be more resistant to the effects of hydration and carbonation than other oxides with different stoichiometries and crystal structures [16,39].

Analysis by XRD and FT-IR confirmed that thermal treatment up to 800°C decomposed hydroxide and carbonate species present in Pr_2O_3, $Pr(OH)_3$, and $Pr_2(CO_3)_3 \bullet xH_2O$. After heating to at least 900°C, all of the Pr compounds were converted to Pr_6O_{11}, which is in agreement with previous studies [14,87-90]. XRD showed that all of the species were in the form of cubic Pr_6O_{11} after the mass loss in Stage IV and they all appeared to be in the phase of Pr_6O_{11} after the mass losses in Stages V and VI. The mass losses in the latter stages are likely due to oxygen loss or non-stoichiometry. During thermal decomposition, the oxygen to Pr ratios (denoted "x") changed as Pr_2O_3 (x = 1.5), $Pr(OH)_3$ (x = 3), and $Pr_2(CO_3)_3 \bullet xH_2O$ (x = 4.5) were converted to Pr_6O_{11} (x=1.83 for Pr_6O_{11}). Pr oxides comprise different stoichiometries and structures including intermediate oxygen-deficient modifications and phases of the fluorite structure type that are denoted PrO_x, where x=1.833, 1.810, 1.800, 1.780, 1.714, 1.667 [91]. It may not have been possible to differentiate these intermediate oxide phases by XRD or account for the weight losses experienced in Stages V-VI.

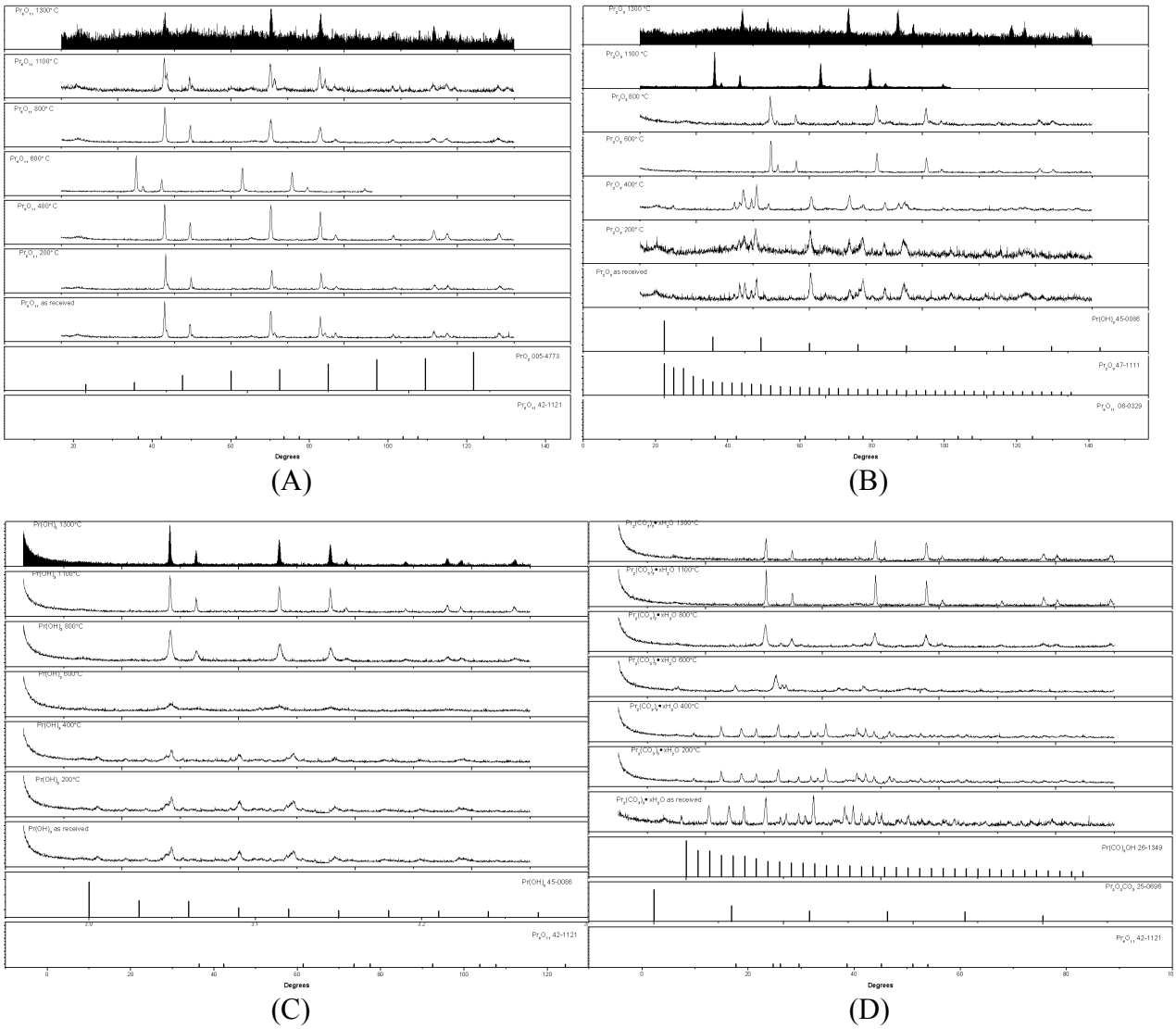

Figure 17. XRD patterns for Pr_6O_{11} (A), Pr_2O_3 (B), $Pr(OH_3)$ (C), and $Pr_2(CO_3)_3 \bullet xH_2O$ (D) as-received and after heat treatment to various temperatures.

The texture, crystal structure, and chemistry of Pr_6O_{11}, Pr_2O_3, $Pr(OH)_3$, and $Pr_2(CO_3)_3 \bullet xH_2O$ were modified by their interaction with atmospheric H_2O and CO_2. Decomposition temperatures and kinetics differed in the presence of water or CO_2 [91]. Conditions that affected the rate and temperature at which H_2O and CO_2 are driven off during thermal decomposition of Pr_2O_3, $Pr(OH)_3$, and $Pr_2(CO_3)_3 \bullet xH_2O$ included the presence of two structurally distinct hydroxyl species and the formation of highly disordered layered CO_2/OH phases. A representative schematic of summarizing the species driven off and phase transformations that take place during the thermal decomposition of Pr_6O_{11}, Pr_2O_3, $Pr(OH)_3$, and $Pr_2(CO_3)_3 \bullet xH_2O$ the can be seen in Figure 18. Each arrow represents the species driven off and number of stages required for the starting material to reach the final stable phase as determined by XRD.

Solid state reactions in the bulk and on the surface of rare earth sesquioxides induce morphological modifications in addition to compositional changes [47,87,90]. To characterize evolution of particle morphology during thermal decomposition, SEM images were collected for Pr_6O_{11}, Pr_2O_3, $Pr(OH_3)$, and $Pr_2(CO_3)_3 \bullet xH_2O$ powders in the as received condition (Figure 19) and following thermal treatment at 1300° C (Figure 20).

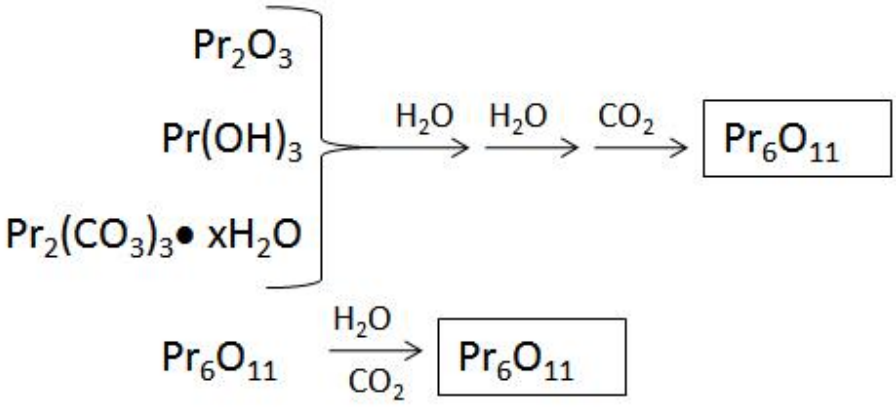

Figure 18. The thermal evolution of Pr_6O_{11}, Pr_2O_3, $Pr(OH)_3$, and $Pr_2(CO_3)_3 \bullet xH_2O$ as determined by TGA/DTA, FT-IR, and XRD characterization.

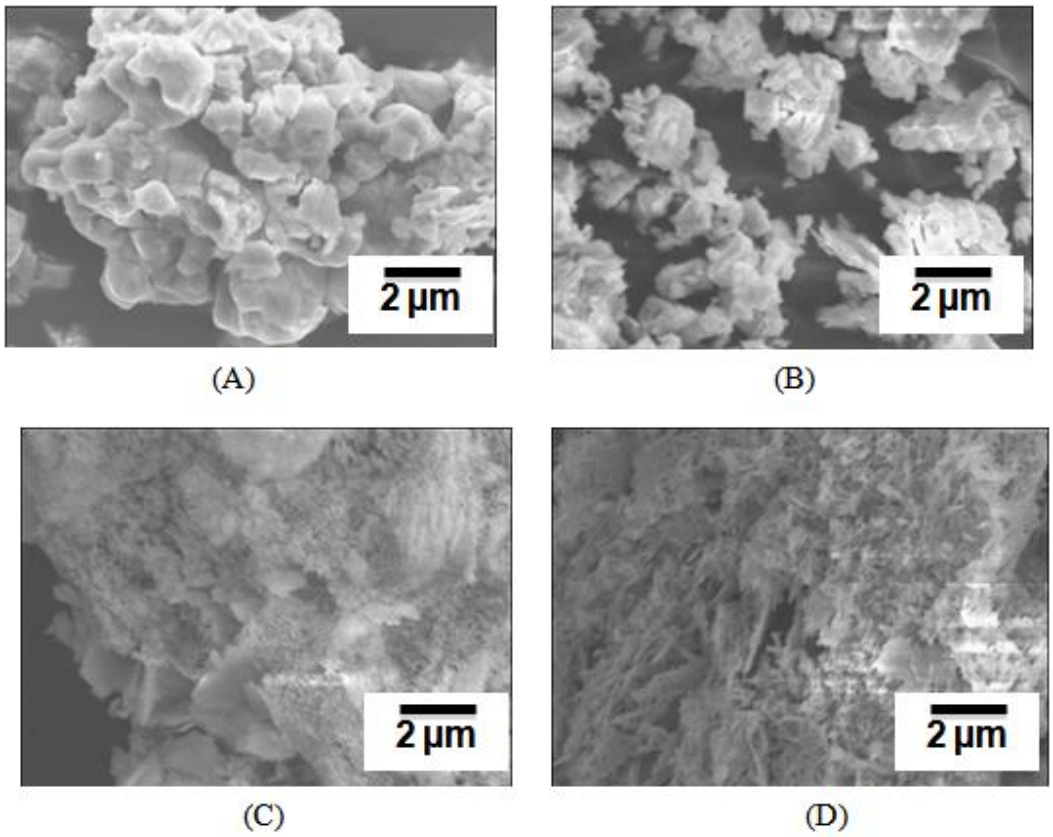

Figure 19. SEM micrographs of Pr_6O_{11}(A), Pr_2O_3 (B), $Pr(OH_3)$ (C), and $Pr_2(CO_3)_3 \bullet xH_2O$ (D) in the as received condition.

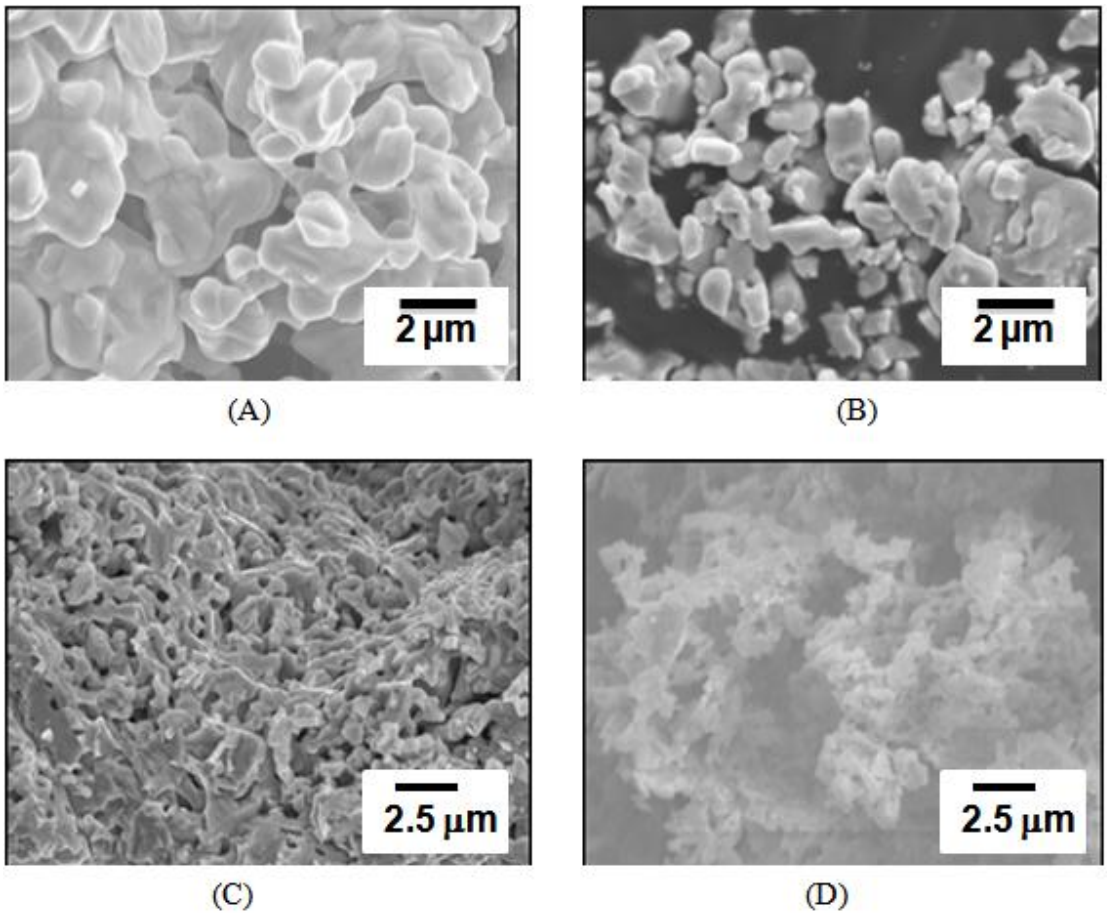

Figure 20. SEM micrographs of Pr_6O_{11} (A), Pr_2O_3 (B), $Pr(OH_3)$ (C), and $Pr_2(CO_3)_3 \bullet xH_2O$ (D) after thermal treatment at 1300°C. Please note the magnification change in (C) and (D) necessary to show the various features.

In general, all powders appeared agglomerated in the as-received condition. BET surface area analysis was performed on each of the powders in the as-received and thermally treated condition (Table 4). In addition, equivalent spherical radii were calculated for each of the materials using the measured surface area and the theoretical density for each compound [92-95]. The surface area of $Pr(OH)_3$ decreased by more than an order of magnitude, which was the greatest decrease. Next, the surface area of Pr_2O_3 decreased by a factor of ~7, $Pr_2(CO_3)_3 \bullet xH_2O$ by about 5, and Pr_6O_{11} by about 2. The as- received Pr_6O_{11} particles pictured in Figure 19(A) had an equivalent spherical diameter calculated from surface area of 0.077 µm and were composed of rounded particles made up of several grains as indicated by the fissures present in the image. Pr_2O_3 (Figure 19(B)) had a different morphology, consisting of layered, platelet-like particulates with a smaller calculated radius of 0.18 µm. $Pr(OH)_3$ and $Pr_2(CO_3)_3 \bullet xH_2O$ (Figure 19(C) and (D)) appeared to be agglomerates that consisted of smaller crystallites based on the highly textured surface morphologies. The $Pr(OH)_3$ (Figure 19 (C)) was composed of fine equiaxed crystallites that had a calculated radius of 0.017 µm. The crystallites that made up the $Pr_2(CO_3)_3 \bullet xH_2O$ agglomerates (Figure 19(D)) appeared to be acicular, which gave them a smaller surface area (3.8 m^2/g) and a larger equivalent radius (0.17 µm).

Table 4. Summary of specific surface area and radius of each sample material as determined by BET analysis prior to and post thermal treatment at 1300° C.

Sample Material	Theoretical Density (g/cm^3)	Condition	Specific Surface Area (m^2/g)	Radius (μm)	Correlation Coefficient
Pr_6O_{11}	6.950	As Received	5.6	0.077	0.999
		1300 °C	2.4	0.18	0.994
Pr_2O_3	7.060	As Received	2.5	0.17	0.999
		1300 °C	0.34	1.26	0.993
$Pr(OH)_3$	3.095	As Received	58.6	0.017	0.999
		1300 °C	4.9	0.20	0.999
$Pr_2(CO_3)_3 \bullet xH_2O$	4.686	As Received	3.8	0.17	0.999
		1300 °C	0.68	0.94	0.999

Heating the as-received powders to temperatures of 1300°C or higher appeared to cause significant changes in the particle morphologies (Figure 20). The Pr_6O_{11}, Pr_2O_3, and $Pr(OH)_3$ powders appeared to have undergone coarsening and/or densification by sintering processes when it was heated to 1300°C as indicated by the rounded particle surfaces. For example, heat treatment caused the surface area of Pr_6O_{11} to decrease from 5.6 m^2/g to 2.4 m^2/g with a corresponding increase in the equivalent particle radius from 0.077 μm to 0.18 μm. Similarly, Pr_2O_3 and $Pr(OH)_3$ showed decreased surface area and increased equivalent spherical radius after heat treatment (Table 4). In contrast, $Pr_2(CO_3)_3 \bullet xH_2O$ did not experience a significant change in morphology, although the surface area decreased while the calculated particle radius increased. BET surface area analysis along with collected micrographs show that while each product is in the phase of Pr_6O_{11}, the surface area and morphology differed. The presence of hydroxyl groups and carbonate groups had an effect on the surface area of the initial species and final product of thermally decomposed species of Pr_6O_{11}, Pr_2O_3, $Pr(OH_3)$, and $Pr_2(CO_3)_3 \bullet xH_2O$. Based on the changes in morphology exhibited post thermal treatment at 1300°C depicted in Figure 20 for Pr_6O_{11}(A), Pr_2O_3 (B), $Pr(OH_3)$ (C), and $Pr_2(CO_3)_3 \bullet xH_2O$ (D), the decreased in surface area for each powder can be attributed to sintering effects, which changed particle morphology.

Disproportionation of Pr_6O_{11}

Pr_6O_{11} reacts in the presence of H_2O to form PrO_2 and $Pr(OH)_3$. Phase stability studies focused on the effects of reaction with hydrated and anhydrous sulfate salts, solvent, temperature, and time on the disproportionation of Pr_6O_{11}. Samples were prepared under static conditions consisting of 1 g Pr_6O_{11}, 3 g $Ca_2SO_4 \bullet 2H_2O$ or Ca_2SO_4, and 10mL H_2O or Oxall (parachlorobenzotrifluoride). A summary of the phases present after reaction at each condition as determined by XRD can be seen in Table 5.

Table 5. A summary of the phases present after reaction at each conditions as determined by XRD when Pr_6O_{11} was reacted in various environments consisting of hydrated or anhydrous sulfate salts, solvent, temperature, and time.

Starting Compound	Time	Temperature (C°)	Solvent	Ca_2SO_4 phase	Final Phases Present
Pr_6O_{11}	3 hours 18 hours 24 hours 2 days	20	Oxall	Anhydrous	Pr_6O_{11}
Pr_6O_{11}	3 hours 18 hours 24hours 2 days	20	H_2O	Anhydrous	Pr_6O_{11}
Pr_6O_{11}	3 hours 18 hours 24 hours 2 days	20	Oxall	Dihydrate	Pr_6O_{11}
Pr_6O_{11}	3 hours 18 hours	20	H_2O	Dihydrate	Pr_6O_{11}
	24 hours 2 days	20	H_2O	Dihydrate	Pr_6O_{11}, PrO_2
Pr_6O_{11}	3 hours 18 hours 24 hours 2 days	85	Oxall	Anhydrous	Pr_6O_{11}
Pr_6O_{11}	3 hours 18 hours 24 hours 2 days	85	H_2O	Anydrous	PrO_2, $Pr(OH)_3$
Pr_6O_{11}	3 hours	85	Oxall	Dihydrate	Pr_6O_{11}
	18 hours	85	Oxall	Dihydrate	Pr_6O_{11}, PrO_2
	24 hours 2 days	85	Oxall	Dihydrate	PrO_2, $Pr(OH)_3$
Pr_6O_{11}	3 hours 18 hours 24 hours 2 days	85	H_2O	Dihydrate	PrO_2, $Pr(OH)_3$
Pr_6O_{11}	1 hour	100	Oxall	Anydrous Dihydrate	Pr_6O_{11}
	1 hour	100	H_2O	Anydrous Dihydrate	PrO_2, $Pr(OH)_3$

Pr_6O_{11} decomposed to PrO_2 during 24 hours at 20°C in the presence of a hydrated sulfate salt and H_2O. After 18 hours at 85°C in the presence of a hydrated sulfate salt and an organic solvent (Oxall), PrO_2 was detected. It took 24 hours at 85°C in the presence of a hydrated sulfate salt and Oxall for PrO_2 and $Pr(OH)_3$ to form. After 3 hours at 85°C in the presence of either a hydrated or anhydrous sulfate salt and H_2O, both PrO_2 and $Pr(OH)_3$ were detected. After 1 hour at 100°C in the presence of a hydrated or anhydrous sulfate salt and H_2O, both PrO_2 and $Pr(OH)_3$ were produced. An increase in temperature and H_2O present as solvent increased the rate at which disproportionation by $Pr_6O_{11} \rightarrow PrO_2 + Pr(OH)_3$ proceeded. Pr_6O_{11} will disproportionate in an

organic medium nominally free of water if hydrated sulfate salts were present, or in water alone regardless if hydrated or anhydrous sulfate salts were present in the system.

Pr-H_2O-CO_2 Phase Stability

Precipitation studies were conducted to study the effect of CO_2 on phase stability in the Pr-H_2O system. Solvated praseodymium species were precipitated under various conditions including temperatures from ambient up to 85°C in 25% tricholoroacetic acid saturated with gases including Ar, O_2, and CO_2. The effects of temperature and dissolved gas composition were evaluated. Analytical characterization of the precipitated powders was performed using XRD, SEM, FT-IR, BET analysis, and gravimetric analysis in order to characterize the composition, crystal structure, morphology, particle size, and solubility of the phases precipitated under different conditions.

The control sample was precipitated at room temperature from an as-prepared solution. In addition to the control material, different gases were bubbled through the Pr^{3+} solution to further control the precipitation environment. Argon was bubbled through some solutions to remove other dissolved gases. Other solutions were bubbled with O_2 or CO_2 to saturate them with those gases. The time required for the initial formation of precipitate was dependent upon the amount of solution chemistry and the temperature of the solution. Precipitation could not proceed until acidic species were decomposed by NaOH addition. In all cases, green powders precipitated at the point where the pH began to increase rapidly as NaOH was added. The resultant precipitate (green powders) from each condition begins to fall out of solution at point before the pH began to rapidly increase to approximately 4.5-5.5. The precipitates were collected by filtration, rinsed with deionized water, and dried prior to characterization. The amount of NaOH required to precipitate Pr-species under each set of conditions can be seen in Figure 21.

A distinct correlation was found between the presence of dissolved CO_2 and the onset of precipitation. In the presence of CO_2, less base (equivalents of 1 M NaOH) was required to start precipitation. Heat had a minimal effect on solubility of the precipitate in the presence of CO_2, but the presence of O_2 and Ar resulted in delayed precipitation as temperature increased. The precipitate was the least soluble at ambient temperature in an O_2 rich environment. Analysis of precipitated Pr-based powders showed that CO_2 played an important factor in the solubility of Pr^{3+} species. The presence of CO_2, either added to the system intentionally or dissolved into solution by exposure of the water to the ambient atmospheric conditions, increased the solubility of Pr-species. Heating the Pr^{3+} solution in a CO_2 free environment increased the rate of precipitation of Pr-species compared to samples precipitated at ambient temperature.

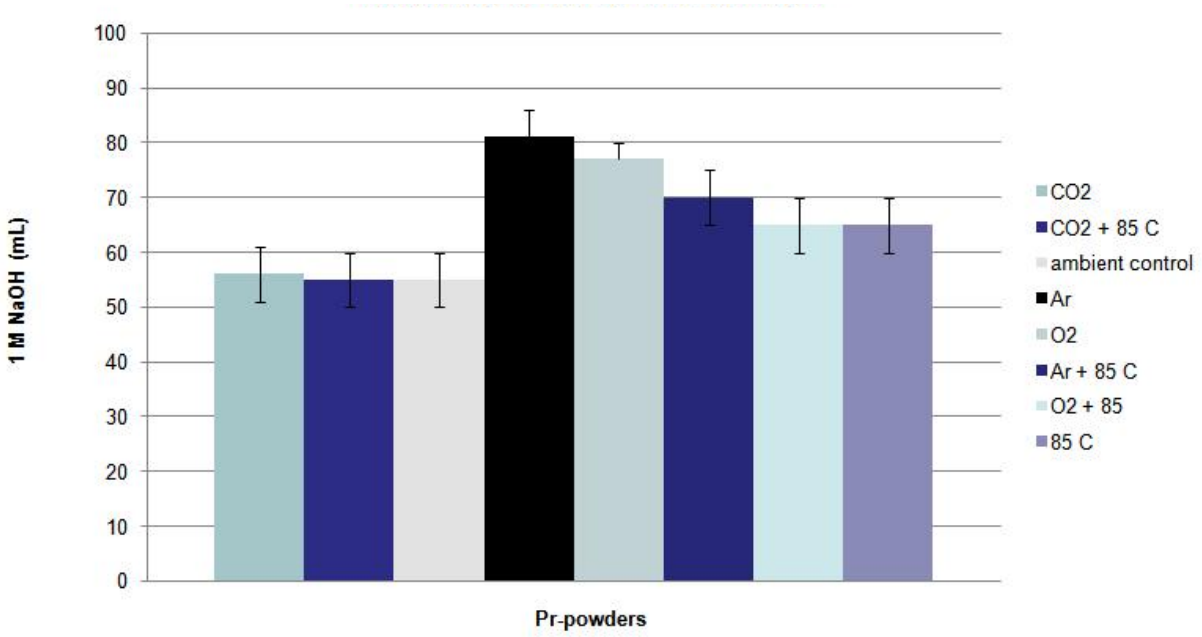

Figure 21. Volume of NaOH required to induce precipitation of Pr-species under various conditions.

Analysis by XRD was consistent with the formation of $Pr(OH)_3$ from the as-prepared solution as well as ambient where O_2, Ar, or CO_2 were bubbled through the solutions. Cases where the solution was heated to 85°C with O_2 and Ar were added via bubbling through the solution also were identified as $Pr(OH)_3$ by XRD. When CO_2 was bubbled through the solution kept at 85°C, the precipitate was nanocrystalline, which prevented unambiguous identification of the crystalline phases by XRD. Using FT-IR analysis, both –OH (~3600 cm^{-1}) and CO_3 (~1500-1600 cm^{-1}) functional groups were detected in each precipitate (Figure 22) indicating the presence of a hydroxycarbonate phase. Previous research by other groups on the Pr_2O_3-H_2O phase indicate that nucleation of a hydroxycarbonate phase occurs on the outer layers of a bulk hydroxide, which produces a nucleus of $Pr(OH)_3$ overcoated by the carbonate phase [23]. Therefore, a precipitated hydroxide, or one which is prepared under conditions with CO_2 present, will be slightly carbonated. Some extent of hydration appears to be favored over complete carbonation under all conditions, since all of the species contained hydroxyl groups regardless of precipitation conditions.

The microstructure of each precipitated powder was investigated via SEM and BET surface area analysis. SEM revealed that the commercial powder and the precipitates from the solutions saturated with O_2 and argon were angular crystallites that were several tens of micrometers in size. The precipitate from the CO_2 saturated solution appeared to contain a large fraction of much finer crystallites, regardless of whether the precipitation was performed at ambient temperature or 85°C. BET Surface Area Analysis was performed on each powder, a data table can be seen in Table 6. The equivalent radius of each material was calculated using the theoretical density of $Pr(OH)_3$=3.095 g/cm^3 [94].

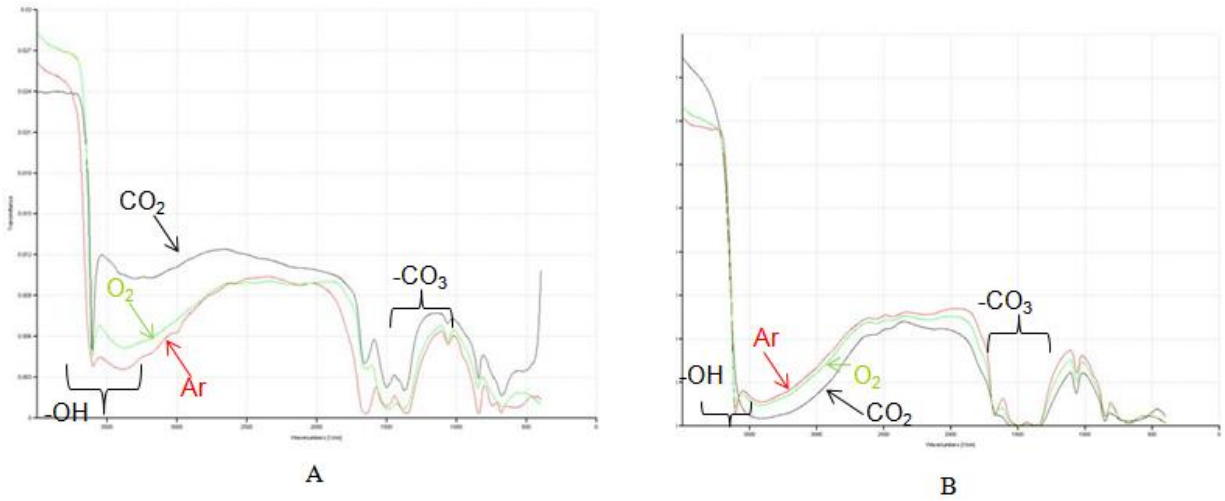

Figure 22. FT-IR spectra of (A) precipitation at ambient temperature and (B) precipitation and 85 °C.

Table 6. Summary of surface area and calculated radii of precipitated Pr-powders under various sets of conditions.

Sample	Surface Area (g/cm^3)	Specific Surface Area (m^2/g)	Radius (nm)	Correlation Coefficient
Control (room temperature/atmospheric conditions)	3.095	55.4	17.51	0.999
85 C (atmospheric conditions)	3.095	7.29	132.9	0.999
CO_2	3.095	16.4	59.22	0.999
CO_2 + 85 C	3.095	5.10	191.3	0.999
Ar	3.095	24.0	40.32	0.999
Ar + 85 C	3.095	5.21	186.1	0.999
O_2	3.095	26.3	36.88	0.999
O_2 + 85 C	3.095	31.5	30.73	0.999

The powder with the highest specific surface area (55.4 m^2/g) was the control specimen prepared under ambient conditions. Other powders produced at ambient temperature in solutions saturated with CO_2 (16.4 m^2/g), Ar (24.4 m^2/g), or O_2 (26.3 m^2/g) had similar specific surface areas, but were not as large as the powder produced in the control experiment. The addition of heat yields similar specific areas for each sample prepared with the addition of heat (CO_2—5.10 m^2/g and Ar—5.21 m^2/g) except for the sample prepared with the addition of O_2 (31.5 m^2/g). The powder produced with the addition of heat and O_2 had an order of magnitude higher specific surface area compared to other materials prepared in the presence of heat. The presence of CO_2, either added to the system intentionally or dissolved into solution by exposure of the water to the ambient atmospheric conditions, increased the solubility of hydroxycarbonate species. The

addition of heat to the system during precipitation will yield Pr-based powders with smaller radii when compared to powders precipitated under the same conditions at ambient temperatures except with the addition of excess O_2. The radius of each Pr-powder particle was calculated and the results are listed in order of largest particle radius to smallest particle radius. CO_2+ 85° C (191.3 nm)→ Ar at 85° C (186.1 nm) → atmospheric conditions at 85° C (132.9 nm) →CO_2 at ambient temperature (59.22 nm)→ Ar at ambient temperature (40.32 nm) →O_2 at ambient temperature (36.88 nm) → O_2+ 85° C (30.73 nm) → atmospheric conditions at ambient temperature (17.51 nm). Except in the presence of O_2, the addition of heat causes particles to precipitate out of solutions with larger radii.

Gravimetric analysis was performed on Pr-powders precipitated from solvated Pr_2O_3 and as received $PrCO_3OH$ and $Pr(OH)_3$ in order to determine the effects of particle size/powder preparation on the solubility of each species (Figure 23).

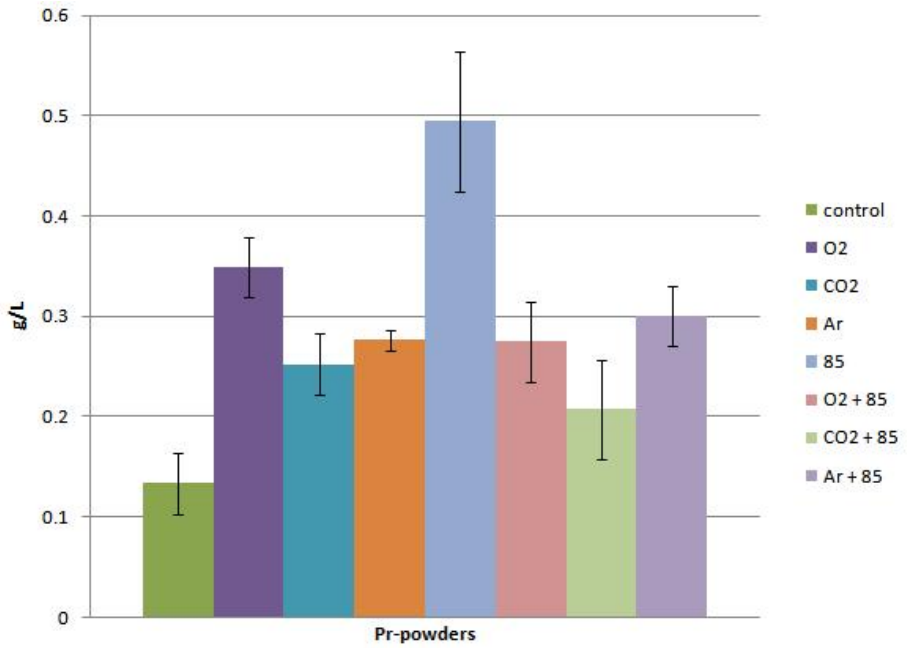

Figure 23. Solubility of each precipitate powder produced under various conditions in g/L.

The Pr-powder precipitated at atmospheric conditions at 85° C was the most soluble with an average of 0.495 ± 0.06 g/L followed by the powder precipitated in the presence of O_2 at ambient temperature (0.349 ± 0.03 g/L), and Ar at 85° C (0.301 ± 0.03 g/L), which were not statistically different as calculated by the student t-test. The Pr-powder precipitated with CO_2 at ambient temperature (0.253 ± 0.03 g/L), Ar at ambient temperature (0.277 ± 0.01 g/L), O_2+ 85° C (0.275 ± 0.04 g/L), CO_2+ 85° C (0.207 ± 0.05 g/L), and Ar at 85° C (0.301 ± 0.03 g/L) were less soluble and all were not statistically different as calculated by the student t-test. The least soluble Pr-powders were precipitated at atmospheric conditions at ambient temperature (0.191 ± 0.10 g/L). For powders of nominally the same composition, particles with smaller radii would be easier to disperse and be more soluble, but the results do not follow this trend. The Pr-powder with one of

the largest radii (atmospheric conditions at 85° C) was the most soluble while the Pr-powder with the smallest radii (atmospheric conditions at ambient temperature) was the least soluble. Both these sample sets were statistically different as calculated by the student t-test but the rest of the data showed no distinct trends and the data sets were not statistically different as calculated by the student t-test. The results indicated significant differences in the chemical composition and/or phase among the precipitates.

Task 3: Coating Deposition

Cerium-Based Conversion Coatings

As part of the mechanistic study, coating deposition parameters were varied to produce CeCCs varied corrosion protection. One parameter that affects corrosion protection is the addition of gelatin to the deposition solution. Coatings produced from solutions that contained gelatin typically provide significant corrosion protection (e.g., no pitting or tailing for two weeks in ASTM B117 salt spray). Coatings deposited from solutions without gelatin do not provide corrosion protection. XRD analysis (Figure 24) showed that CeCCs deposited from solutions containing gelatin converted from the as-deposited hydrated cerium oxide ($CeO_2 \bullet 2H_2O$) to hydrated cerium phosphate ($CePO_4 \bullet H_2O$) during post treatment. Formation of hydrated cerium phosphate has been correlated to improved corrosion protection in previous research at Missouri S&T.[54] CeCCs deposited from solutions without gelatin do not convert to the protective form, but remain in the as-deposited hydrated cerium oxide state. In subsequent studies, coatings deposited from solutions with and without gelatin will be characterized to determine structural, morphological, and electrochemical differences between coatings that provide corrosion protection and those that do not as well as the changes in these quantities during corrosion.

Previous characterization studies have revealed that CeCCs typically contain highly cracked areas after deposition and post-treatment. A representative micrograph of a CeCC on Al 2024-T3 with cracked areas present is show in Figure 25. For coatings that provide corrosion protection, the highly cracked areas typically make up around 10% of the total area. Approximately 90% of the surface area of the coatings (labeled “typical”) has a network of fine cracks. Further analysis has shown that the “large” surface cracks are often associated with sub-surface damage in both Al 2024-T3 and Al 7075-T6 substrates. The cracks not only penetrate through the coating, but are also associated with crevices and larger porous areas beneath the surface of the aluminum alloy panel surfaces. Formation of the sub-surface data was due to the combined effects of chloride ions and H_2O_2 present in the coating solution. Cross sections of CeCCs on Al 2024-T3 and Al 7075-T6 were produced using an *in-situ* focused ion beam (FIB) milling. Cross sections were examined to observe the extent. Figure 26 shows a SEM image of the cross section of a cracked CeCC with a sub-surface crevice directly below a surface crack.

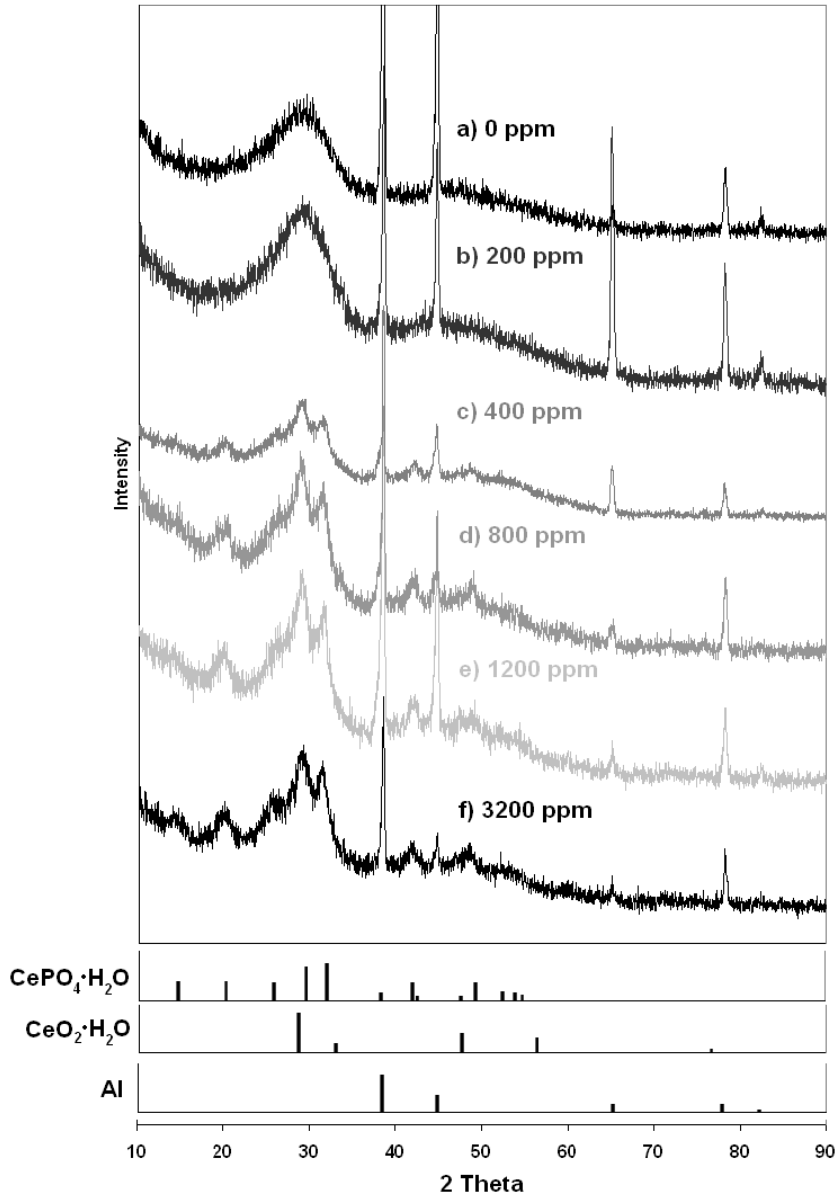

Figure 24. XRD patterns of post-treated CeCCs deposited from solutions with varying amounts of gelatin showing the formation of $CePO_4 \bullet H_2O$ in coatings deposited from solutions with gelatin contents of 400 ppm or higher and nanocrystalline $CeO_2 \bullet 2H_2O$ in coatings deposited from solutions with less gelatin.

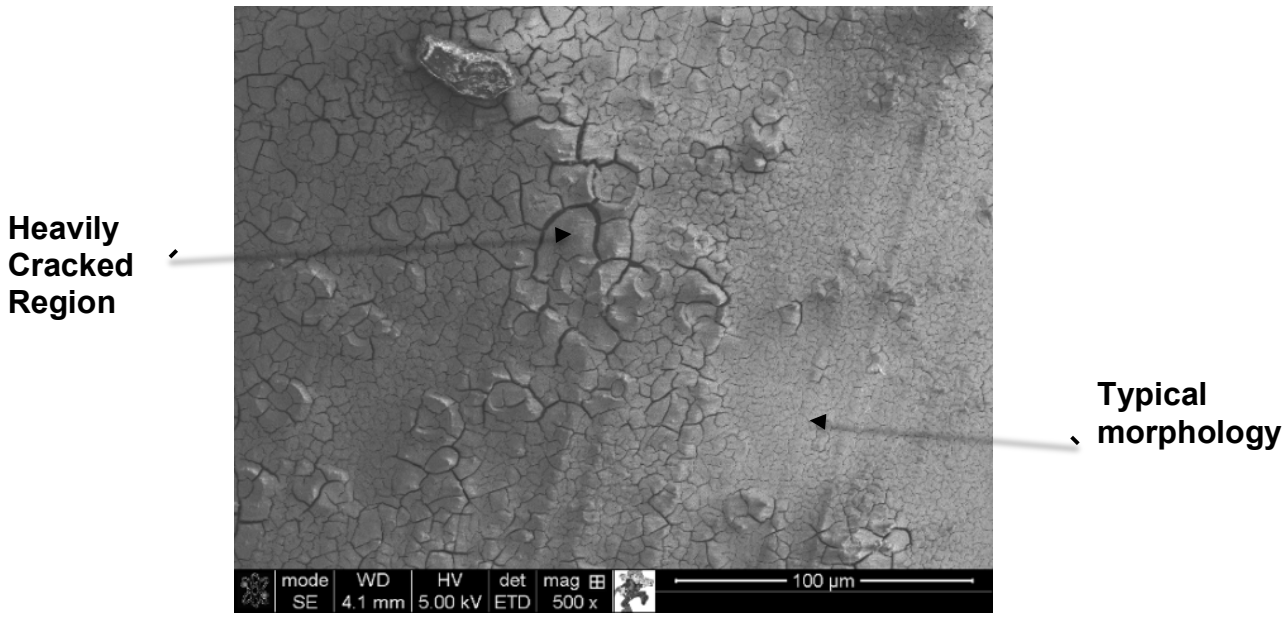

Figure 25. Typical SEM image of a CeCC capable of providing corrosion protection showing a highly cracked area and a more typical surface morphology.

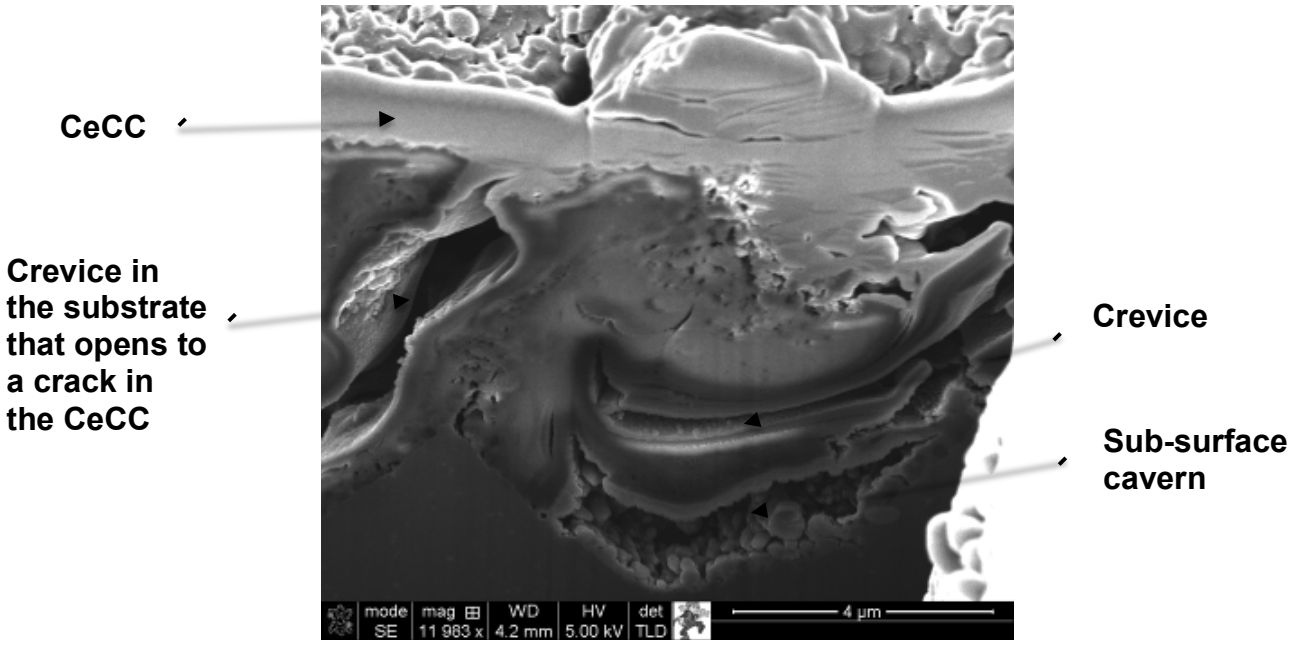

Figure 26. SEM image of cross-section of a CeCC produced by FIB milling.

The area selected for the cross section included large cracks in the coating. EDS analysis of these areas (Figure 27) showed increased the oxygen concentrations compared to the bulk Al alloy. The amount of Cu detected in the crevices was similar to the bulk areas. The milled areas also had high concentrations of gallium, which is an artifact of the FIB milling process that employs a gallium ion beam. Additionally, a visually lighter (less dense) layer outlining the

crevices was observed, which will be further characterized to determine its elemental composition and determine its role in crevice formation and corrosion protection.

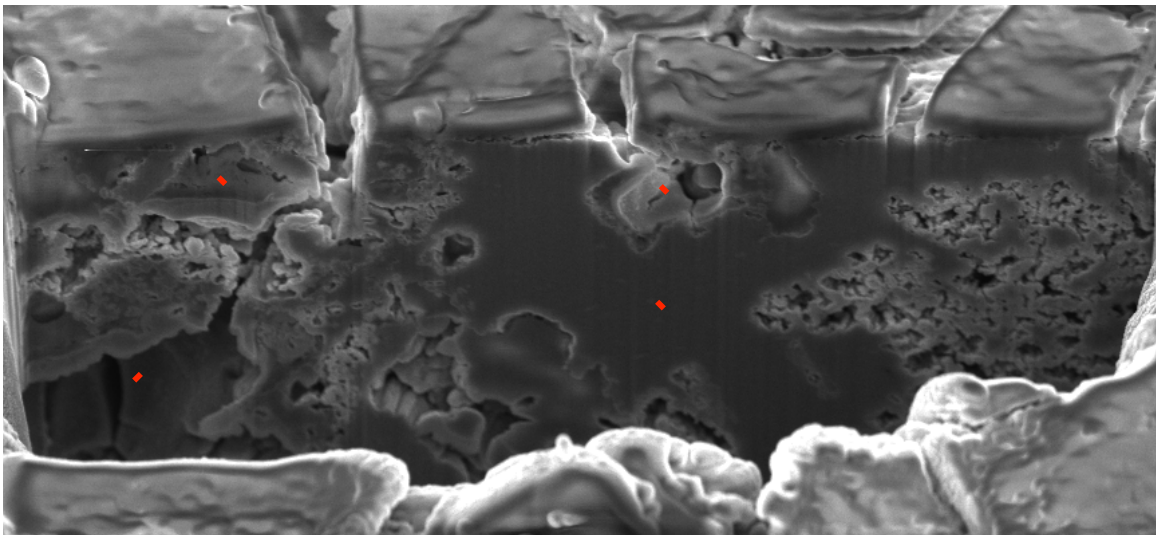

O	**14.02**
Ga	**3.73**
Al	**75.27**
Cu	**6.97**

Crevice

O	59.3
Ga	2.48
Al	35.53
Cl	0.56
Cu	2.14

Dark Area

O	10.86
Ga	2.96
Al	84.05
Cu	2.13

Bulk Alloy

O	14.09
Ga	7.08
Al	70.09
Cu	8.04

Light Area

Figure 27. SEM image of a FIB cross section of a CeCC on Al 2024-T3 showing surface cracks in the coating connected to sub-surface damage in the substrate. Chemical analysis shows oxygen enrichment in the damages areas.

The evolution sub-surface crevice formation in Al 2024-T3 substrates has been correlated to the number spray applications of the CeCC solution using similar FIB analysis. Initial data showed crevices increased in volume and depth with an increasing number of spray cycles used to deposit the coating. As part of research on a related project (WP-1519) [96], specific reaction schemes were developed to further understand the role of substrate dissolution during the deposition of CeCCs. As part of the present project (WP-1618), the role of crevices in corrosion was investigated.

Formation of Sub-Surface Crevices During CeCC Deposition

The CeCC depositon solution, which contains 0.3 M chloride ions and 1 M H_2O_2, causes localized, excessive dissolution of aluminum near intermetallic particles over approximately

10% of the substrate surface resulting in formation of voids a few microns below the surface during deposition. Alternate CeCC deposition methods/chemistries were explored whereby an alternate oxidizing agent, $NaClO_4$ (1.42 M), was added to offset the impact of a decreased concentration of H_2O_2 (0.05 M). CeCCs were deposited without sub-surface voids with decreased amounts of H_2O_2. To determine if the dissolution of Al^{3+} was due to the surface pretreatment or the electrochemical effects of the Ce^{3+} salt, potentiodynamic scans were performed in solutions containing the species of interest. Representative potentiodynamic curves of bare Al 7075-T6 in three different solutions, 2 wt% NaOH, 0.3 M NaCl and 1 M H_2O_2 (pH adjusted to 2.3 with HCl), or 0.3 M $NaNO_3$ and 1 M H_2O_2 (pH adjusted to 2.3 with HNO_3), can be seen in Figure 28.

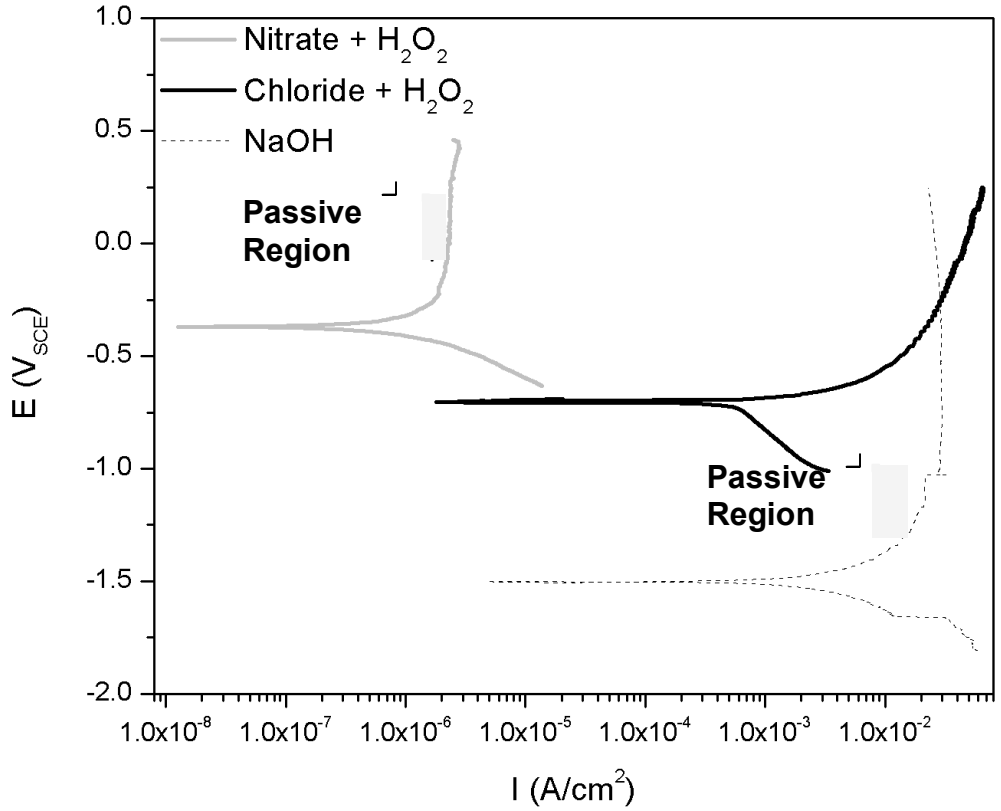

Figure 28. Bare 7075-T6 exposed to aqueous solutions containing either 0.3 M $NaNO_3$ with 1 M H_2O_2, 0.3 M NaCl with 1 M H_2O_2, or 2 wt% NaOH. Scan rate 1.0 mV/s vs. SCE.

The anodic sweep of potentiodynamic curves performed in 2 wt% NaOH and 0.3 M $NaNO_3$ with 1 M H_2O_2 both exhibited a passive region whereas potentiodynamic curves performed in 0.3 M NaCl and 1 M H_2O_2 only exhibited active behavior. The panels retained a passive film on the surface that provided some corrosion resistance when exposed to NaOH and $NaNO_3$ electrolytes, but when chloride were present, no such passive films were formed. Passivity is a condition of corrosion resistance due to thin surface films under highly oxidizing conditions at high anodic

polarization. These films passivate the underlying substrate only if they are adherent and are dense (i.e. Al_2O_3)[97]. The presence of a passive film will alter the anodic polarization behavior.

The native oxide present on the Al substrate is affected during exposure to each different type of electrolyte employed during the potentiodynamic experiments. In the potentiodynamic scan for bare Al 7075-T6 exposed to the NaOH solution, an OCP of -1.5 V was reached and a passivation region was observed in the potential region between -1.4 V and -1.0 V. The low OCP of -1.5 V indicated that the NaOH solution caused the substrate to be very active. An OCP of -0.3 V was reached by the panel exposed to a nitrate and H_2O_2 solution, which showed a passivation region in the potential range between -0.3 V and 0.3 V. It has been shown that nitrate ions help passivate the surface of Al alloys by incorporation into the surface oxide [98]. The more noble OCP value and passivation region indicated the nitrate solution caused the substrate to become inactive. When exposed to a solution containing chloride ions and H_2O_2, an OCP of -0.75 V was reached and passivation of the bare Al 7075-T6 panel did not occur. The flat anodic curve was indicative of native oxide that was converted to non-protective salt film due to high concentration of chloride ions. Based on the OCPs obtained from potentiodynamic scans, the Al matrix was more active in the NaOH solution, but still relatively active in the chloride ion and H_2O_2 solution. Lack of an anodic passivation region indicated pitting of the substrate occurred in the presence of chloride ions and H_2O_2. The combination of nitrate and H_2O_2 was not as aggressive as the combination of chloride ions and H_2O_2 in altering the native oxide layer on the Al substrate.

Potentiodynamic scans indicated that the combination of chloride ions and H_2O_2 will not passivate the surface of Al 7075-T6, whereas NaOH and the combination of nitrate ions and H_2O_2 caused surface passivation. Depending on the composition of the coating solution whether it was chloride ion/H_2O_2 based or nitrate/H_2O_2 based, the surface of Al 7075-T6 will be altered and the surface morphology will change. The surface morphology of Al 7075-T6 exposed to aqueous solutions containing NaOH, a combination of chloride ions and H_2O_2, or a combination of nitrate ions and H_2O_2 are show in Figure 29.

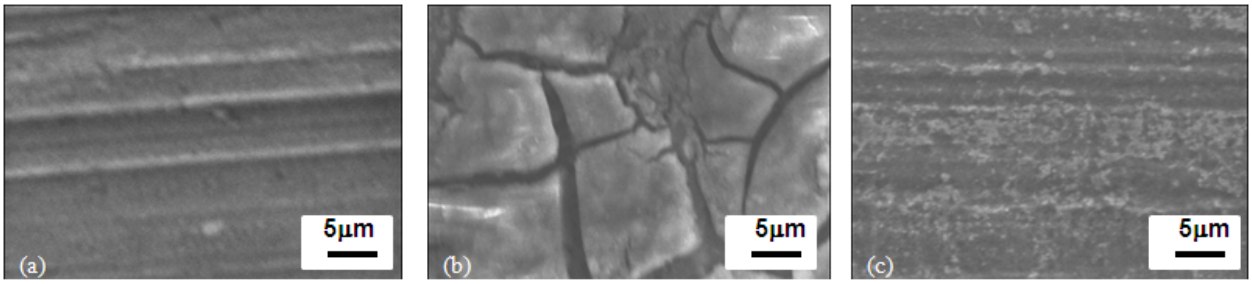

Figure 29. Surface morphology of Al 7075-T6 exposed to (a) 2 wt % NaOH, (b) an aqueous solution an aqueous solution containing 0.3 M chloride ions and 1 M H_2O_2, and (c) an aqueous solution containing 0.3 M nitrate ions and 1 M H_2O_2.

Basic activation lightly etched the surface of Al 7075-T6 (Figure 29a). Other than some minor compositional contrast that was likely due to roll marks in the alloy, no distinct surface features were observed after basic etching. In contrast, the combination of chloride ions and H_2O_2 heavily etched the Al 7075-T6 panel (Figure 29b). Extensive etching of the bare Al alloy resulted

in a non-uniform surface on which cracks and crevices were apparent. When exposed to a nitrate and H_2O_2 solution, the surface morphology of Al 7075-T6 resulted in the formation of a non-uniform corrosion product (Figure 29c). The surface was not heavily etched compared with the chloride and H_2O_2 solution, but unlike the NaOH treated panel, a thin visible coating was produced in some areas. The combination of nitrate and H_2O_2 did not produce an aggressive enough solution to achieve the same etching effects as the chloride ion and H_2O_2 solution.

Previous research has confirmed that basic activation of Al 7075-T6 increased surface activity by reducing the native oxide corrosion resistance, which accelerated the spontaneous deposition of CeCCs using a spray process [99]. The significant etching produced by the combination of chloride ions and H_2O_2 present in the coating solution allowed for increased surface activity and enhanced the spontaneous deposition of CeCCs. When chloride ions and H_2O_2 were employed in the CeCC deposition solution, Al^{3+} was dissolved and the surface of the substrate was etched.

The "heavily" cracked regions of the CeCCs were most likely due to a thicker CeCC layer in this localized area and can be seen in Figure 30. It is hypothesized that these sites contain a higher concentration of noble Cu-based IMCs compared to the rest of the substrate. During CeCC deposition, the solution caused extensive, localized Al dissolution, which, in turn, caused the growth of sub-surface voids beneath the highly cracked areas of the CeCC. These regions typically constituted ~10% or less of the surface area of coated panels. Exposure to chloride ions and H_2O_2 converted the native oxide to a non-protective salt film and promoted pit formation, which allowed electrolyte to channel beneath the substrate and react. Sub-surface voids were typically observed beneath areas of CeCCs that had crack sizes of ~200 nm in size, which are shown in Figure 30.

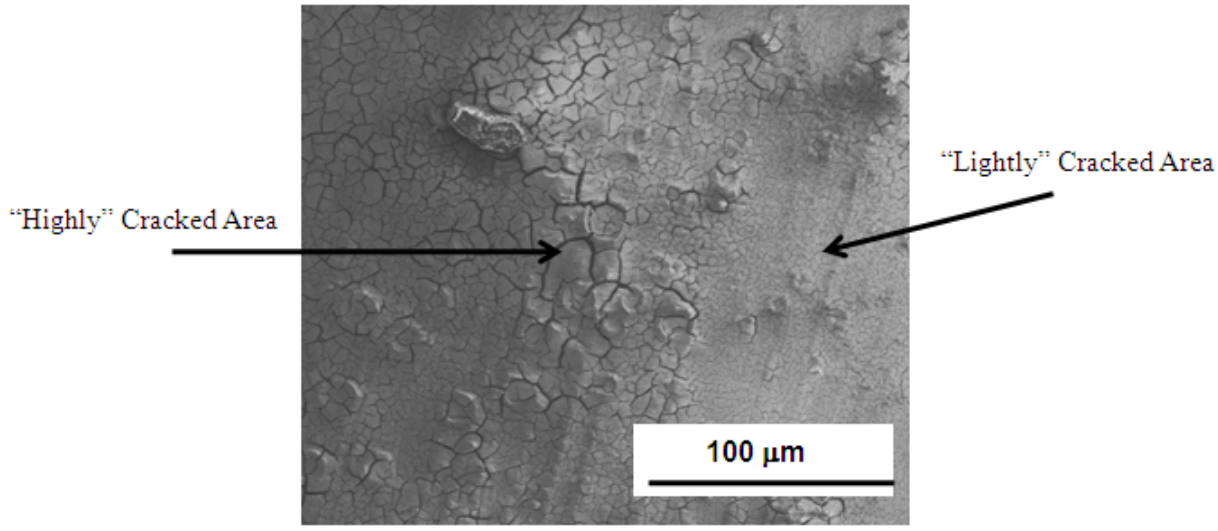

Figure 30. Surface morphology of a CeCC deposited from a solution containing chloride ions and H_2O_2 on Al 7075-T6.

In addition to altering the surface morphology of the Al substrate, the combination of chloride ions and H_2O_2 in the deposition solution resulted in localized sub-surface voids during CeCC deposition (Figure 31). Compositional information was collected from cross-sections of regions

with sub-surface voids. For Al 7075-T6 panels, areas where material had been removed had higher concentrations of Cu compared to the bulk alloy. Table 7 lists the chemical composition of three different areas analyzed (area A, area B, and area C labeled in Figure 31). Compositional data showed copper enrichment in areas where sub-surface crevices evolved. Sub-surface voids did not occur throughout the entire Al substrate, but were isolated to specific regions. It is possible the presence of Cu-rich IMCs induced localized dissolution of Al from susceptible regions. The localized reactions of chloride ions and H_2O_2 occurred due to galvanic coupling of noble Cu-based IMCs and the active Al matrix with chloride ions serving as the charge transfer carrier. Al^{3+} is preferentially removed more readily in areas where Cu-rich IMCs are present compared to surrounding regions in which Cu-rich IMCs are not present.

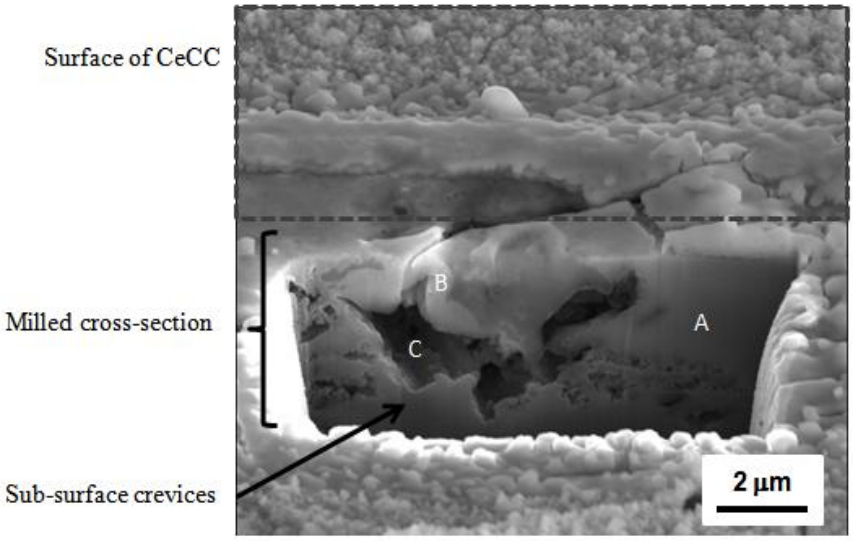

Figure 31. Surface morphology of a CeCC deposited from a solution containing chloride ions and H2O2 on Al 7075-T6.

To deposit CeCCs without sub-surface voids, alternate deposition methods/chemistries were explored. Sub-surface voids were caused by the combination of chloride ions and H_2O_2 in the deposition solution, so reducing the concentration or removing either of these components from the coating solution should reduce or eliminate sub-surface voids. Previous research has shown that coatings can be deposited using a spontaneous immersion process, which uses a coating solution containing the same concentration of chloride ions as the spray solution (0.3M), but with significantly less H_2O_2 (0.05M in the immersion solution compared to 1M in the spray solution) [73]. The immersion solution employs $NaClO_4$ as an oxidizing agent in addition to a small concentration of H_2O_2. The addition of oxidizers can reduce the coating times from hundreds of hours (original Hinton process [82]) to a matter of a few minutes. CeCCs produced using the immersion process with this coating solution did have cracks in the film but did not have sub-surface voids (Figure 32). Compositional information was collected from cross-sections of regions of the coating produced with no sub-surface voids. Table 8 lists the chemical composition of three different areas analyzed (area A, area B, and area C labeled in Figure 32).

Table 7. Compositional analysis of three different regions within the cross-sectional area of a standard CeCC as labeled in Figure 31.

Area A (Bulk Alloy)		Area B (Light Area)		Area C (Crevice)	
Element	**Atomic Percent**	**Element**	**Atomic Percent**	**Element**	**Atomic Percent**
O	2.19	O	25.6	O	8.50
Mg	1.49	Mg	0.80	Mg	1.51
Al	95.7	Al	69.5	Al	87.4
		P	0.97	P	1.21
		Cl	1.86	Cl	0.80
		Cu	1.32	Cu	0.15
				Zn	0.46

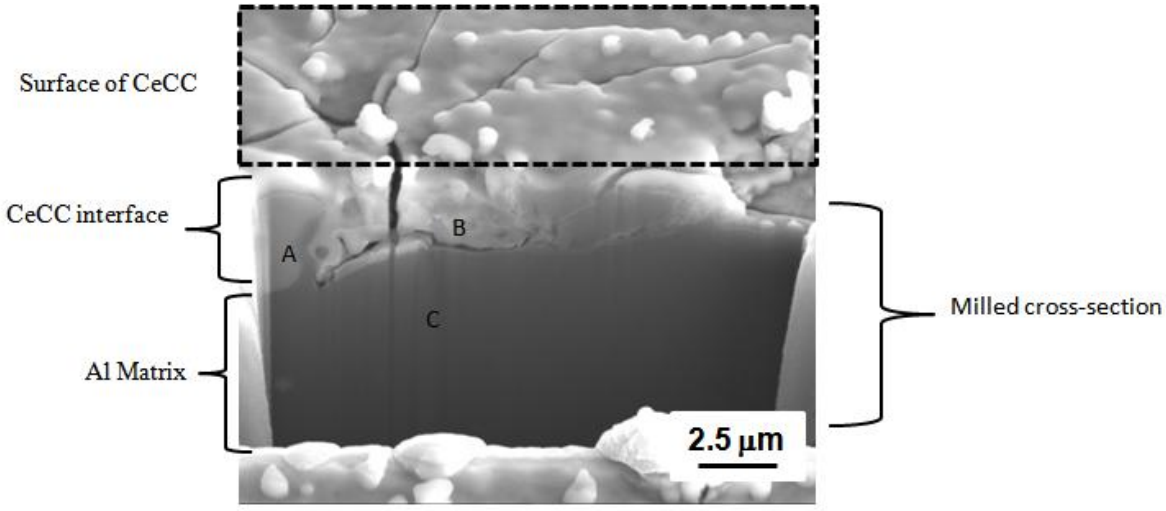

Figure 32. FIB cross section of an immersion deposited CeCC on Al 7075-T6.

Compositional analysis showed copper enrichment in areas where the coating had formed, but no sub-surface voids were observed in the substrate in contrast to what was observed for the standard coating process. The coating area adjacent to the copper rich IMC appeared to have cracked due to the thickness of the coating in that region indicating this area would likely be identified as "heavily cracked" and a potential site for sub-surface voids if it were deposited with the standard coating process. Although no sub-surface voids were observed, the corrosion protection provided by this coating was significantly less than that for a standard spray-deposited

coating as multiple pits were detected on the coatings within 24 hours when tested per ASTM B117 standards.

Table 8. Compositional analysis of three different regions within the cross-sectional area of a standard CeCC as labeled in Figure 32.

Area A (Bulk Alloy)		Area B (Light Area)		Area C (Crevice)	
Element	**Atomic Percent**	**Element**	**Atomic Percent**	**Element**	**Atomic Percent**
O	3.75	O	31.07	Mg	2.62
Mg	17.33	Mg	1.40	Al	94.73
Al	49.60	Al	49.87	Cu	0.78
Cu	22.96	P	1.34	Zn	1.82
Zn	1.30	Zn	0.30		
Ce	0.61	Ce	13.95		

Chloride-Free and Chloride-Based CeCC Deposition Solutions

The type of cerium (III) salt and oxidant employed into the deposition solution of cerium-based conversion coatings (CeCCs) determines the presence of sub-surface voids in the aluminum substrate along with contributing to the corrosion performance of the coatings. In an effort to produce coatings with improved corrosion resistance, but without sub-surface voids in the substrate, CeCCs were spray deposited from solutions using different combinations of $CeCl_3$ and $Ce(NO_3)_3$, but with the standard concentration of H_2O_2 (1M). The concentration of cerium was fixed at 0.1 M with the following combinations of Ce^{3+} sources: 1) a chloride-free solution containing only $Ce(NO_3)_3$; 2) a solution containing 10 wt.% $CeCl_3$ and 90 wt.% $Ce(NO_3)_3$; 3) a solution containing 67 wt.% $CeCl_3$ and 33 wt.% $Ce(NO_3)_3$; and 4) the standard solution using only $CeCl_3$ as the Ce^{3+} source. Little to no coating was visible for the panels deposited from the chloride-free solution. The resultant CeCCs from each solution were more apparent with increasing amounts of chloride ions. Coating thickness and uniformity were judged based on the observation of a golden yellow color on the substrate surface.

Coating thicknesses were measured for CeCCs produced from the nitrate/chloride ion solutions by AES (Figure 33). Coating thickness was determined using the crossover point for the Ce and Al signals from the spectra. The thickness of the Al-oxide layer between the CeCC and the Al substrate was represented by the crossover of the Al and O lines. With an increase in chloride ion concentration in the deposition solution, the electrochemical activity at the substrate surface was the predominant driving force allowing for thicker coatings to be produced. A more uniform coating was visible with increasing amounts of chloride.

CeCCs deposited using a chloride ion-free solution (Figure 33a) produced a coating that was ~60 nm thick, while the 10 wt. % chloride ion solution (Figure 33b) produced a coating that was ~70 nm thick. When the chloride ion content was increased to 67 wt. % (Figure 33c), the thickness increased to ~200 nm and CeCCs produced from the standard solution (Figure 33d) were ~400 nm thick. AES data confirmed that a higher chloride ion concentration was needed to achieve the optimal CeCC thickness, which has been shown to be ~300 nm to 400 nm in previous studies [53,71]. The combination of $Ce(NO_3)_3$ and H_2O_2 did not produce an aggressive enough solution to achieve the same etching effects as a $CeCl_3$ and H_2O_2 based coating solution and interfered with the electrochemical interactions needed for coating deposition. The Ce^{3+} salt employed in the deposition solution affected coating thickness. The combination of chloride ions and H_2O_2 etched the surface of the Al alloy, which aided in the rapid deposition of thicker and more uniform CeCCs. Standard concentrations of chloride ions (0.3 M) yielded thicker CeCCs than solutions with reduced chloride ion concentrations.

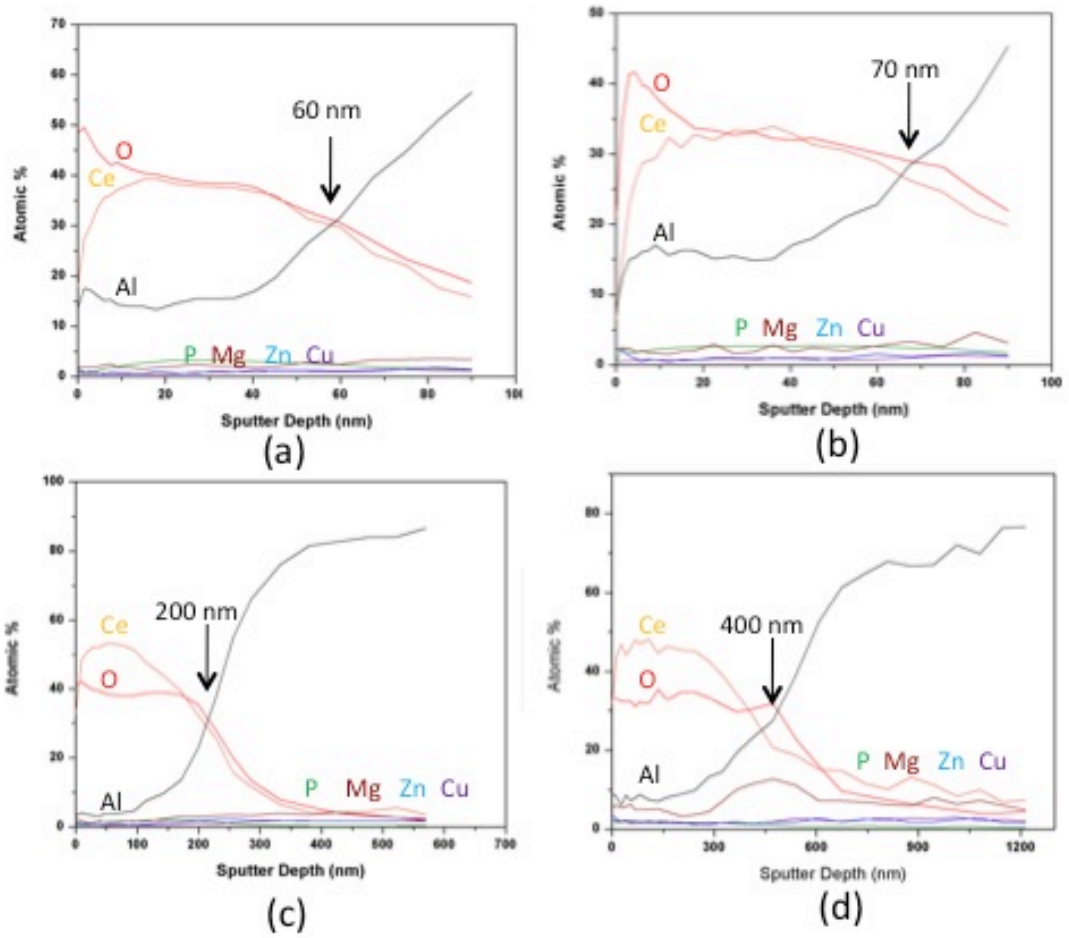

Figure 33. AES depth plots profile analysis of CeCCs deposited on Al 7075-T6 from (a) a chloride free solution, (b) the 10 wt.% chloride solution, (c) the 67 wt.% chloride solution, and (d) the standard solution on Al 7075-T6.

Electrochemical methods were used to characterize the corrosion protection of coatings prepared from solutions with different ratios of nitrate to chloride in precursors. Representative

potentiodynamic curves are shown in Figure 34. The corresponding corrosion potentials (E_{corr}) and corrosion current density (i_{corr}) calculated using Tafel fits are reported in Table 9.

The E_{corr} values were not affected significantly by the chloride concentrations employed in this study. The i_{corr} values for CeCCs decreased with increasing chloride concentration in the deposition solution. CeCCs deposited from the chloride-free solution had an i_{corr} of 17.3 $\mu A/cm^2$, while CeCCs prepared from the standard solution had an i_{corr} of 0.288 $\mu A/cm^2$, a decrease of about two orders of magnitude. A noticeable increase in anodic pitting potential (E_{pit}) can also be noticed with the increase in chloride ion concentration, which is an indication of passivation. In CeCCs deposited from the chloride ion-free solution E_{pit} was almost equal to E_{corr} indicating no passivation, i.e., no corrosion protection due to coatings, while CeCCs prepared from the standard solution had the highest E_{pit} value indicating strong passivation. The decrease in i_{corr} and increase in E_{pit} for CeCCs deposited from solutions with higher chloride concentrations was most likely due to formation of a more uniform, thicker coating (~400 nm). The higher coating thickness and more uniform coating were likely the result of the more aggressive coating solution. Regardless of the presence of sub-surface voids, CeCCs deposited with solutions containing chloride and H_2O_2 exhibit a decrease in i_{corr} and increase in E_{pit}. This suggests that CeCCs deposited with only nitrates or lower concentrations of chloride ions may allow exposed active sites in the substrate subject to interact with electrolyte influencing the i_{corr} and impact the ability of the coating to protect.

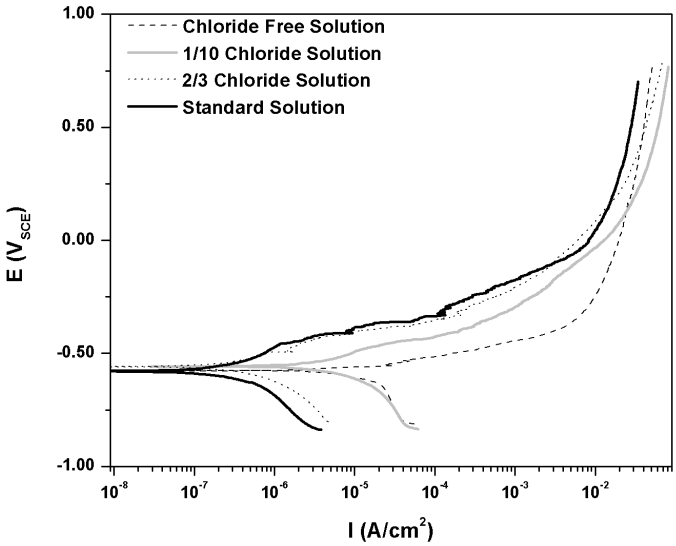

Figure 34. Potentiodynamic scans for CeCCs deposited on 7075-T6 from solutions containing different fractions of $CeCl_3$ and $Ce(NO_3)_3$ ranging from chloride ion-free to the standard solution containing only chloride ion. The scan rate was 1mV/s vs. SCE and the electrolyte consisted of 0.35 wt. % NaCl + 0.70 wt. % $(NH_4)_2SO_4$.

Table 9. Values for corrosion currents and corrosion potentials calculated from potentiodynamic analysis of CeCCs deposited on 7075-T6 formulated from solutions containing different fractions of $CeCl_3$ and $Ce(NO_3)_3$.

	i_{corr} ($\mu A/cm^2$)	E_{corr} (mV)
Chloride Free	17.3	-560
10 wt.% Chloride	2.50	-514
67 wt.% Chloride	0.629	-524
Standard	0.288	-530

In addition to potentiodynamic scans, EIS was used to characterize the overall impedance of CeCCs prepared using different amounts of chloride and nitrate precursors (Figure 35).

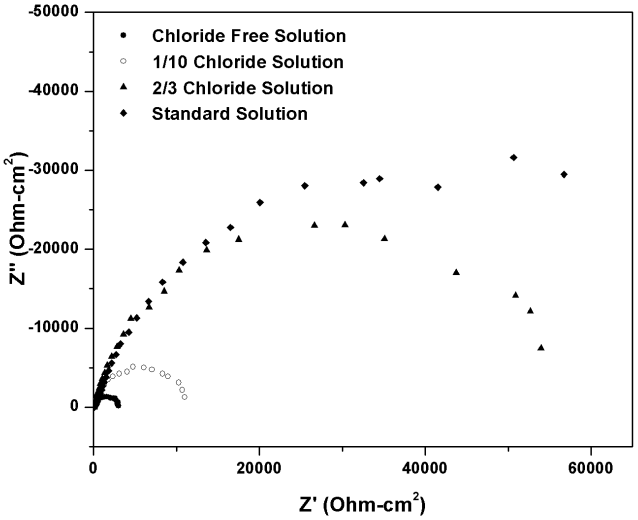

Figure 35. EIS analysis of CeCCs deposited on Al 7075-T6 from deposited on Al 7075-T6 from solutions containing different fractions of $CeCl_3$ and $Ce(NO_3)_3$ ranging from chloride ion-free to the standard solution containing only chloride ions.

The overall coating impedance increased with increasing chloride ion concentration in the deposition solution. CeCCs deposited from standard solution had the highest total impedance (~95000 Ω-cm^2) compared to CeCCs deposited from the chloride ion-free solution (~3000 Ω-cm^2). Coatings with higher total impedance typically exhibit better corrosion protection as do coatings that exhibit a passivation region following a potentiodynamic scan. Electrochemical characterization of each CeCC of interest showed the corrosion protection increased with increasing concentration of chloride in the deposition solution. Standard CeCCs exhibited the highest total impedance when compared to chloride-free CeCCs in which sub-surface voids were not present. CeCCs produced from chloride ion and H_2O_2 containing solutions allow for thicker and more uniform coatings compared to chloride ion-free containing solutions impacting the overall impedance of each coating.

To better understand the effects of increased chloride ion concentration in the deposition solution, the EIS data were fit to equivalent circuit models and then compared to other physical characteristics of the coatings. Two models with physical representations for coatings produced from chloride ion-free solutions, 10 wt.% chloride ion solutions, 67 wt.% chloride ion solutions, and standard coating solutions were proposed. The impedance results were fit into an equivalent circuit where R_{soln} represents the solution resistance, C_p represents the geometric capacitance, R_p is the bulk resistance of the coating in parallel with it, Q_{dl} represents the constant phase element, and R_{ct} is the charge transfer resistance of the corrosion processes occurring at the interface in parallel with Q_{dl}. For each sample, the n value was attributed to constant phase element depending on the calculated value [100-101102]. Values for each of these components are shown in Table 10 and the highest χ^2 value (a direct measure of how close a model fits experimental data calculated from the sum of the squares of all residuals)[103,104] given by the software ZSimpWin was 0.007. Actual values less than 1 were considered sufficient to indicate a good fit of a model to experimental data.

Table 10. Summary of values calculated with ZSimpWin software version 3.21 by fitting EIS data to equivalent circuit models using individual component values.

Parameter	Chloride Free	10 wt.% Chloride	67 wt.% Chloride	Standard Coating
R_{sol}	25	31	31	33
C_p	---	---	1.31×10^{-6}	4.6×10^{-7}
R_p	---	---	136	74
Q_{dl}	1.1×10^{-5}	5.1×10^{-6}	4.9×10^{-6}	2.6×10^{-5}
n	0.92	0.93	0.80	0.77
Rct	3053	11390	57898	94770
χ^2	0.0008	0.002	0.004	0.006

EIS data for CeCCs deposited from chloride ion-free solutions and 10% chloride ion solutions could be fit to one semicircle with a single associated time constant and was modeled as a capacitor. The equivalent circuit used to model both of these coatings can be seen in Figure 36 and values of each component are listed in Table 10.

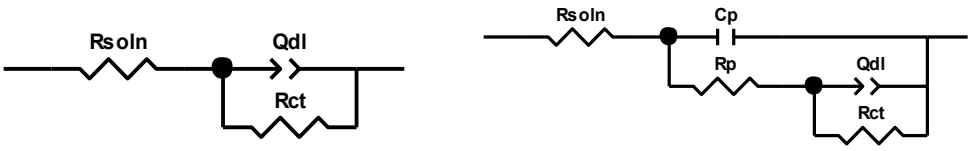

(A) (B)

Figure 36. Equivalent circuits used to fit EIS data for coatings produced from (a) chloride ion-free and 10 wt.% chloride ion and (b) 67 wt.% chloride ion, and standard solutions.

When $n \neq 1$, a system shows behavior attributed to surface heterogeneity or continuously distributed time constants for charge-transfer reactions [100]. Typically, if the value of n is greater than 0.8, it can be viewed as a capacitor, which indicates the presence of a double layer at the electrolyte/surface interface of the substrate [101]. CeCCs produced from chloride ion-free and 10 wt.% chloride ion based solutions were non-uniform and thinner (~60 to 70 nm) compared to the coating thickness (~300 to 400 nm) produced by the standard coating solution. The thinner, less uniform coating allows for a greater interaction between the electrolyte and substrate surface causing the corrosion process of the substrate to dominate.

CeCCs deposited from 67 wt.% chloride ion and standard coating solutions were comprised of two semicircles, which could be fitted to two time constants indicating one component was due to the coating and the other due to a corrosion process [101]. The equivalent circuit used to model both of these coatings can be seen in Figure 36b and values of each component are listed in Table 10. The n value was slightly less than 0.8 indicating it behaved as a constant phase element rather than capacitance along with surface heterogeneity or continuously distributed time constant at the interface. CeCCs produced from solutions containing 67 wt.% chloride ion and standard solutions were more uniform and thicker (~200 nm to 400 nm) compared to coatings produced from chloride ion-free and 10 wt.% chloride ion solutions (~60-70 nm). This caused the coatings to dominate the corrosion resistance of the sample.

The fact that two time constants were present for CeCCs deposited from 67 wt.% chloride ion solutions and standard coating solutions and only one time constant was present in coatings produced from chloride ion-free solutions and 10 wt.% chloride ion solutions indicated that each coating behaved differently electrochemically due to differences in uniformity. More aggressive chloride ion-containing coating solutions led to thicker coatings in the same number of spray cycles when compared to coating solutions with decreased concentrations of chloride ions. As shown in the fitted equivalent circuits, despite the presence of sub-surface voids, the coatings produced from 67 wt.% chloride ion containing solutions and standard coating solutions had impacted corrosion resistance when compared to coatings with no sub-surface crevices produced from chloride ion-free or 10 wt.% chloride ion solutions due to the fact thicker and more uniform coatings are produced by these solutions.

The improvement in corrosion protection with the increasing chloride percentage in the deposition solution can also be seen in optical images of panels after exposure to salt spray corrosion testing (Figure 37).

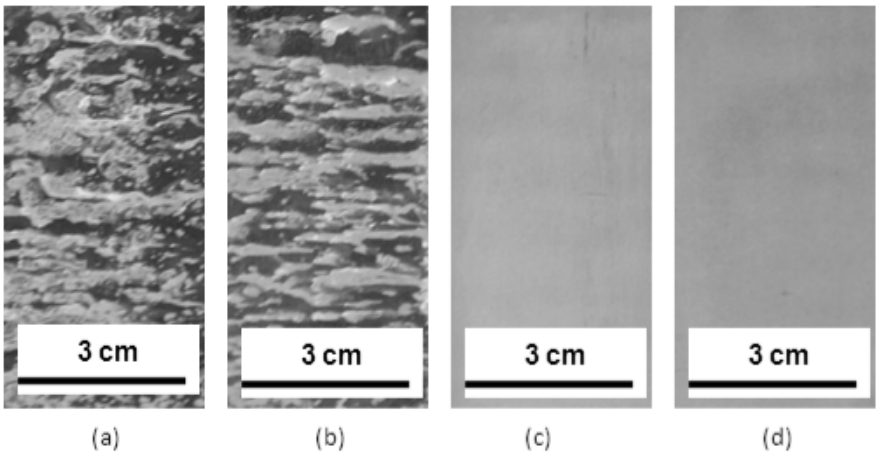

Figure 37. CeCCs deposited on 7075-T6 from $Ce(NO_3)_3$/ $Ce(NO_3)_3$ solutions after 24 hours in salt spray testing: (a) chloride ion-free, (b) 10 wt.% chloride ions, (c) 67 wt.% chloride ion, and (d) standard solutions.

CeCCs prepared from the chloride ion-free solution (Figure 37a) had numerous pits and salt tails and appeared to erode, offering no corrosion protection. CeCCs prepared from the 10 wt.% chloride ion solution (Figure 37b) also performed poorly in salt spray testing. CeCCs prepared from the 67 wt.% chloride ion solution (Figure 37c) offered marginally better corrosion protection than the CeCCs prepared from the chloride-free and 10 wt.% chloride ion solution, but was not as protective as the CeCCs deposited using the standard solution. As expected based on results of the electrochemical characterization, the CeCCs prepared from the standard (all chloride) solution (Figure 37d) provided excellent corrosion protection and exhibited no pits or salt tails after 24 hours in salt spray testing. These studies revealed that while the combination of chloride and H_2O_2 caused surface and sub-surface etching, CeCCs deposited from chloride and H_2O_2 containing solutions were also thicker and more uniform, passivated the surface more effectively, had increased overall impedance, and exhibited better corrosion protection.

Surface Activation of 7075-T6

Previous research has described the role of different processing parameters on the thickness and corrosion resistance of CeCCs [54-56,64,65,67,69,70,72,83]. Recent studies have shown that alkaline cleaning (also referred to as degreasing) followed by acid activation using sulfuric acid increased the deposition rate and corrosion resistance of CeCCs on Al 2024-T3 [54,70].Stable species for aluminum and magnesium were determined at various pH values by calculating E-pH diagrams. Diagrams were constructed at room temperature with and without the presence of carbonate ions (Figure 38 and Figure 39)

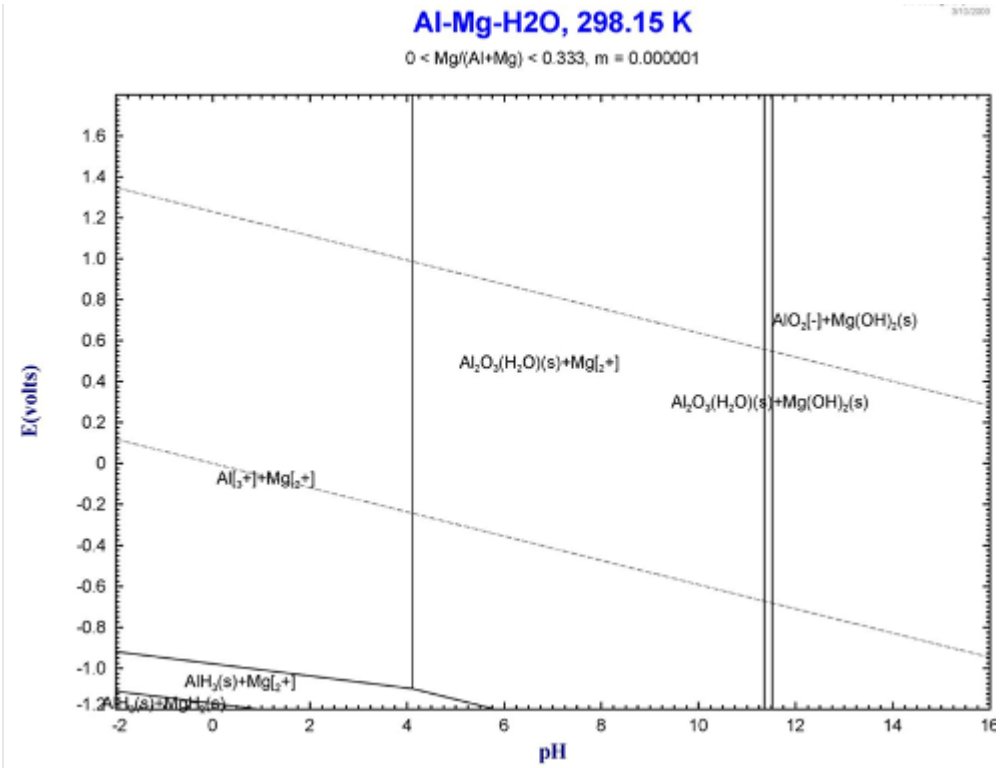

Figure 38. E-pH diagram for the Al-Mg-H_2O system at 298 K.

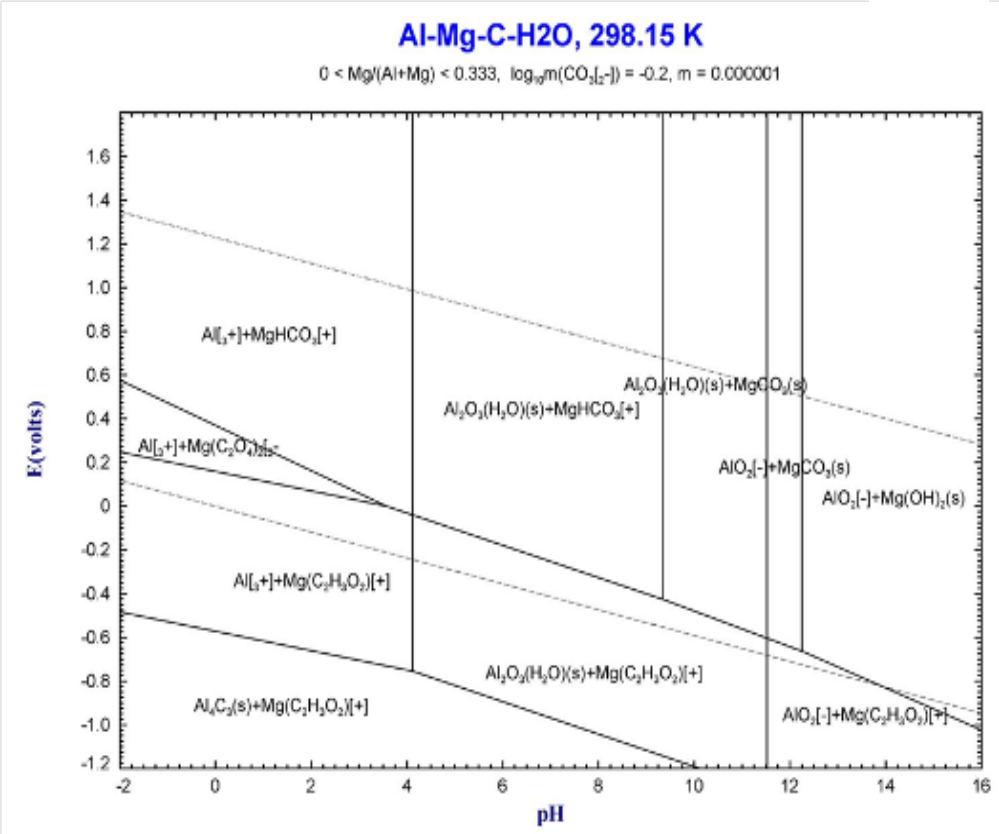

Figure 39. E-pH diagram for the Al-Mg-C-H_2O system at 298 K.

For dilute concentrations of magnesium and aluminum (10^{-6} M) at zero solution potential, Figure 38 (without carbonate ions) shows that aluminum is stable as AlOOH (designated $Al_2O_3 \bullet H_2O$) in the pH range 4 to 11.5. Below pH 4, aluminum dissolves as Al^{3+} ions, while above pH of 11.5, aluminum dissolves in the form of aluminate (AlO_2^-) ions. When the temperature was increased to 55°C, the stability regions did not change significantly. Therefore, Figure 38 can be used over the range of temperatures of interest in this study, which was room temperature to the temperature of the degreasing solution (55°C). Considering magnesium species, $Mg(OH)_2$ is stable at pH values greater than ~11.5, but dissolves as Mg^{2+} at lower pH values. Based on the diagram, aluminum should form a stable, protective oxide when the pH value is between 4 and 11.5, but should dissolve or corrode at higher or lower values. In contrast, magnesium dissolves at pH values below ~11.5, but is protected by $Mg(OH)_2$ at higher pH values.

Figure 39 shows the effect of the presence of carbonate ions (CO_3^- 0.6 M) on stability of magnesium and aluminum species. Carbonate ions do not affect the stability of aluminum species. In contrast, the presence of CO_3^- ions favors the formation of $MgCO_3$ at pH values from ~9.5 up to 12.2 at potentials above ~ -0.5 V. The stable magnesium species was $Mg(OH)_2$ at higher pH values and potentials above ~ -0.6 V. At the lower pH values, magnesium should dissolve as $MgHCO_3^+$ ions at higher solution potentials. At lower potentials $Mg(C_2H_3O_2)^+$ or $Mg(C_2O_4)_2^{2-}$ were the stable solution species. Hence, the addition of carbonate ions increases the pH range for stability of magnesium by forming a stable carbonate phase.

The pH of the degreasing solution used in this study was 9.1 and the solution temperature was maintained at 55°C. Figure 38 suggests the stable species for aluminum and magnesium are AlOOH and Mg^{2+}. During degreasing, magnesium on the surface should be converted to Mg^{2+}, but alumina should not be affected. Therefore, immersion in the degreasing solution should dissolve a magnesium-rich oxide, but not affect an aluminum-rich oxide.

The pH values of the 1NaOH and 2NaOH solutions were both above 12.9. At these higher pH values, Figure 38 suggests the stable species should be $Mg(OH)_2$ and aluminate ions. During surface activation in NaOH solutions, magnesium should be converted to stable $Mg(OH)_2$ while aluminum should dissolve as aluminate ions. The pH of $5Na_2CO_3$ is 11.5. In the presence of carbonate ions at this pH, magnesium on the surface should be converted to stable $MgCO_3$, while aluminum should be dissolved as aluminate ions (Figure 39). While more complex than the effect of the degreasing solution, exposure of degreased surfaces to the alkaline activation solutions should dissolve aluminum species, but stabilize magnesium-species as $Mg(OH)_2$ or $MgCO_3$.

Figure 40 shows the AES depth profiles for acetone rinsed Al 7075-T6. Acetone should remove surface contamination such as dust or oil without altering the surface oxides. After acetone rinsing, the concentrations measured at the surface were 4 at% Al, 22 at% Mg, and 22 at% O, suggesting a magnesium-rich oxide was present. The total oxide thickness was ~30 nm, based on the point where the aluminum and oxygen lines crossed. The ~20 nm of the upper surface oxide was magnesium-rich. The aluminum content increased near the oxide-metal interface, but the oxide still had a significant magnesium content (~20 at%). Therefore, magnesium appeared to be surface active in the aluminum alloy because it was present in higher quantities (>20 at%) compared to its content in the alloy (2.5 wt% or 2.9 at%).

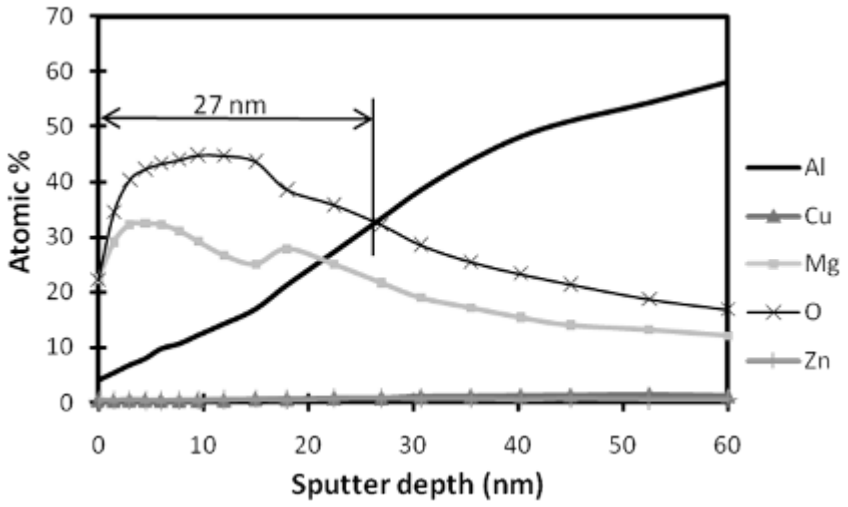

Figure 40. AES depth profile of acetone-rinsed Al 7075-T6.

Figure 41 shows the AES depth profile after degreasing. The aluminum line crossed the oxygen line at ~10 nm, suggesting that the oxide layer was ~10 nm thick. Further, the oxide layer was aluminum-rich compared to the acetone rinsed surface. The magnesium content at the surface decreased from the original value of ~20 at% in the acetone rinsed substrate (Figure 40) to less

than 10 at% (Figure 41) after degreasing. Based on the E-pH diagrams, magnesium-species should dissolve as Mg^{2+} ions at the pH of the degreasing solution, but aluminum species are stable as AlOOH.

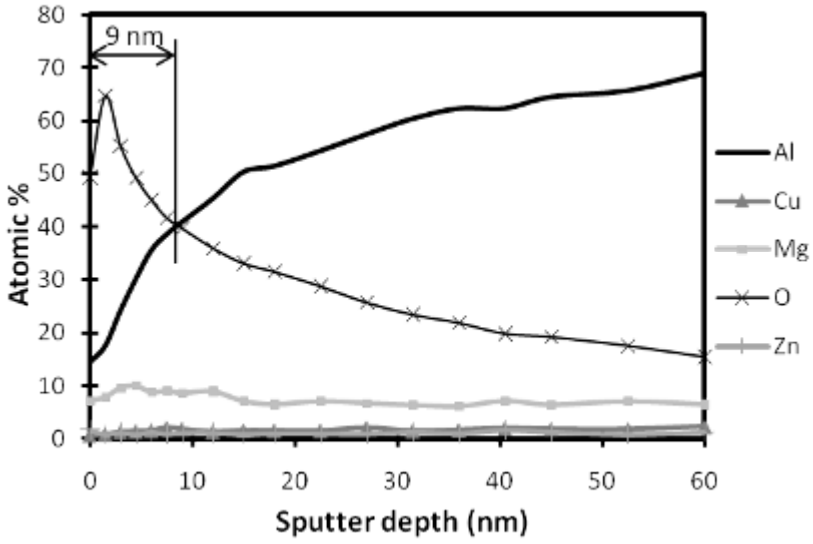

Figure 41. AES depth profiling of Al7075-T6 after degreasing.

Comparing the AES results in Figure 40 with those in Figure 41, it appears that outer portion of the magnesium-rich native oxide layer was removed by degreasing, which left an aluminum-rich oxide that was ~10 nm thick.

AES depth profile analyses were performed on Al 7075-T6 after surface activation in three different solutions: 1) 1NaOH (Figure 42), 2) 2NaOH (Figure 43), and 3) $5Na_2CO_3$ (Figure 44). Comparison of AES data for degreasing (Figure 41) with those of surface activations suggests surface activation caused an increase in surface oxide thickness from ~10 nm after degreasing to 20-30 nm after activation in 1NaOH or $5Na_2CO_3$ and ~60 nm after activation in 2NaOH.

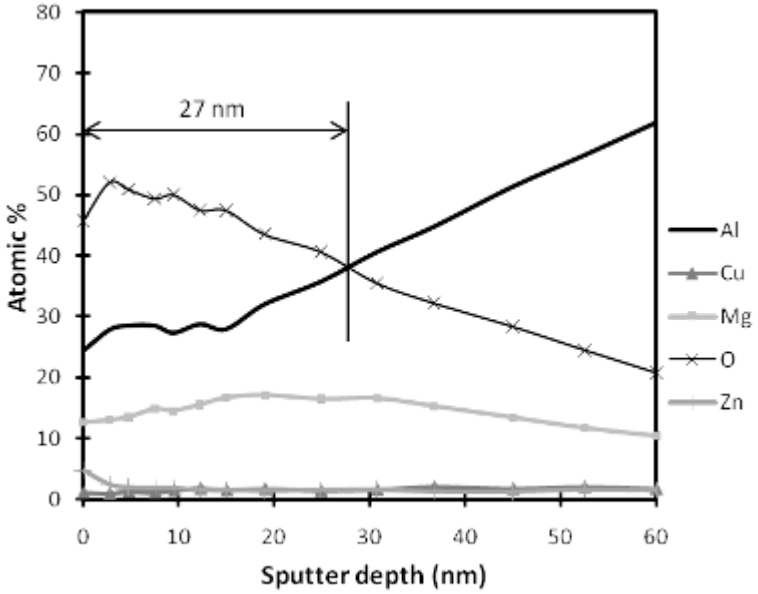

Figure 42. AES depth profiling of Al7075-T6 after degreasing followed by activation in 1NaOH.

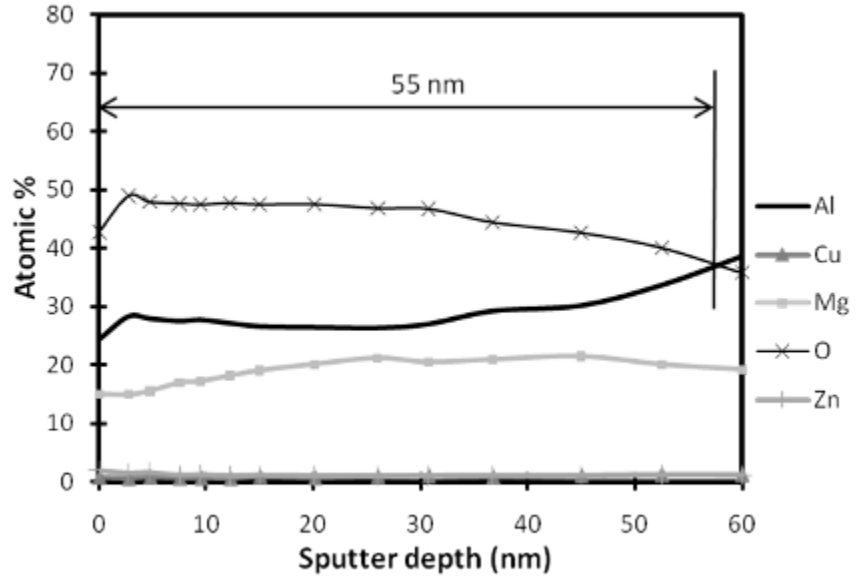

Figure 43. AES depth profiling of Al7075-T6 after degreasing followed by activation in 2NaOH.

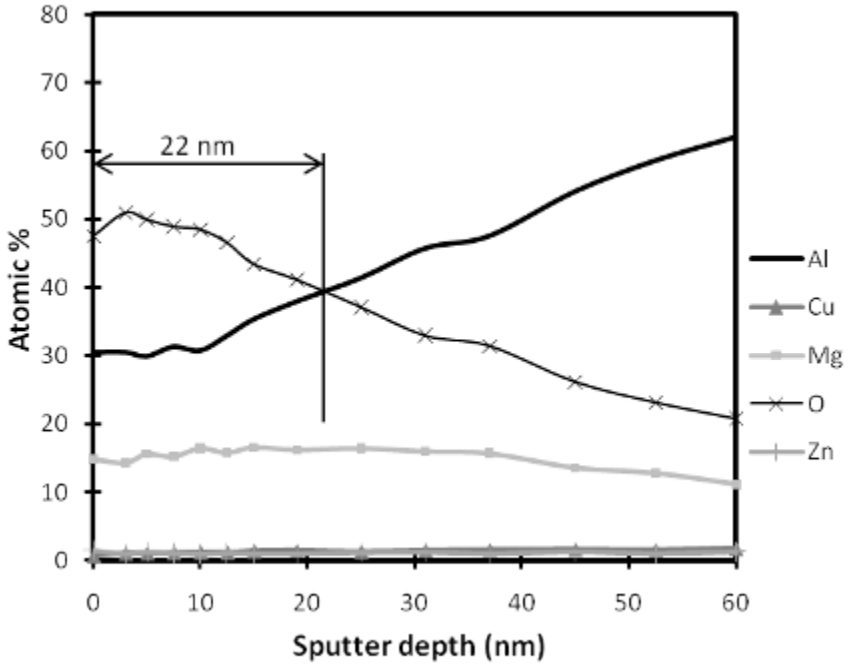

Figure 44. AES depth profiling of Al7075-T6 after degreasing followed by activation in $5Na_2CO_3$.

The increase in thickness of the oxide layer on the panel activated with 2NaOH is an indication of the higher activity of this solution compared to the other two solutions. The magnesium content of the oxide layer after activation was higher than it was after degreasing. At the high pH of the activation solutions, aluminum species should dissolve as aluminate ions, but magnesium is stable as $Mg(OH)_2$ or $MgCO_3$, depending on the activation solution used. AES data for each surface activation showed the concentrations at the panel surfaces were 25 to 30 at% Al, 15 to 20 at% Mg, and ~50 at% O. These compositions were similar through the oxide to within ~10 nm of the aluminum alloy substrates surface. The ~10 nm oxide layer closest to the interface with the substrate appeared to be similar to the native oxide present on the surface after degreasing. Based on the AES results, during activation it appears that a magnesium-rich oxide formed on top of the aluminum-rich layer that was present after degreasing.

Degreasing and alkaline activation are part of the standard process for deposition of CeCCs. The purpose of these steps is to alter the surface oxide composition and thickness to promote deposition of uniform CeCCs with sufficient thickness to provide corrosion protection. After only degreasing, AES depth profiling showed that the CeCC thickness after one spray cycle was ~30 nm. For comparison, CeCCs on alkaline activated panels had thicknesses in the range of 100 to 250 nm after one spray cycle (Table 11).

Table 11. Coating thickness by AES depth profiling of spray deposited CeCCs after degreasing and alkaline activation (denotes not measured).

	Degreasing	$5Na_2CO_3$	1NaOH	2NaOH
1 spray (nm)	30	100	175	250
5 sprays (nm)	-	230	380	500

Visually, no color change was observed for the surface of degreased panels after one spray cycle, whereas the color of alkaline activated panels changed to yellow after one spray cycle, indicating deposition of cerium-based coatings. Increasing the number of spray cycles to five on a degreased panel showed only a faint color change indicating insignificant deposition (thickness was not measured). In contrast, five spray cycles produced a more intense color change on alkaline activated panels indicating thicker deposition, which was determined to be in the range of 250 nm to 500 nm for the different activation processe. While degreasing removed the magnesium-rich oxide layer, it did not alter the dense native alumina layer on the panels. Apparently this layer protected the alloy surface during deposition and did not allow the coating solution to penetrate the oxide and react with the substrate, which is required for spontaneous deposition of coatings. In the case of alkaline activated panels, the surface oxide was altered such that the deposition solution could react with the substrate to produce coatings. Panels cleaned in $5Na_2CO_3$ produced thinner coatings than 1NaOH and 2NaOH, which indicated that it was less aggressive than the NaOH solutions. Based on observed color changes and measured coating thicknesses, degreasing followed by activation altered the surface

The corrosion resistance of CeCCs on degreased and alkaline activated panels was evaluated in salt spray testing conducted in accordance with ASTM B117. With only one spray cycle, degreased and $5Na_2CO_3$ activated panels showed significant corrosion in the form of pits and salt tails within 24 hours. The coatings on these panels were too thin to provide significant protection. Increasing the spray cycle to five for degreased panel did not improve the corrosion resistance and the panels showed the formation of pits and salt tails within 24 hours. In contrast, coatings produced by one spray-drain cycle on panels activated in1NaOH or 2NaOH performed better and inhibited the formation of pits and salt tails for at least 24 hours. When the number of deposition spray cycles was increased to five, the coatings on the substrate prepared using any of the three alkaline activation solutions provided better corrosion protection as compared to the coatings deposited with one spray cycle. In this analysis, seven out of ten CeCCs prepared using five spray-drain cycles on alkaline activated panels inhibited the formation of visual pits and salt tails for up to 2 weeks in salt spray testing. Thus, alkaline surface activation on Al 7075-T6 not only helped promoted deposition of uniform CeCCs with increased thickness, but the subsequent CeCCs also demonstrated enhanced corrosion resistance.

The EIS results for the acetone rinsed panel using a test electrolyte with a natural pH of ~5.5 showed significant noise at $\leq$ 1 Hz (Figure 45). Similar EIS curves were obtained for degreased or degreased and alkaline activated panels (not shown here). The OCP for all these curves ranged from -0.60 to -0.65 V_{SCE}. Due to the noise at $\leq$ 1 Hz, the low frequency results from EIS could not be analyzed with equivalent circuit (EC) models. Mansfeld and Fernandes [105] observed an inductance loop at low frequencies, and they attributed it to the similarity of the OCP and pitting potentials. Based on the present results along with those of Mansfeld and

Fernandes, the impedance data were reliable at frequencies above 1 Hz; no meaningful data were obtained below this frequency.

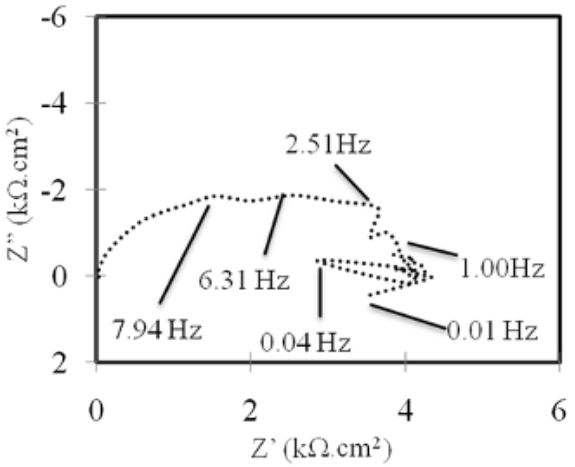

Figure 45. EIS test result for acetone rinsed Al 7075-T6 panels.

The polarization scans of an acetone rinsed and a 2NaOH activated panel using the test electrolyte with a pH of ~5.5 showed nearly vertical cathodic slopes and lack of passivation (Figure 46). Similar polarization scans of degreased or degreased and 1NaOH or $5Na_2CO_3$ activated panels were obtained and the OCP ranged between -0.57and -0.49 V_{SEC}. The lack of passivation indicated that the OCP and pitting potential were almost equal. The cathodic slopes for all of the panels were nearly vertical, indicating that corrosion was controlled by diffusion-limited transport of oxidizing agents. Thus, the polarization scans showed that the test electrolyte at pH 5.5 was corrosive to the alloy and was capable of causing pitting at OCP.

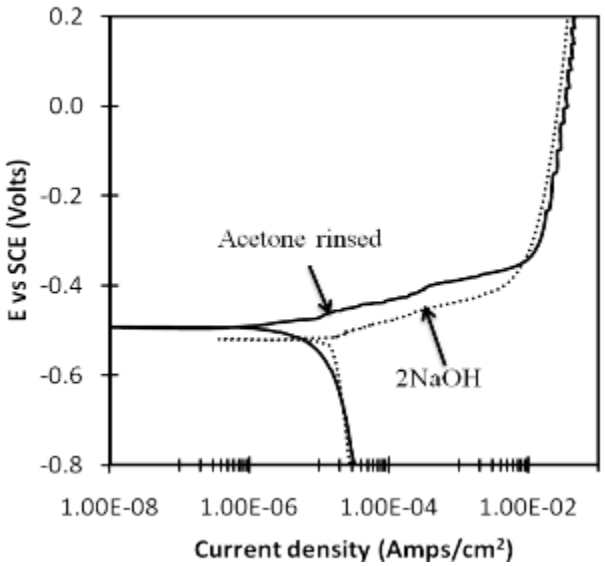

Figure 46. Polarization scans of acetone rinsed and 2NaOH activated panels. The polarization scans of degreased or degreased and 1NaOH or $5Na_2CO_3$ activated panels were similar to these two scans and are not included here.

Optical image and SEM micrographs of a panel after EIS testing using the test electrolyte with a pH of ~5.5 showed pits and tails (Figure 47a). The optical image (Figure 47a) validates the electrochemical results shown in Figure 45 in that severe corrosion in the form of pits and tails occurred at OCP. Figure 47b is a micrograph of a pitted area showing one large pit (~200 µm in diameter) and two smaller pits (~20 µm in diameter). One of the small pits shown in Figure 47b is magnified in Figure 47c. Point EDS analysis near the center of the pit on the spot shown by the cross in Figure 47c revealed an elevated copper content (1.7 at%). For comparison, the amount of copper detected by EDS on the matrix where no pitting corrosion occurred was ≤ 0.1 at%. The EDS result and SEM micrographs suggest that during EIS testing chloride ions caused pitting of the alloy at OCP near copper-rich sites.

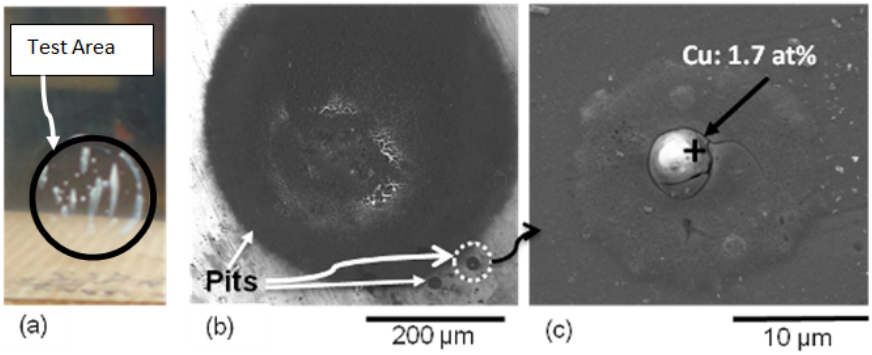

Figure 47. Pits developed after EIS testing using a test electrolyte of pH 5.5: (a) optical image of the 1 cm^2 test area showing white salt tails, (b) SEM micrograph displaying one large pit and two smaller pits, and (c) magnified SEM micrograph of one of the small pits shown in (b).

EIS results using a test electrolyte with a pH of 9.0 for all surface treatments are shown in Figure 48. The impedance plots were different from those obtained using the same test electrolyte at its natural pH of ~5.5. All curves in Figure 48 had maxima around 7.94 Hz and minima around 6.3 kHz and 1 Hz. At this electrolyte pH, the OCP at which EIS testing was conducted ranged from -0.65 to -0.70 V_{SCE} for all panels, whether acetone rinsed or alkaline activated. At low frequencies (<1.00 Hz), the EIS data exhibited no noise. The EIS plots exhibited trends similar to those shown by Mansfeld and Fernandes [105], which was stabilized in 0.5 N NaCl electrolyte for at least 24 hours before conducting EIS testing. Thus, by increasing the test electrolyte pH to 9.0, the EIS test could be performed at low frequencies on these surfaces within 1 hour of stabilization in the test electrolyte.

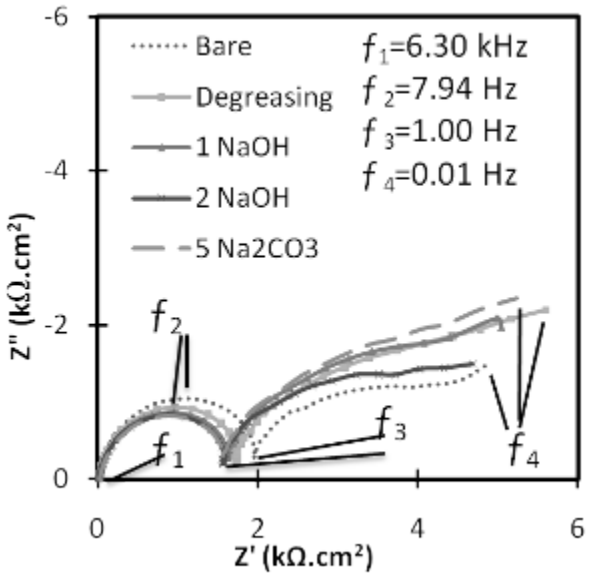

Figure 48. Impedance plots with key frequencies for Al 7075-T6 using a test electrolyte of pH 9.0 for various surface treatments.

Similar polarization scans were obtained for degreased or degreased and 1NaOH or $5Na_2CO_3$ activated panels (Figure 49). The anodic slopes exhibited passivation, that is, a separation between pitting potential and OCP. The cathodic slope was less vertical than when the test electrolyte was at pH 5.5, indicating corrosion was not diffusion-limited. Polarization scans showed that increasing the test electrolyte pH to 9.0 made the solution less corrosive to the alloy.

Significantly less pitting was observed after testing in the electrolyte with a pH of 9 (Figure 50). Prior to testing, the panel was polished, degreased, and activated using the 2NaOH solution. Optical image (Figure 50a) revealed no pitting or tailing after EIS testing. Pits could be observed only at higher magnification (Figure 50b). Figure 50c shows a cross-section micrograph of the pit in Figure 50b. Point EDS analysis around the pitted area at points labeled A, B, and C revealed an elevated copper content (1-5 at%) in the pit compared to the matrix (labeled D in Figure 50c), which only had ~0.1 at% copper. As when the test electrolyte at pH ~5.5 was used, the pits that developed at OCP formed near copper-rich sites. SEM micrographs show that during EIS testing, pitting was less severe when the test electrolyte was used at pH 9.0.

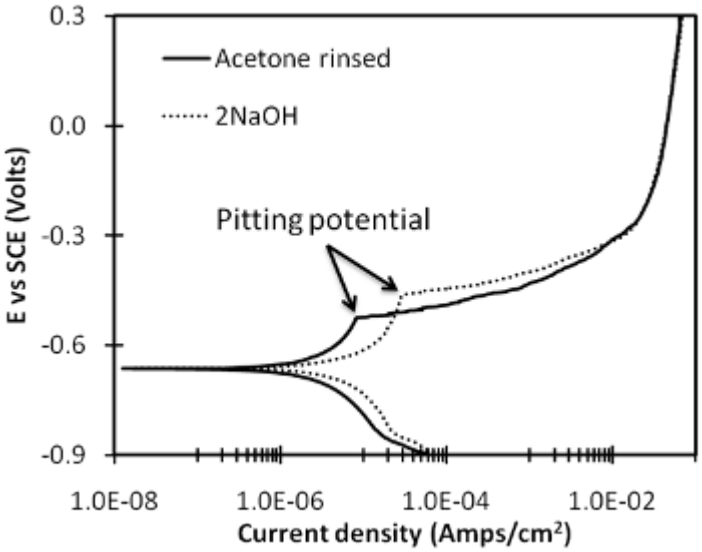

Figure 49. Polarization scans for an electrolyte of pH 9.0 on panels after surface cleaning and 2NaOH activation. Similar polarization scans were obtained for degreasing or degreasing plus 1NaOH or 5 Na_2CO_3 activations, so those scans are not shown here.

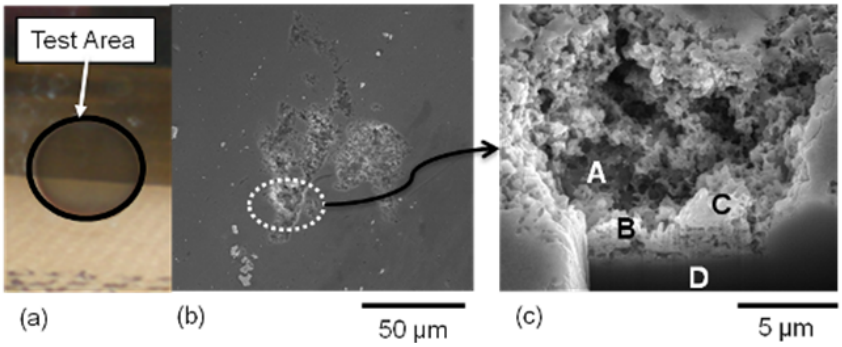

Figure 50. Post-EIS testing using test electrolyte of pH 9.0: (a) optical images displaying the 1 cm^2 test area, (b) SEM micrographs of a pit, and (c) SEM cross section micrograph of the pit shown in b. (Note the copper contents detected by EDS in at% at A, B, C, and D were 1.0, 5.0, 2.1, and 0.1 at%, respectively).

The effect of test electrolyte pH on the corrosion behavior of aluminum alloys is dependent on the thermodynamic stability of water [106]. In the E-pH diagram of water at 1atm (Figure 51), line X represents oxygen-water equilibrium, and line Y represents hydrogen-water equilibrium. The stable potential region for water is between lines X and Y and is expressed by equation I. Below line Y, hydrogen liberation is favored (equation II), which is one of the cathodic reactions that occurs during metal corrosion [82,107-109]. The other common cathodic reaction that occurs during metal corrosion is reduction of dissolved oxygen (equation III) [109].

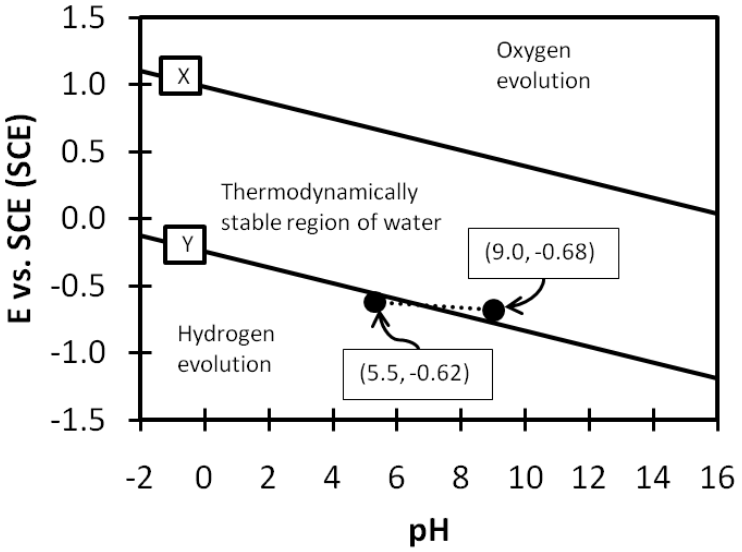

Figure 51. An E-pH diagram constructed to illustrate the thermodynamic stability of water at 1 atm pressure and 298 K.

$$-(0.242 - 0.0592\text{pH}) \leq \xi(\text{vs SCE}) \leq (0.986 - 0.592\text{pH}) \quad \text{(I)}$$

$$2H^+ + 2e^- \rightarrow H_2 \quad \text{(II)}$$

$$O_2 + 4H^+ + 4e^- \rightarrow 2H_2O \quad \text{(III)}$$

Using a test electrolyte with a pH 5.5, the final OCP was in the range of -0.60 to -0.65 V_{SCE} during stabilization. This value falls below line Y as seen in Figure 51. When the pH was increased to 9.0, the OCP decreased slightly (-0.65 to -0.70 V_{SCE}), but remained within the stable region of water. Therefore, increasing the test electrolyte pH to 9.0 from the natural pH of 5.5 inhibited the hydrogen evolution reaction, which can be identified by the difference in the cathodic slopes in the polarizations test shown in Figure 46 and Figure 49. The polarization scan with a test electrolyte of pH 5.5 in Figure 46 exhibited a nearly vertical cathodic slope indicating diffusion-limited mass transport, which was dependent on how fast water reduced to form hydrogen gas on the metal surface. Figure 49 does not display this behavior, indicating that the corrosion was less dependent on water reduction. Instead, corrosion was likely dependent on reduction of dissolved oxygen on the metal surface. The OCP values calculated by fitting Tafel slopes in Figure 46 were in the range of -0.50 to -0.60 V_{SCE}, higher than the OCP obtained during stabilization (0.68 V_{SEC}). This increase is likely due to buildup of a hydrogen gas layer given by expression II, which created an overpotential. Thus, the E-pH diagram shows that corrosion can be mitigated by changing the pH to stabilize water.

The EIS plot for all surface treatments using test electrolyte pH 9.0 exhibited two time constants, which were apparent in the data as capacitive loops (). One time constant is associated with response of the bulk oxide at high frequency (10^5-10^0 Hz) and the other with pits at low frequency (10^0-10^{-2} HFigure 49z). Figure 52 shows a schematic diagram and proposed EC of the

surface oxide with a pit. Thus, a less corrosive test electrolyte at pH 9.0 permitted collection of stable EIS data that could be fitted to an EC model to describe the corrosion behavior of the surface oxide.

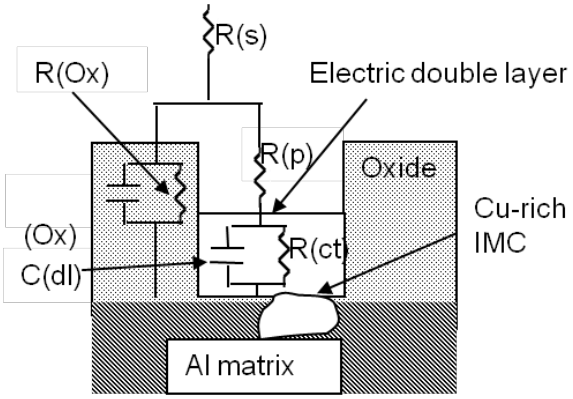

Figure 52. Schematic diagram and proposed EC of an oxide coating with a pit after reaching steady-state in an electrolyte.

Table 12 lists the values for each EC component and its standard deviation calculated by regression of the model (Figure 52) to the data (Figure 48). The term R(s) represents solution resistance, which was nearly constant (15-22 $\Omega \bullet cm^2$) for all panels whether, surface cleaned or activated. The oxide is a high resistance insulator and can be considered a partially blocked surface, i.e., one using only capacitance denoted by C(Ox). Incorporating oxide resistance, R(Ox), in the model generated errors $>10^6$. The term R(p) represents the polarization resistance of the passive surface, and R(ct) is the charge transfer resistance of the pitted area. The capacitance arising from the charge separation at the dielectric double layer is denoted by C(dl), which was also nearly constant (1.0-1.4 mF/cm^2) for all panels, whether acetone rinsed or activated. The chi-square value for each fit was less than 0.02, indicating very good fits. The EIS plot can be fitted into various circuit models that may lead to different physical interpretations due to differences in the individual parameters. However, the value of overall resistance, R(T), that is, the sum of R(p) and R(ct), is significant because it is independent of the models used to fit the data.

Table 12 shows that the oxide layer capacitance, C(ox), of the acetone rinsed substrate had the lowest value, which was 5.6 $\mu F/cm^2$. Capacitance is inversely proportional to thickness, and this low value indicates that the original oxide was the thickest before cleaning. After degreasing, C(ox) increased to 8.7 $\mu F/cm^2$ and remained in the range of 8.5-9.6 $\mu F/cm^2$ after activation. The increase in capacitance value from the EC modeling is consistent with previously reported oxide thickness [66] obtained by Auger electron spectroscopy measurements, which showed that the oxide layer thickness decreased from ~30 nm on the original panel to ~10 nm after degreasing and remained at ~10 nm after subsequent surface activation.

Table 12. Equivalent ciruit values for EIS data from Figure 48.

	Acetone Rinsing	Degreasing	1NaOH	2NaOH	$5Na_2CO_3$
R(s) [Ω•cm²]	17.6 ± 0.5	20.7 ± 0.3	22.4 ± 0.3	15.1 ± 0.3	18 ± 0.3
R(p) [kΩ•cm²]	2.4 ± 0.5	1.90 ± 0.03	1.80 ± 0.02	1.58 ± 0.02	1.61 ± 0.02
C(Ox) [μF/cm²]	5.6 ± 0.1	8.7 ± 0.1	9.6 ± 0.1	8.5 ± 0.1	9.3 ± 0.1
R(ct) [kΩ•cm²]	3.5 ± 0.2	4.1 ± 0.2	3.0 ± 0.1	2.6 ± 0.1	3.2 ± 0.1
C(dl) [mF/cm²]	1.00 ± 0.06	1.28 ± 0.05	1.31 ± 0.05	1.4 ± 0.05	1.4 ± 0.05
OCP [V]	-0.67	-0.70	-0.67	-0.70	-0.66
R(T) (Ω•cm²)	5925	5950	4800	4235	4800
% Change in R(T) from Acetone rinse	0	0.4%	-19.0%	-28.5%	-19.0%
Chi-square	0.018	0.013	0.010	0.007	0.009

The average overall resistance of panels that were rinsed with acetone and degreased was ~5.9 kΩ•cm^2. Panels that had only an acetone rinse had a high resistance variance (standard deviation ~1.1 kΩ•cm^2), but after degreasing the measured range was 5.7-6.1 kΩ•cm^2. Thevariance was also apparent from the high standard deviation of R_p for acetone rinse (0.5 kΩ•cm^2) than from alkaline treated panels (0.03 kΩ•cm^2). With such high variance, coatings deposited on this surface tend to be non-uniform. The variance in the overall resistance also indicated that the surface of as-received panels must be treated to produce a surface with uniform electrochemical properties, which improve the adhesive properties of any subsequent coatings. The results show that as-received Al 7075-T6 had a strong corrosion resistant surface oxide and that cleaning by degreasing made the oxide more uniform, but did not alter its overall resistance.

After degreasing, R(ct) increased from 3.5 kΩ•cm^2 (acetone rinsed) to 4.0 kΩ•cm^2, which countered the loss in R(p); therefore, the R(T) value did not change significantly. The decrease in R(p) and the increase in R(ct) is likely due to thinning of the passive oxide layer from ~30 nm on the starting surface to ~10 nm after degreasing due to removal of magnesium-rich oxide layer. Therefore, no change in R(T) was detected after degreasing, indicating the overall corrosion resistance of the natural alumina layer was not significantly affected. The changes in R(p) and R(ct) indicated that the oxide had been altered, resulting in less variance in R(T).

Surface activation using 2NaOH decreased the overall resistance of Al 7075-T6 surface oxide to ~4.2 kΩ•cm^2, which was ~30% lower than the overall resistance after degreasing (~5.9 kΩ•cm^2). Activation with $5Na_2CO_3$ or 1NaOH decreased overall resistance to ~4.8 kΩ•cm^2, which is a decrease of ~20%. The decrease was less for these two activations because the solutions have lower pH values than 2NaOH solution and are less chemically aggressive.

Both R(p) and R(ct) decreased after alkaline activations, indicating the surface oxide electrochemical resistance had been decreased. The decrease in overall resistance is an indication that the surface oxide is more susceptible to corrosion. This susceptibility to corrosion can be observed during the deposition of CeCCs from aqueous solutions. Previous research [66]

showed that on a degreased panel, a coating that was only ~30 nm thick was deposited after a single spray-drain cycle. In contrast, deposition on alkaline activated panels produced coating thicknesses that were in the range of 100-250 nm. Because 2NaOH activation decreased the overall resistance the most, it also produced the thickest coatings (~250 nm). Activation in 1NaOH and $5Na_2CO_3$ both decreased the overall resistance, but less than the 2NaOH activation, and, therefore, produced coatings with intermediate thicknesses (~175nm for 1NaOH and ~100 nm for $5Na_2CO_3$). The decrease in resistances indicated that during surface activation the native oxide was altered, making it more susceptible to attack by the coating solution, such that the coating deposition solution could easily penetrate the oxide and react with the substrate to deposit the coatings.

Deposition of CeCCs on Aluminum Alloy 380

AA380 alloy sheets 0.3 cm thick were cut into test panels 2.5 cm by 7.6 cm in size. The composition of AA380 is summarized in Table 13. Pretreatment of the panels prior to coating started with an isopropyl alcohol wipe followed by degreasing in an aqueous solution of a commercial alkaline cleaner (5 wt% Turco 4215 NC-LT in deionized water) for 5 minutes at 55°C. After degreasing, the panels were activated by immersion for 10 min at 60°C in an aqueous solution containing 1 wt% sulfuric acid. Following cleaning and activation, the panels were rinsed in deionized water that was either at room temperature (nominally 25°C) or heated to 100°C. After rinsing, the panels were immersed in the deposition solution for different time intervals of up to 8 min.

Table 13. Nominal Composition of Aluminum Alloy 380.

element	Si	Fe	Cu	Mn	Mg	Ni	Zn	Sn	Other	Al
wt%	7.5-9.5	2.0	3.0-4.0	0.50	0.10	0.50	3.0	0.35	0.50	balance

The CeCC deposition solution was prepared from a stock solution consisting of 40 g $CeCl_3 \cdot H_2O$ (Alfa Aesar, 99.9%), 780 g of de-ionized water, pH adjusted to 2.07 with HCl. For the deposition solution, 205 g of the stock solution was mixed with 0.8 g of a water soluble gelatin (DSF, Rousselot) that was dissolved in 25 g of de-ionized water. Just before deposition, 15 ml of H_2O_2 (Fisher Chemical, 30 wt.%) was added.

Coated panels were post-treated by immersion for 5 minutes in a water solution containing 2.5 wt% Na_3PO_4 (pH adjusted to 4.5 with phosphoric acid) that was heated to 85°C. The corrosion resistances of the coated panels were evaluated using salt spray testing (Q-Fog, Q-Panel Lab Products) per ASTM standard B117. Panels with CeCCs were stored at room temperature in the laboratory for at least 24 h before characterization or salt spray testing.

The crystalline phases in the alloy and coatings were characterized by X-ray diffraction (Philips X-Pert Pro) using copper Kα radiation. Scanning electron microscopy (SEM; Hitachi S-4700) with energy dispersive X-ray spectroscopy (EDS; Phoenix System) was used to characterize the surface morphologies and compositions of CeCCs.

Electrochemical impedance spectroscopy (EIS) was carried out at open circuit potential with amplitude of 10 mV in the frequency range from 10^5 to 10^{-2} Hz. Measurements were made after stabilization in the test electrolyte for 1500 s. All experiments were conducted with a frequency response analyzer (Schlumberger SI 1255 HF) and a potentiostat/galvanostat (EG&G Princeton Applied Research Model 273A). Potentiodynamic analysis was carried out after EIS, the initial potential was -0.4 VSCE and final potential is 0.8 VSCE with respect to the open circuit potential, and the scan rate was 1mV/sec. The electrochemical cell was a 250 mL water jacketed beaker maintained at 25°C. The cell electrolyte was a modified prohesion solution, which consisted of 0.70 wt% $(NH_4)_2SO_4$ and 0.35 wt% NaCl in deionized water. The exposed area of the working electrode was 1 cm^2. A saturated calomel electrode (SCE) was used as the reference electrode and Pt mesh with an area of 12 cm^2 was used as the counter electrode.

X-ray diffraction analysis of bare AA380 alloy detected five different phases, specifically the Al matrix phase, a second phase of Si, and three intermetallic phases that were present in trace quantities, Al_2Cu, $FeSi_2$ and $Al_{4.5}FeSi$. Combining analysis of surface morphology (Figure 53a and b) and EDS (not shown) of the substrate after pretreatment, it appears that $FeSi_2$ and/or $Al_{4.5}FeSi$ intermetallic particles were dissolved by the alkaline and acid pretreatment. Dissolution sometimes left holes in the substrates that were up to about 20 μm in diameter (Figure 53c and d).

Pretreatment also altered the electrochemical response of the substrates. From the potentiodynamic curves shown in Figure 54a pretreatment increased the open circuit potential from about -600 mV_{SCE} for the starting panel to about -500 mV_{SCE} after alkaline cleaning, acid activation and rinsing. Figure 2a also shows that the pretreatment increased the corrosion current from 0.3 $\mu A/cm^2$ before pretreatment to 2.0 $\mu A/cm^2$ after pretreatment. However, the rinsing temperature, 25°C or 100°C, did not produce significant differences in either the open circuit potential or the corrosion current. The increase in corrosion current after pretreatment indicates that the alloy surface is more electrochemically active and easier to coat. From the corresponding electrochemical impendence spectra, Figure 54b, the impedance of starting panel was around 40 $k\Omega \cdot cm^2$, which was much larger than the impedance after pretreatment (~7.5 $k\Omega \cdot cm^2$ for both rinsing temperatures). In comparison to previous studies [54], the pretreatment process likely reduced the thickness of the native oxide layer, which decreased the impedance of the substrate. Previous analysis showed that the reduction in impedance and increase in corrosion current were necessary to promote deposition of CeCCs [54].

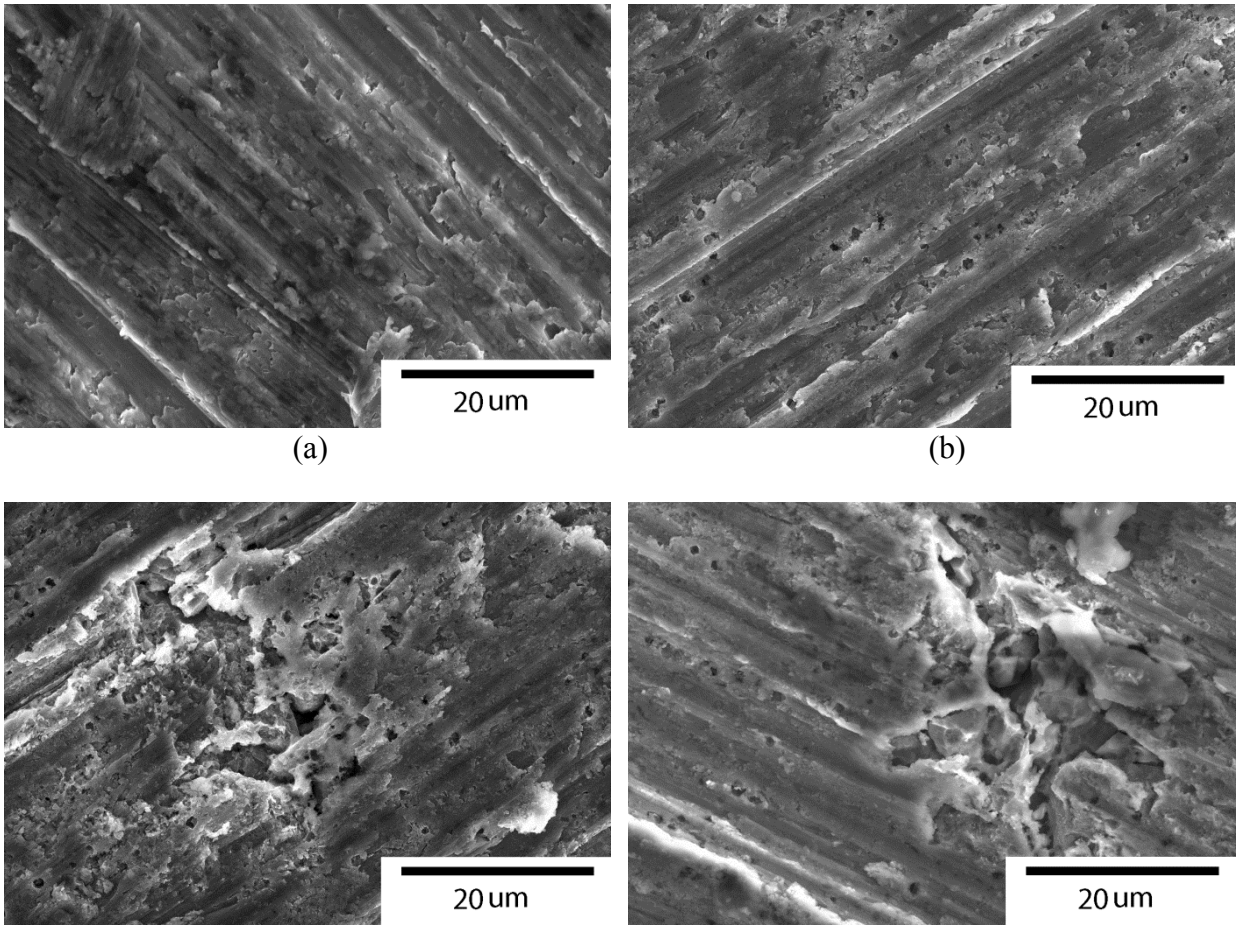

(a) (b)

(c) (d)

Figure 53. SEM surface morphology of AA380 cleaned panel; a) 180 grit polished, b) 25°C rinsed, c) 25°C rinsed showing an area with removal of material; and d) 100°C rinsed.

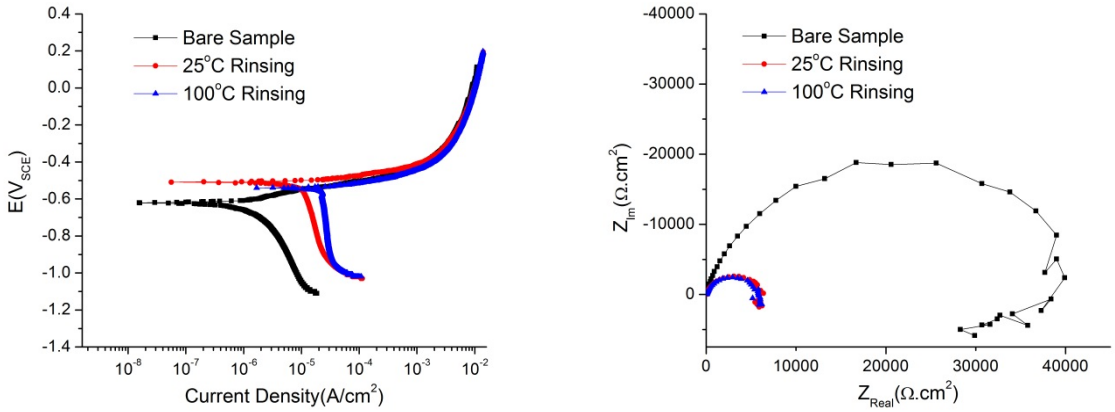

(a) (b)

Figure 54. (a) Potentiodynamic Polarization curves and (b) Impedance spectroscopy of bare, rinsing at 25°C and 100°C of AA380 alloy.

The substrates rinsed at 25°C prior to coating deposition, increasing the immersion time in the coating solution made the surface more electrochemically active. From the potentiodynamic curves in Figure 55a, the corrosion current increased from 0.82 μA/cm^2 after two minutes in the coating solution to 1.6 μA/cm^2 after 5 minutes and 2.7 μA/cm^2 after eight minutes (Table 14). In contrast, the open circuit potential did not vary significantly among the three panels, with all having values around -530 mV. The increasing corrosion current with the increasing immersion time suggests that the surface of the AA380 is more susceptible to chloride attack and dissolution. Therefore, the potentiodynamic curves for coatings on substrates rinsed at 25^{o}C, increasing the immersion time appears to increase attack of the substrate by the coating solution.

For substrates rinsed at 100^{o}C prior to coating deposition, increasing the immersion time in the coating solution increases the corrosion resistance. The potentiodynamic curves shown in Figure 55b reveal that the corrosion current decreased from 0.73 μA/cm^2 after immersion for 2 minutes to 0.54 μA/cm^2 after five minutes and to 0.34 μA/cm^2 after eight minutes (Table 14). The open circuit potential was about the same after immersion in the deposition solution for 2 or 5 minutes (-480 mV), but decreased to about -540 mV after immersion for eight minutes. The decreasing corrosion current indicated that the coatings had better corrosion resistance as the immersion time increased. Compared to panels rinsing at 25^{o}C (0.82 μA/cm^2), rinsing at 100^{o}C for 2 minutes resulted in a coating with better corrosion resistance (0.73 μA/cm^2) and the corrosion resistance, as measured by corrosion current, continued to increase as deposition time increased. Therefore, rinsing at 100^{o}C prior to coating deposition appears to be a better choice for deposition of CeCCs on AA 380 alloy.

Table 14. Electrochemical parameters derived from EIS and Potentiodynamic measurements of CeCCs deposited on AA 380 substrates rinsed at different temperatures.

Immersion Time (min)	Corrosion Parameters					
	R_p (kΩ•cm^2)		I_{corr} (μA/cm^2)		E_{corr} (mV_{SCE})	
	25^{o}C	100^{o}C	25^{o}C	100^{o}C	25^{o}C	100^{o}C
2	32	36	0.82	0.73	-540	-480
5	16	49	1.60	0.54	-550	-480
8	10	76	2.70	0.34	-510	-540

The EIS results were consistent with potentiodynamic analysis. Rinsing at 25^{o}C prior to deposition resulted in coatings with impedance values that decreased as immersion time increased (Figure 55c). For panels rinsed at 25°C prior to coating, the impedance was 32 kΩ•cm^2 after 2 minutes of immersion in the coating solution and the value decreased to 16 kΩ•cm^2 after 5 minutes and 10 kΩ•cm^2 after eight minutes. However, for panels rinsed at 100°C prior to coating deposition, the impedance was 36 kΩ•cm^2 after immersion in the coating solution for 2 minutes, and it increased to 49 kΩ•cm^2 after 5 minutes and 79 kΩ•cm^2 after 8 minutes (Figure 55d). For panels rinsed at 100°C prior to coating deposition, the impedance of 79 kΩ•cm^2 after 8 minutes of immersion in the coating solution was more than double the highest value for coatings deposited on panels rinsed at 25°C, which was 32 kΩ•cm^2 after 2 minutes of immersion

in the coating solution. These results indicate that rinsing at 25°C prior to deposition led to corrosion resistance that decreased with increasing immersion time in the coating solution whereas rinsing at 100°C prior to coating deposition led to corrosion resistance that increased with the increasing immersion time.

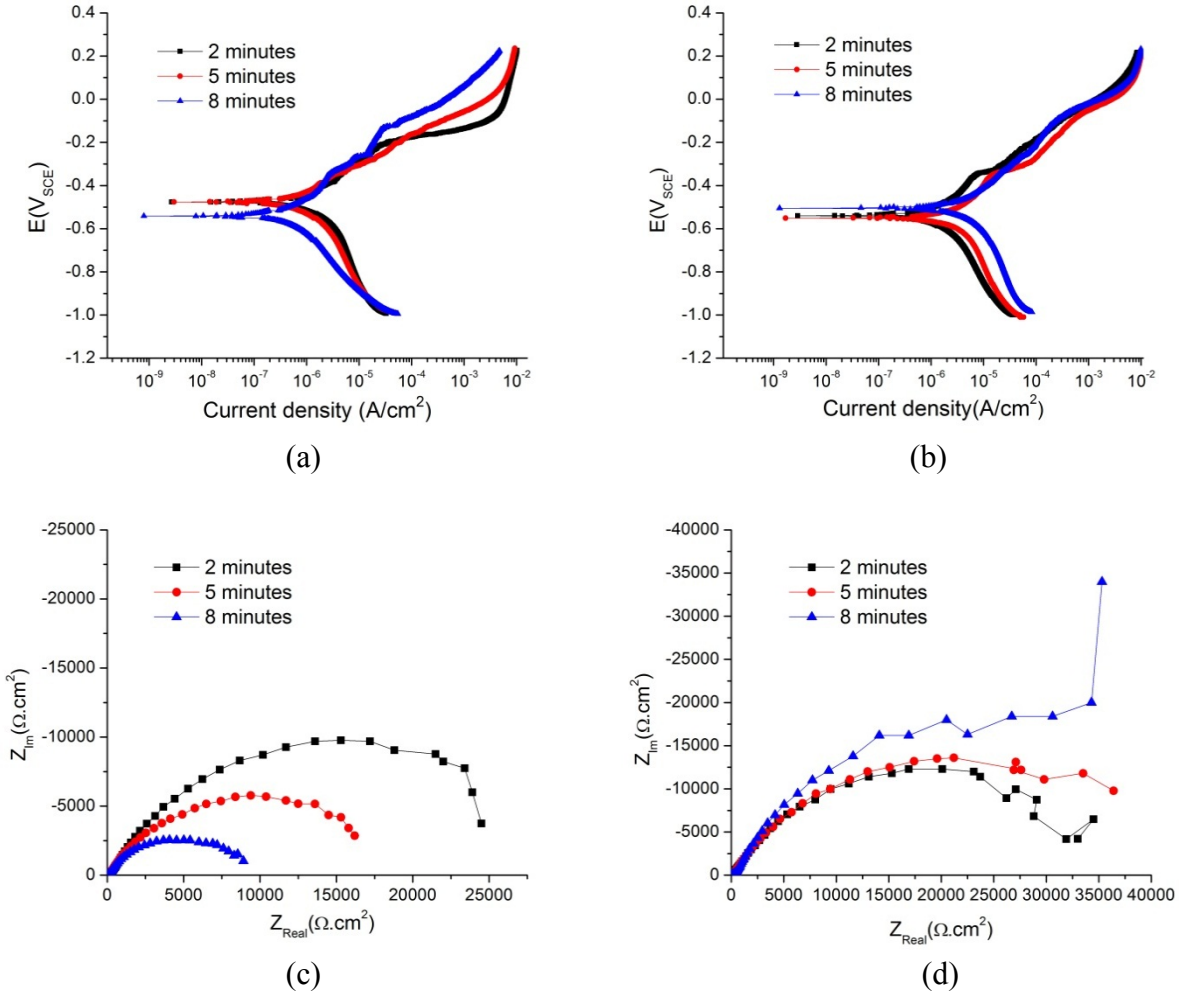

Figure 55. Electrochemical behavior of CeCCs deposited AA380 alloy in prohesion solution; potentiodynamic curve a) 25°C, b) 100°C, and impedance spectra, c) 25°C, and d) 100°C.

Coatings that were deposited on substrates that were rinsed at 25°C were cracked and had large holes. As shown in Figure 56, the cracks became larger as coating time increased. In addition to the cracks, large holes that were about 5 µm in diameter were also observed on the panel surfaces. Even though the coatings were cracked, the average thickness in areas with coating increased as immersion time increased. For example, the coating thickness (Figure 57) was about 350 nm after 2 min, but increased to nearly 2 µm after 8 min of immersion in the coating solution. However, the thickness was not uniform and it varied across the panel. The surface morphology is consistent with the electrochemical test results that showed that coating impedance decreased as immersion time increased for coatings on substrates rinsed at 25°C. The

impedance approached a value of 10 kΩ•cm^2 for deposition times of 8 min, which was about one third of the value (32 kΩ•cm^2) after immersion for 2 minutes. Hence, SEM analysis is consistent with electrochemical results that showed that coatings deposited on substrates rinsed at 25°C did not serve as effective barriers to corrosion due to non-uniform coverage of the AA380 surface.

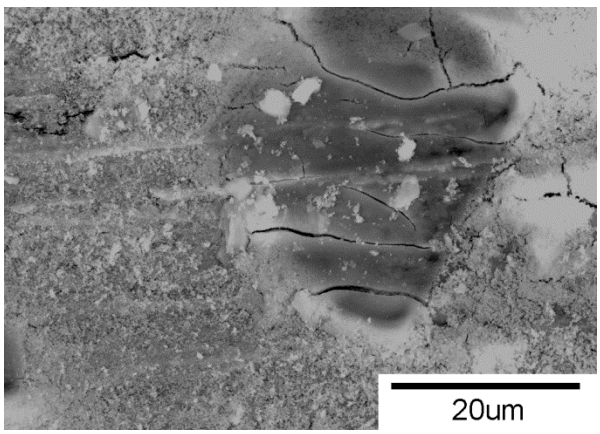

(a)

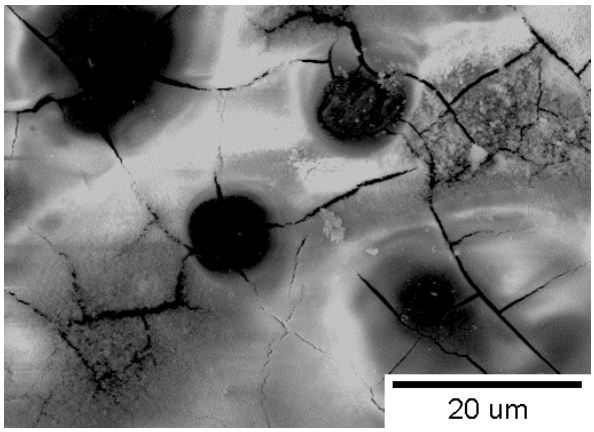

(b)

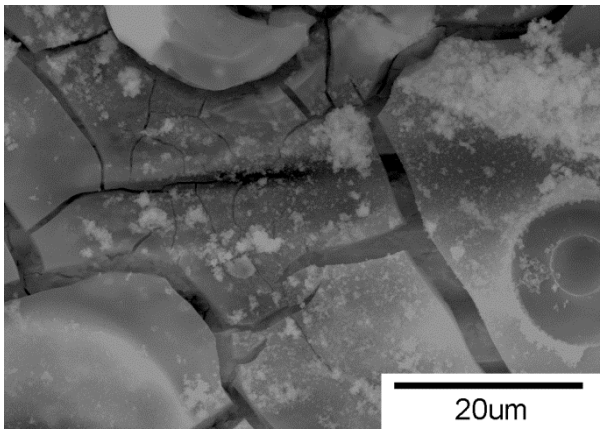

(c)

Figure 56. Surface morphology of coatings deposited on AA380 panels rinsed at 25°C after immersion in the coating solution; (a) 2 min, (b) 5 min, and c) 8 min.

Coatings that were deposited on substrates rinsed at 100°C had a nodular appearance (Figure 58) similar to previous work.[71] The coatings covered the substrates and only a few, small cracks (<0.5 μm wide) were observed. As with coatings deposited on substrates rinsed at 25°C, the thickness of CeCCs deposited on substrates that were rinsed at 100°C increased as deposition time increased. After 2 min of immersion, the coating thickness was just over 200 nm and it increased to ~700 nm after 8 min (Figure 57). Despite being thicker than CeCCs on high strength aluminum alloys such as 2024-T3 and 7075-T6, the coatings had only a few small cracks. As shown by the electrochemical analysis in (Figure 55d), coating impedance increased as immersion time increased, which is consistent with the formation of a thicker, continuous coating. Therefore, the surface morphology and thickness of the coating are consistent with

electrochemical results, which showed that coatings on substrates that were rinsed at 100°C prior to deposition increased the impedance compared to uncoated substrates.

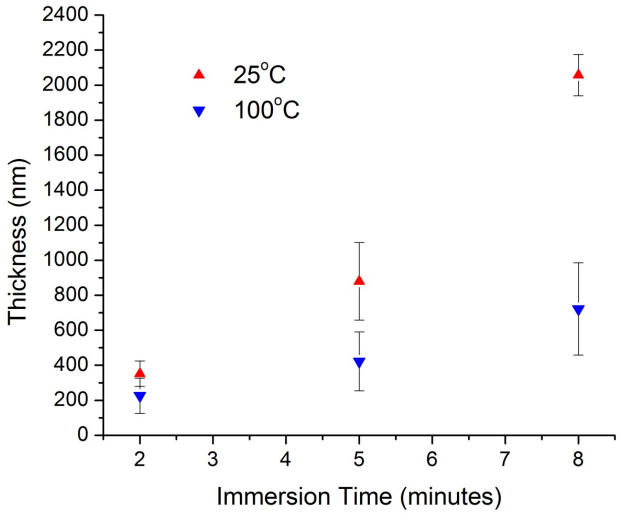

Figure 57. Thickness as a function of immersion time for CeCCs deposited on panels rinsed at 25°C and 100°C.

Coatings had a yellow-gold appearance (Figure 59a and Figure 60a) after post-treatment. Coatings deposited on substrate rinsed at 25°C prior to immersion showed a significant amount of white product corrosion after salt spray testing. Corrosion pits and salt tails were visible after 24 hours in salt spray testing as shown in Figure 7b. Coatings continued to degrade with further time in salt spray testing (Figure 59c and d). In contrast, coatings deposited on substrates rinsed at 100°C prior to deposition showed better corrosion resistance. After 24 hours, a few corrosion pits were present (Figure 60b), but significant salting was not observed until after 192 hours of salt spray testing. Therefore the results of salt spray testing were consistent with electrochemical characterization and surface morphology. Coatings deposited on substrates that were rinsed at 25°C prior to immersion had higher corrosion currents, lower impedance values, and were cracked, which led to more severe corrosion in salt spray testing. However, coatings that were deposited on substrates that were rinsed at 100°C prior to deposition had lower corrosion currents, higher impedance values, and were free of large cracks. As a result, coatings deposited on substrates rinsed at 100°C provided improved corrosion protection for AA380 alloy substrates.

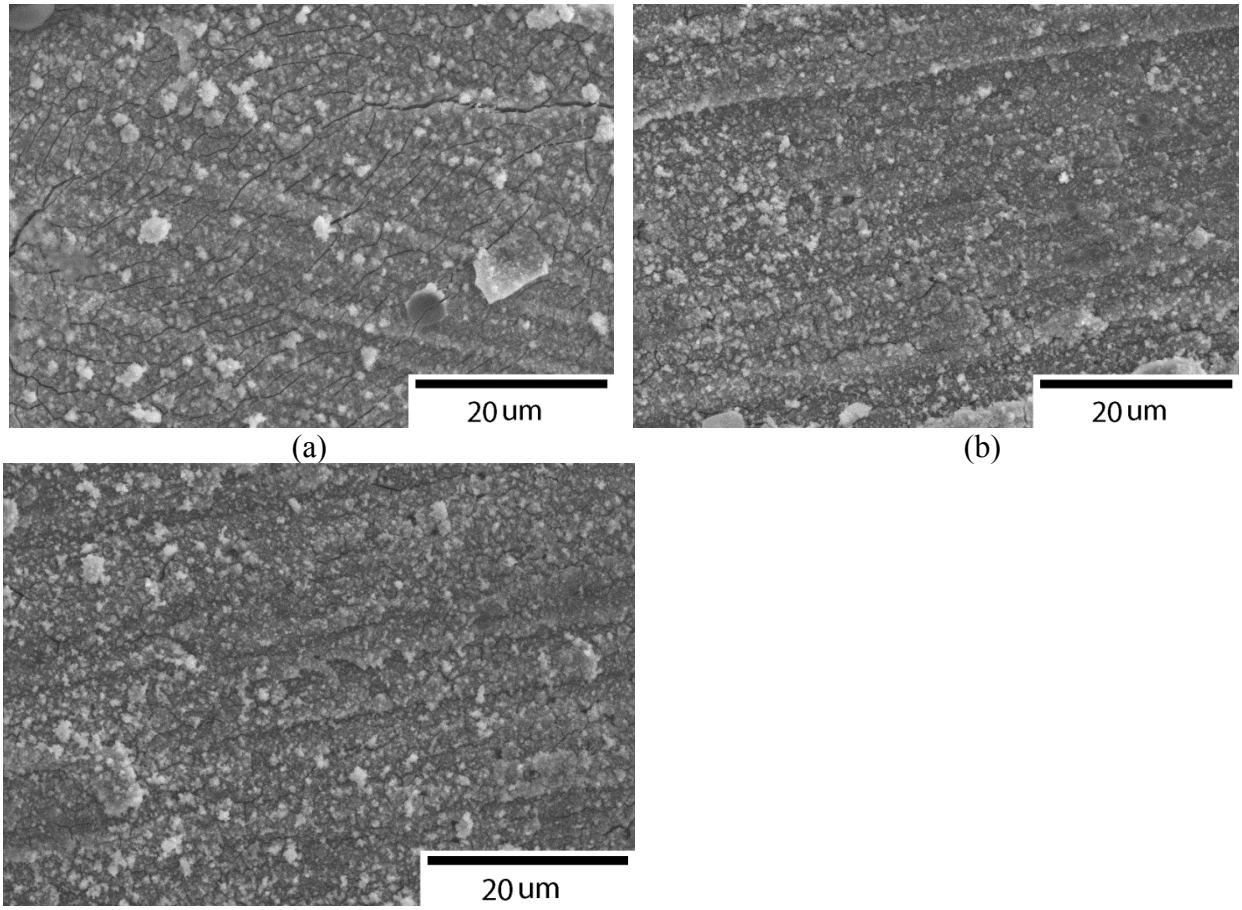

(a) (b) (c)

Figure 58. Surface morphology of coatings deposited on panels rinsed at 100°C after immersion in the coating solution; (a) 2 min, (b) 5 min, (c) 8 min.

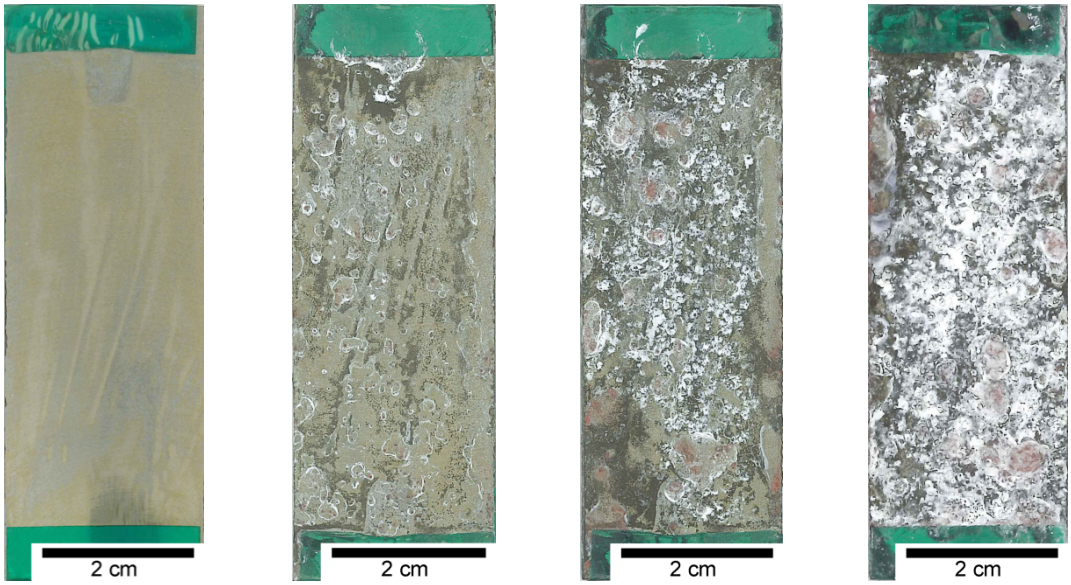

(a) (b) (c) (d)

Figure 59. Optical Images of coatings deposited on substrates rinsed at 25°C, a) as deposited, and after salt spray performance b) 24 hours, c) 96 hours, and d) 192 hours.

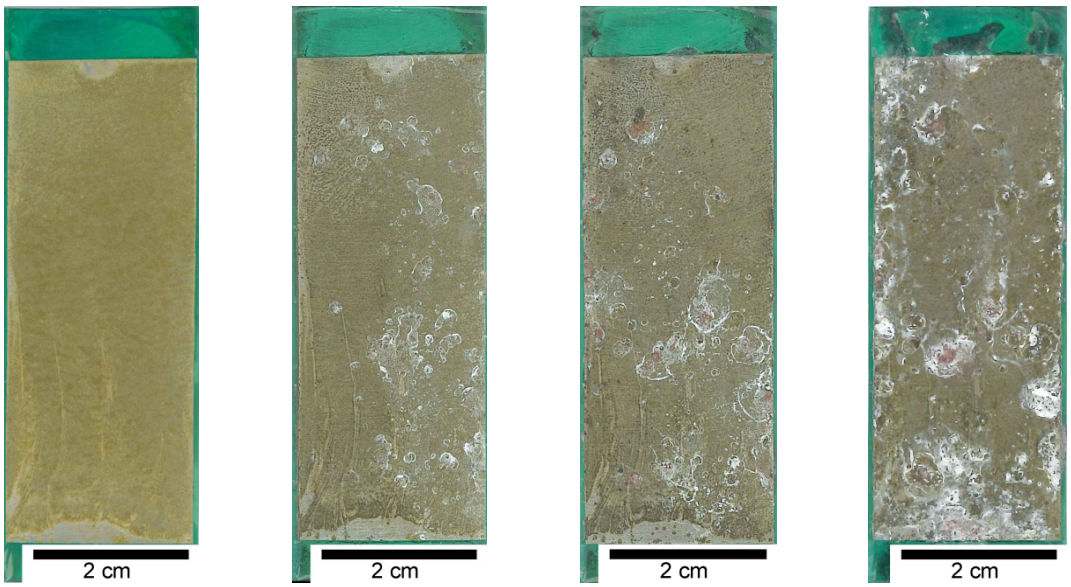

Figure 60. Optical images of coatings deposited on substrates rinsed at 100°C, a) as deposited, and after salt spray performance b) 24 hours, c) 96 hours, and d) 192 hours.

Epoxy-Polyamide Primers with Praseodymium-Based Inhibitors

The first year efforts focused on primers deposited onto Al alloys 2024-T3 and 7075-T6 with CrCC pre-treatments. Primer formulation and deposition was performed by Deft. The initial set

of samples consisted of both solvent (02GN084 series) and water-based (44GN098) primers coated on CrCC on top of Al 2024-T3. Both systems have shown that they can inhibit corrosion of high strength Al alloy panels scribed to bare metal for at least 3000 hours in ASTM B117 salt spray. The Deft epoxy-polyamide primers with Pr-based inhibitors have the best performance on CrCCs.

During the second and third years of the project, efforts remained focused on primers deposited onto Al alloys 2024-T3 and 7075-T6 with CrCC pre-treatments. Primer formulation and deposition were again performed by Deft. The set of samples discussed in this report consisted of both solvent and water-based primers coated on CrCCs on Al 2024-T3 panels. Both systems have shown that they can inhibit corrosion of high strength Al alloy panels scribed to bare metal for at least 3000 hours in ASTM B117 salt spray. The Deft epoxy-polyamide primers with Pr-based inhibitors have the best performance on CrCCs. In light of results seen with the solvent-based and water-based series samples Deft formulated test coatings containing Pr-phases only (Pr_2O_3 and Pr_6O_{11}) and coatings containing only acid extenders (Ca_2SO_4, $Ca_2SO_4 \bullet 2H_2O$, $BaSO_4$, and talc). These samples were subjected salt spray exposure similar to the standard formulations and characterized to pinpoint key components in the coating and their relationship to the overall corrosion protection mechanism.

Task 4: Characterization of Corrosion Behavior

This task focuses on characterization of the rare-earth phases in as-deposited coatings, reactions that occur during corrosive attack, and phases present after attack. The characterization effort has three main aspects, physical characterization (Task 4.1), electrochemical characterization (Task 4.2), and performance evaluation (Task 4.3). The goal of physical characterization is to identify the composition, crystal structure, and morphology of chemical species that are present in as-deposited coatings, that migrate during corrosive attack, and that are present after corrosion. For primer coatings, analysis focuses on the phase of the rare-earth inhibitor in the coating, dissolution and transport during corrosive attack, and the deposition of passivating species in exposed regions. Standard electrochemical techniques along with newly developed electrochemical techniques are being used to characterize and evaluate the protection provided by rare earth inhibitors. The primary method for performance evaluation is salt spray testing according to military specifications. To understand the mechanisms, characterization is being performed through the entire period of performance evaluation.

Physical Characterization

Conversion coatings and primer coatings were being characterized after deposition and as a function of time in performance evaluation (salt spray testing or electrochemical testing). The primary characterization techniques used to examine coating surfaces and cross sections were XRD, AES, and SEM with simultaneous chemical analysis by EDS. Focused ion beam processing was also used to produce cross section specimens from selected areas in as-deposited and corroded coatings for further analysis.

Cerium-Based Conversion Coatings

The study of the mechanisms by which Ce compounds provide corrosion protection was the main goal of this portion of the project. As discussed previously, during deposition of CeCCs, sub-surface crevices are formed due to the interaction between the spray solution and Al alloy.

The study of the mechanisms by which CeCCs provide corrosion protection is the main goal of this portion of the project. As discussed previously, during deposition of CeCCs, sub-surface voids are formed due to the interaction between the spray solution and Al alloy. Analysis of CeCCs (using Missouri S&T's processing parameters) using the FIB/SEM system revealed the sub-surface extended ~5 µm into the substrate beneath the coating (Figure 61). This discovery impacted the original scope of studying the protection mechanism of CeCCs because of the more complicated structure that was observed. Not only do CeCCs have to act as a barrier that protects the underlying substrate, but they must also provide protection to the sub-surface crevices beneath the panel surface. Hence, the protection mechanism is more complicated than originally envisioned.

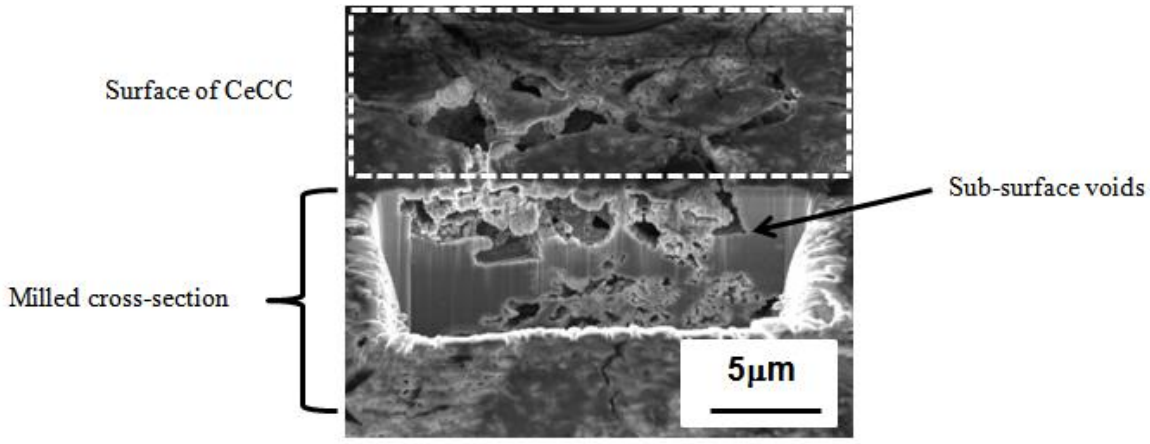

Figure 61. FIB cross section of a CeCC on Al 2024-T3 showing sub-surface voids underneath an area exhibiting large cracks.

These features were found underneath areas of the coating that exhibited large cracks, which typically covered ~10 % of the surface. It is thought the presence of sub-surface voids affected the overall corrosion protection of CeCCs deposited from solutions containing $CeCl_3$ and H_2O_2.

Cerium-based conversion coatings on Al 2024-T3 substrates were characterized after various exposure times in salt spray corrosion testing. As-deposited coatings performed poorly in salt spray corrosion testing, exhibiting light salt tailing after as little as one hour of exposure. With longer exposure times, the degree of salting present on the as-deposited coatings grew more severe to the point that after 24 hours the panels appeared corroded over the entire surface. In comparison, post-treated CeCCs exhibited improved corrosion protection. No visible corrosion was observed on post-treated coatings through seven days of salt spray exposure. After 14 days of testing, post-treated CeCCs showed some visible salt tails.

Electrochemical changes occurring in CeCCs during salt spray exposure were characterized using EIS analysis. Nyquist plots of EIS data for post-treated coatings (Figure 62) showed that impedance values were ~40 kΩ-cm^2 prior to salt spray exposure (0 hours). Upon exposure, impedance values of the post-treated CeCC increased during the first 12 hours, and then

stabilized at values of more than 100 kΩ-cm^2. Impedance values remained at about this level until ~14 days, when salt tailing was observed on the sealed coatings and the impedance decreased to ~70 kΩ-cm^2. Assuming that impedance is directly related to corrosion resistance, EIS testing showed that sealed CeCCs exhibited improved corrosion resistance after the first 12 hours of salt spray exposure and remained stable for up to ~2 weeks.

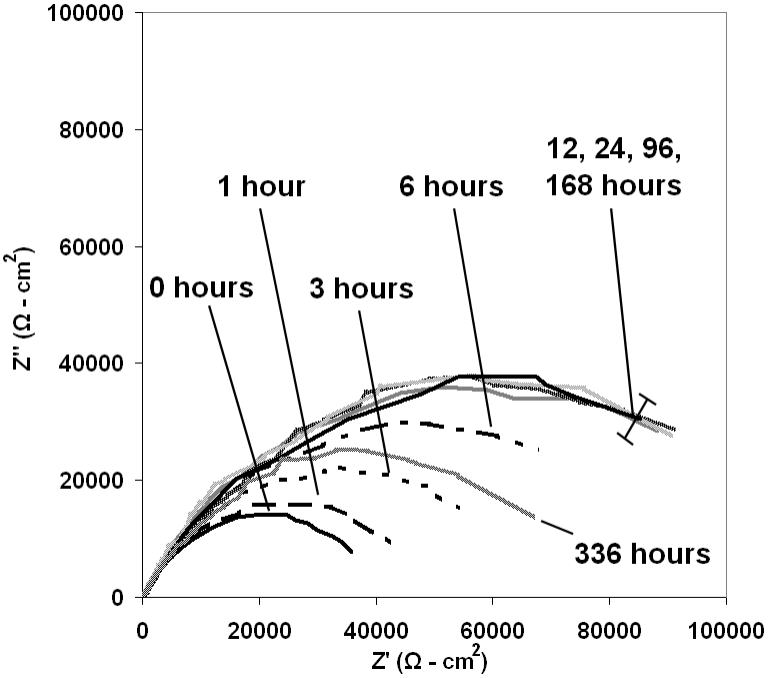

Figure 62. Nyquist plots of electrochemical impedance spectroscopy data for post-treated CeCC after various salt spray exposure times.

Nyquist plots of EIS data for as-deposited coatings (Figure 63) did not exhibit similar trends to post-treated coatings. Measured impedances of as-deposited CeCCs were an order of magnitude less than the values observed for post-treated coatings. Prior to salt spray exposure, as-deposited coatings had impedances of ~8 kΩ-cm^2. The impedance dropped after one hour of salt spray exposure to ~5 k Ω-cm^2, then increased back to its initial values for exposures ranging from three to 12 hours. Impedance values increased again to about 12 kΩ-cm^2 after about 24 hours, at which point panels exhibited heavy salting.

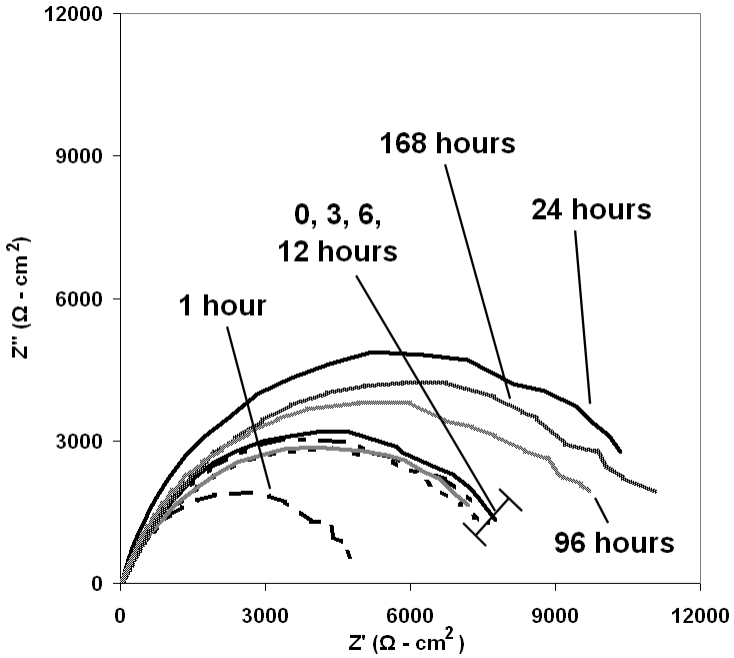

Figure 63. Nyquist plots of electrochemical impedance spectroscopy data for as-deposited CeCCs after various salt spray exposure times.

To understand how coatings changed during salt spray exposure, EIS data were fit to equivalent circuit models, which are illustrated in Figure 64a and b. The calculated parameter values for post-treated and as-deposited coatings are listed in Table 15 and Table 16, respectively.

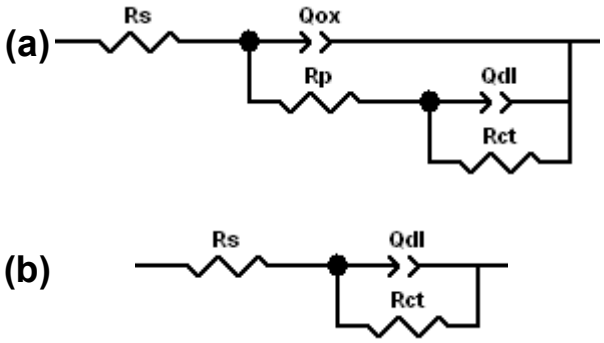

Figure 64. Models of the equivalent circuits used to fit EIS data from (a) post-treated and (b) as-deposited CeCCs

Table 15. Parameter values for post-treated CeCCs, fitted from the equivalent circuit shown in Figure 24a: $R_s(Q_{ox}(R_p(Q_{dl}R_{ct})))$ (R_s – solution resistance, Q_{ox} – coating capacitance, R_p – polarization resistance, Q_{dl} – double layer capacitance, R_{ct} – charge transfer resistance)

Salt Spray Exposure Time	R_s (Ω-cm^2)	Q_{ox} ($\mu\Omega^{-1}$sec^{n}cm^{-2})	R_p (Ω-cm^2)	Q_{dl} ($\mu\Omega^{-1}$sec^{n}cm^{-2})	R_{ct} (kΩ-cm^2)
0 hours	16 ± 1	19 ± 4	190 ± 26	42 ± 10	46 ± 3
1 hour	14 ± 1	20 ± 6	356 ± 43	27 ± 5	51 ± 5
3 hours	17 ± 2	12 ± 2	355 ± 92	19 ± 11	74 ± 8
6 hours	16 ± 3	14 ± 3	317 ± 98	21 ± 7	99 ± 8
12 hours	8 ± 5	11 ± 2	246 ± 52	21 ± 3	126 ± 4
24 hours	12 ± 6	24 ± 3	308 ± 67	28 ± 1	130 ± 5
48 hours	10 ± 1	23 ± 8	316 ± 24	33 ± 5	125 ± 12
168 hours	14 ± 5	17 ± 4	339 ± 36	30 ± 10	125 ± 8
336 hours	7 ± 3	22 ± 6	290 ± 30	21 ± 4	87 ± 8

Table 16. Parameter values for as-deposited coatings, fitted from the equivalent circuit shown in Figure 24b: $R_s(Q_{dl}R_{ct})$ (R_s – solution resistance, Q_{dl} – double layer capacitance, R_{ct} – charge transfer resistance).

Salt Spray Exposure Time	R_s (Ω-cm^2)	Q_{dl} ($\mu\Omega^{-1}$sec^{n}cm^{-2})	R_{ct} (kΩ-cm^2)
0 hours	15 ± 8	29 ± 6	9 ± 1
1 hour	20 ± 3	38 ± 6	6 ± 1
3 hours	21 ± 2	59 ± 15	8 ± 1
6 hours	23 ± 2	50 ± 3	8 ± 2
12 hours	18 ± 1	33 ± 19	9 ± 1
24 hours	20 ± 2	76 ± 8	12 ± 1
48 hours	19 ± 2	75 ± 6	12 ± 2
168 hours	22 ± 5	83 ± 18	13 ± 2

For post-treated coatings, the best fits were produced using models with two time constants, while data from as-deposited coatings could be fit to circuits with one time constant. These same equivalent circuits were used successfully in previous studies to calculate coating parameters in

which the total resistance was made up of components from the solution (R_s), coating (R_p), and double layer (R_{ct})[70,102]. In these studies, the measured capacitances were attributed to the capacitance of the coating (Q_{ox}) and double layer (Q_{dl}) [70,102]. The errors between the fitted equivalent circuits and the data were under ten percent for all coatings in the present study.

Post-treated coatings exhibited no significant changes in capacitance, solution resistance, or coating resistance as salt spray exposure times increased. In contrast, the charge-transfer resistance increased from an initial value of 46 kΩ-cm^2 prior to salt spray exposure to 130 kΩ-cm^2 after 12 hours of exposure. Charge-transfer resistance remained between 120 – 130 kΩ-cm^2 through 168 hours of salt spray testing, then exhibited a decrease to 87 kΩ-cm^2 after 336 hours, at which time sealed coatings began to exhibit visible pitting and salt tailing. Thus, the increase in impedance of sealed coating with salt spray exposure was attributed to an increase in the charge-transfer resistance of the coatings. Charge-transfer resistance is related to the corrosion protection of exposed areas of the coating, such as cracks or other defects. Changes in the charge-transfer resistance can be due to break down or build up of corrosion protection in these areas and due to the formation of a passive layer. Therefore, based on the increases in charge-transfer resistance, EIS testing showed post-treated coatings formed a protective layer or otherwise passivated areas on the substrate that were exposed and not covered by the coating.

For as-deposited coatings, neither capacitance nor solution resistance exhibited significant changes during salt spray exposure. As with post-treated coatings, the charge-transfer resistance of as-deposited coatings exhibited change with increasing salt spray exposure time. Before salt spray exposure, the charge-transfer resistance of as-deposited CeCCs was ~9 kΩ-cm^2. After an initial drop to ~6 kΩ-cm^2 after the first hour of exposure, the resistance increased and remained between 8 and 9 kΩ-cm^2 through 12 hours of salt spray testing. For longer exposure times, as-deposited coatings exhibited an increase in impedance, which was due to an increase in the charge-transfer resistance to ~12 kΩ-cm^2, where remained through 168 hours of exposure. Thus, changes in impedance observed in as-deposited coatings were also the result of changes in the charge-transfer resistance, just as was observed for post-treated coatings. The impedance and the degree of change, however, were both significantly less for as-deposited coatings with increases of ~ 3 to 6 kΩ-cm^2 for as-deposited coatings compared to increases of ~60 kΩ-cm^2 for post-treated coatings after 24 hours of salt spray testing.

Changes in surface compositions of CeCCs during salt spray exposure were analyzed using AES depth profiling. Prior to corrosion testing, sealed CeCCs (Figure 65a) were ~450 nm thick, based on the depth at which cerium concentrations fell below those of aluminum. In addition, AES detected ~40 at% oxygen, but minimal aluminum (<5 at%) at the surface of the coatings before salt spray exposure. After six hours of exposure (Figure 65b), aluminum and oxygen concentrations at the surface increased to 20 at% and 50 at% respectively. After 24 hours of exposure (Figure 65c), an aluminum-rich layer ~150 nm thick, based on the depth at which the aluminum concentrations fell below that of cerium, was detected on the surface. The thickness of the aluminum-rich layer remained in the range of 100 to 150 nm through 14 days of salt spray exposure for post-treated coatings.

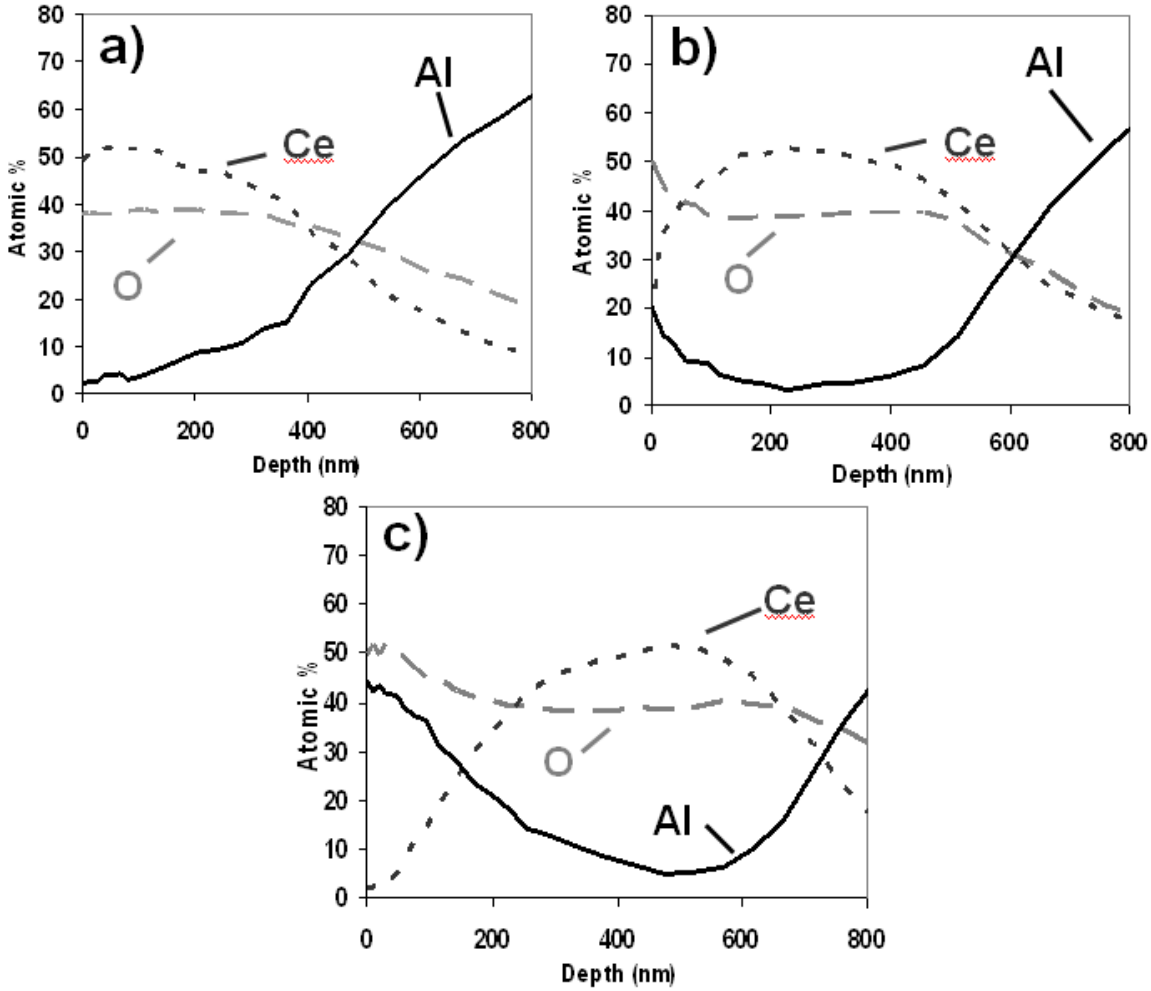

Figure 65. AES depth profiles for post-treated CeCCs a) before salt spray exposure and after b) 6 hours and c) 24 hours of salt spray exposure.

Prior to salt spray exposure, as-deposited CeCCs exhibited an AES depth profile (Figure 66a) similar to that of the sealed coatings. The coating thickness was ~450 nm with aluminum and oxygen concentrations at the surface of the coating of ~5 at% and 40 at%, respectively. After six hours of salt spray exposure (Figure 66b), an aluminum-rich layer ~150 nm thick was present on the as-deposited coatings, which had surface concentrations of aluminum and oxygen of 40 at% and 50 at%, respectively. The thickness and composition of the alumina layer remained at ~150 nm after 24 hours of testing (Figure 66c) and through 14 days of exposure.

During the first 24 hours of salt spray exposure, post-treated CeCCs exhibited significant increases in impedance and developed an aluminum-rich layer ~150 nm thick on the surface while having no visible corrosion. Given the correlation between the increase in impedance and the development of the aluminum-rich layer, it is hypothesized that post-treated CeCCs facilitated the formation of a protective alumina layer during salt spray exposure. The source of aluminum, phase of the layer, and areas covered by the layer have not been investigated extensively, but remain the subject of continuing research on the corrosion protection mechanisms of CeCCs.

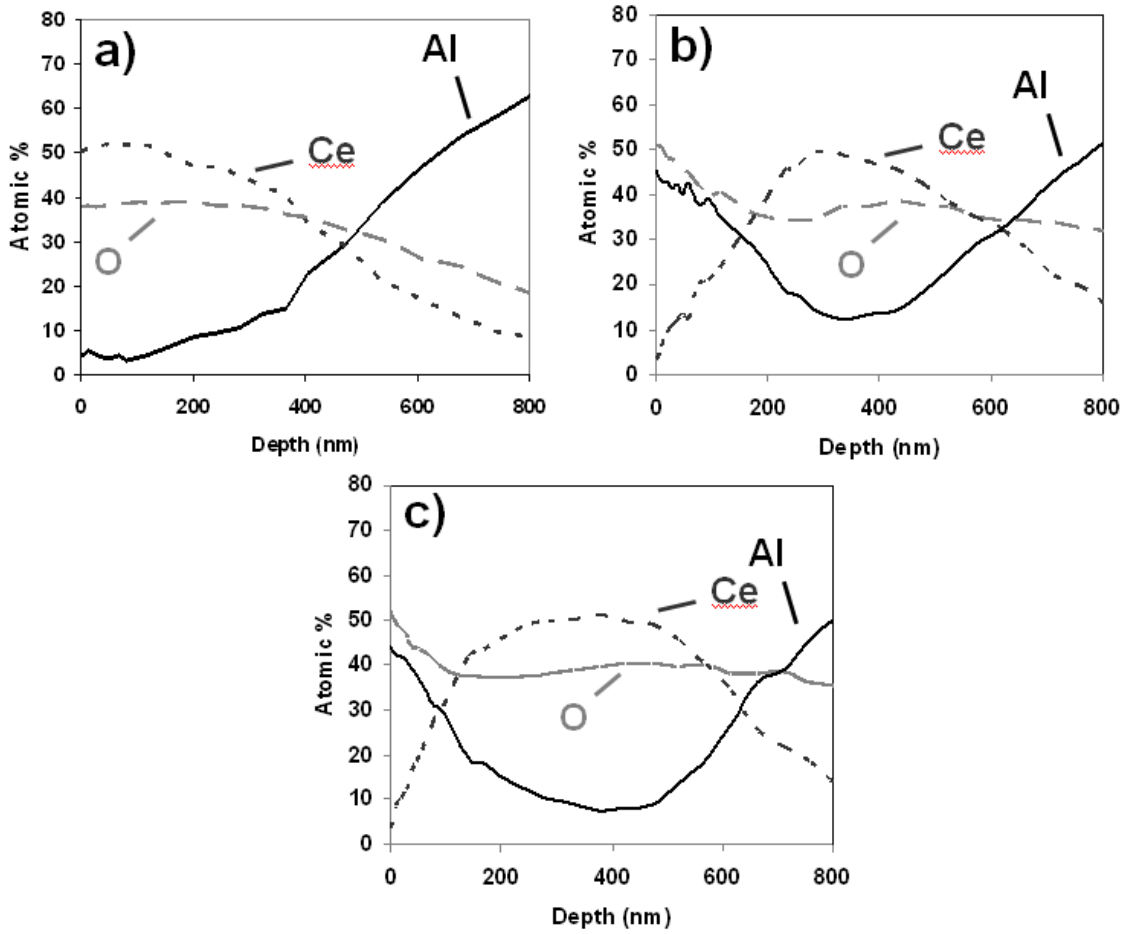

Figure 66. AES depth profiles of as-deposited CeCCs a) before salt spray exposure and after b) 6 hours and c) 24 hours of salt spray exposure.

In contrast to post-treated coatings, as-deposited CeCCs did not exhibit the same increases in impedance during salt spray exposure. Instead, the impedance remained relatively constant (after an initial drop) during the first 24 hours of salt spray exposure. The aluminum-rich layer on the surface of as-deposited coatings was thicker (based on AES depth profiling) after the same salt spray exposure times as compared to the aluminum-rich layer on post-treated coatings. Unlike the aluminum-rich layer that formed on sealed CeCCs, the aluminum-rich layer on unsealed coatings did not appear to be protective, since coating impedance did not increase with the presence of the layer. Additionally, significant salting was observed on as-deposited coatings after 24 hours of salt spray exposure. Thus, the aluminum-rich layer that formed on as-deposited CeCCs during salt spray exposure did not exhibit protective properties, appearing to be a corrosion product rather than a protective layer.

In addition to studying the electrochemical and surface chemical changes that occurred during salt spray exposure, structural changes were also characterized. Specifically, subsurface voids were found in both sealed and unsealed coatings. Subsurface voids were found in areas of CeCCs that exhibited large cracks on the surfaces. For post-treated CeCCs, large cracks were present

over ~10% of the area of the coated surfaces and sub-surface voids were found in most of these areas. After six hours of salt spray exposure, large cracked areas of post-treated CeCCs exhibited small pits (Figure 67). With longer exposure times, pits were still observed, but neither the number nor the size appeared to change.

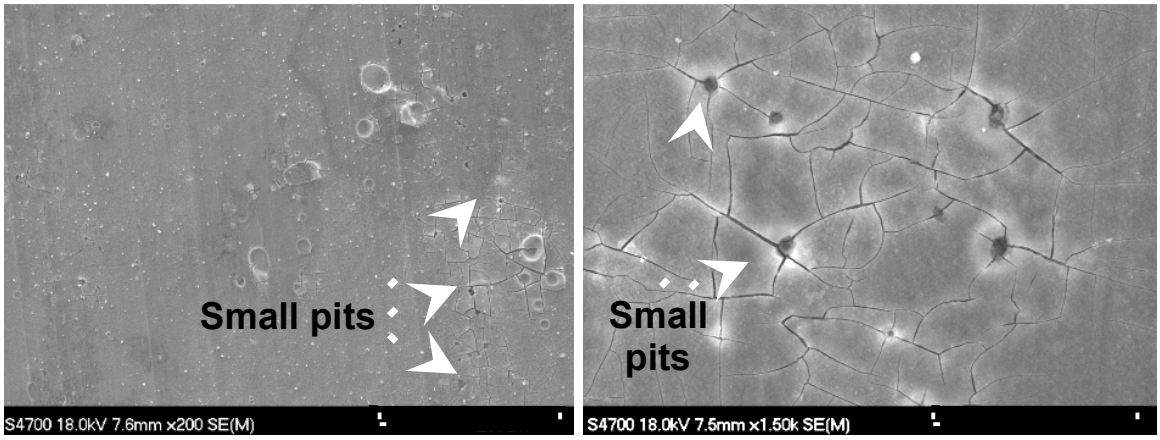

Figure 67. SEM images of a post-treated CeCC after six hours of salt spray exposure in which areas of the coating (~10% of the total area) exhibiting large cracked were found to have developed small pits.

FIB cross sectioning was done on a corrosion pit found in an area with large cracks on a post-treated CeCC after seven days salt spray exposure (Figure 68). The cross section of the pit revealed the presence of subsurface voids underneath the pit. In addition, a dark aluminum-rich phase was observed surrounding most of the perimeter of voids. After seven days of salt spray testing, the dark aluminum-rich phase in the void remained intact, with few, if any, defects such as pores or cracks. Given the lack of corrosion product either in the voids or on the surface of the panels, post-treated CeCCs appear to be able to protect the alloys from corrosion even inside subsurface voids. Within the voids, the protection may be due to the oxide surrounding these features, which could be resistant to the corrosive conditions that develop in salt spray testing.

As-deposited coatings had large cracks present in over half of the area of the coated surface; however, sub-surface voids were found in only a small fraction of the areas with large cracks. Large cracked areas of as-deposited coatings did not develop pits as was observed for post-treated CeCCs. Rather, these areas developed nodules that were rich in aluminum and oxygen after 6 hours of salt spray exposure (Figure 69a). The alumina nodules became more prevalent with time until ~24 hours of exposure at which time the large cracked areas were completely covered by the aluminum-rich material (Figure 69b).

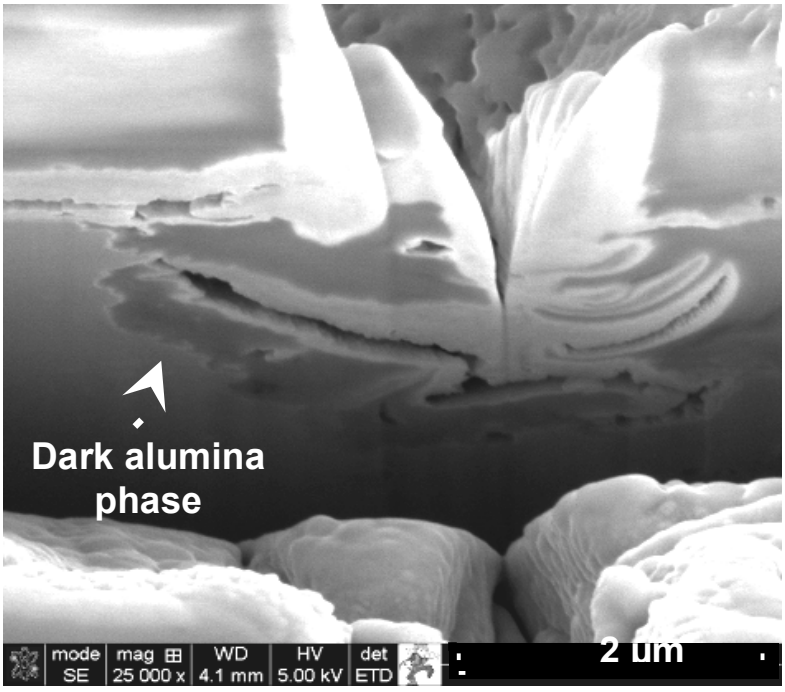

Figure 68. FIB cross section of a pit found in a post-treated CeCC after seven days of salt

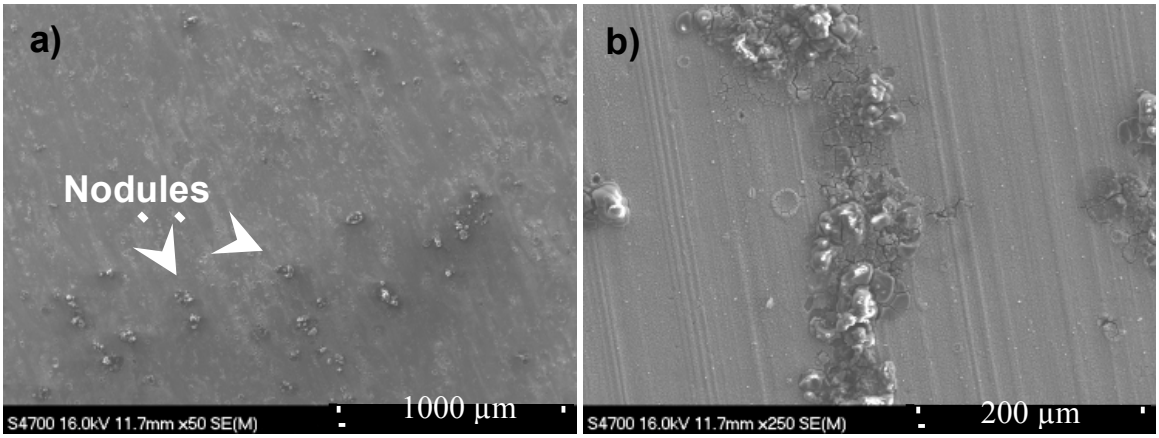

Figure 69. Surface morphology of as-deposited CeCCs after a) six hours and b) 24 hours of salt spray exposure.

Combined with the observation of salt tails and analysis of the EIS data, the aluminum-rich phase on these coatings was a corrosion product that deposited on isolated areas of the coating surfaces, not a protective layer that formed in the post-treated CeCCs.

The cross sectional structure, prepared by FIB milling, of an aluminum-rich nodule found on an as-deposited CeCC after 6 hours of salt spray exposure (Figure 70) revealed subsurface voids present underneath these features, just as they were found underneath pits in the post-treated coatings. The dark oxide phase around these voids exhibited a large degree of porosity. This morphology indicated that the oxide found around the perimeter of the voids in as-deposited

coatings did not have the protective properties of the dense, coherent oxide found around the voids of post-treated coatings.

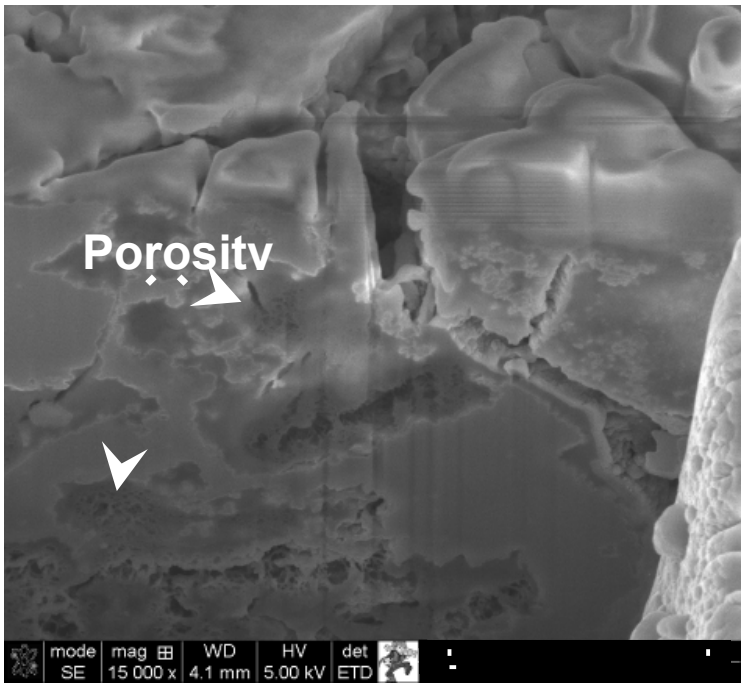

Figure 70. FIB cross section of an alumina nodule found in an unsealed CeCC after 6 hours of salt spray testing.

The FIB/SEM analysis revealed that the corrosion protection of CeCCs depended on the coating processing conditions. Specifically, post-treatment affected the morphology of aluminum-rich oxide phases that formed inside subsurface voids and on the surfaces of CeCCs. The surfaces of as-deposited CeCCs exhibited a large degree of corrosion product (aluminum-rich nodules) in the first 24 hours of salt spray exposure, while the surfaces of post-treated coatings developed small pits with no visible corrosion product. Based on these observations, post-treated coatings were able to protect the alloys to a greater degree than as-deposited coatings. The CeCCs protected the alloys despite the presence of uncoated subsurface voids that formed during coating deposition. While further studies are needed to understand this behavior, SEM imaging of cross sectional structures showed that the oxide present around the voids in post-treated coatings was dense and coherent, while the oxide present in the voids of as-deposited coatings exhibited a significant amount of porosity after salt spray exposure. This result suggests that post-treatment may alter the oxide present around subsurface voids to a phase and/or structure that can better protect the surrounding substrate compared to the oxide present in the voids of an unsealed coating.

Chemical and Structural Analysis of Sub-Surface Crevices Formed During Spontaneous Deposition of CeCCs

The spontaneous deposition of CeCCs from coating solutions containing soluble chlorides and H_2O_2 produced subsurface crevices in the alloy substrates. Cross-sectional microscopy has shown that these areas were exposed to the surface through cracks in the CeCCs. Additional EDS analyses indicated that no cerium was present on crevice surfaces, consistent with previous

analyses [110]. Since these regions were not protected by CeCCs, areas containing crevices should be more susceptible to the formation of stable pits, which would lead to corrosion of the specimen. Because subsurface crevices are formed during CeCC deposition, crevices were present in as-deposited and post-treated CeCCs. As-deposited coatings contained visible corrosion pits and salt tails after 3 days of salt spray exposure, but post-treated CeCCs have been shown to withstand up to 14 days of salt spray exposure without exhibiting visible corrosion. The significant improvement in the corrosion resistance of CeCCs after phosphate post-treatment has been attributed to factors that affect barrier properties (i.e., minimization of cracks and the formation of $CePO_4 \cdot H_2O$ within the coating) as well as characteristics that indicated active corrosion inhibition (i.e., structural changes and interfacial layer formation) during salt spray exposure [74,111]. Cross-sectional analyses of as-deposited and post-treated CeCC specimens indicated that post-treatment also affects subsurface crevices, increasing the corrosion resistance of crevices separately from its effect on the crystalline phase present in CeCCs.

Localized subsurface crevices in an as-deposited CeCC specimen are shown below as Figure 71. A FESEM/FIB equipped with a STEM detector was used to collect cross-sectional images and perform chemical mapping. As labeled in the figure, an Al-O containing phase was present on the interior surfaces of the crevices. In as-deposited specimens, electron diffraction patterns from this phase did not exhibit diffracted spots or rings (Figure 72a), indicating it was amorphous. A previous investigation has shown that the combination of soluble chlorides and hydrogen peroxide species aggressively etches the aluminum alloy substrate during coating formation [110]. This etching introduces Al^{3+} ions into the near surface environment where the estimated pH is > 5 based on the precipitation of Ce species. Under these conditions, the formation of an $Al(OH)_3$ gel-like phase is favored for Al in contact with an aqueous solution. The amorphous $Al(OH)_3$ phase present in regions containing subsurface crevices in as-deposited specimens was also found to contain up to 1.6 at. % Cl. In an aqueous environment, chloride ions will act to destabilize the aluminum hydroxide structure, providing a plausible explanation for the accumulation of aluminum corrosion product on the coating surface that has been reported elsewhere [112]. Earlier studies examining the corrosion of nominally pure aluminum by water reported that amorphous aluminum hydroxide exhibited a higher solubility in water compared to other crystalline forms of hydrated aluminum oxides/hydroxides such as boehmite, bayerite, or gibbsite [113]. A detailed study of the hydration of passive oxide films on aluminum is available elsewhere [114].

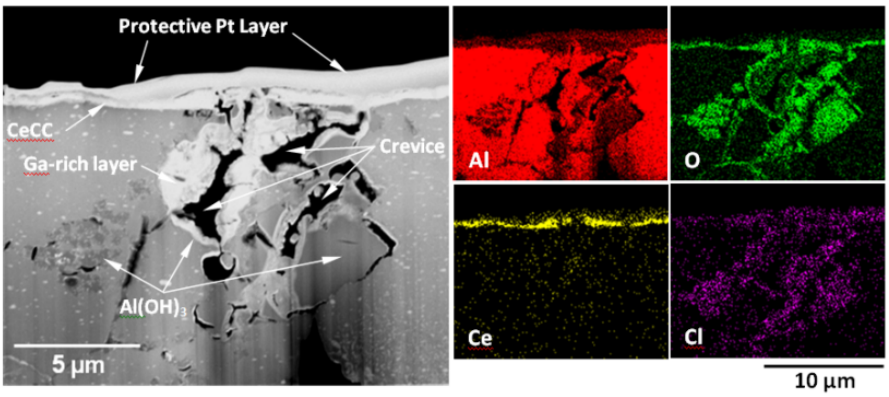

Figure 71. A high angle annular dark field STEM image of subsurface crevices on an as-deposited CeCC (no salt spray exposure) and corresponding EDS maps.

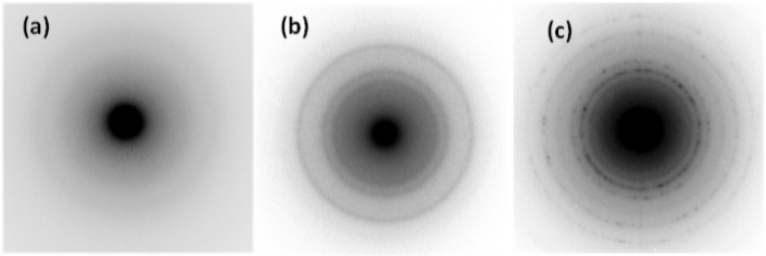

Figure 72. Diffraction patterns taken from phase formed on the surface of subsurface crevices for (a) as-deposited CeCC and (b-c), post-treated CeCC.

Analysis of the Al-O phase inside crevices of specimens that were post-treated in an orthophosphate solution at 85 °C for 5 min revealed several differences. For post-treated specimens, electron diffraction within the $Al(OH)_3$ phase produced ring patterns (Figure 72b and Figure 72c), indicating this phase crystallized during post-treatment. Analysis by EDS, shown in Figure 73, suggested that processes active during post-treatment removed the majority of chlorine from these regions, reducing the detected concentration to ≤ 0.30 at. %. Since as-deposited and post-treated specimens were cross-sectioned in the same manner (i.e., FIB milling), the difference in chlorine concentration did not appear to be an artifact of sample preparation. The reduced chlorine concentration may help explain the increased pitting potentials observed from post-treated coatings since the concentration of chlorine in aluminum oxide/hydroxide films is inversely proportional to pitting potential (i.e., lower chloride concentrations correspond to more anodic pitting potentials). Some of the diffraction patterns of the crystallized phase match closely to that of gibbsite, a crystallized form of $Al(OH)_3$. However, the structure of the phase located on crevices surfaces was not uniform and probably consisted of various forms of hydrated aluminum hydroxides and/or oxides. None of the diffraction patterns matched aluminum phosphate phases, nor did EDS analysis indicate the presence of phosphorus. The structural transition of amorphous $Al(OH)_3$ to transition alumina structures upon exposure to aqueous environment appears to be consistent with other data reported in literature [113,113]. Hart investigated the phase of films formed on aluminum after exposure to pure water at temperatures of 25 – 100 °C. A critical temperature near 65 °C was defined, above which the developed films consisted only of boehmite and below which growth of the oxide film was believed to progress from an amorphous film, to boehmite, and finally bayerite. Therefore, it appears reasonable for amorphous aluminum hydroxide that formed during CeCC deposition to be at least partially crystallized during exposure to 85 °C aqueous phosphate solution. During extended exposure to salt spray environment this phase may slowly transform to boehmite or bayerite. Compared to an amorphous $Al(OH)_3$ layer, a crystalline layer should have fewer defects and function as an improved barrier coating, thus improving corrosion resistance.

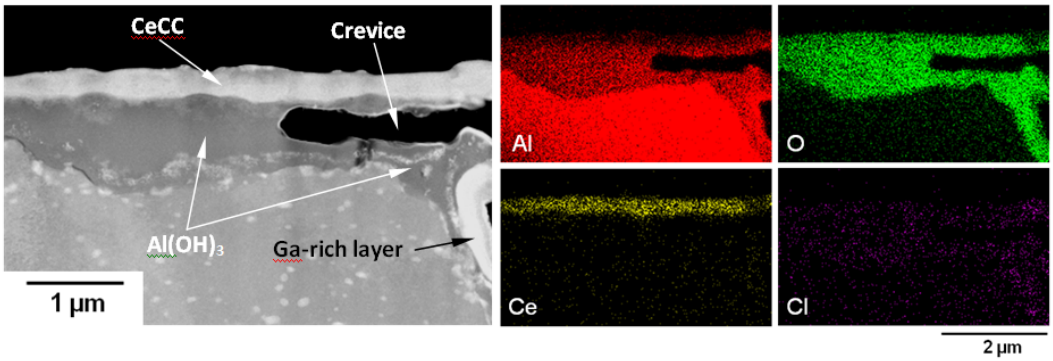

Figure 73. A high angle annular dark field STEM image of a subsurface crevice on a post-treated CeCC specimen and corresponding EDS maps (no salt spray exposure).

When analyzed in conjunction with the data reported by Pinc et al.,[110] it can be concluded that post-treatment in a phosphate solution has a significant impact on the subsurface crevices, which, in turn, has an effect on their corrosion resistance. The effect on the crevices appears to be separate from the effect of post-treatment on CeCCs (i.e., conversion of as-deposited hydroxy and peroxy species to hydrated $CePO_4$). By introducing crevices into an electrodeposited CeCC specimen (which does not form crevices during deposition), the corrosion performance was adversely affected by the formation of an amorphous $Al(OH)_3$ phase containing chlorine. This effectively generated regions that were more susceptible to corrosion, significantly reducing the corrosion resistance of the specimen. Phosphate post-treatment restores the corrosion resistance of these specimens. The mechanism of restoration appears to be a result of reduction of the chloride concentrations and crystallization within the Al-O layer inside crevices during post-treatment.

Directly Deposited Cerium Phosphate Coatings on Al 2024-T3

Cerium phosphate coatings were deposited directly on Al 2024-T3 substrates using conditions initially defined by Fair, et al [115]. The solutions were formulated to yield 5, 15, 30, or 60 g of $CePO_4$ per liter of solution. All of the solutions had a Ce:P:citrate ratio of 1:1:2. Coatings deposited with the 5 g/L solution appeared to deposit slowly, with visible deposition only observed after multiple coatings cycles had been performed. Visual examination of coatings deposited from solutions designed to yield 15, 30, or 60 g/L $CePO_4$ indicated that the coating thickness increased with increasing $CePO_4$ in the deposition solution. Since the deposition times were the same for each coating, the thicker coatings corresponded to faster deposition rates. Deposition from the 5 g/L solution resulted in coatings with the least cracking as shown in Figure 1a. Coatings deposited from the 15, 30, and 60 g/L solutions exhibited similar morphologies and did not change significantly as a function of precursor concentration (Figure 74). When the deposition solution was heated, precipitation appeared to occur uniformly throughout the solution and was not observed to preferentially precipitate on the alloy surface. Hence, the adhered coating was formed by precipitation of species in close proximity to the substrate with the majority of the remaining precipitate being removed during subsequent rinsing steps. Electron diffraction of the resulting coatings, Figure 75, indicated that hydrated $CePO_4$, rhabdophane or $CePO_4 \cdot H_2O$, was present. After 18 hours of salt spray exposure, corrosion pits

and tails were evident across the panel surface for each of the directly deposited coatings as shown in Figure 76. Coatings deposited from 5 g/L solutions exhibited less corrosion than coatings deposited with higher concentration solutions because they contained fewer cracks, thereby functioning as a better barrier coating.

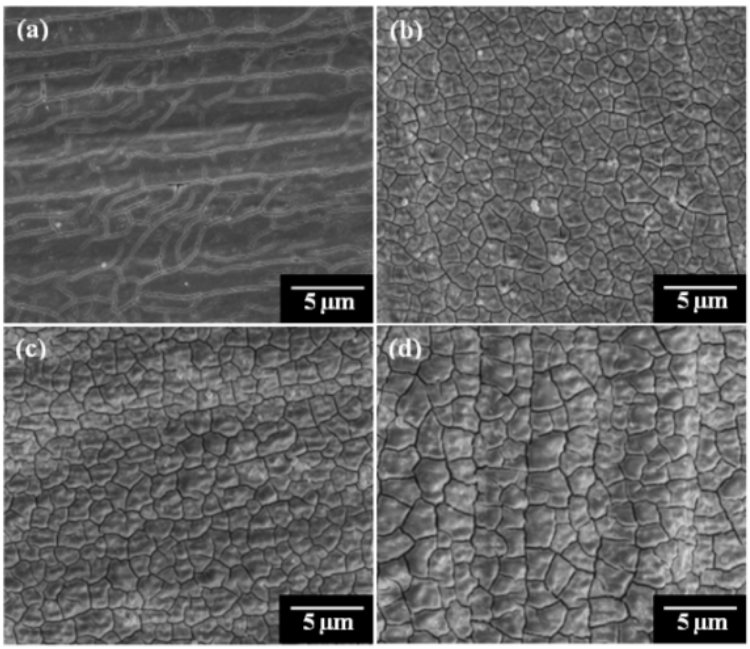

Figure 74. Surface morphology of directly deposited $CePO_4$ coatings produced using precursor solutions designed to yield (a) 5, (b) 15, (c) 30, and (d) 60 g/L $CePO_4$.

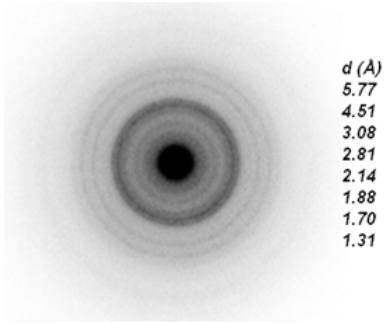

Figure 75. Electron diffraction ring pattern observed from a directly deposited $CePO_4$ coating. The ring pattern is indicative of hydrated $CePO_4 \cdot H_2O$, rhabdophane (PDF 35-0614).

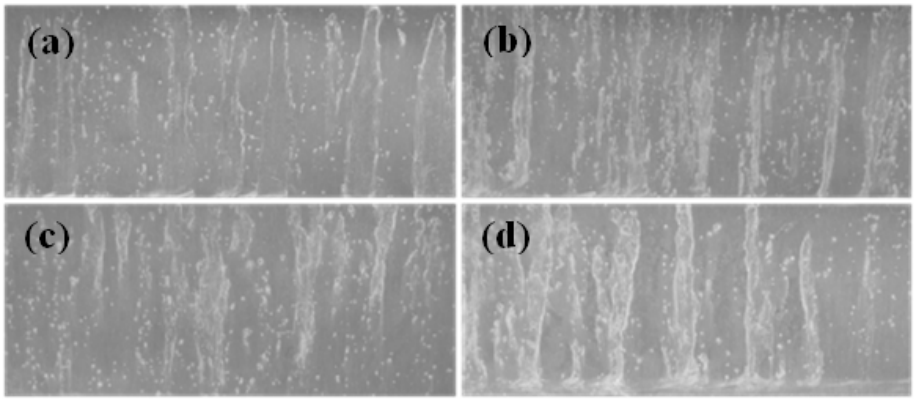

Figure 76. Directly deposited $CePO_4$ coatings after 18 hours of salt spray exposure, (a) 5 g/L, (b) 15 g/L, (c) 30 g/L, (d) 60 g/L. The tested areas shown for the panels measure about 2.5 cm x 6.5 cm.

The ratio of Ce, P, and citrate present in the precursors solutions was varied in an attempt to alter the deposition rate and/or morphology of the resulting coatings. These permutations did not have a significant effect on coating morphology (Figure 77) or corrosion performance (Figure 78). Coating solutions containing higher amounts of Ce and P were believed to have higher deposition rates based on visual observations of thicker $CePO_4 \cdot H_2O$ layers per coating cycle. Also, solutions with less citric acid exhibited faster precipitation compared to those with higher concentrations of citric acid, indicating that the $CePO_4 \cdot H_2O$ formation was slower from solutions containing the cerium citrate complex as compared to free Ce^{3+} ions. To some extent this allows control of the precipitation rate, which can be used to slow deposition and produce coatings with less noticeable cracking as citrate concentration is increased, Figure 77. Changing the relative concentrations of cerium and phosphate in the solution influenced the observed deposition rate more strongly than citrate concentration, with higher concentration of phosphoric acid resulting in significantly faster (and less controlled) precipitation. In addition, higher phosphate contents resulted in coating morphologies that exhibited larger cracks and even some spalling of the coating, Figure 77f. These changes in morphology did not have a significant impact on the corrosion performance of the directly deposited $CePO_4$ coatings. Despite their poor corrosion performance, the $CePO_4 \cdot H_2O$ coatings had uniform morphology across the alloy substrate surfaces.

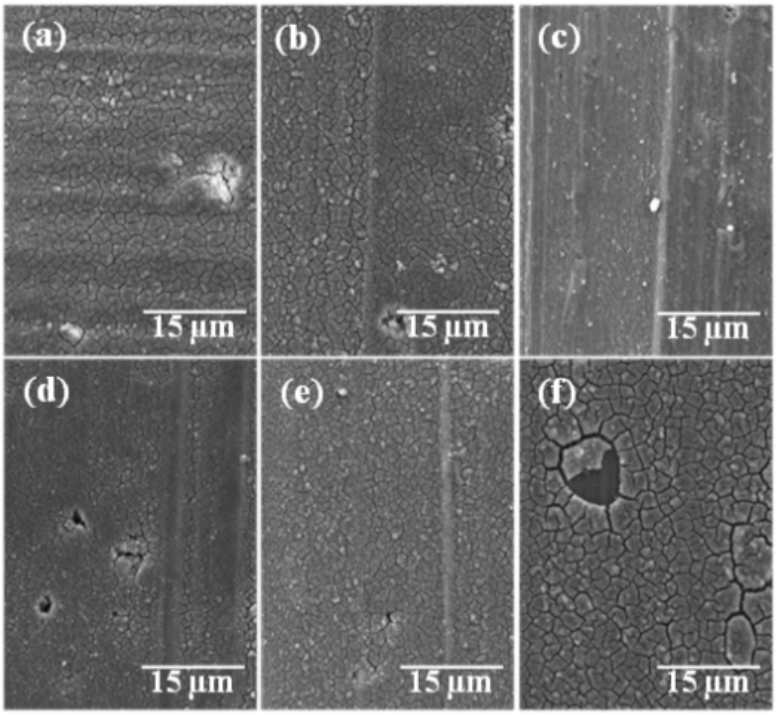

Figure 77. Surface morphology of directly deposited $CePO_4$ coatings deposited with different ratios of Ce:P:citrate in the precursor solutions, (a) 1:1:0.5, (b) 1:1:1, (c) 1:1:2, (d) 1:0.5:2, (e) 1:0.5:0.5, and (f) 1:2:2

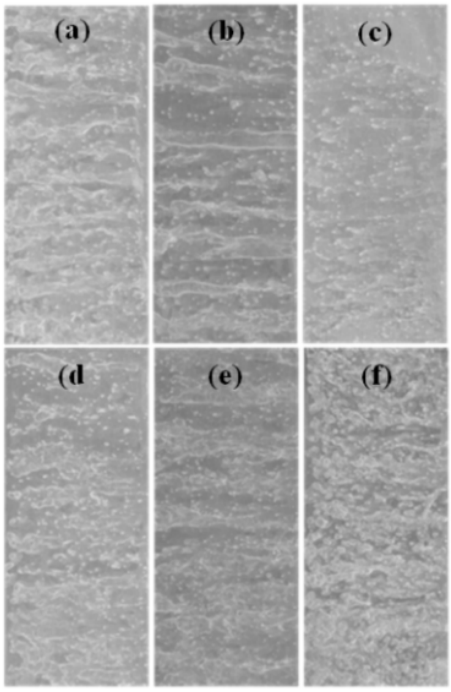

Figure 78. Directly deposited coatings (60 g/L $CePO_4$) after 18 hours of salt spray exposure, (a) 1:1:0.5 (Ce:P:citrate), (b) 1:1:1, (c) 1:1:2, (d) 1:0.5:2, (e) 1:0.5:0.5, (f) 1:2:2. The panels measure about 2.5 cm x 6.5 cm.

The morphology of spontaneously spray deposited CeCCs was less uniform than the directly deposited coatings. Approximately 90 % of the surface of phosphate post-treated conversion coatings contained fine (< 150 nm wide), or no, cracks whereas the remaining 10 % exhibits larger cracks that had widths > 1 μm. However, these CeCCs provide significant corrosion protection. Previous studies have shown that CeCCs prepared using similar conditions can withstand up to 336 hours of salt spray exposure without exhibiting significant corrosion pits or tails.

Polarization and EIS data were collected from directly deposited coatings, bare Al 2024-T3, and a post-treated CeCC. Representative polarization scans are shown in Figure 79 and a summary of values measured by fitting polarization and impedance data is included as Table 17. Just as varying the direct deposition process parameters had little effect on corrosion performance, no large differences in total resistance, corrosion current, or pitting potential were observed among the directly deposited specimens. Compared to the bare Al 2024-T3 substrate, directly deposited $CePO_4$ coatings had a small influence on electrochemical properties, increasing the total resistance by only 2 – 6 times, from 1.1 kΩ cm^2 to 2.1 – 6.9 kΩ cm^2. However, neither the measured corrosion current densities (≈2 μA/cm^2 to ≈4 μA/cm^2) nor the pitting potentials (≈-570 mV) changed significantly. The increased total resistance may correspond to partial coverage of the substrate or fewer defects in the coating, but the changes did not have a significant effect on corrosion performance. For comparison, parallel measurements collected from CeCCs showed a six-fold increase in total resistance compared to directly deposited $CePO_4$ coatings on average (from ≈4 kΩ cm^2 to ≈24 kΩ cm^2), a corresponding decrease in the corrosion current (≈2.5 μA/cm^2 to ≈0.45 μA/cm^2), and pitting potentials that were approximately 30 mV more anodic. The improved electrochemical properties of CeCCs correlate to improved corrosion performance such as during ASTM B117 salt spray corrosion testing used in this study. Post-treated CeCCs are consistently able to withstand at least 168 hours of salt spray exposure without exhibiting corrosion pits or tails, whereas directly deposited $CePO_4$ coatings show extensive corrosion after only 18 hours.

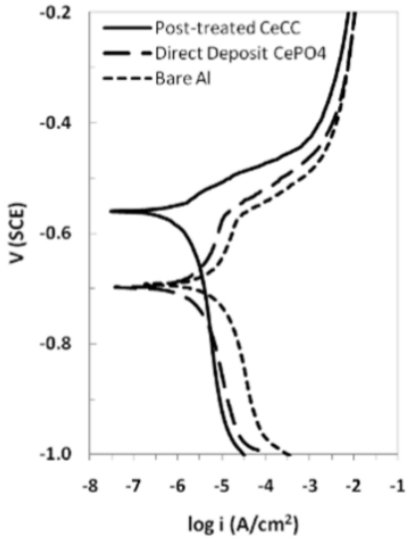

Figure 79. Representative polarization scans of bare Al 2024-T3, directly deposited $CePO_4$, and post-treated CeCC.

Table 17. Summary of electrochemical properties measured from bare Al 2024-T3, directly deposited $CePO_4$ coatings, and post-treated CeCCs.

	R_p (kΩ cm²)	E_{corr}, mV(SCE)	i_{corr} (μA/cm²)	E_{pit}, mV(SCE)
Bare	1.16	-695	3.93	-573
5 g/L	2.45	-697	3.36	-583
15 g/L	5.55	-727	4.07	-568
30 g/L	5.66	-709	2.72	-578
60 g/L	6.93	-693	1.53	-565
1:0.5:0.5	6.94	-711	1.19	-575
1:0.5:2	2.13	-716	3.66	-577
1:1:1	4.82	-716	2.65	-573
1:1:0.5	3.59	-693	2.76	-585
CeCC	24.4	-567	0.466	-548

The lack of corrosion inhibition of directly deposited $CePO_4$ coatings is attributed to the deposition mechanism, which is primarily driven by a change in temperature rather than pH or surface chemistry as is the case with CeCCs. The temperature driven mechanism operates independently of localized chemical or electrochemical gradients and, therefore, does not exhibit preferential deposition near active sites. As a consequence, local cathodes distributed throughout the alloy matrix may, or may not, have been adequately covered during coating deposition. In contrast, deposition of CeCCs relies on electrochemical interactions with the substrate to precipitate cerium compounds. Initial deposition of CeCCs occurs on or near intermetallic particles (serving as local cathodes) before spreading to cover the remaining substrate [63]. In part, the corrosion protection provided by CeCCs is via a barrier mechanism in which the oxygen reduction reaction is inhibited by the selective deposition of cerium compounds onto local cathodes. However, CeCCs commonly have defects such as surface cracking and subsurface

crevices [110]. These features expose localized areas of the substrate that should be susceptible to corrosion, similar to a directly deposited coating that only partially covers a localized, electrochemically active area.

Cross sectional analysis of directly deposited $CePO_4$ coatings and post-treated CeCCs after salt spray exposure revealed that the two coatings exhibited significantly different responses to corrosive environments, Figure 80 and Figure 81. For directly deposited coatings, exposed areas at the base of cracks that extended to the substrate showed evidence of pit initiation at the crack/substrate interface as well as the formation of corrosion product beneath the coating adjacent to the cracks. Corrosion products were also evident on the surface of the coatings as a highly porous, fibrous layer rich in aluminum and oxygen. The coating/substrate interface farthest from the cracks remained unchanged, suggesting that the directly deposited coatings functioned as barriers. While cracks in the post-treated CeCC also extended to the substrate, no signs of pitting corrosion were observed at the crack/substrate interface after seven days of salt spray exposure and no visible evidence of corrosion was evident on the specimen surface. Furthermore, a 60 – 100 nm thick layer had formed at the CeCC/substrate interface. The CeCCs appear to be capable of providing protection by reacting to the corrosive environment and protecting areas of the substrate exposed by defects in the coating. Likewise, chromate based conversion coatings provide excellent protection and release hexavalent chromium ions that reduce to form a hydrated Cr(III) oxide on electrochemically active sites, thereby protecting limited areas of exposed substrate. This interfacial reaction layer is believed to improve the corrosion performance of CeCCs and demonstrates that post-treated CeCCs are not acting solely as inert barriers, but respond to the salt spray environment.

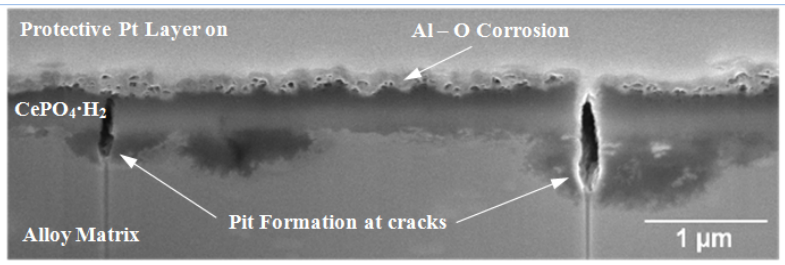

Figure 80. Cross sectional montage of a directly deposited $CePO_4$ coating after 3 days of salt spray exposure. Image is a cross-section of a bulk specimen viewed 45° from the sample surface.

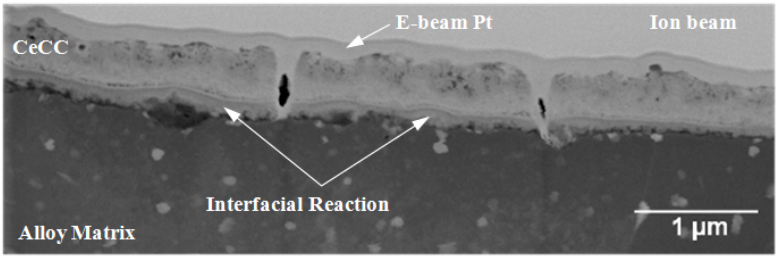

Figure 81. Cross sectional montage of a phosphate post-treated CeCC after 7 days of salt spray exposure imaged in STEM/HAADF mode.

Analysis of the interfacial reaction layer by EDS did not reveal the presence of phosphorous, but rather showed its composition to consist predominately of Ce, Al, and O. The mechanism by which the interfacial layer formed during corrosion testing is not understood, but the layer has been observed only in CeCCs subjected to a phosphate post-treatment. It is theorized that the formation process may be sensitive to changes in the local pH, facilitating the reaction between cerium and aluminum hydroxide species to potentially form a thermodynamically favorable cerium aluminate phase. Analysis by EDS also suggests that chloride ions from the deposition process may have been trapped at the CeCC/substrate interface during the initial stages of coating formation. The residual chloride ions, or the introduction of chloride ions at the coating/substrate interface during salt spray exposure, may act to destabilize the aluminum oxides and/or hydroxides present near the interface, facilitating reaction with neighboring cerium species. Post-treatment transforms many of the cerium hydroxy/peroxy species present after coating deposition to $CePO_4 \cdot H_2O$, and prior analysis has suggested nearly complete reduction of Ce(IV) species to hydrated Ce(III) phosphate at the surface [116]. However, post-treated CeCCs did not exhibit a uniform rhabdophane phase throughout the coating thickness, but rather exhibited heterogeneity of structures and compounds (e.g., unconverted cerium hydroxy/peroxy species and cerium hydrogen phosphate species) that may be metastable [111]. These compounds may be predisposed to react with neighboring species during salt spray exposure, acting to protect exposed areas of the substrate, whereas a uniform $CePO_4 \cdot H_2O$ coating containing only the rhabdophane phase (i.e., directly deposited $CePO_4$ coatings) would remain unchanged under the same conditions, responding like a static barrier coating by only protecting areas of the substrate that were coated.

Alkaline Activation of Al 7075-T6

After spraying the coating deposition solution on the alkaline activated panels, the surface turned yellow. This color change was an indication that a coating was deposited. With degreasing only (no activation), a uniform light color change occurred after ~5 spray cycles indicating that coatings were very thin. Pinc et al. [54] also reported similar results on degreased Al 2024-T3. For NaOH activated panels, the color changed instantly upon contact with the coating solution during the first spray cycle. In contrast, Na_2CO_3 activated panels changed color after ~5-10 seconds of contact with the solution during the first spray cycle, and the yellow color grew more intense as drain time increased. Thus, visual observation indicated that NaOH activation promoted rapid coating deposition, Na_2CO_3 activation led to slower deposition, and no alkaline activation resulted in very thin coatings being deposited.

Surface morphology of as-deposited coatings on $5Na_2CO_3$ activated surfaces showed uniform coating deposition (Figure 82a). Large cracks and network of scissures in the coatings were only visible at higher magnification (Figure 82b). The surface morphology of as-deposited coatings on NaOH activated surface were very different than a $5Na_2CO_3$ surface as the surface was dominated with craters and surface defects such as large cracks (greater than 0.5 μm wide) and areas of exposed substrate (Figure 83a-b).

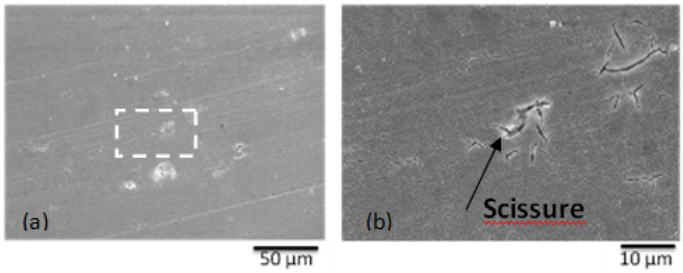

Figure 82. As-deposited CeCCs on Al 7075-T6 that underwent $5Na_2CO_3$ activation: (a) General appearance of surface and (b) enlargement of the rectangular area marked in (a).

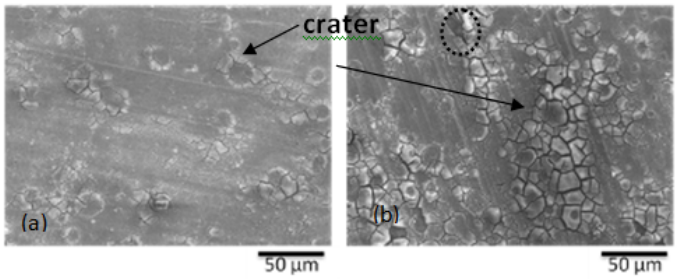

Figure 83. As-deposited CeCCs on Al 7075-T6 that underwent NaOH activation: (a) 1NaOH and (b) 2NaOH. Note: the dotted circled regions show areas where the substrate is exposed.

Craters are defined as white circular features surrounding a dark phase, often with cracks on the white areas that extended into the dark phase. Previous research [66] showed that the 2NaOH activation decreased the electrochemical resistance of the surface oxide by ~28% compared to as-received Al 7075-T6, which was the most among the three different activations and contributed to deposition of the thickest coatings (~500 nm). However, examination of Figure 82 and Figure 83 revealed that CeCCs on 7075-T6 that underwent 2NaOH activation had more surface defects than coatings on substrates with a different activation. One notable difference between the surface morphology of CeCCs deposited on substrates that underwent Na_2CO_3 activation and those on substrates that underwent NaOH activation was that few, if any, craters were observed on coatings deposited on $5Na_2CO_3$ activated surfaces. Therefore, it is clear from the micrographs that surface preparation influenced the morphology and integrity of CeCCs, with $5Na_2CO_3$ activation leading to the most uniform coating coverage.

After sealing CeCCs had fewer visible cracks compared to as-deposited coatings; however, certain areas with large cracks still remained (Figure 84 and Figure 85). Higher magnification of coatings deposited on $5Na_2CO_3$ activated surfaces (Figure 84b) showed that very few scissures were visible after sealing, but areas with large cracks were still visible. Similar to $5Na_2CO_3$ activation, few scissures were visible on sealed coatings deposited on NaOH activated surfaces. In addition, exposed areas of the substrates were not found on sealed coatings, indicating that sealing may promote better adhesion of coatings to the substrate and of the coatings. Thus, the

micrographs revealed that even though alkaline activation produced coatings with surface defects, sealing reduced the number of defects and may have also promoted better adhesion of the coatings to the substrate.

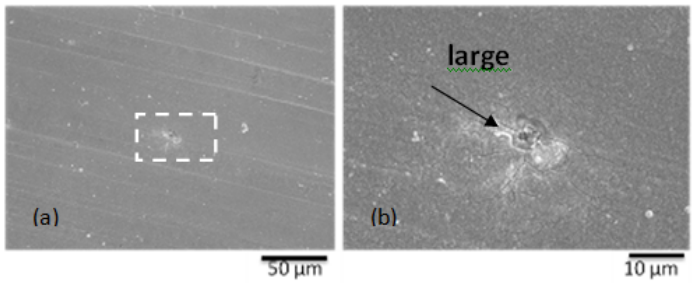

Figure 84. Sealed CeCCs on Al 7075-T6 that underwent $5Na_2CO_3$ activation: (a) General appearance of surface and (b) enlargement of the rectangular area marked in (a).

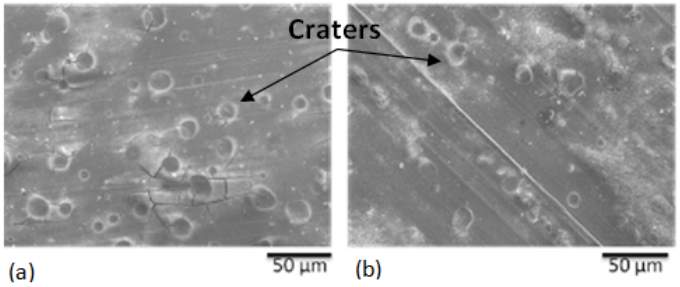

Figure 85. Micrographs of sealed CeCCs on Al 7075-T6 that underwent alkaline activation: (a) 1NaOH and (b) 2NaOH.

Subsurface crevices were found under regions with large cracks or craters (Figure 85). Subsurface crevices are the result of localized dissolution of aluminum adjacent to noble IMCs such as copper-based IMCs [77]. Because the localized dissolution of aluminum is accompanied by generation of electrons that are consumed during coating deposition, crevice formation produced thicker coatings near the dissolution site. Typically, CeCCs were more than 1 µm thick near areas of active dissolution as shown in Figure 86.

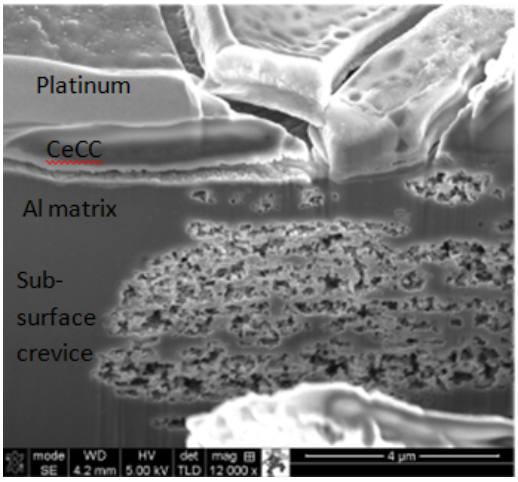

Figure 86. SEM cross-section micrograph (tilted 45° from vertical axis) of a subsurface crevice formed during CeCC deposition after $5Na_2CO_3$-activation.

In addition, large cracks were observed in these regions. Analysis of the micrographs in Figure 82, Figure 83, Figure 84, and Figure 85 indicated that CeCCs deposited on $5Na_2CO_3$ activated surfaces were more uniform in appearance and had fewer surface defects and craters compared to CeCCs on substrates that underwent either of the NaOH activations. Therefore, CeCCs deposited on $5Na_2CO_3$ activated substrates likely contained fewer subsurface crevices than coatings on NaOH activated substrates. The density of large cracks and craters revealed that Na_2CO_3 activation was likely to result in less localized dissolution of the aluminum substrate during coating deposition, which could indicate that dissolution was more uniform across the surface. These results suggest that proper surface activation can be used to control and mitigate not only cracks in the CeCCs, but also the extent of subsurface crevice formation.

The electrochemical response was measured for as-deposited and sealed CeCCs deposited on substrates that underwent $5Na_2CO_3$, 1NaOH, and 2NaOH alkaline activations (Figure 87). These plots showed subtle inflections were present at high frequencies (~0.63 kHz) for all coatings. At 1.25-0.05 Hz, maxima were obtained for all curves. The inflections and maxima indicated that corrosion protection was produced by two different processes. Thus, impedance plots needed to be fitted to an equivalent circuit model with two time constants (Figure 88), each comprising a capacitance in parallel with a resistance to represent each of the corrosion protection mechanisms.

In the equivalent circuit shown in Figure 88, R_{soln} represents the solution resistance. The electrochemical behavior of the coatings is represented by the capacitance C_p and bulk resistance R_p. The corrosion process that occurs at the interface between the electrolyte and the substrate is represented by a constant phase element Q_{dl} in parallel with the charge transfer resistance $R_{ct.}$ The overall resistance, RT, is the sum of R_p and R_{ct}. The impedance plot can be fitted to various equivalent circuit models, each using different parameters and thus suggesting different physical interpretations. However, the value of the overall resistance, RT, is significant because it is independent of the models used to fit the data.

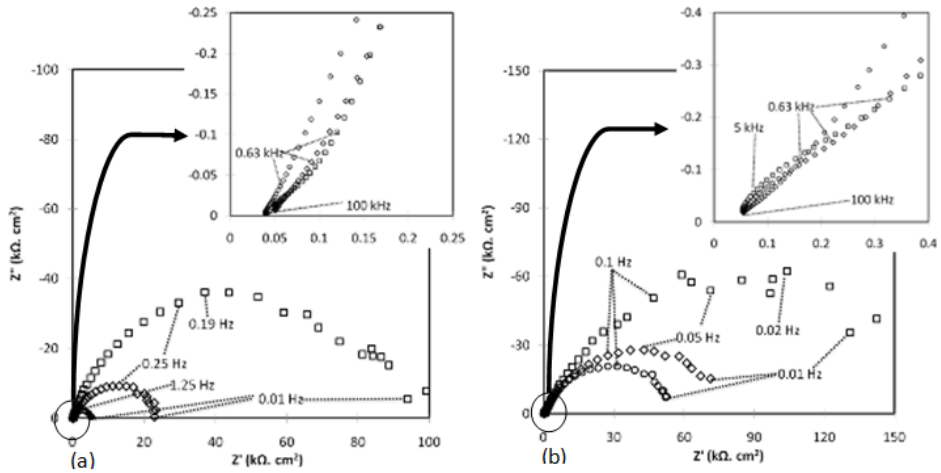

Figure 87. Impedance plots of CeCCs on Al 7075-T6 after various surface activations: (a) as-deposited and (b) sealed. Note: Square symbols denote $5Na_2CO_3$, diamonds denote 1NaOH, and circles denote 2NaOH-activations.

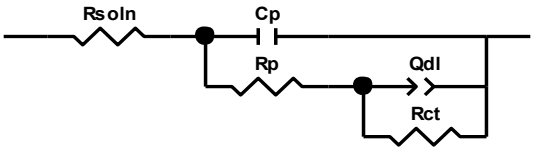

Figure 88. Equivalent circuit model to fit the impedance plots in Figure 87.

The term Q_{dl} is used to describe the frequency dependence of non-ideal capacitance behavior given by Equation IV.

$$Z = Z_o(j\omega)^{-n} \qquad \text{(IV)}$$

When n is not equal to 1, the system behavior can be attributed to surface heterogeneity or continuously distributed time constants for charge-transfer reactions. If n is equal to 1, Q_{dl} is a capacitor with capacitance of $1/ Z_0$, which indicates the presence of a double layer at the electrolyte/surface interface of the substrate. If n is equal to 0, Q_{dl} is a resistor with a resistance of the value of Z_0. Q_{dl} can be converted to capacitance by Equation V

$$C_{dl} = Q_{dl}(\omega_{max})^{n-1} \qquad \text{(V)}$$

where ω_{max} is the angular frequency at which the imaginary part of the impedance has maximum value. Table 18 lists the values with the standard deviations obtained for all components in the equivalent circuit model for each of the coatings. The value of χ^2 is a measure of the model fit to experimental data, with lower values indicating better fit. The range of χ^2 values given by the software ZSimpWin was 0.003 to 0.011, indicating a very good fit of the data to the equivalent circuit models.

Table 18. Summary of values calculated with the standard deviation for fitting EIS data to equivalent circuit models for CeCCs deposited on Al 7075-T6.

Parameter	Sealed			As-deposited		
	$5Na_2CO_3$ seal	1NaOH seal	2NaOH seal	$5Na_2CO_3$ as-dep	1NaOH as-dep	2NaOH as-dep
R_{sol} (Ω-cm^2)	57 ± 2	58 ± 2	56 ± 2	50 ± 1	51 ± 1	41 ± 1
C_p (μF/cm^2)	0.18 ± 0.01	0.28 ± 0.02	0.32 ± 0.03	0.45 ± 0.03	1.15 ± 0.01	3.9 ± 0.3
R_p (Ω-cm^2)	252 ± 14	175 ± 11	96 ± 7	65 ± 4	51 ± 5	54 ± 8
Q_{dl} (s^n/(MΩ-cm^2))	17.4 ± 0.5	30.2 ± 0.9	24.9 ± 0.8	11.31 ± 0.2	26.2 ± 0.7	30.0 ± 1.0
n	0.72	0.69	0.72	0.81	0.76	0.79
C_{dl} (μF/cm^2)	31.3	43.32	54.21	10.83	23.5	19.80
R_{ct} (kΩ-cm^2)	189 ± 11	94 ± 5	64 ± 3	96 ± 2	25.3 ± 0.5	5.18 ± 0.01
RT (kΩ-cm^2)	189	94	64	95	25	5
χ^2	0.011	0.011	0.010	0.003	0.003	0.003

CeCCs deposited on $5Na_2CO_3$ activated substrates had the lowest coating capacitance (C_p) values (as-deposited: 0.46 μF/cm^2 and sealed: 0.18 μF/cm^2) in both the as-deposited and sealed conditions. The highest values were for coatings deposited on substrates that underwent 2NaOH activation (as-deposited: 3.8 μF/cm^2 and sealed: 0.32 μF/cm^2). Since capacitance is inversely proportional to dielectric thickness for equivalent charge separation, the $5Na_2CO_3$ activated panels would be expected to have the thickest coatings. This result appears to contradict previous research [117], which showed that CeCCs deposited on substrates activated with 2NaOH produced the thickest coatings (~500 nm) and those activated with $5Na_2CO_3$ produced the thinnest coatings (~250 nm). As shown in Figure 83 and Figure 85, the density of surfaces defects caused by the more aggressive NaOH activation solutions helps explain this discrepancy. Surface defects make coatings less effective barriers to corrosion, and some of the measured response may be due to the exposed native thin oxide layer rather than the thicker CeCCs. Thus, the lower capacitance value for thinner coatings deposited using $5Na_2CO_3$ activation is due to more uniform coating coverage.

The double layer capacitance values (C_{dl}), derived from Q_{dl}, shown in Table 18 for both as-deposited and sealed conditions were the lowest for CeCCs deposited on substrates activated with $5Na_2CO_3$ (as-deposited: 5.26 μF/cm^2 and sealed: 1.54 μF/cm^2) and the highest for coatings on substrates activated with NaOH (as-deposited: 9.08 μF/cm^2 and sealed: 3.67 μF/cm^2). This trend was similar to that for coating capacitance and indicated that the dielectric double layer between the electrolyte and the substrate where corrosion occurs was thicker for CeCCs

deposited on substrates that underwent $5Na_2CO_3$ activation compared to coatings on substrates that underwent either of the NaOH activations. These results indicate that alkaline activation also influenced the dielectric double layer thickness where corrosion occurred.

CeCCs deposited on substrates that underwent $5Na_2CO_3$ activation exhibited the highest impedance (Sealed: 189 kΩ-cm^2 and as-deposited: 96 kΩ-cm^2) while those deposited with 2NaOH activation exhibited the lowest (Sealed: 64 kΩ-cm^2 and as-deposited: 5 kΩ-cm^2). The total resistance offered by as-deposited CeCCs deposited with 2NaOH activation was comparable to that of bare Al 7075-T6, which previous research showed to be ~8 kΩ-cm^2 [117]. The similarity of the measured values of the total resistance of the as-deposited coatings on 2NaOH activated substrates and bare Al 7075-T6 panels indicated that the corrosion resistance of the as-deposited coatings was primarily due to the native oxide, not to the coatings. Even though coatings covered a large fraction of the surface of the panels, the corrosion behavior appeared to be dominated by defects in the coatings (Figure 84b). These results also reflected the discrepancy seen in coating capacitance (C_p) values since the measured capacitance was likely due mainly to the thinner native oxide layer rather than the thicker CeCC. The two components of the total resistance (bulk resistance and charge transfer resistance) both showed higher values for as-deposited and sealed CeCCs deposited with $5Na_2CO_3$ activation than for those deposited with NaOH activation. These results show that less aggressive activation can produce uniform coatings that exhibit better corrosion resistance.

Cathodic polarization scans of as-deposited CeCCs showed that those activated with 2NaOH had the highest cathodic current density and those activated with $5Na_2CO_3$ had the lowest (Figure 89a). These results indicated that the coatings deposited using $5Na_2CO_3$ activation exhibited better cathodic inhibition. The OCP for all three as-deposited CeCCs ranged from -0.62 to -0.57 V_{SCE}. The corrosion current density obtained after fitting the Tafel slopes for $5Na_2CO_3$, 1NaOH, and 2NaOH were 0.42, 0.98, and 4.3 µAmps/cm^2, respectively. The polarization data and SEM results indicated that coatings with fewer large cracks and more uniform coverage had fewer exposed areas, which resulted in fewer areas for cathodic reduction reactions during corrosion.

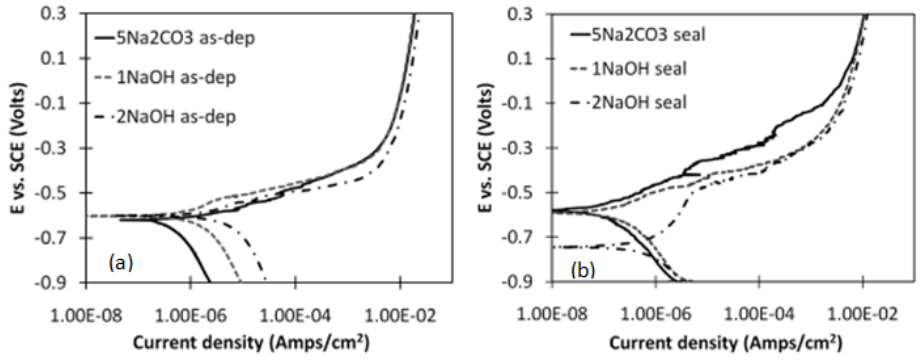

Figure 89. Polarization scans of CeCCs on Al 7075-T6 after various surface activations: (a) as-deposited and (b) sealed.

Polarization scans of sealed CeCCs using all three activation solutions showed similar cathodic current densities (Figure 89b). The OCPs of the coating deposited on a 2NaOH activated surface

was the lowest (-0.75 V_{SCE}), whereas those for CeCCs deposited on $5Na_2CO_3$ and 1NaOH activated surfaces exhibited more noble potentials (~-0.57 V_{SCE}). The corrosion current densities of sealed panels obtained after fitting the Tafel slopes for CeCCs deposited on $5Na_2CO_3$, 1NaOH, and 2NaOH surfaces were 0.12, 0.23, and 0.75 μAmps/cm^2, respectively. Sealing measurably reduced the corrosion current density for all coatings, but the corrosion current density was still the lowest for Na_2CO_3 activated panels, further indication that coatings deposited on substrates that underwent the $5Na_2CO_3$ activation provided the best corrosion protection. An anodic scan of sealed coatings showed that CeCCs deposited on $5Na_2CO_3$ surfaces exhibited lower current density at the same oxidizing potentials compared to those deposited using NaOH activations, suggesting that the former provided better passivation and higher pitting potentials. The polarization scans of sealed panels showed lower corrosion current density and better passivation for coatings deposited on substrates that underwent Na_2CO_3 activation compared to coatings on substrates that underwent NaOH activation, which is an indication of better corrosion protection.

Salt spray testing showed that as-deposited CeCCs deposited with 2NaOH activation showed severe pitting corrosion after 24 hours. In the case of as-deposited CeCCs on substrates that underwent 1NaOH and $5Na_2CO_3$ activations, no pits were observed after 24 hours in salt spray. Pitting corrosion could be observed on as-deposited CeCCs using 1NaOH and $5Na_2CO_3$ activations after 48 hours, although $5Na_2CO_3$ activation produced fewer pits. Severe pitting was observed after 168 hours of salt spray testing for as-deposited CeCCs using 1NaOH and $5Na_2CO_3$ activations. For all three alkaline activation processes, seven out of ten sealed CeCCs panels inhibited pit formation for 336 hours in ASTM B 117 salt spray testing. Electrochemical testing also showed CeCCs deposited with $5Na_2CO_3$ activation exhibited the highest corrosion impedance and the lowest corrosion current density. Combined, these two testing showed CeCCs deposited on Al 7075-T6 with $5Na_2CO_3$ activation provide the best corrosion protection among the three alkaline activation solutions.

Effect of Humidity on CeCCs on 7075-T6

The impedance of CeCCs increased with exposure to humidity (Figure 90). The increase was most significant for as-deposited coatings, with the impedance increasing from ~5 kΩ-cm^2 before humidity exposure to ~60 kΩ-cm^2 after 24 hours of humidity exposure and then to ~90 kΩ-cm^2 after 168 hours of humidity exposure. The increase was lower for sealed CeCC panels, increasing only from ~65 kΩ-cm^2 before exposure to ~90 kΩ-cm^2 after 168 hours of humidity exposure. Previous research has also shown an increase in impedance during salt spray testing conducted per ASTM standard B117 [63]. Thus, placing a CeCC high strength aluminum alloy panels in a humid environment increased the measured impedance.

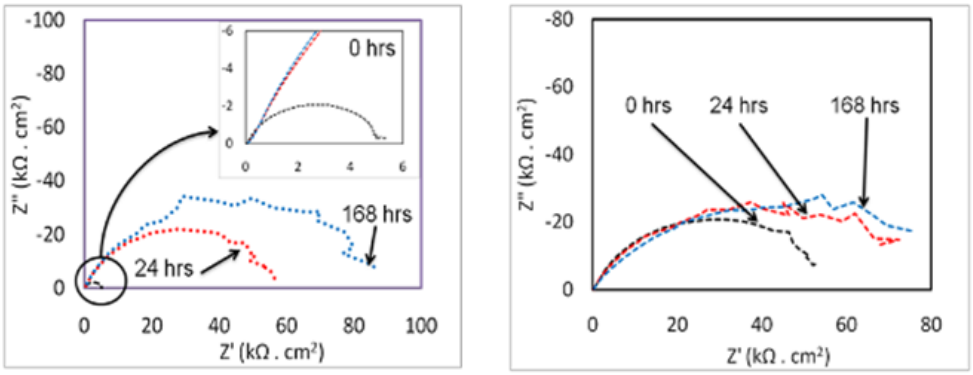

Figure 90. EIS testing results for CeCCs placed in a humid environment: (a) as-deposited and (b) sealed.

The EIS data were fitted to two different equivalent circuit models (Figure 91) to permit comparison to various physical characteristics of the coatings. The values of each of the components are listed in Table 19. Solution resistance, R_{soln}, was nearly constant in the range of 40-60 Ω-cm^2 for all specimens The bulk resistance of the coatings, R_p, which was also fairly constant at 70-100 Ω-cm^2, is in parallel with the geometric capacitance of the coatings, C_p. Charge transfer resistance, R_{ct}, is related to the corrosion processes occurring at the metal-electrolyte interface in parallel with the constant phase element Q_{dl}. The increase in impedance due to exposure to humidity was caused by an increase in charge transfer resistance as this value increased from 5 to 94 kΩ-cm^2 for as deposited coatings and 64 to 91 kΩ-cm^2 for sealed coatings. Q_{dl} is an empirical impedance given by Equation IV above.

When n is greater than zero but less than 1, the system shows behavior attributable to surface heterogeneity or continuously distributed time constants for charge-transfer reactions. If n is equal to 1, Q_{dl} is a capacitor with $C = 1/ Z_0$, which indicates the presence of a double layer at the electrolyte/surface interface of the substrate. If n is equal to 0, Q_{dl} is a resistor with $R = Z_0$. The value of n for all of the CeCCs was in the range of 0.65 to 0.79, which indicates a distribution of time constants in these specimens. The value of χ^2 is a measure of the model fit to experimental data as it is calculated from the sum of the squares of all residuals, with lower values indicating better fitting .The highest χ^2 value given by the ZSimpWin was 0.01, indicating very good agreement between the data and the equivalent circuit models.

Figure 91. Equivalent circuits used to fit EIS data: (a) one time constant and (b) two time constants.

Table 19. Summary of values calculated to fit EIS data (Figure 90) to equivalent circuit models (Figure 91) for CeCCs deposited on Al 7075-T6. Note: AD: As-deposited and S: sealed.

	Time (hr)	Rsol (Ω-cm^2)	Cp (μF/cm^2)	Rp (Ω-cm^2)	Qdl ($s^n/(M\Omega^{-1}$-cm^{-2}))	n	Rct (Ω-cm^2)	χ^2
AD	0	41	-	-	3.73E-05	0.79	5331	0.005
AD	24	49	5.6E-07	102	1.89E-05	0.77	60620	0.005
AD	168	53	3.93E-07	104	1.61E-05	0.76	93700	0.005
S	0	56	3.25E-07	96	2.49E-05	0.72	63730	0.010
S	24	50	2E-07	82	1.99E-05	0.70	79810	0.006
S	168	52	2.01E-07	70	2.3E-05	0.65	91010	0.003

A Bode phase diagram of as-deposited CeCCs showed slight inflection at ~10^4 Hz after the panels were subjected to the humid environment (Figure 92a). There was no significant difference in the Bode phase diagrams of sealed panels before and after exposure to humidity (Figure 92b). The presence of an inflection at ~10^4 Hz for as-deposited CeCCs indicates development of a new time constant. As-deposited CeCCs could be fitted to an equivalent circuit with only one time constant before exposure to the humid environment (Figure 91a). After exposure, as-deposited panels were fitted to an equivalent circuit with two time constants (Figure 91b), indicative of an impedance due to the coating itself as well as and the metal-electrolyte interface.

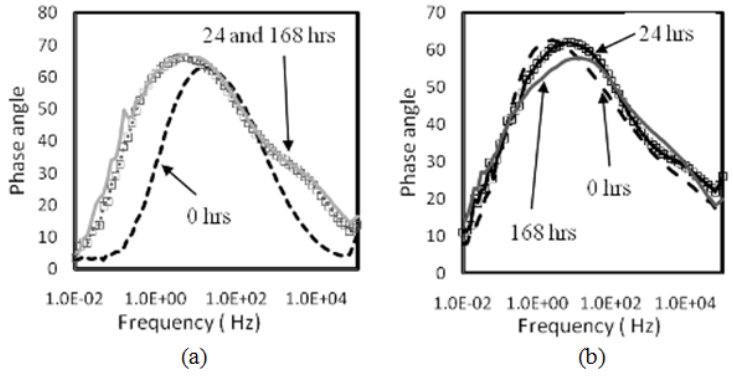

Figure 92. Phase angle Bode plot of CeCCs that were (a) as-deposited and (b) sealed.

Polarization scans of CeCCs exposed to humidity are shown in Figure 93. As-deposited CeCCs exposed to humidity for 24 hours showed a decrease in corrosion current density from ~0.4 μAmps/cm^2 before exposure to ~0.1 μAmps/cm^2 after exposure when calculated using Tafel plots. Additional exposure up to 168 hours resulted in a corrosion current density of 0.07 μAmps/cm^2. Sealed panels exposed to humidity for 24 hours showed the lowest corrosion current density (~0.04 μAmps/cm^2) and multiple pitting potentials, indicating that the coating

provides electrochemical protection in addition to serving as a barrier. After 168 hours of exposure, the corrosion current density of a sealed panel increased (~0.30 µAmps/cm^2) similar to the original sealed panel with no exposure to humidity (~0.25 µAmps/cm^2). The polarization scans indicated that exposure to humidity changed the electrochemical response toward a more passivating condition.

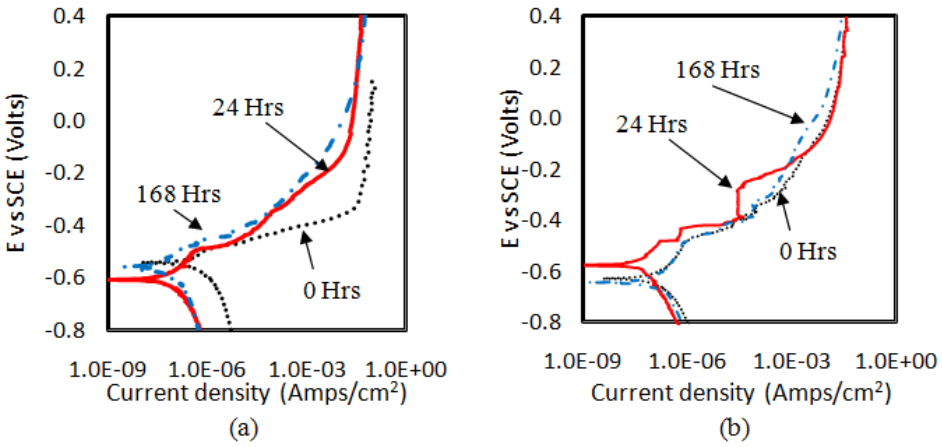

Figure 93. Polarization scans as a function of time exposed to the humidity chamber for (a) as-deposited and (b) sealed CeCCs.

AES depth profiling was performed to determine whether humidity affected the elemental composition of CeCCs (Figure 94). For both as-deposited and sealed CeCCs, a constant elemental signal was detected for the outer ~250 nm before the aluminum signal began to increase. Previous research has shown that after salt spray testing, aluminum had been transported to the surface where it produced an aluminum and oxygen-rich layer, which was accompanied by an increase in impedance [112,118]. The AES data for panels exposed to humidity clearly showed that no aluminum was detected on the surface; thus, the increase in impedance from humidity exposure was not due to the formation of an aluminum and oxygen-rich layer on the surface of the CeCCs.

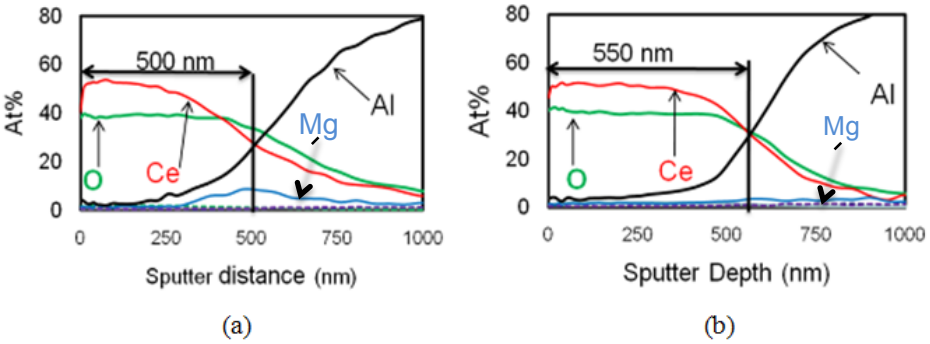

Figure 94. AES depth profiling of CeCC after 168 hours of exposure to humidity: (a) as-deposited and (b) sealed.

SEM was used to characterize the surface morphology of CeCCs before and after exposure to humidity (Figure 95 and Figure 96). Figure 95 shows that the as-deposited CeCCs had both large cracks (>0.5 μm wide) and incomplete coverage of the underlying aluminum substrate. Exposure to humidity did not appear to affect the crack size. Incomplete substrate coverage appears to be due to spallation of the coating. Figure 96 shows that sealed CeCCs had much smaller cracks (<0.5 μm wide) and complete coverage of the underlying aluminum substrate. Further, exposure to humidity did not affect surface morphology. Thus, humidity does not appear to affect the surface morphology of as-deposited or sealed CeCCs.

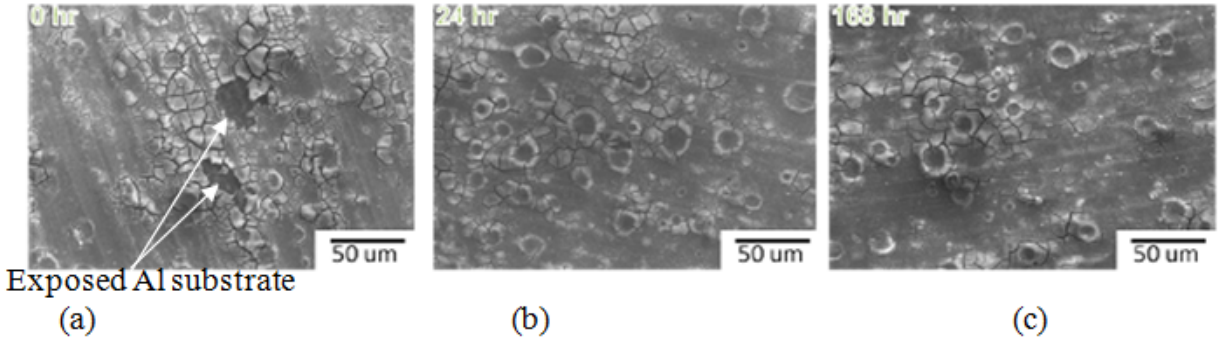

Figure 95. Micrographs of as-deposited CeCCs after exposure to humidity for: (a) 0 hours, (b) 24 hours, and (c) 168 hours.

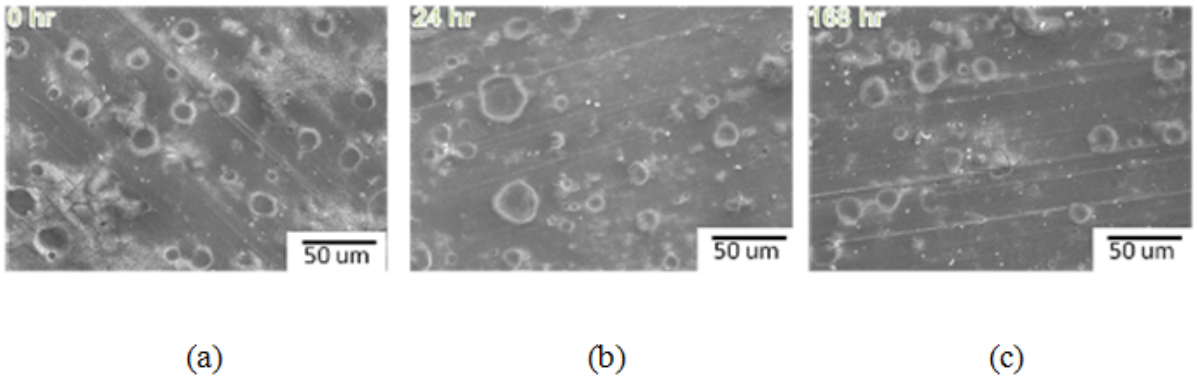

Figure 96. Micrographs of sealed CeCCs after exposure to humidity for: (a) 0 hours, (b) 24 hours, and (c) 168 hours.

XPS analyses were performed to determine whether humidity changed the valence state of cerium in the top surface of CeCCs (Figure 97). During the coating deposition process, cerium precipitated as Ce(IV) species, most likely $CeO_2 \cdot 2H_2O$, to form the coatings. Sealing transformed $CeO_2 \cdot 2H_2O$ to $CePO_4 \cdot H_2O$, resulting in a reduction from Ce(IV) to Ce(III) [116,119]. A high resolution XPS scan was performed on the Ce 3d spectrum to determine the oxidation state. As-deposited panels had an intense peak at 916 eV, which is exclusively

associated with the Ce(IV) valence state [102,119]. XPS of sealed panels showed that the intensity at this binding energy was greatly diminished, indicating that the panels were predominately in a Ce(III) valence state. The Ce 3d spectra for an as-deposited CeCC after 168 hours of humidity exposure showed another peak beginning to appear at 902 eV (indicated by a circle in Figure 90a). This peak corresponds more closely to the Ce(III) valence state [119-120]. In the case of sealed panels, the valence state of the top surface of the coating did not appear to change, indicating that the Ce(III) in the sealed coating was electrochemically stable, but polarization scans indicated active protection. Therefore, the protection appears to be provided by some means other than a cerium redox reaction within the coating. However, it is possible that some portion of the increase in impedance of as-deposited panels exposed to humidity may have been due to a change in the valance state of the cerium.

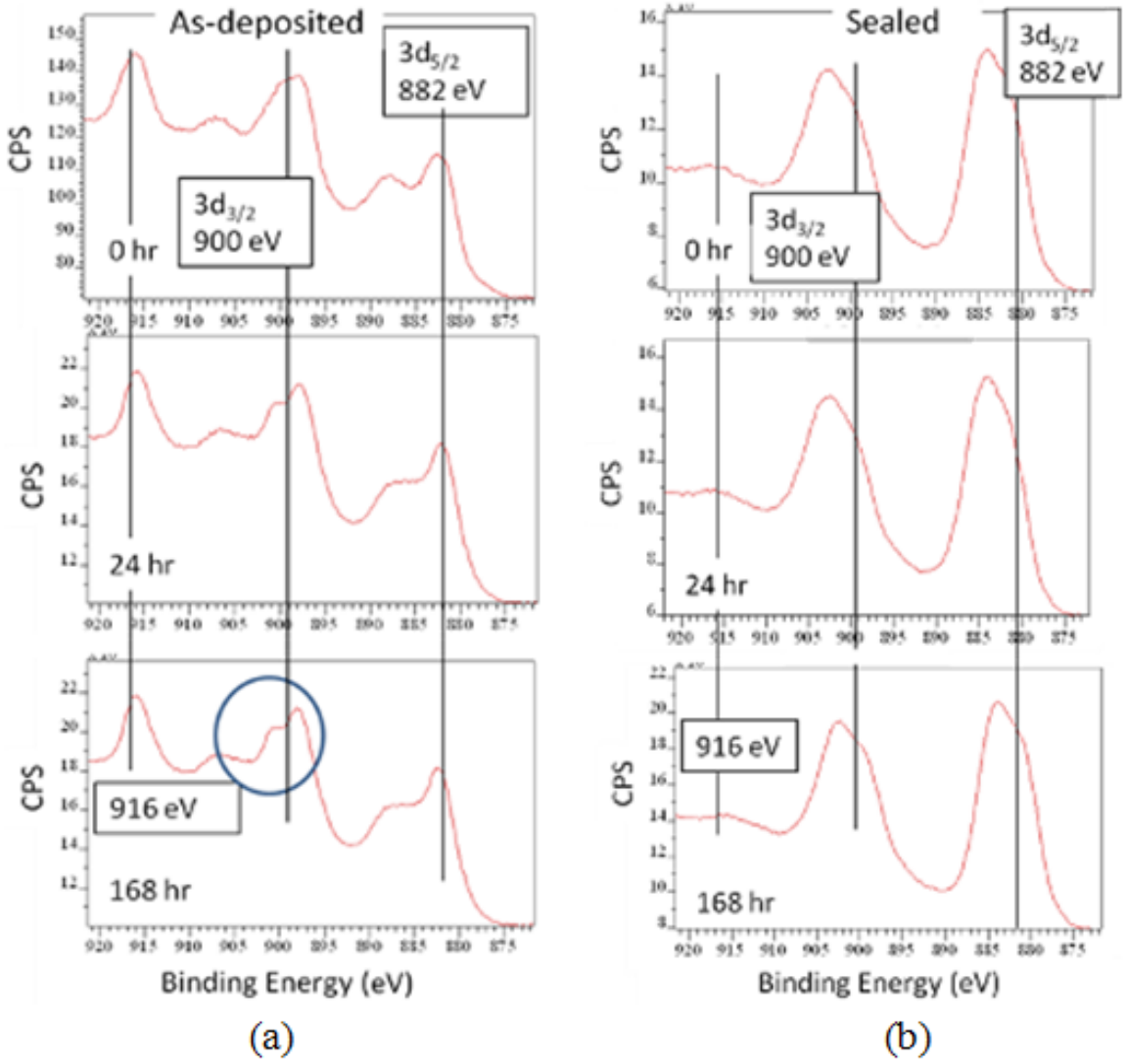

Figure 97. XPS spectra of CeCCs exposed to humidity for: (a) as-deposited and (b) sealed coatings.

Salt spray testing per ASTM standard B117 was also done to characterize the corrosion resistance of the coatings exposed to humidity. Sealed panels either before or after exposure to humidity can inhibit corrosion (i.e., formation of corrosion pits and salt tails) for up to 336 hours of salt spray testing, so the corrosion resistance of these sealed CeCCs was not further characterized. Results from salt spray testing of as-deposited CeCCs showed that exposure to humidity for 168 hours enhanced corrosion resistance. After 24 hours of salt spray testing, no corrosion products had formed on the surfaces of as-deposited CeCCs that had been exposed to humidity for 168 hours (Figure 98). In contrast, pits and salt tails formed within 4 hours on as-deposited panels with no exposure to humidity or with 24 hours of exposure to humidity. However, although the charge transfer resistance of as-deposited panels exposed to humidity (94 kΩ-cm^2) increased significantly and was greater than that of standard sealed CeCCs (64 kΩ-cm^2), corrosion still occurred within four days in salt spray testing. These results demonstrate that exposure to a humid environment improved the impedance as measured by EIS, but that alone did not provide significant corrosion protection during salt spray testing.

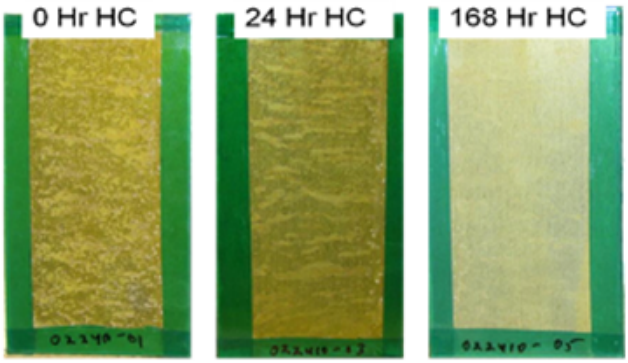

Figure 98. Images of panels after 24 hours of salt spray testing for as-deposited CeCCs exposed to the humid environment for: (a) 0 hours, (b) 24 hours, and (c) 168 hours. Note that the panel size was 2.5 cm by 7.6 cm.

As a comparison, uncoated (bare) Al 7075-T6 panels that underwent only alkaline cleaning were also exposed to the humid environment for 24 and 168 hours. EIS showed a significant increase in impedance from ~10 kΩ-cm^2 before exposure to ~280 kΩ-cm^2 after 168 hours humidity (Figure 99a). A Bode phase diagram showed two time constants (Figure 99b). The EIS data were fitted to equivalent circuits as shown in Figure 91a-b; and the values for each of the components are listed in Table 20. The highest value of χ^2 was 0.02, indicative of a good fit of the data. Prolonged exposure to humidity showed a significant increase in impedance and development of a second time constant, indicating an altered surface layer was likely responsible for the increase in impedance.

Table 20. Summary of values calculated to fit EIS data (Figure 99a) to equivalent circuit models (Figure 91) for bare Al 7075-T6.

Time (hr)	Rsol (Ω-cm^2)	Cp (μF/cm^2)	Rp (Ω-cm^2)	Qdl ($s^n/(M\Omega^{-1}$-cm^{-2}))	n	Rct (Ω-cm^2)	χ^2
0	43	-	-	7.52E-06	0.87	8248	0.006
24	49	7.36E-07	746	5.15E-06	0.76	92780	0.006
168	27	8.31E-07	1700	3.30E-06	0.82	275000	0.022

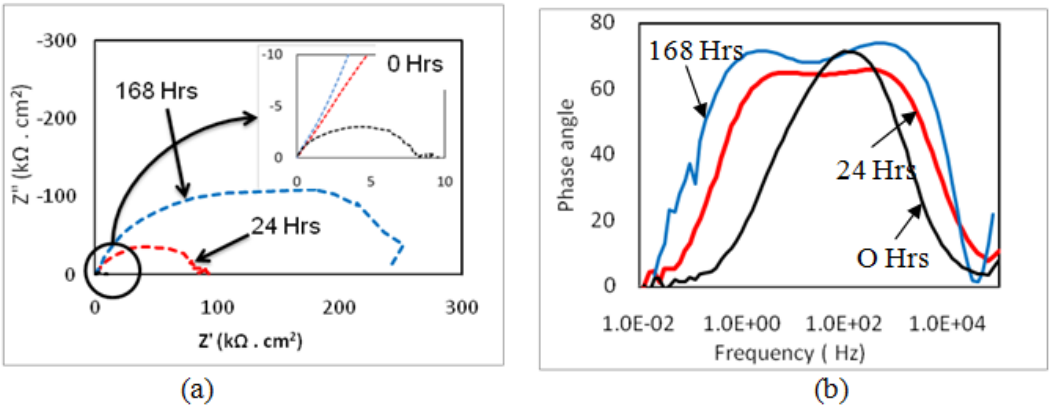

Figure 99. EIS analyses of bare Al 7075-T6 after humidity treatment: (a) Nyquist plot and (b) Bode phase angle.

A polarization scan of alkaline cleaned Al 7075-T5 exposed to the humid environment showed that the corrosion current density decreased from an initial value of 6.4 to 0.16 µAmps/cm^2 after exposure for 168 hours (Figure 100). The decrease in corrosion current density was accompanied by a significant increase in pitting potential (E_{pit}) (-0.4 V_{SCE}) compared to panels not placed in the humidity chamber. Figure 100 shows that the pitting potential of bare Al 7075-T6 not placed in humid environment is approximately the same as the OCP (-0.65 V_{SCE}) when using the electrolyte composed of 0.6 wt% NaCl and 0.6 wt% $(NH_4)_2SO_4$. After exposure, the separation between the pitting potential and the OCP was significant (~0.25 V_{SCE}), indicating development of a passivation region. Even with only 24 hours of exposure to humidity, the corrosion current density decreased by ~0.15 µAmps/cm^2 and the pitting potential was higher (-0.55 V_{SCE}) compared to the OCP (-0.65 V_{SCE}). Thus, electrochemical testing showed improvement in the corrosion resistance of bare Al 7075-T6 after exposure to humidity. The previous surface chemical analysis showed the development of a surface layer rich in Al and O. Combined, the two results indicate that the increase in corrosion resistance is due to the development of the altered surface layer.

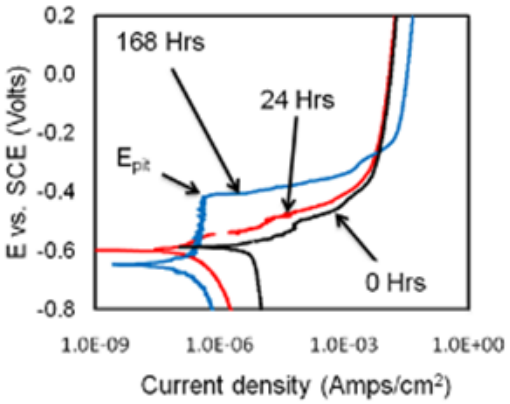

Figure 100. Polarization scans of bare Al 7075-T6 exposed to humidity for times ranging from 0 to 168 hours.

In contrast to the increase in corrosion resistance inferred from electrochemical testing, bare Al 7075-T6 panels that had been exposed to humidity for 24 and 168 hours developed a significant number of pits and tails upon exposure to salt spray for only 4 hours. The amount of corrosion indicated that the altered surface layer did not protect the alloy against corrosion attack during salt spray testing. Even though electrochemical testing showed a significant increase in corrosion impedance and an order of magnitude decrease in corrosion current density, the panels could not prevent corrosion for four hours in salt spray testing. Hence, the altered surface layer was vulnerable to attack by chloride ions.

Figure 101 provides a schematic model of the proposed interaction between humidity and the substrate through cracks in the coatings. Through the cracks in the coating and exposed areas of the substrate, humidity interacts with the surface of the alloy and alters it. The changes in the surface of the substrate increase the impedance as measured by EIS. Since sealed panels have fewer and smaller cracks a smaller area of the substrate is exposed. Therefore, the increase in impedance was less for sealed CeCCs. The impedance of sealed CeCCs increased from ~65 kΩ-cm^2 before exposure to ~90 kΩ-cm^2 after exposure compared to as-deposited CeCCs, which increased from ~5 kΩ-cm^2 before exposure to ~95 kΩ-cm^2 after exposure. Exposure to humidity also increased the impedance of bare Al 7075-T6 from ~10 kΩ-cm^2 to ~280 kΩ-cm^2. Electrochemical analysis indicated that the increase in impedance was due to an increase in charge transfer resistance between electrolyte and the substrate, which indicates the development of an altered surface layer on the substrate. Although exposure to the humid environment increased the impedance of all of the specimens, the resistance to corrosion in salt spray testing was not significantly improved. Therefore, it appears that the altered surface layer is not resistant to corrosion in the salt spray environment.

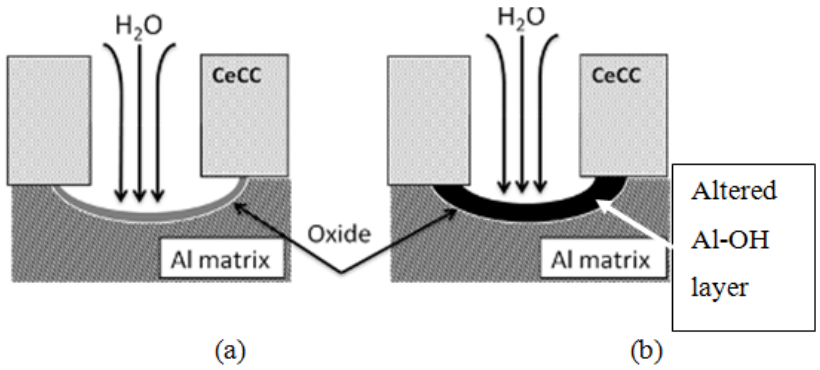

Figure 101. Schematic diagram of interactions between humidity and a CeCC: (a) pre-humidity and (b) post-humidity.

Initial Detection of Pr-species Outside of The Matrix of Epoxy-Polyamide Primers
Primers with Pr-based inhibitors had not been fully characterized prior to this project. One of the primary goals of this research was to identify the composition, crystal structure, and morphology of species (Pr, Ca, S, Cr) present in the as-deposited coating, in the coating after corrosion, and in the scribes of corroded panels. Following salt spray testing in 500 hour increments up to 3000 hours, AES, SEM-EDS, and XRD analyses were performed to characterize changes occurring during corrosion.

The initial effort focused on coated panels. Both SEM and EDS were performed to characterize the field and scribe areas to identify the chemical composition of species present. A representative micrograph of a particle containing Pr, Ca, and O is shown in Figure 102 along with elemental analysis. This particular specimen was a water-based primer deposited on an Al 2024-T3 substrate that had a CrCC. The particle was present after 1500 hours in salt spray. A SEM image with elemental analysis of a scribed area of an Al 2024-T3 panel coated with a solvent-based primer on top of a CrCC following 1500 hours in salt spray is shown in Figure 103.

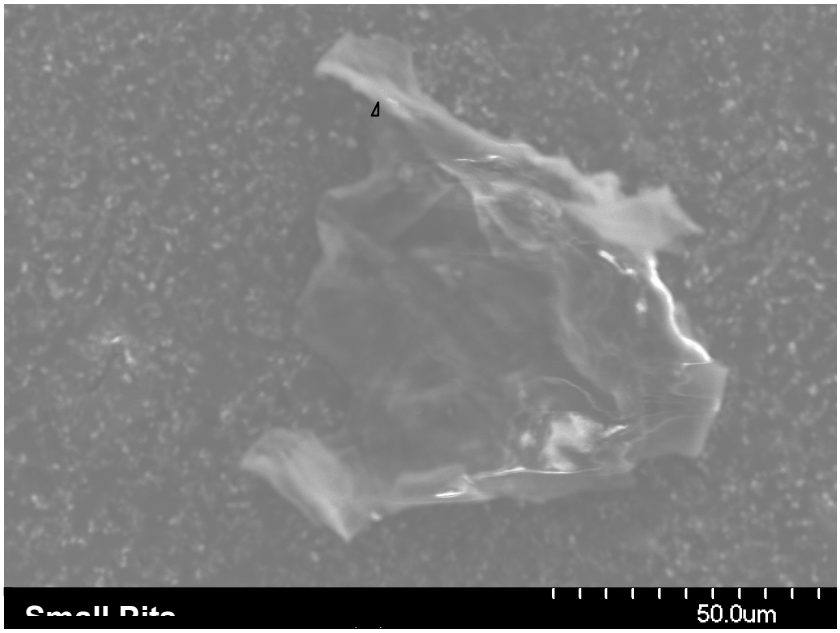

Element	Atomic %
C	46.02
O	42.11
Na	1.01
Al	1.16
Si	1.1
Cl	2.22
Ca	0.4
Ti	4.7
Pr	1.28
Total	100

Figure 102. SEM image of a particle present in the field of a water-based primer coating after 1500 hours of salt spray testing along with EDS analysis showing the particle contains Pr and O in addition to other species.

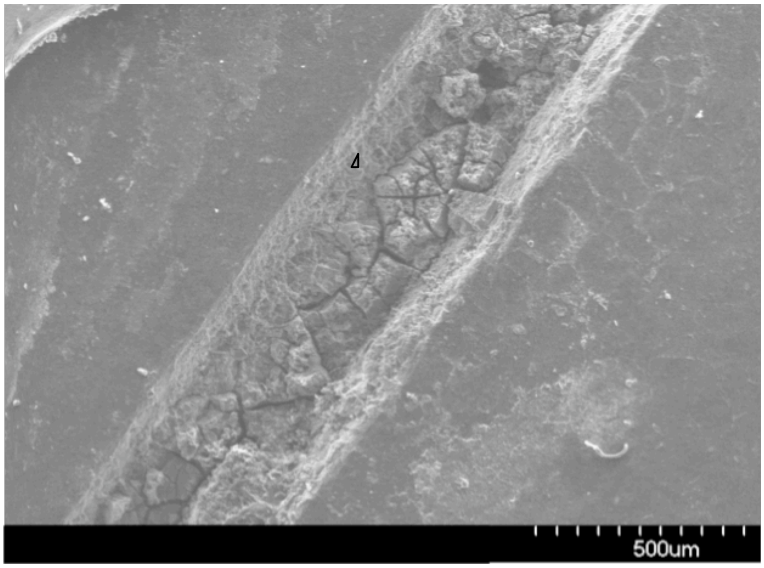

Element	Atomic %
C	20.34
O	64.46
Na	0.18
Al	13.03
Cl	0.97
Ca	0.22
Pr	0.24
Ti	0.56
Total	100

Figure 103. SEM image of the scribe in a solvent-based primer on CrCC coated Al 2024-T3 following 1500 hours in salt spray with accompanying elemental analysis.

SEM-EDS is consistent with analysis of the field of a panel. The table in Figure 102 is representative of species and concentrations found in each sample regardless of hours spent in salt spray. When used to identify the concentration of Pr and Ca found in the scribe following salt spray testing, SEM-EDS analysis has not been consistent. The presence or absence of various species is not directly related to corroded or shiny areas of scribes. Unlike the

conclusions drawn from the AES data for Ca migration, at this time, no direct correlation has been identified between time in salt spray and Pr/Ca concentration in the scribe as determined by AES. The results suggest that Pr migrates to the scribe during salt spray testing, but the concentration is not directly proportional to time spent in salt spray. Scribe analysis will continue for test panels as a function of times in salt spray up to 3000 hours. In addition, work will continue on optimization and refinement of characterization methods.

XRD was also used to identify crystalline species in the field of primers before, during, and after corrosion. Initial XRD studies have detected the presence of $Ca_2SO_4 \bullet 2H_2O$, $Pr(OH)_3$, and TiO_2 in primers prior to salt spray testing and for test times up to 1500 hours. These compounds are consistent with other analysis of the species in the field of the primer. In addition, Reitveld refinement of the XRD spectra provided evidence of fluctuating levels of $Ca_2SO_4 \bullet 2H_2O$ and $Pr(OH)_3$ (the presumed active corrosion inhibitors) following periods of varying time in salt spray testing. Duplicate experiments are in progress to confirm the initial findings and further identify the concentrations of species in the primer as a function of time in salt spray testing.

SEM-EDS, XRD, and FIB-cross sectional analyses were performed on panels prepared by Deft. Both solvent-based and water-based series primers coated on top of CrCCs on Al 2024-T3 were characterized to track changes occurring during corrosion. Coated panels were imaged in the SEM and EDS was performed in both the field and in the scribe to identify the chemical composition of species present. Scribed test panels were placed in ASTM B117 salt spray and selected panels removed after increments of 500 hours, up to 3000 hours, were characterized for Pr-species, which previously have only been found in trace amounts. Initially it was thought the corrosion product in the scribe would contain a uniform distribution of Pr-species, but Pr species were found in localized areas and had an acicular/dendritic morphology. Chemical analysis by EDS showed Pr was not detected in the scribes of as-received panels (solvent-based and water-based series). However, following salt spray testing, Pr species were detected at discrete locations within the scribes. A representative micrograph and EDS mapping of a Pr-rich precipitate can be seen in Figure 104.

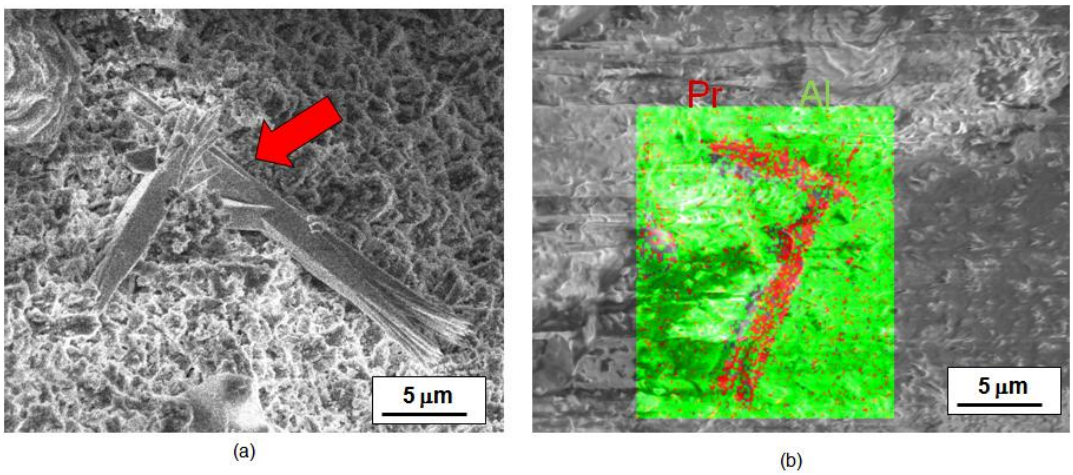

Figure 104. Micrograph and EDS mapping of a Pr-rich precipitate found within the scribe of a solvent-based series panel following 3000 hours salt spray exposure.

Discrete Pr-rich areas were also found near the primer-scribe interface, which appeared to indicate that Pr-species were migrating out of the primer matrix and re-precipitating in the scribe (Figure 105).

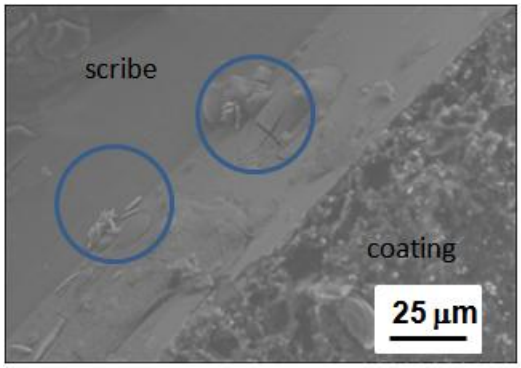

Figure 105. Micrograph of several clusters (denoted by circles) of Pr-rich precipitates found within the scribe of a water-based series panel following 1000 hours salt spray exposure.

Areas where Pr-precipitation products were found were also Cu rich, suggesting that the presence of Cu-containing intermetallic particles in the substrate influenced the precipitation of Pr. This may be an indication that Pr species were precipitating to passivate galvanic couples within the scribed areas. Work is in progress to identify the exact phase/composition of the Pr-precipitation products as well as to determine the growth mechanism within the scribe.

Screening for the presence Pr in the scribes of panels following corrosion testing without complicated instrumentation would be a quick and easy method to screen panels to determine if the primer were providing corrosion protection. The organic azo dye Arsenaso III was employed in an attempt to detect the presence of Pr in the scribes of panels after salt spray testing. An aqueous solution of 0.05% Arsenazo III (4 mL), formate buffer pH 3.5 (1 mL), and 1% ascorbic acid (2 mL) was first added to commercially available $Pr(OH)_3$ and Al_2O_3 as a control study. Shown in Figure 106, no color change was observed (the reagent remained purple) in the presence of Al_2O_3. In contrast, the color changed to teal when the solution was mixed with $Pr(OH)_3$. The scribe of a panel that had a water-based series Deft primer exposed to 3000 hours of salt testing and then stripped of its primer coating was tested. The reagent solution was distributed along the scribe using a syringe as shown in Figure 107. It was found that heavily salted areas were Pr-rich, but no Pr was detected in darkened areas. This study indicated that Pr species were present in greater concentrations in salted areas as compared to shiny/darkened areas of the scribe following exposure to salt spray. Arsenazo III, when used at the right pH with ascorbic acid as a mask for Al^{3+}, appears to be a viable qualitative colormetric reagent for the detection of Pr-species.

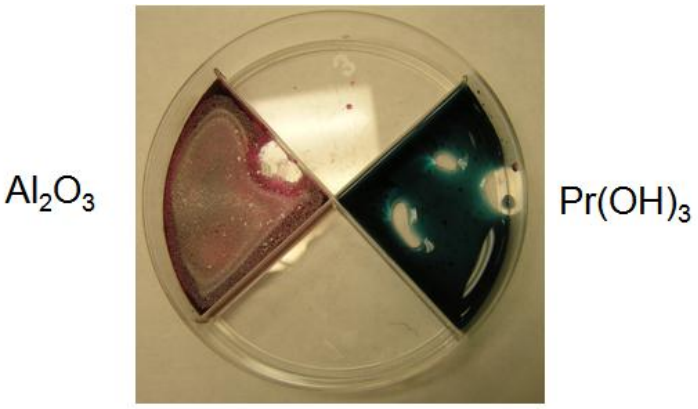

Figure 106. Control experiment of Al_2O_3 and $Pr(OH)_3$ powders reacted with the Arsenazo III reagent. The reagent should remain purple when Pr is not present and turn teal when reacted with Pr.

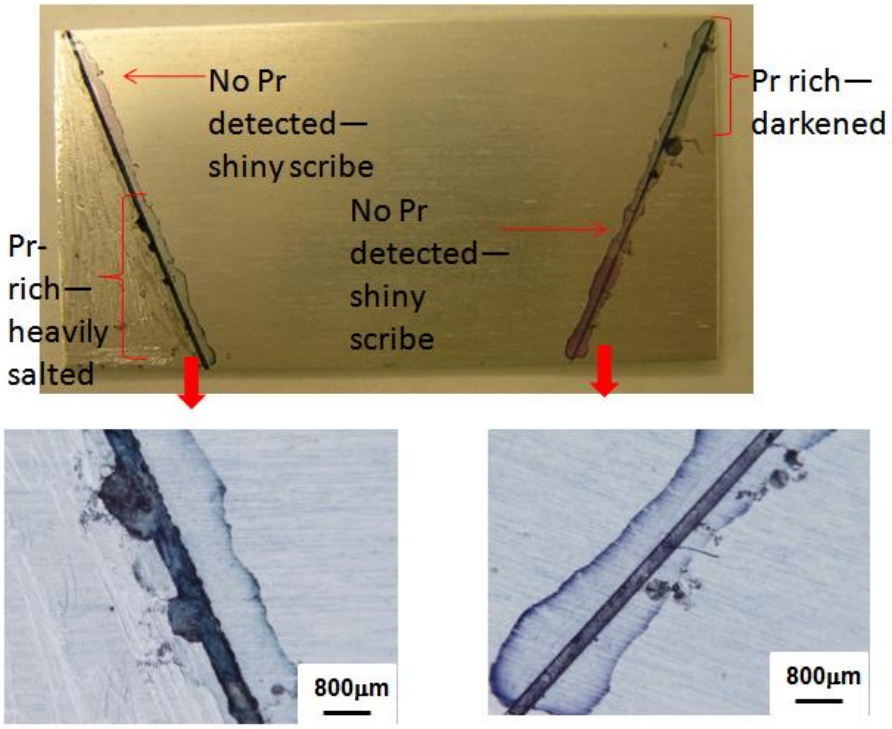

Figure 107. Colormetric detection of Pr-species in the scribe of a stripped panel that was coated with a water-based series primer on top of a CrCC on Al 2024-T3 following 3000 hours of salt spray exposure.

Evolution of Primer Composition During Corrosion

XRD analysis was performed to quantify the amounts of crystalline phases present in primer coatings as a function of time in salt spray testing. Selected panels of both solvent-based and water-based series primers prepared by Deft were removed from salt spray after increments of 500 hours up to 3000 hours to evaluate changes in the composition. Reitveld refinement was

performed to quantify the amounts of the different crystalline phases ($Pr(OH)_3$, $CaSO_4 \bullet 2H_2O$, and TiO_2) that were present at each time increment. The amount of $Pr(OH)_3$ and $CaSO_4 \bullet 2H_2O$ detected in the coating was normalized against TiO_2, which was assumed to be inert and not changing in composition during salt spray exposure. The results are summarized in Figure 108.

The amount of $Ca_2SO_4 \bullet 2H_2O$ decreased after 500 hours of salt spray exposure for both the solvent-based and water-based series primers. For the water-based series, a $Ca_2SO_4 \bullet 2H_2O$ diffraction peak was not detected after 3000 hours in salt spray testing, indicating that all of the species had been depleted. Analysis showed that the $Ca_2SO_4 \bullet 2H_2O$ concentration also decreased in the solvent-based series primer, but a small diffraction peak was detected after 3000 hours, indicating that some of the $CaSO_4 \bullet 2H_2O$ was retained in the matrix. In both the solvent-based and water-based series, the amount of $Pr(OH)_3$ remained nearly constant within the primer matrix for the duration of the corrosion tests. The results indicated that the Pr_2O_3 that was formulated into the primer converted to $Pr(OH)_3$ at some point prior beginning of the analysis. The data also indicated that $Ca_2SO_4 \bullet 2H_2O$ was being depleted from the primer during salt spray exposure.

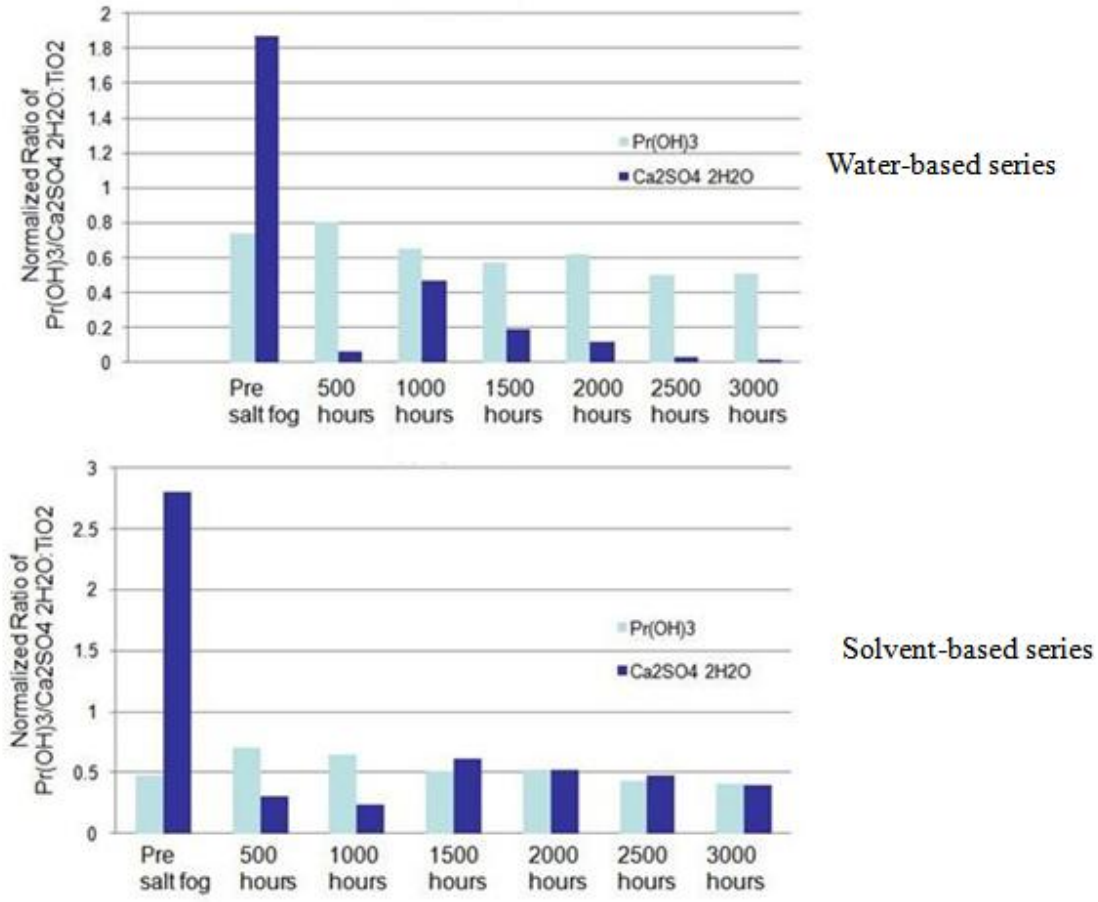

Figure 108. A quantitative summary of the amounts of $Pr(OH)_3$ and $CaSO_4 \bullet H_2O$ in both the water-based and solvent-based series following the specified times in salt spray testing. The amounts are normalized to the TiO_2 content.

Morphological changes (Figure 109) were also detected in the coating matrix during salt spray exposure. Comparing samples in the "as-received" condition to those that had been exposed to salt spray revealed that the primer matrix was not homogeneous. The as-received primer contained Ca, S, and Pr-rich aggregates that had areas ranging from 1 μm^2 to 8 μm^2 with an average particle area of~ 3 μm^2. Voids were present in the matrices of the solvent-based and water-based series primers following 500 hours salt spray (water-based), 1000 hours salt spray (solvent-based) and 3000 hours salt spray testing (solvent and water-based). The voids were typically approximately 2 μm or more below the primer surface and ranged in surface area of 1 μm^2 to 400 μm^2. The voids found in primer matrices following salt spray testing were a result of the depletion of the aggregates. The evolution of voids correlated to XRD studies that showed the depletion of $CaSO_4 \bullet 2H_2O$ from both the water and solvent-based primers. Hence, it seems likely that the voids in the primer matrix were formed by removal of $CaSO_4 \bullet 2H_2O$.

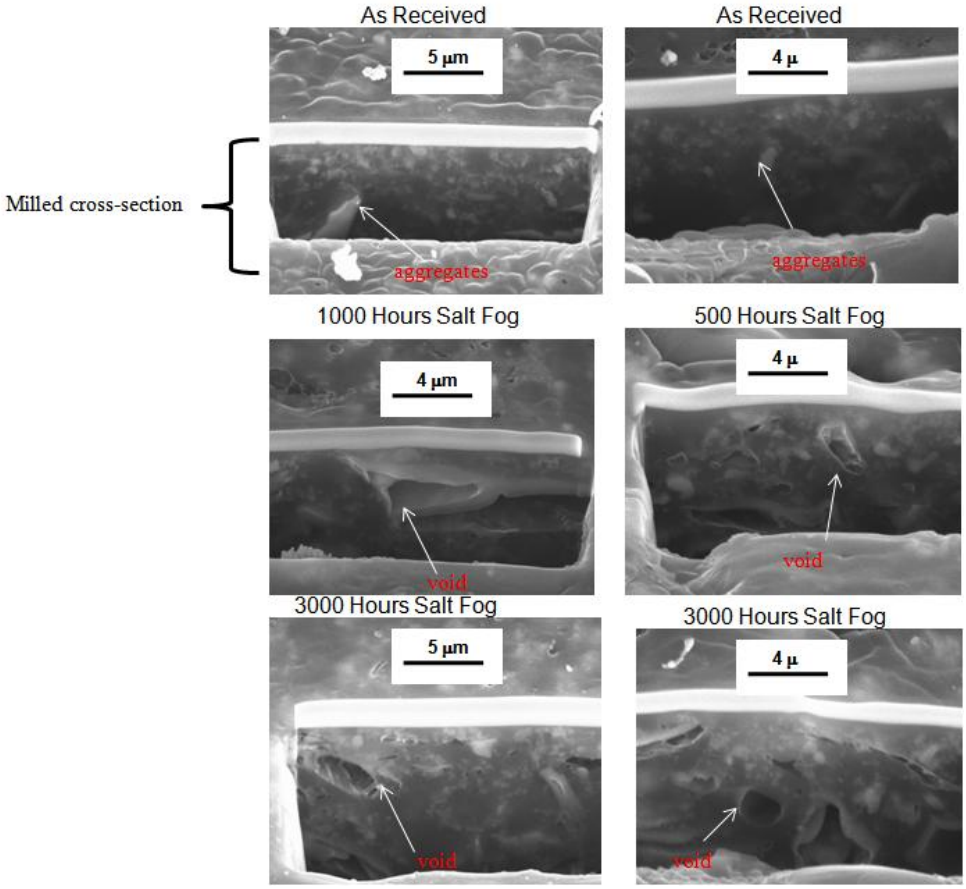

Figure 109. Representative FIB-milled SEM images of (a) solvent-based and (b) water-based series primers in the as-received state and following 1000 and 3000 hours of salt spray exposure.

Corrosion of Model Primer Systems

The crystalline phases present in primer coatings containing Pr-based inhibitors were characterized after various increments of salt spray testing up to 3000 hours. Characterization was performed using SEM-EDS, XRD, and LA-ICP-MS analyses. The formulations consisted

of the Deft solvent-based primer (084 series) formulation and TiO_2, but with the standard rare-earth inhibitor replaced with individual additions of: 1) gypsum ($CaSO_4 \cdot 2H_2O$); 2) talc ($Mg_3Si_4O_{10}(OH)_2$); 3) Pr_2O_3; or 4) Pr_6O_{11}. The 084 series primer formulation contains both Pr_2O_3 and gypsum. A separate series with the same additives were also analyzed, but with the addition of a commercially available fluorinated top coat was used. A series of scribed test panels of each formulation were placed in ASTM B117 salt spray. Selected panels were removed after increments 500 hours and up to 3000 hours of salt spray exposure.

X-ray diffraction analysis and SEM-EDS were used to characterize the evolution of phases and morphologies for as-received primers containing gypsum, Pr_2O_3, Pr_6O_{11}, or talc. SEM-EDS detected Ca, S, and O present in as-received panels formulated with gypsum and XRD confirmed the presence of gypsum (33-0311) in these coatings (Figure 110A). In the as-received talc primer, the primary components of talc (Mg, Si, and O) were detected by SEM-EDS. Analysis by XRD confirmed the presence of talc (01-073-0147) in these coatings (Figure 110B). Talc was inert and remained unchanged upon incorporation into the primer matrix. In as-received coatings formulated with Pr_2O_3, Pr_6O_{11}, and the 084 series primer Pr-species were detected in the bulk of the coatings by SEM-EDS analysis. Further analysis by XRD identified the species found in as-deposited coatings formulated with Pr_2O_3 as $Pr(OH)_3$ (01-083-2304) (Figure 110C). After incorporation of Pr_6O_{11} into the primer matrix, XRD analysis determined that $Pr(OH)_3$ (01-083-2304 Pr_6O_{11} (00-42-1121) and PrO_2 (24-1006) were in as-deposited coatings (Figure 110D). In as-deposited 084 primer coatings $Pr(OH)_3$ (45-0086) and gypsum (33-0311) were present and identified by XRD (Figure 110E).

Following 500 hours of salt spray testing, coatings formulated with either Pr_2O_3 or gypsum (no top coat) had either shiny scribes or partially shiny scribes with minimal darkening (Figure 111A and Figure 111C). Coatings prepared with Pr_6O_{11} and the standard 084 series primer (no top coat) had minimal salting and shiny/darkened scribes (Figure 111D and Figure 111E). Coatings prepared with talc (no top coat) had darkened and salted scribes, which was expected based on the chemical inertness of talc (Figure 111B).

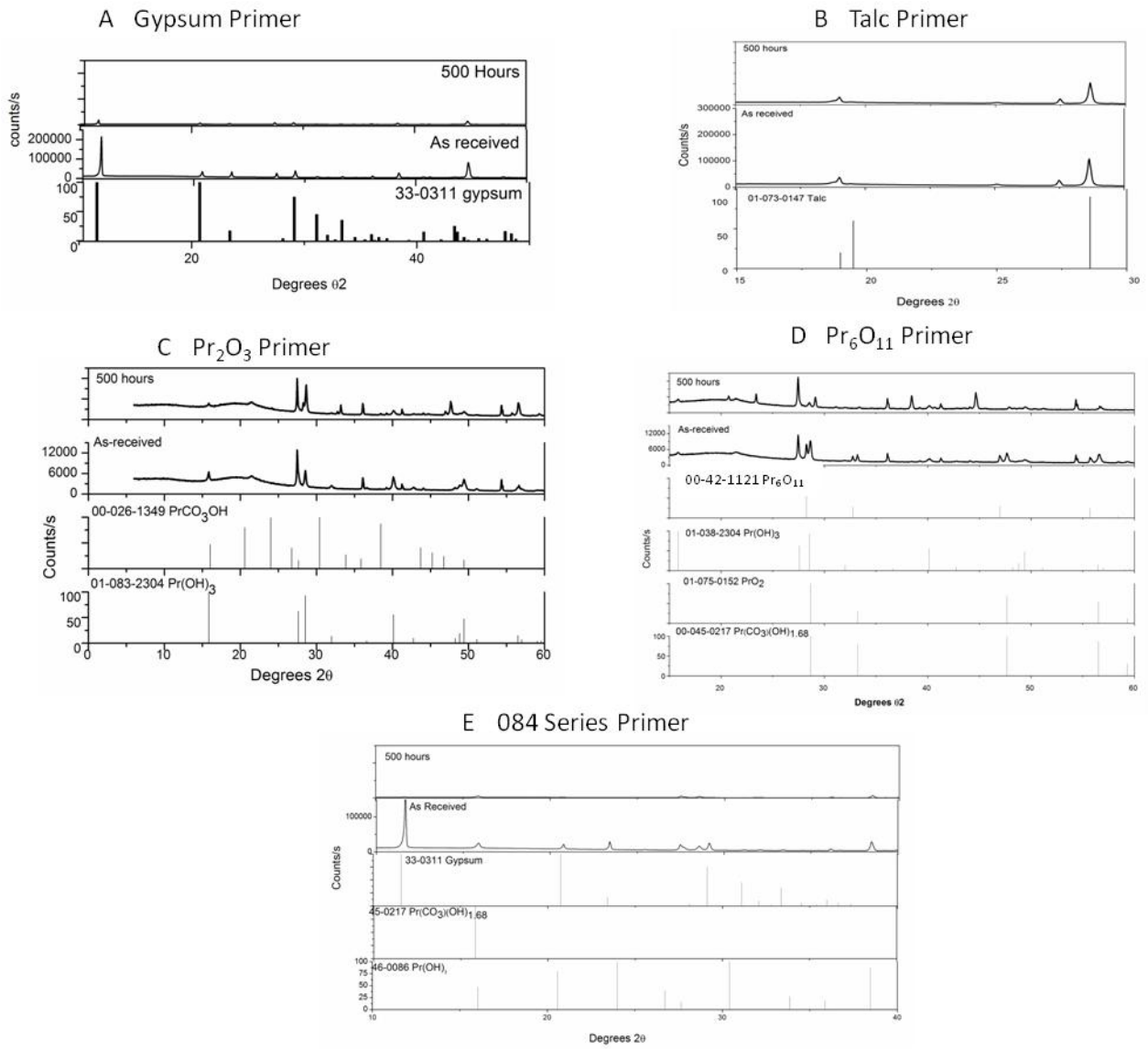

Figure 110. XRD patterns collected from the field region of primer coatings formulated with (A) gypsum, (B) talc, (C) Pr_2O_3, (D) Pr_6O_{11}, and (E) 084 series primer in the as-deposited condition and following 500 hours of salt spray exposure.

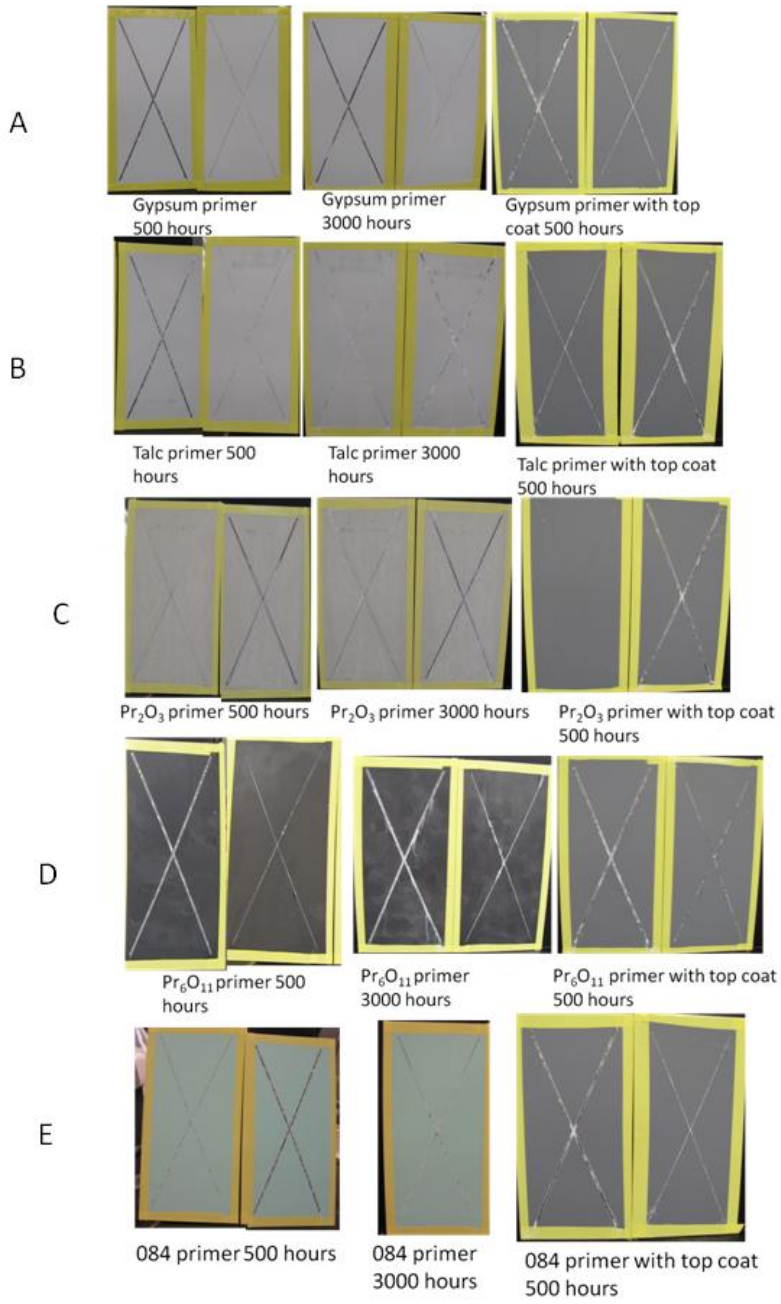

Figure 111. Representative primers formulated with (A) gypsum, (B) talc, (C) Pr_2O_3, (D) Pr_6O_{11} f, and (E) 084 series primers solvent-based on Al 2024-T3 with CrCC after 500 and 3000 hours of salt spray evaluation and top coated panels with the same formulations after 500 hours of salt spray evaluation.

Pr-rich precipitates were observed in the scribes of panels coated with primers formulated with Pr_2O_3 and Pr_6O_{11} as well as the 084 series primer whereas no Pr-rich precipitates had been observed in the scribes prior to salt spray testing. The crystals formed dense layers or localized patterns (Figure 112).

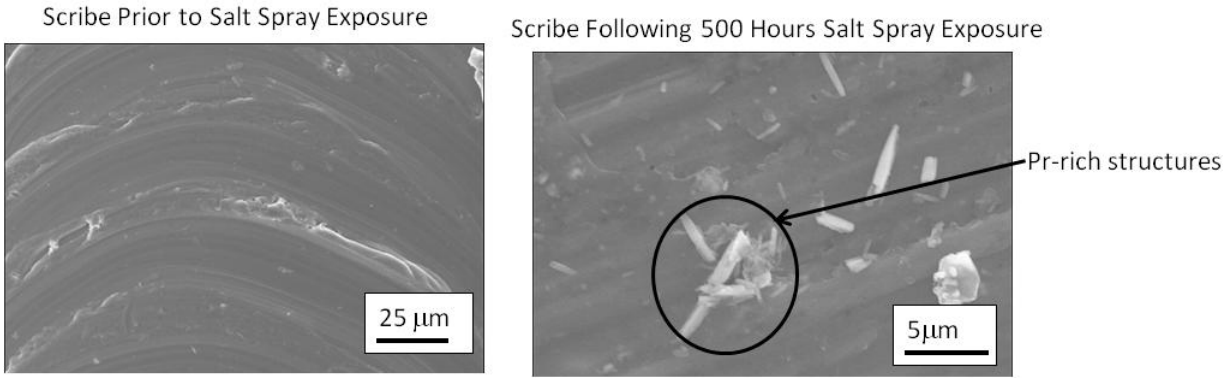

Figure 112. SEM image of a scribed area from a primer formulated with Pr_2O_3 following 500 hours of salt spray exposure. Pr-rich precipitates appeared as white, acicular deposits that were distributed around scribed areas with an example circled.

Although neither the crystal structure nor the exact stoichiometry has not been determined, EDS identified the major elements present as O, Al, and Pr. Because Pr was present only in the primer matrix and not the substrate prior to salt spray testing, this analysis provided evidence that Pr species dissolved from the matrix, transported out of the primer, and re-precipitated in scribes in response to the corrosive environment. Only corrosion products consisting of Al and O were detected in the scribes of panels coated with the primer formulated with gypsum or talc. Based on this analysis, PrO_x species appear to afford corrosion protection when incorporated into the primer matrix by transporting from the coating and re-precipitating in areas where the underlying metallic substrate is exposed. The addition of PrO_x species to the epoxy-polyamide primer matrix provided corrosion protection, while the talc-containing control primer did not. Based on salt spray performance, Pr_2O_3 provided better corrosion protection than Pr_6O_{11} at short (i.e., up to 500 hours of salt spray exposure) testing times. SEM-EDS characterization confirmed that Pr-rich species formed were present in the scribes for both Pr_2O_3 and Pr_6O_{11} containing coatings after salt spray testing.

Quantitative analysis of Ca, S, and Pr in the corrosion product found in the scribe of 084 series primers following 500 hours of salt spray exposure was done by usingLaser Ablation-Inductively Coupled Plasma-Mass Spectrometry (LA-ICP-MS) to further understand which species in the primer matrix transport and migrate during attack. A micrograph of the specific area sampled can be seen in Figure 113.

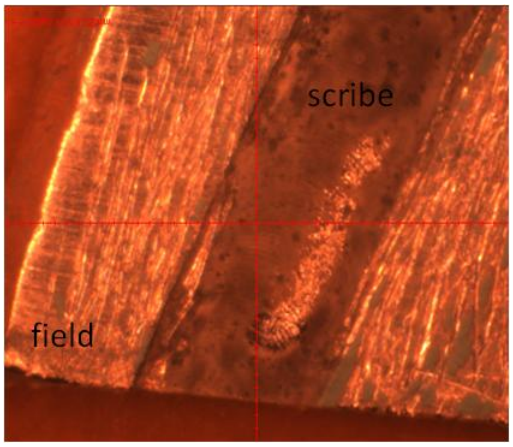

Figure 113. Micrograph of 084 primer series scribe following 500 hours of salt spray exposure where the laser ablated a 150 µm diameter spot size along a linear path for a 90 s span in order to analyze the corrosion material present.

For comparison an 084 primer as received scribe, 084 primer darkened scribe, and 084 salted scribe were analyzed. No significant difference was detected between the concentration of Ca or S in scribes of as-deposited panels as compared to scribes in panels that had undergone 500 hours of salt spray exposure. However, higher concentrations of Pr were present following salt spray exposure (Table 21). Although the absolute value varied considerably,, the values were consistent on a relative level. Multiple mechanisms were responsible for the variation in concentration of Ca, S, and Pr: (1) Lack of appropriate standards for LA-ICP-MS – the coupling between the laser and glass standard and the laser to aluminum samples is not ideal for comparing the standards to these samples; and (2) The samples are not of uniform thickness. It is possible that the laser went through the corrosion product layers in some places. This data suggests that Pr-species are the only primer components that dissolve from the coating, transport to the scribe, and re-precipitate in scribed areas of panels.

Table 21. Elemental analysis data of corrosion product in an 084 primer series scribe following 500 hours of salt spray exposure as detected by mass spectrometry.

Sample	ppm S	+/-	ppm Ca	+/-	ppm Pr	+/-
As-received	579	116	26318	15748	87	26
Darkened Scribe	548	148	7526	2491	513	146
Salted Scribe	237	22	7236	4623	610	127

The field areas of scribed panels were also examined by SEM-EDS and XRD as a function of exposure time in ASTM B117 salt spray testing. Analysis was focused on the identifying species that had leached out of the primers during corrosion testing of 500 hours (Figure 114).

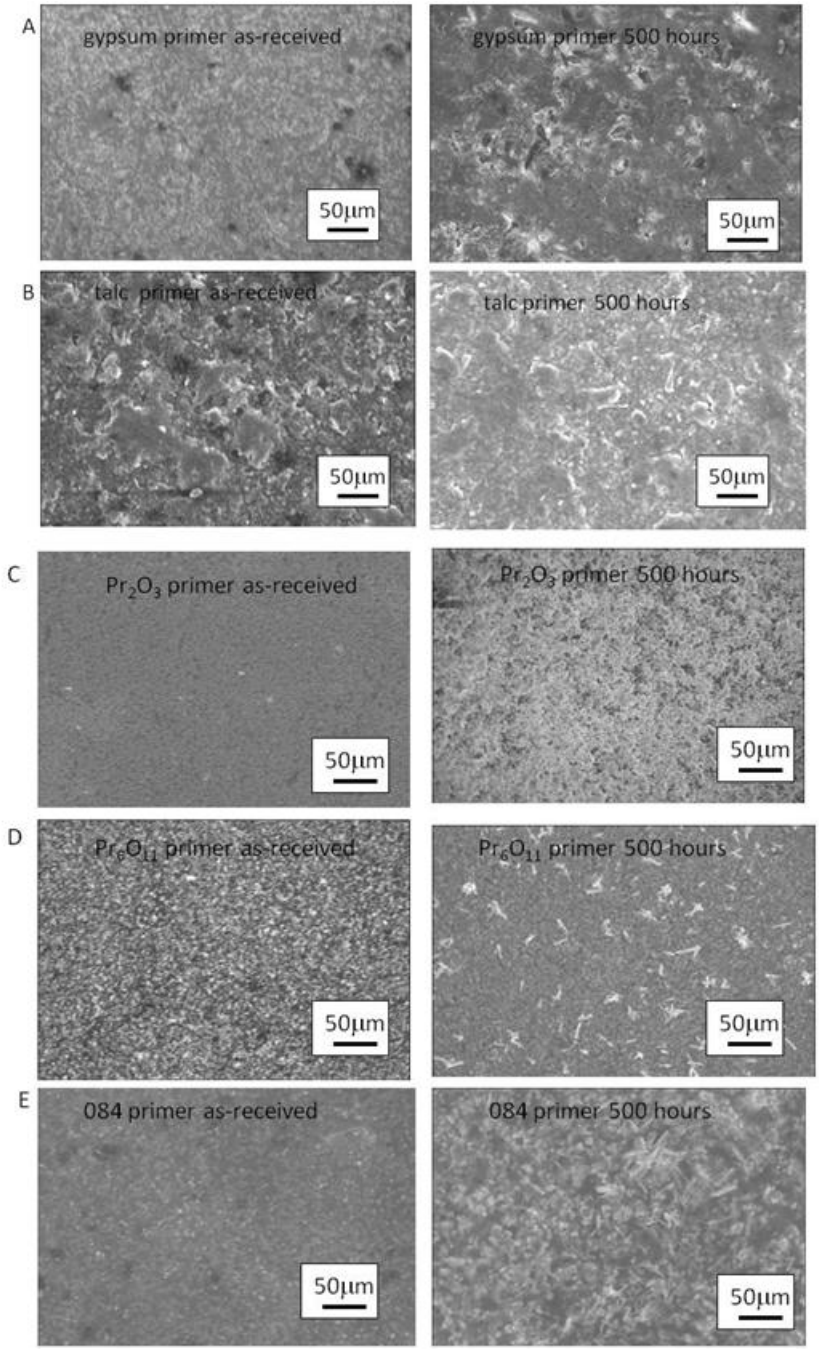

Figure 114. SEM images of the surfaces of as-deposited primers and primers following 500 hours of salt spray exposure formulated with (A) gypsum, (B) talc, (C) Pr_2O_3, (D) Pr_6O_{11}, and (E) 084 series primers on Al 2024-T3.

Following salt spray exposure, primers formulated with gypsum or talc formulated primers did not undergo a phase or morphological change (Figure 110A, Figure 114A, Figure 110B, and Figure 114B). Following salt spray exposure of the primer containing Pr_2O_3, Pr_6O_{11}, and the 084 series primer Pr-rich species were found to have precipitated on the surface of the coatings (Figure 114C, Figure 114D, and Figure 114E). In the primer formulated with Pr_2O_3,Pr-rich

species re-precipitate in dense patterns (Figure 114C). XRD identified the re-precipitated species formed during salt spray testing as a mixed Pr-hydroxyide/hydroxycarbonate composed of $Pr(OH)_3$(01-083-2304) and $Pr(CO_3)OH$(00-026-1349) crystalline phase (Figure 110C). For primers formulated with $Pr_6O_{11,}$ salt spray testing resulted in the precipitation of Pr-rich species in localized clusters in areas areas of the scribe (Figure 114D). A single Pr-hydroxycarbonate phase, $Pr(CO_3)(OH)_{1.68}$ (00-045-0217) along with $Pr(OH)_3$ and PrO_2 were detected after salt spray exposure of these coatings (Figure 110D). This compound had a different stoichiometry than the mixed Pr-hydroxycarbonate phase identified in the primer containing Pr_2O_3 and did not form as dense of a layer. Pr-rich precipitates also formed on the surface of the 084 series primer, which is formulated with Pr_2O_3 and gypsum inhibitors. Similar to the Pr_2O_3 formulated primer XRD identified a mixed Pr-hydroxyide/hydroxycarbonate composed of $Pr(OH)_3$(01-083-2304) and $PrOHCO_3$(00-027-1376) as being present in the coating following salt spray exposure (Figure 110E). Pr-rich species species partially re-precipitated from the 084 primer series coatings differing in morphology from coatings containing Pr_2O_3 only (Figure 114E). Comparison of SEM images showed that Pr-hydroxide/hydroxycarbonate species were more concentrated on the surfaces of primers containing Pr_2O_3 coatings as compared to primers containing Pr_6O_{11}. This observation is consistent with previous research that concluded that Pr_6O_{11} did not hydrate as readily as Pr_2O_3 and was more thermodynamically stable [10,15,32]. Once incorporated into the primer matrix, Pr_2O_3 appears to be more soluble, which allows it to dissolve, transport, and re-precipitate more rapidly than Pr_6O_{11}. Also, the presence of gypsum in the 084 primer series seems to suppress the rapid re-precipitation of Pr^{3+} species. During exposure to a salt spray environment, Pr^{3+} actively transported within the coating, reacted with atmospheric H_2O and $CO_{2,}$ and re-precipitated in form of a mixed Pr-hydroxide/hydroxycarbonate on the surface of the coating.

During short exposure times the Pr_2O_3 and gypsum only formulation coatings provided the best corrosion protection but, after 3000 hours of salt spray exposure, the primers formulated with individual inhibitors of Pr_2O_3, Pr_6O_{11}, gypsum, or talc all experienced pitting, salting, and tailing within the scribed area (Figure 111A, Figure 111C, and Figure 111D). Following 3000 hours of salt spray exposure the 084 series primer maintained better overall performance while salting and darkening of the scribe still occurred (Figure 111E). Data indicates Pr_2O_3 is the more favorable starting Pr-phase for enhanced corrosion protection and gypsum by itself can also provide corrosion protection for moderate testing times (i.e. up to 1500 hours). The talc primer provided no corrosion protection due to the fact no active inhibitors were present in the primer matrix (Figure 111B). Primers containing either gypsum or Pr_2O_3 showed significant corrosion protection on their own. When both Pr_2O_3 and gypsum were present a more robust coating system provided protection for longer exposure times when compared to the coatings with each individual component alone or the talc, which contained no corrosion inhibitor.

After 3000 hours of salt spray exposure the composition and crystal structure of components of interest in primer-coated panels following salt spray exposure were compared to the as-sprayed condition and quantified using Reitveld XRD refinement (Figure 115).

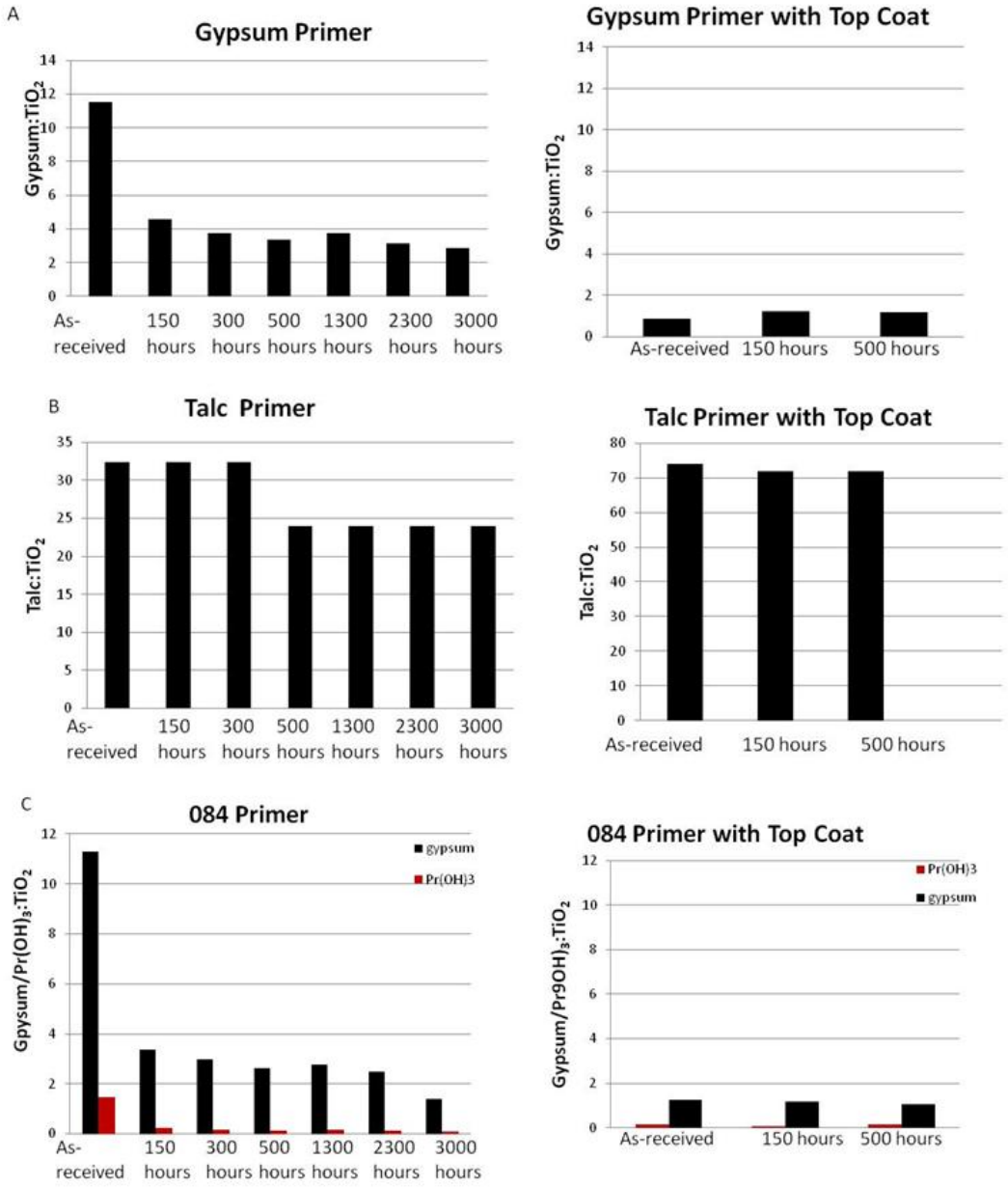

Figure 115. The composition and crystal structure of components of interest following salt spray exposure in (A) gypsum, (B) talc, and (C) 084 series primer coated panels and top coated panels compared to the as-received condition as quantified by Reitveld XRD refinement.

The primer formulated with only gypsum exhibited a ~4x decrease in gypsum content (Figure 115A) during 3000 hours of salt spray exposure. For comparison, the primer formulated with talc experienced a loss of about half of the talc (Figure 115B). Quantitative analysis could not be performed on primers formulated with Pr_2O_3 or Pr_6O_{11} due to peak overlap. However, analysis by XRD identified the species present following salt spray exposure as discussed above (Figure 115C). It is likely that $Pr(OH)_3$ was both being transformed within Pr-containing coatings as well as being depleted from the coating. The standard 084 series primer exhibited a ~10x decrease in

gypsum content after 3000 hours salt spray exposure. In the 084 series primer, of $Pr(OH)_3$ did not change during exposure (Figure 115C).

When a top coat was added to each primer formulation 1) gypsum ($CaSO_4 \cdot 2H_2O$); 2) talc ($Mg_3Si_4O_{10}(OH)_2$); 3) Pr_2O_3; or 4) Pr_6O_{11} and standard 084 series primer corrosion protection of each primer was degraded. After 500 hours of salt spray exposure heavy salting and darkening occurred in the scribes of panels of each formulation. The Pr_2O_3 only primer formulation was the only primer series tested that maintained shiny scribes after 150 hours of exposure and had the least amount of salting and tailing after 500 hours of salt spray exposure.

When as-received top coated panels were compared to top coated primers following 500 hours of salt spray exposure, only small changes were observed in the concentrations of the inhibitor species (Figure 115). Based on qualitative comparisons, the relative amounts of Pr_2O_3 or Pr_6O_{11} did not change in those formulations. It appears the addition of top coat affects the "release" capability of gypsum, which, in turn, affects the salt spray corrosion performance of top coated specimens. Top coated panels formulated with Pr_2O_3 yielded the best corrosion protection compared to all other formulations and standard 084 series. When exposed to salt spray, the scribes of all other top coated specimens began to salt/darken within 150 hours, except for the one that had the primer formulated with only Pr_2O_3. The transformation of Pr_2O_3 into either $Pr(OH)_3$ or a Pr-hydroxycarbonate affected the ability of the coating to provide protection. From these studies it was evident that the mobility of gypsum or other extenders in the primer matrix during salt spray exposure played a role in the corrosion protection capability of the primer. In addition, Pr_2O_3 was the preferred starting Pr-phase for the best corrosion protection.

Electrochemical Characterization

Corrosion Response of Primer After Salt Spray Testing

Electrochemical tests were performed on Al 2024-T3 with CrCCs and primers formulated with 1) gypsum ($CaSO_4 \cdot 2H_2O$); 2) talc ($Mg_3Si_4O_{10}(OH)_2$); 3) Pr_2O_3; or 4) Pr_6O_{11} and standard 084 series primer solvent-based Pr-primer at various electrolyte pHs ranging from 5 to 8. For each test panel, the exposed substrate encompasses an area of ~2.0 mm^2 (Figure 116).

Figure 116. Representative artificial defect (~1.6 mm i.d.) machined into field areas of panels to provide a controlled test area.

The passivation range was calculated from the potential values in the region between E_{pit} and E_0 on the anodic sweep and calculated corrosion current (i_{corr})/corrosion potential (E_0) values were obtained by a Tafel fit. The electrochemical response of an artificial defect mechanically induced in primers formulated with different additives was studied at various electrolyte pHs to determine the effect of Pr-phase on the corrosion protection. Representative potentiodynamic

plots can be seen in Figure 117 and cumulative results are summarized in Figure 118. No increase in the passivation range for bare Al 2024-T3 or Al 2024-T3 with CrCCs with a change in electrolyte pH was observed in previous studies, indicating the passivation observed in the solvent-based Pr-primers was not due to self-passivation of the substrates or CrCCs alone, but rather inhibition by Pr-species from the primer.

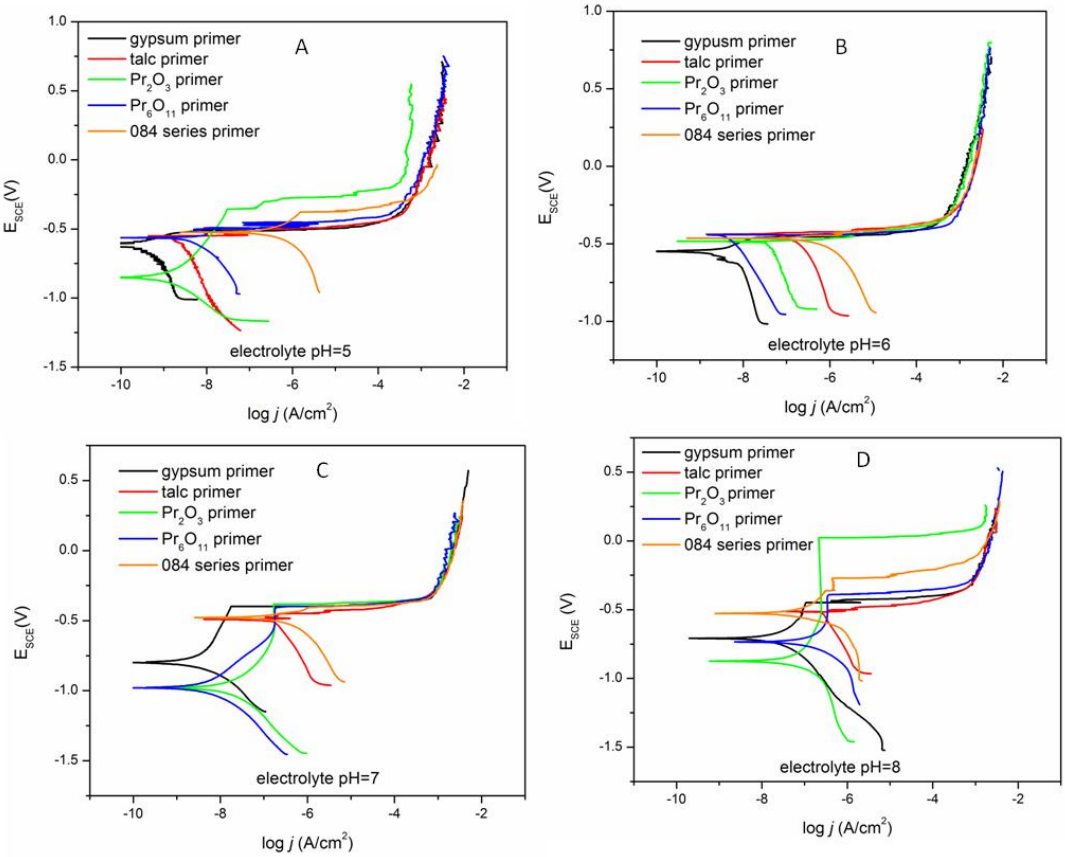

Figure 117. Representative potentiodynamic curves for Al 2024-T3 panels coated with CrCCs and primers formulated with (A) gypsum, (B) talc, (C) Pr_2O_3, (D) Pr_6O_{11}, and (E) 084 series. Primer coatings all had machined artificial defects (~1.6 mm i.d.) and were exposed to electrolytes with (A) pH=5, (B) pH=6,(C) pH=7, or (D) pH=8.

At a pH of 5 (Figure 117A) a passive region extending ~39 mV was observed on the anodic sweep for the primer formulated with Pr_2O_3. In contrast the primer formulated with Pr_6O_{11} had a passivation range only of ~5 mV, the gypsum primer had a passive region of ~10mV, and the 084 series primer ~10 mV. The primer formulated with talc exhibited little or no passivation. The E_{corr} values shifted towards more negative potentials at pH of 5 when either Pr_2O_3, Pr_6O_{11} or gypsum was used independently to formulate the primers, indicating corrosion reactions were suppressed in the presence of inhibitor species at this pH. The gypsum primer showed i_{corr} values on the order of 10^{-10} A/cm^2 and the 084 series primer had values on the order of 10^{-7} A/cm^2 at pH of 5. The i_{corr} values were on the order of 10^{-9} A/cm^2 for the Pr_2O_3, Pr_6O_{11}, and talc formulation

at pH of 5; however, i_{corr} values for the Pr_2O_3 primer (1.31 x 10^{-9} A/cm^2) were slightly lower than values obtained for the talc primer (3.55 x 10^{-9} A/cm^2).

At a pH of 6, no passive region was detected in the anodic sweep for any of the primers tested (Figure 117B). The E_{corr} value for the primers formulated with inhibitor present exhibited only a slight shift at this pH. The i_{corr} values obtained for the primers formulated with Pr_2O_3, gypsum, or Pr_6O_{11} (~10^{-8} to ~10^{-9} A/cm^2) were all at least an order of magnitude lower than values measured for the talc or 084 series primer (10^{-7} A/cm^2). It is not known why no passive region was measured.

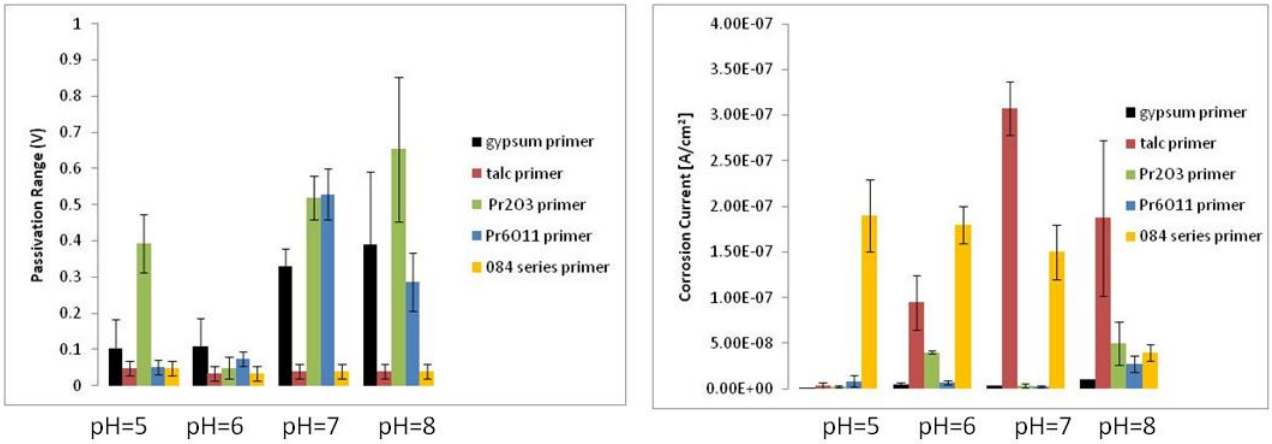

Figure 118. A summary of (A) passivation range results and (B) corrosion current values (i_{corr}) for each primer formulation at each electrolyte pH that was studied.

At a pH of 7, the primers formulated with Pr_2O_3, Pr_6O_{11}, and gypsum exhibited passive regions of ~40 mV or larger. In contrast, the 084 series primer showed a passive region extending ~5 mV. For comparison, the primer formulated with talc primer did not exhibit a passive response at this pH (Figure 117C). The E_{corr} values of the Pr_2O_3, Pr_6O_{11}, and gypsum primer both shift by ~50 mV compared to E_{corr} values of the talc or 084 series primer. The i_{corr} values obtained at pH of 7 for the primers formulated with Pr_2O_3, Pr_6O_{11}, and gypsum were on the order of 10^{-9} A/cm^2 which is two orders smaller than i_{corr} values determined for the primer formulated with talc or the 084 series primer.

The primer formulated with Pr_2O_3 exhibited the largest passivation range at a pH of 8 extending over ~65 mV, which was larger than any primer examined at any pH (Figure 117D). The primer formulated with Pr_6O_{11} also exhibited passive behavior at pH of 8, with a passive region extending ~30 mV as well as the gypsum primer which had a passive region extending ~40 mV. At pH of 8 the 084 series primer showed a passivation region extending ~20 mV, larger than at any other pH examined. In contrast, the primer formulated with talc did not exhibit a passive response. The E_{corr} values for the primers formulated with Pr_2O_3, Pr_6O_{11}, and gypsum shifted to more negative potentials by ~50 mV when compared to the primer formulated with talc or the 084 series primer at pH of 8. The calculated i_{corr} values for the primers formulated with Pr_2O_3, Pr_6O_{11}, gypsum, and the 084 series were an order of magnitude smaller (10^{-8} A/cm^2) compared to i_{corr} values obtained for the primer formulated with talc. Based on the electrochemical

measurements, the addition of PrO_x species and gypsum to the primer matrix inhibited the corrosion of Al 2024-T3 by increasing the passivation range, shifting E_{corr} values towards more negative potentials, and decreasing i_{corr} values. The magnitudes of the shifts depended on both the Pr phase present and the pH of the electrolyte. In contrast to the primers formulated with Pr-species or gypsum, the primer formulated with talc afforded no corrosion protection to exposed areas of Al 2024-T3 and this behavior was independent of the electrolyte pH. Electrochemical data indicates Pr_2O_3 and gypsum alone may provide a "rapid" response to defect exposed to a corrosive environment but together provide a "controlled" response. This synergetic process is supported by salt spray exposure results for the 084 primer series, which show that the 084 series is a more robust primer that provides superior corrosion protection for 3000 or more hours.

To further understand the role of gypsum as an inhibitor, cathodic sweeps (-0.42 V to 0.10 V) were performed on Pr_2O_3 and gypsum only primers in natural pH electrolyte (~pH 5-6) to determine the cathodic response of each. The cathodic slopes differed for the gypsum formulation compared to the Pr_2O_3 primer (Figure 119).

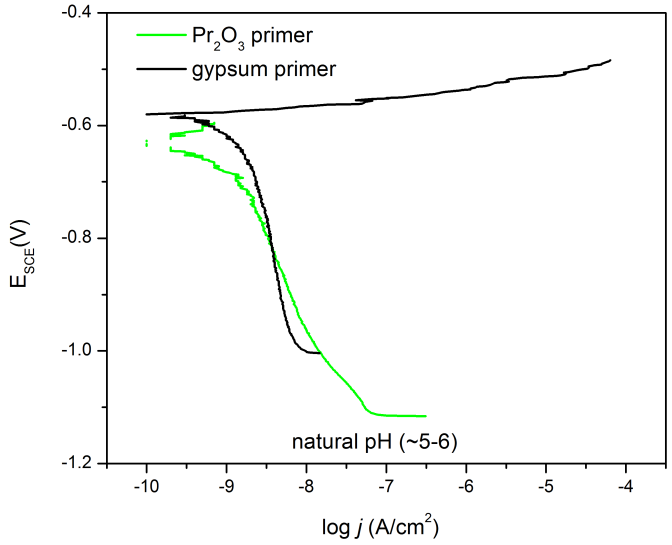

Figure 119. Representative cathodic sweeps for Al 2024-T3 panels coated with CrCCs and primers formulated with gypsum or Pr_2O_3 with machined artificial defects (~1.6 mm i.d.) exposed to electrolytes with natural pH.

The gypsum primer exhibited a passive region on the cathodic sweep whereas the Pr_2O_3 primer did not. It could be inferred that gypsum offered cathodic protection capabilities whereas Pr_2O_3 provided anodic protection.

Visible corrosion was minimized for exposed areas of the substrate by coatings that exhibited a larger passivation range in electrochemical measurements. The least amount of corrosion was observed after testing at pH of 5 for the primer formulated with Pr_2O_3, which also had a large passivation range of ~40 mV (Figure 120).

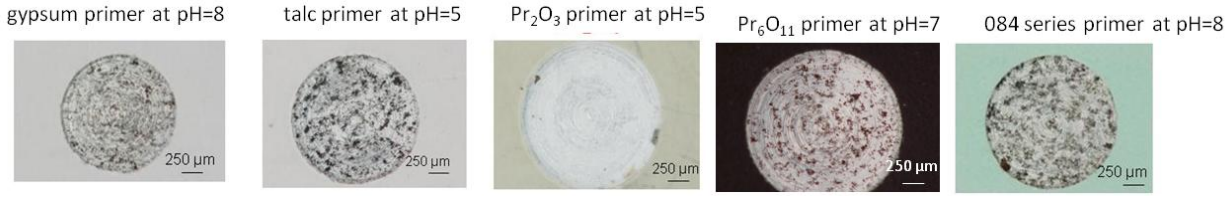

Figure 120. Micrographs of the exposed areas of substrates that were coated with primers formulated with gypsum following electrochemical testing in an electrolyte pH of 8, talc following electrochemical testing at pH of 5, Pr_2O_3 following electrochemical testing in an electrolyte pH of 5, Pr_6O_{11} following electrochemical testing in an electrolyte pH of 7, and (C) 084 series primer following electrochemical testing in an electrolyte pH of 8.

The least corrosion was observed after testing at pH of 7 where one of the larger passivation ranges (~50 mV) was measured for primers formulated with Pr_6O_{11} (Figure 120). Exposed areas of the gypsum and 084 series primer both showed less visible corrosion product at pH of 8 than the other primers, which also corresponded with their large passivation ranges (~40 mV for gypsum and ~20 mV for the 084 series primer) shown in Figure 120. For the primer formulated with talc, significant corrosion was observed in exposed areas of Al 2024-T3 at all electrolyte pH values (Figure 120). The electrochemical results and corroded specimens that were observed for the primers formulated with Pr_2O_3, Pr_6O_{11}, gypsum, and talc indicated that Pr_2O_3 alone provided the best corrosion protection. Results also indicated that gypsum can act as a corrosion inhibitor when introduced into the primer matrix. XRD and SEM-EDS characterization showed that Pr_2O_3 was more soluble than Pr_6O_{11}, which led to enhanced corrosion protection when Pr_2O_3 was incorporated into the primer matrix. In addition, the "rapid" corrosion response of Pr_2O_3 species in the 084 series primer is inhibited by the addition of gypsum. The nature of the relationship between pH and passivation is still unclear but the evidence presented indicated that primers formulated with PrO_x species protected exposed areas of aluminum alloy substrates from corrosion environments by means of dissolution and re-precipitation and that pH affects the corrosion response. Species solubility within the primer matrix is the primary factor in the ability of inhibitors to transport and react effectively.

Microelectrochemical Test Development

Preliminary potentiodynamic and impedance tests were performed using a micro-scale electrochemical test cell that is under development. Studies were conducted on polished Al 7075-T6 panels using capillaries with diameters of less than 100µm. The electrolyte used was water containing 0.35 wt% NaCl and 0.70 wt% $(NH_4)_2SO_4$. The electrode apparatus and the capillary are shown in Figure 121. A polarization curve produced with the new cell is compared to one collected using a conventional test cell in Figure 122.

When fully developed, the microelectrochemical test tool will allow the team to extract electrochemical information from specific areas of substrates and coated test panels. Optimization of the test cell is still in progress, including design of the test cell to offset the surface tension of the capillary to assure the area affected by the test cell is not compromised by electrolyte leaking from the electrode.

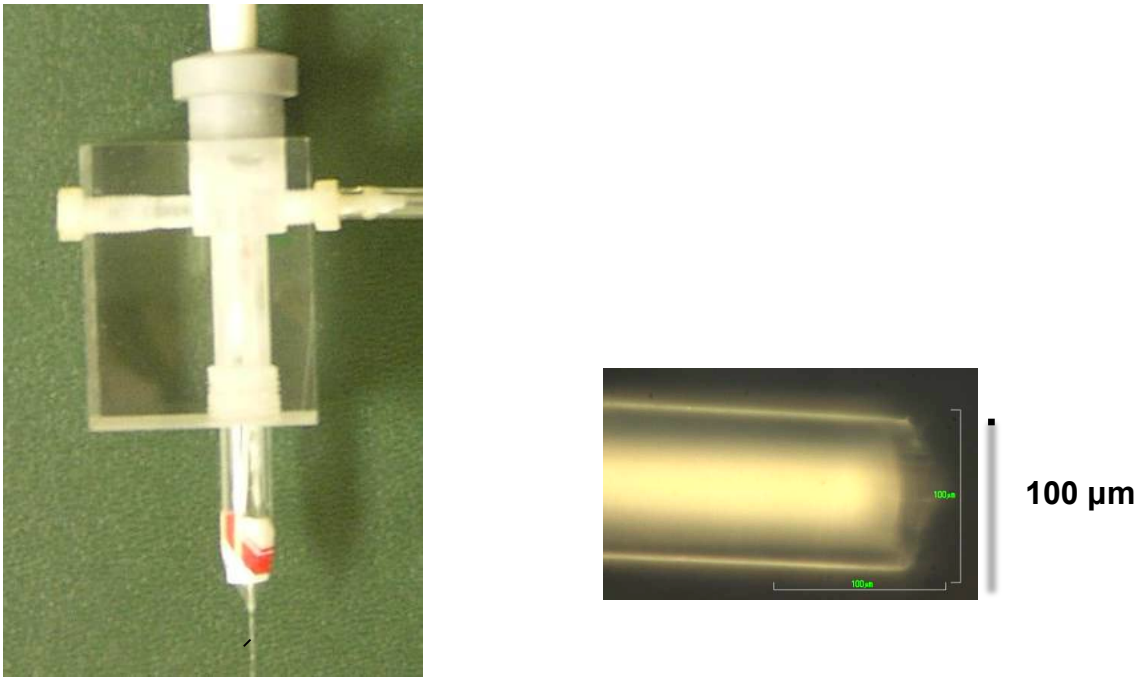

Figure 121. Capillary tube and pressure controlling cell that were constructed to conduct microelectrochemical testing. The outside diameter of the capillary tube is approximately 100 µm.

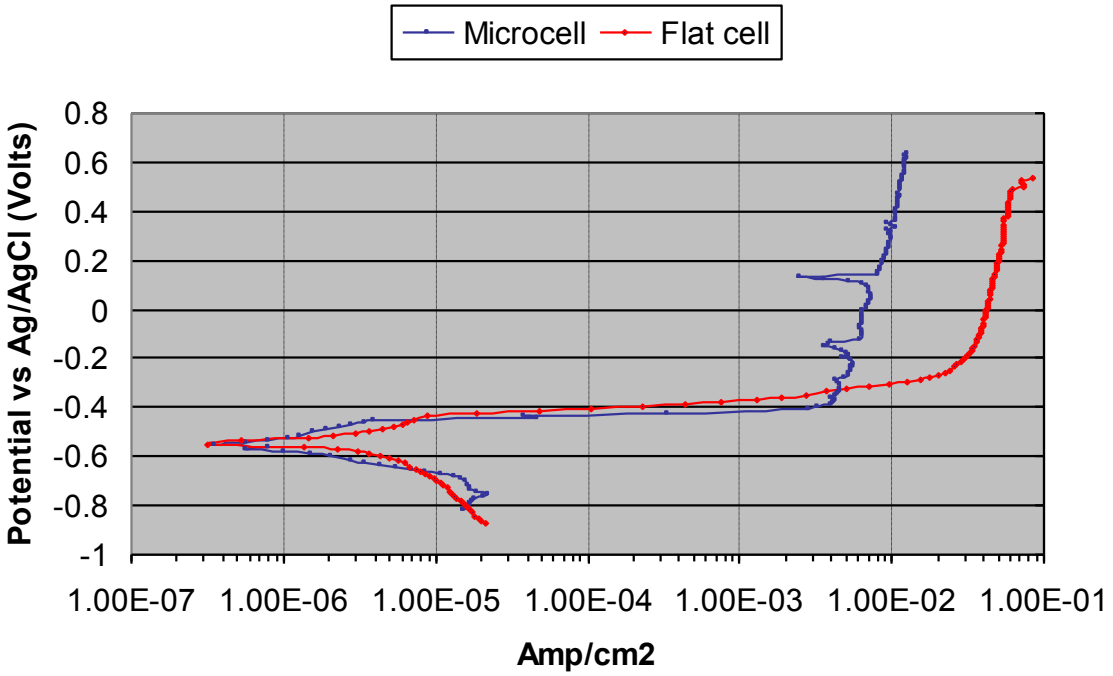

Figure 122. Comparison of polarization tests conducted using a standard commercial test cell (labeled "Flat cell") compared to the micro-electrochemical cell. The electrolyte was water containing 0.35 wt% NaCl and 0.7 wt% $(NH_4)_2SO_4$. An Ag/AgCl reference electrode was employed for all tests.

In addition to the development of a new electrochemical tool, electrochemical testing was conducted using precisely machined circular holes, which are referred to as "drilled pits." These surfaces provided a more controlled environment for characterization than typical machine scribes. Electrochemical test were performed on water-based primers with artificial pits, at various electrolyte pHs ranging from 5 to 8. Representative data can be seen in Figure 123. The polarization curves indicate that the passivation region increased with increasing pH, up to a pH of at least 8. At an electrolyte pH of 8, the passivation region extended for over 0.5 volts. Electrochemical tests were performed on acid etched, bare Al 2024-T3 panels, with artificial pits as a control experimental to determine if the increased passivation with increasing electrolyte pH was due to self-passivation of the bare aluminum alloy surface (Figure 123). The polarization curves for the control specimen (i.e., bare Al 2024-T3) showed very little passivation and no significant changes with pH, indicating the passivation observed in the primers is not due to self-passivation of the substrates, but activity from the primer. Results will be further analyzed to identify mechanisms responsible for corrosion protection of primer-coated substrates as well as inherent electrochemical properties of the initial coatings.

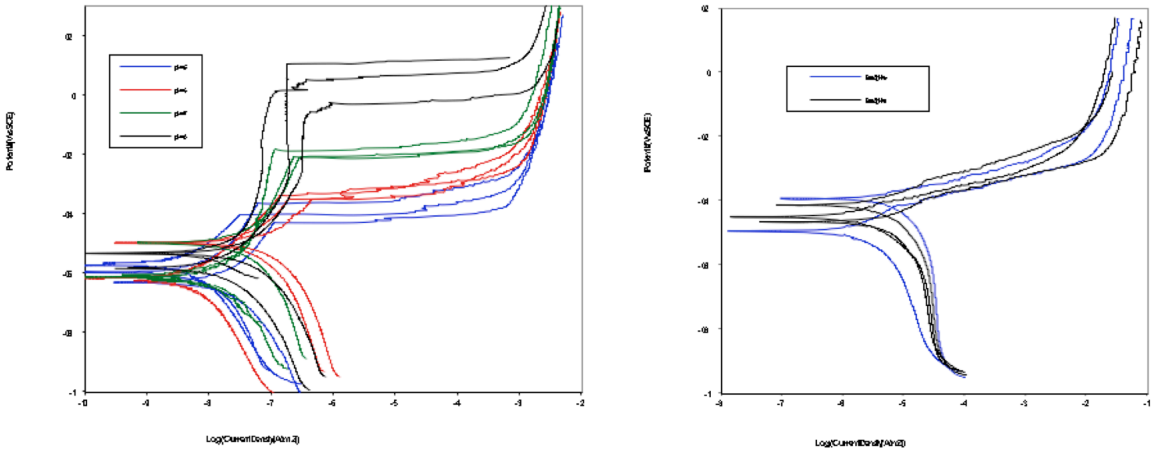

(A) (B)

Figure 123. Polarization curves for water based Pr primer with artificial pits conducted at various electrolyte pH values ranging from 5 to 8 (A). Polarization curves of acid etched, bare Al 2024 with drill pits at various electrolyte pH (B).

Microelectrochemical Testing

The corrosion resistance of cerium-based conversion coatings was evaluated using a ~50 µm diameter capillary probe. Different areas of coatings were probed to understand the effect of surface morphology on localized corrosion behavior. Three distinct regions of the coatings, active, passive, and intermediate, were detected using microelectrochemical testing on CeCCs on 7075-T6 (Figure 124). Active regions had an i_{corr} that was greater than 1×10^{-4} Amps/cm^2 and a total impedance of less than 200 Ω•cm^2. Passive regions had an i_{corr} that was less than 1×10^{-5} Amps/cm^2 and total impedance that was greater than 10 KΩ•cm^2. Finally, intermediate regions had i_{corr} and total impedance values that were between those of the active and passive regions. Twelve tests were conducted and all results fell within these ranges.

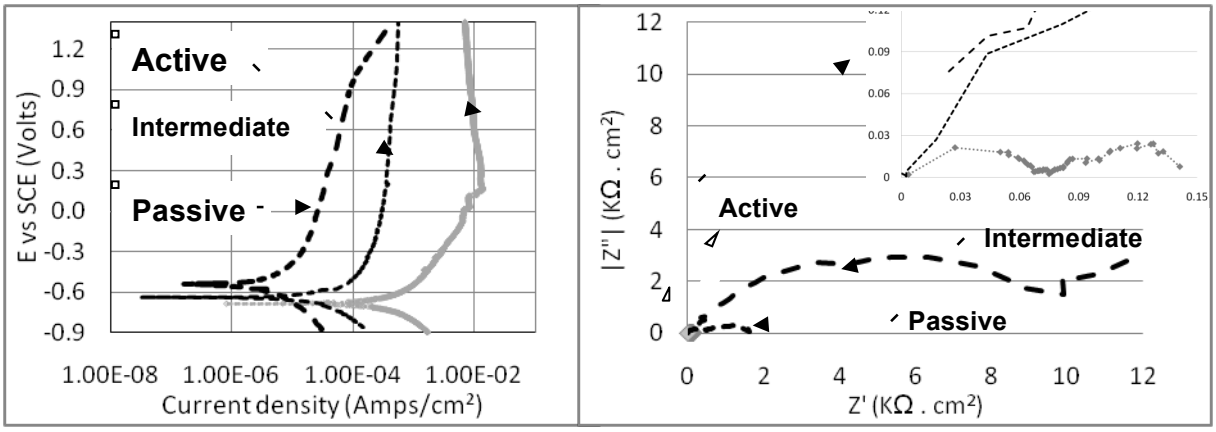

(a) (b)

Figure 124. Microelectrochemical (a) Potentiodynamic scan and (b) EIS curves showing that CeCCs on 7075-T6 had distinct active, intermediate, and passive regions.

Figure 125 is a compilation of potentiodynamic scans and EIS data from active regions of a CeCCs on 7075-T6. The figure demonstrates active regions had a mixed potential ranging from -0.63 V to -0.78 V vs. SCE. Most had a low anodic pitting potential (< -0.40 V vs. SCE). In some cases, such as the one shown by the curve labeled 2 in Figure 125, extensive corrosion caused the sample to passivate at ~ -0.15 V vs. SCE, which, in turn, caused the current density to decrease during testing. The total impedance for active regions of CeCCs on 7075-T6 (Figure 125b) was lower than 200 Ω•cm^2 and as low as 20 Ω•cm^2. The tests indicated that active regions provide very little corrosion resistance and can easily form pits. Optical micrographs of active region of CeCCs before and after testing are shown in Figure 126.

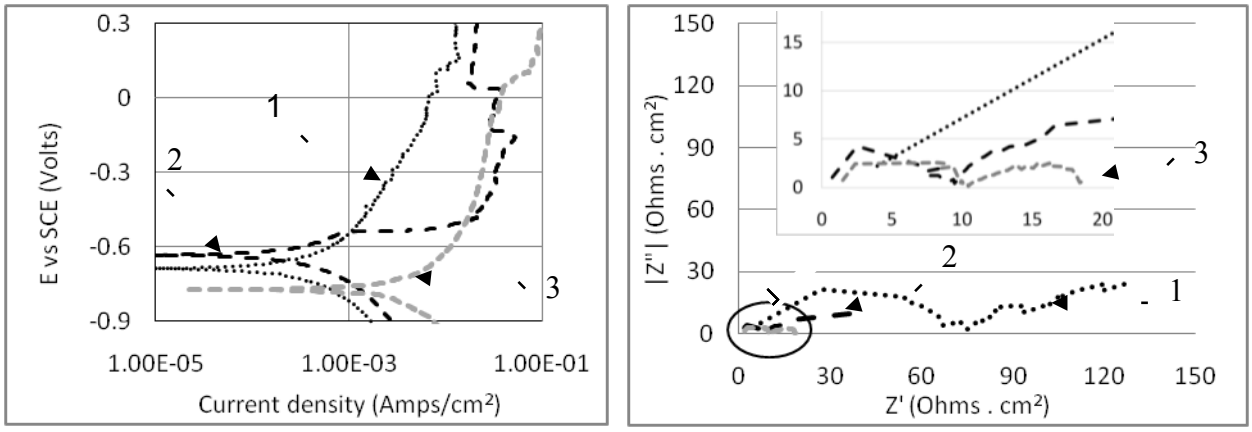

Figure 125. (a) Potentiodynamic scans and (b) EIS curves from an active area of a CeCC on Al 7075-T6 showing the variation in behavior among various regions.

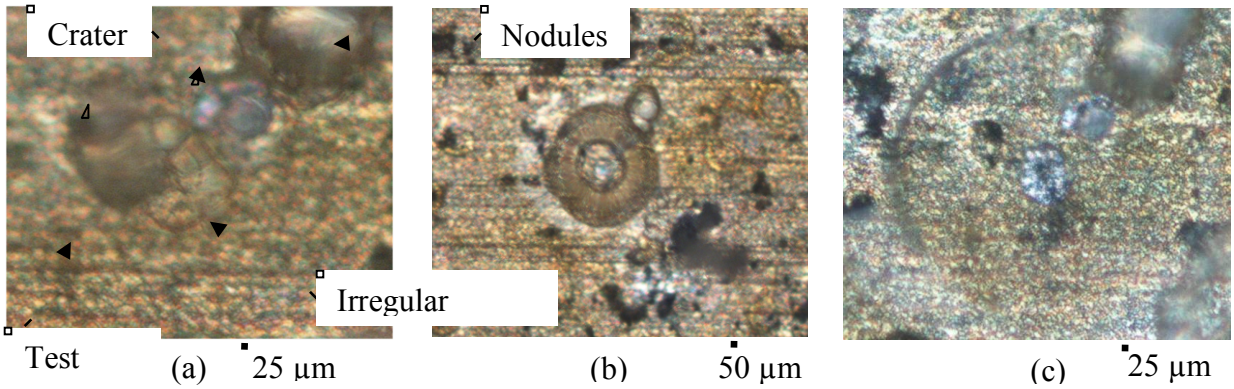

Figure 126. Optical micrographs of test areas on CeCCs on 7075-T6: (a) before testing, (b) immediately after testing, and c) after rinsing tested area with DI water.

The electrochemical data for the specific area shown in Figure 126a are labeled 1 in Figure 125. The test area included a small crater-like surface feature and irregular surfaces with dark lines running across it as seen by optical microscopy (Figure 126a). What appears to be a nodule is visible on the upper right of the crater. Electrochemical testing was also performed on similar looking nodules, which demonstrated passive behavior as will be discussed below. Figure 126b shows that only the region inside the capillary was affected while the surrounding coating was not altered by testing. Testing showed that coatings with irregular surfaces and craters provided little corrosion resistance. Post-test micrographs showed that crater-like objects remained relatively intact; however, irregular surfaces were damaged and removed. This suggests that pre-existing defects in coatings such as irregular surfaces and craters can be electrochemically active and, therefore, susceptible to corrosion. Images of another active region on a CeCC on 7075-T6 are shown in Figure 127. The electrochemical data for this test are shown by the curves labeled 3 in Figure 125. The measured OCP was low (-0.77 V vs. SCE) indicating this site was very active. Point EDS elemental analyses on the dark (corroded) spot shown by the cross in Figure 127c are listed in Table 22. EDS showed an elevated copper content (6.6 wt%) compared to other areas that did not corrode, which had copper contents of less than 0.5 wt%. The SEM/EDS analysis suggested that a copper based IMC may have been present beneath the coating at the spot that corroded, which led to the high i_{corr} and low total impedance in this area. After testing, the full extent of damage was seen in Figure 127b and Figure 127c. The high copper content found by EDS shown in Table 22 suggests that these types of sites may be the primary location for galvanic corrosion, which is consistent with the formation of microgalvanic corrosion couples.

Table 22. Chemical composition of corroded area obtained by EDS

Element	O	Al	Zn	Mg	Cu	Ce
Weight %	42.5	43.6	2.5	1.9	6.6	2.9
Atomic %	59.0	35.9	0.9	1.3	2.3	0.7

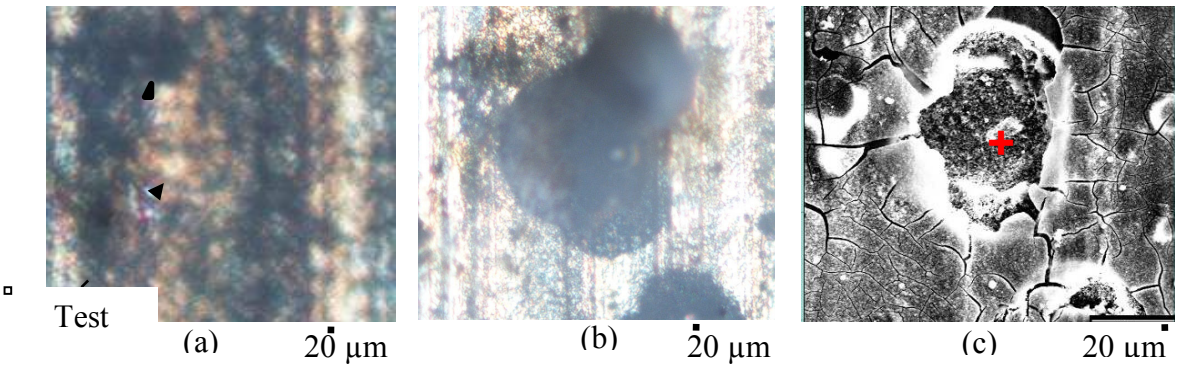

Figure 127. Images of test area of CeCCs on Al 7075-T6: (a) before testing, (b) after testing, and (c) a SEM image of affected area.

Optical micrographs of areas that exhibited passive behavior during microeletrochemical testing are shown in Figure 128. The first test (Figure 128a and b) was performed on what appeared to be nodules in the coatings. Similar nodules were also observed near an active spot (Figure 123). The nodule was near a possible active region because bubbles were observed about 75 µm above the tested area shown in Figure 128a. The second test (Figure 128c and d) was performed near a dark spot on a coating in an area that did not have any cracks, craters, or other obvious damage. Because the area was found to be electrochemically passive, little, if any, corrosion damage was visible making it difficult to find the affected area after the experiment. After the test, few, if any bubbles were observed to evolve from passive test regions. For passive regions, both potentiodynamic scans and EIS had results that were consistent from run to run (Figure 129). One of the curves did not display a clearly defined anodic pitting potential, while the other displayed a defined pitting potential at two places followed by repassivation. Both of the passive regions that were studied had OCP values of around -0.60 V vs. SCE. The EIS data in Figure 129 showed that both also had total impedance values that were greater than 10 KΩ•cm^2. Based on these studies, passive regions provide very good corrosion resistance and were not likely to corrode during electrochemical testing.

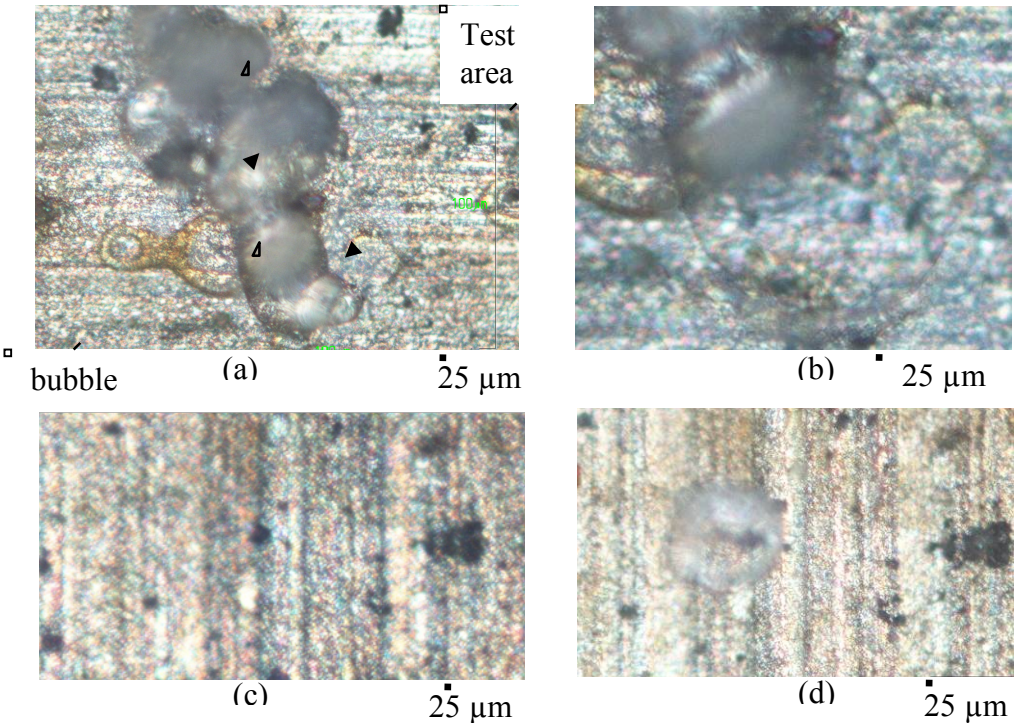

Figure 128. Optical micrographs of two passive regions on CeCCs on 7075-T6: (a) Exp 1 before testing, (b) Exp1 after testing, (c) Exp 2 before testing, and (d) Exp 2 after testing.

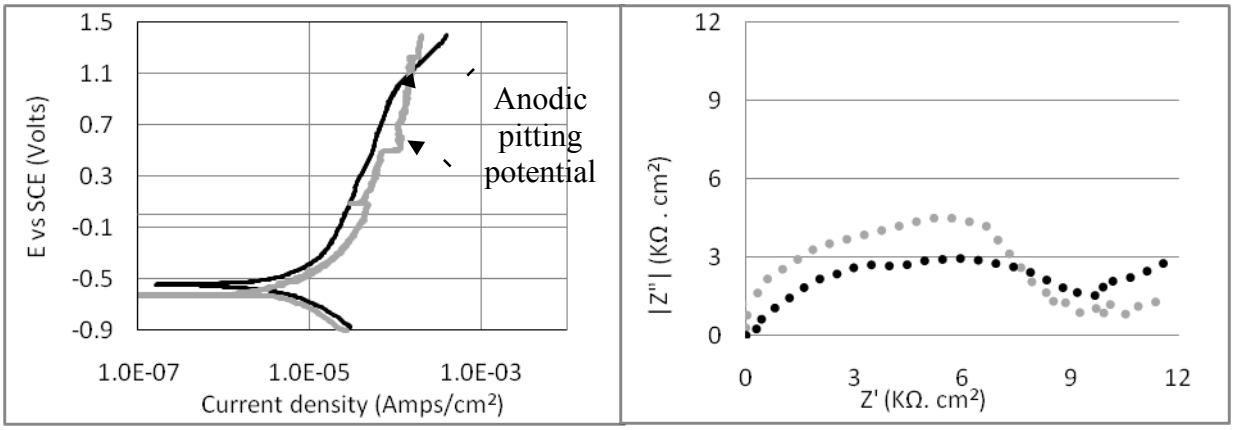

Figure 129. (a) Potentiodynamic scans and (b) EIS curves from a passive area of a CeCC on Al 7075-T6 showing similar behavior between two different regions.

Representative electrochemical test results for the intermediate regions on CeCCs on Al 7075-T6 are shown in Figure 130. Total impedance values ranged from 1 KΩ•cm^2 to 3 KΩ•cm^2 with OCP values between -0.50 V to -0.77 V vs. SCE (Figure 130). Post test analysis showed the physical structure of the tested regions had not changed noticeably, including the region with the lowest OCP (-0.77 V vs. SCE) and lowest impedance (~1 KΩ•cm^2) and the effects of the

microelectrochemical testing were similar to that of the passive region test shown in Figure 128c and d. Figure 131 shows optical micrographs before and after microelectrochemical testing of a thinly coated area, as evidenced by the bare aluminum alloy that was visible. The electrochemical data for this region are shown by the curves labeled 1 in Figure 130. The total impedance was ~2.7 KΩ•cm^2 and the potentiodynamic curve showed that the anodic pitting potential was high (0.90 V vs. SCE). The electrochemical test results indicated that thinly coated sites may not necessarily become active during corrosion. The total impedance of intermediate regions was lower than passive regions, but the corrosion resistance was sufficient to prevent observable differences in the morphology of the test area during analysis. In addition, the areas had high anodic pitting potentials (0.90 V vs. SCE). Based on the results, sites with the lowest OCP (-0.77 V vs. SCE) and lowest total impedance (1.2 KΩ•cm^2) have the potential to become active during corrosion testing.

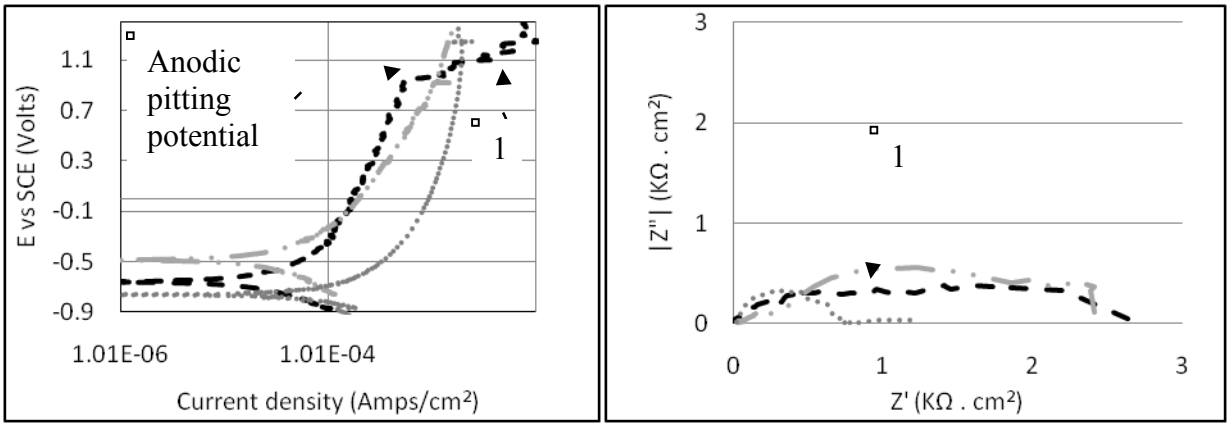

(a) (b)

Figure 130. (a) Potentiodynamic scans and (b) EIS curves from intermediate areas of a CeCC on Al 7075-T6 showing a range of OCP and total impedance values.

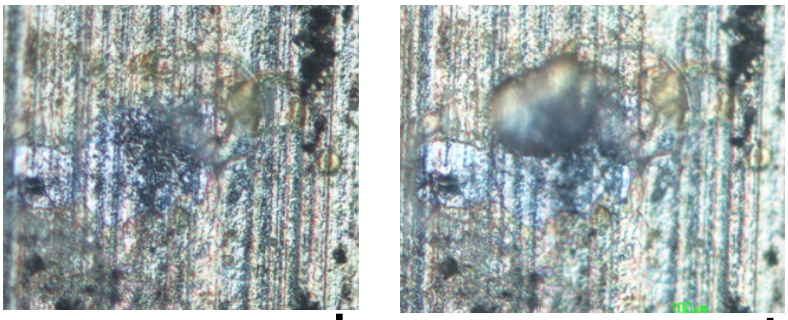

Figure 131. Optical micrographs of an intermediate region on a CeCC on 7075-T6: (a) before testing and (b) after testing.

Performance Evaluation

Initial Non-Chromate Primer Evaluation

Traditional ASTM B117 salt spray evaluation (2 weeks for conversion coatings, 3000 hours for primers) was employed. A series of non-chromate specimens were deposited on CrCCs by Deft for characterization. Multiple duplicate specimens were prepared so that specimens for characterization could be removed from salt spray at regular intervals to evaluate incremental changes. At this point, panels have been evaluated before salt spray and after 500, 1000, and 1500 hours of salt spray testing. The scribes in the water-based primers on Al 2024-T3 remained partially shiny with some darkened areas through 1000 hours of salt spray testing. At longer times, some limited salting was observed in the scribes. The scribes on the solvent-based samples began to turn dark and started to salt after 500 hour in salt spray testing. Figure 132 shows the panels of each type of primer after each time increment and Figure 133 are representative magnified images of selected shiny and darkened/salted scribe areas. By the end of 3000 hours the scribes of both coatings had darkened areas, salted areas, and pits and tailing around the scribe as shown in Figure 134.

Water-based primer 500 hours

Solvent-based primer 500 hours

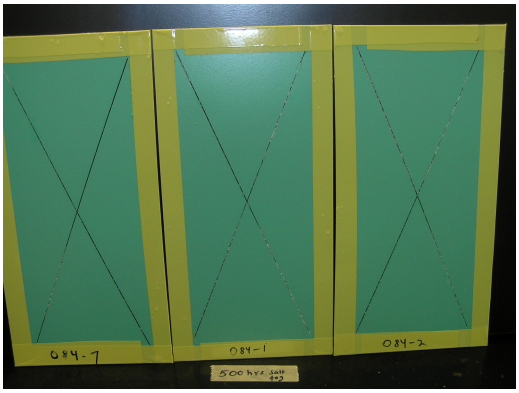

Water-based primer 1000 hours

Solvent-based primer 1000 hours

Water-based primer 1500 hours

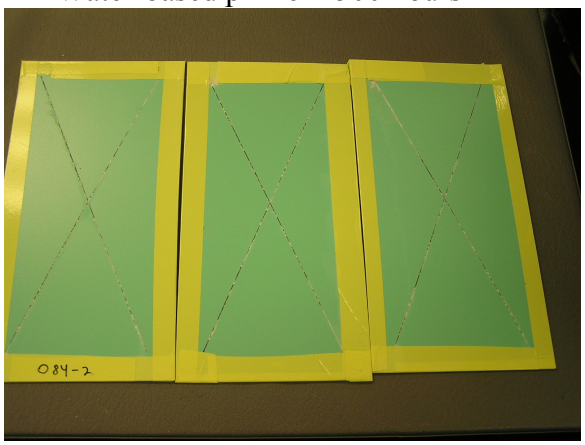

Solvent-based primer 1500 hours

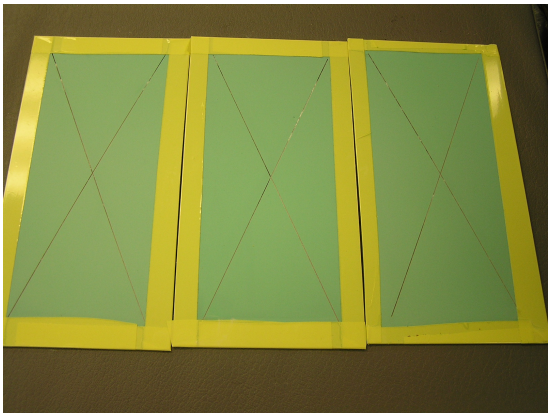

Figure 132. Water-based and solvent-based primers on CrCCs on Al 2024-T3 panels after various intervals of salt spray evaluation.

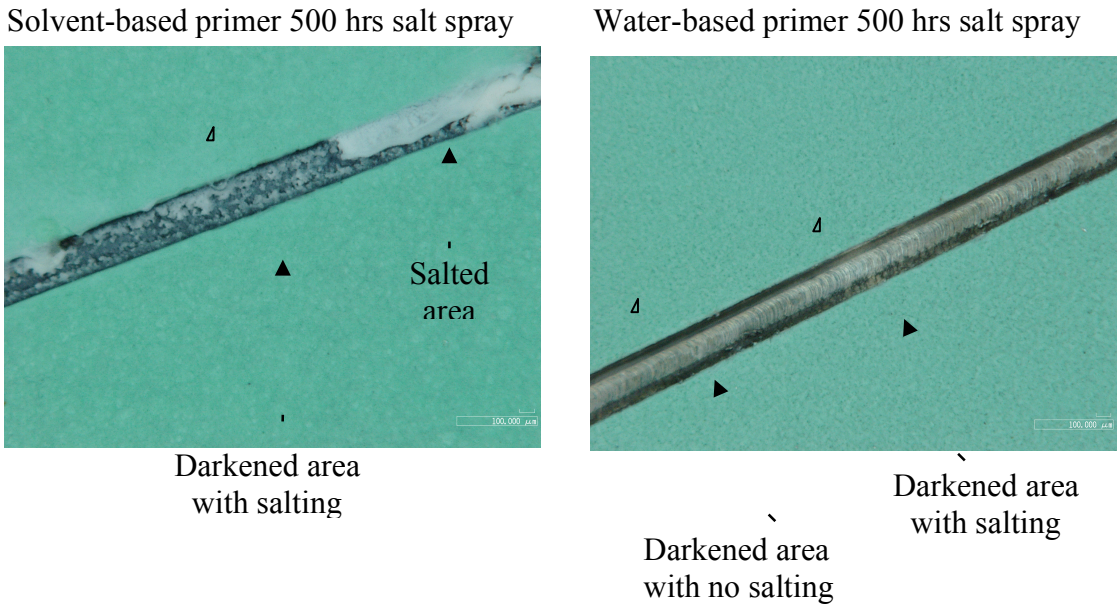

Figure 133. Magnified images of selected scribes on primer coated Al 2024-T3 test panels following salt spray testing.

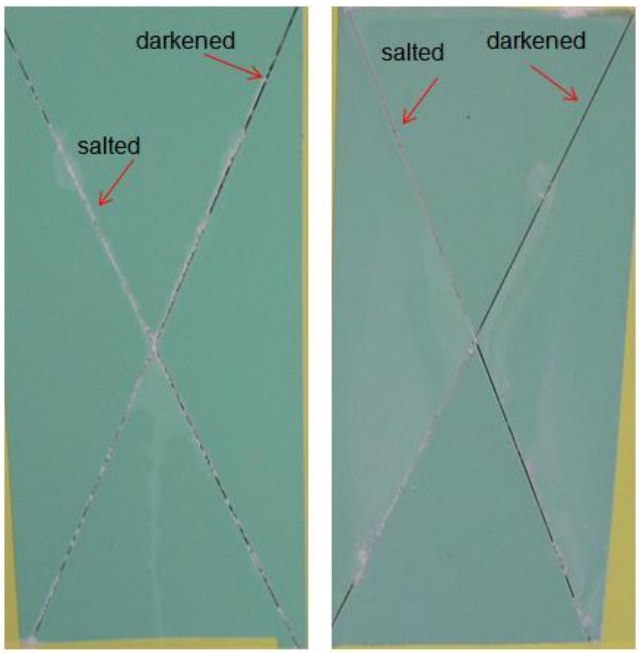

(a) (b)

Figure 134. Representative (a) solvent-based and (b) water-based primers on Al 2024-T3 after 3000 hours of salt spray evaluation.

Evaluations of Pr-Based Inhibitors on Other Pretreatments

Aluminum alloy Al 2024-T3 panels with one of four conversion coatings were coated with Deft series 084 primer, which incorporates a praseodymium-based inhibitor package and has been

qualified for military use per MIL-PRF-23377J, Type I, Class N. The conversion coatings were: 1) conventional chromate based conversion coatings (CrCC); 2) trivalent chromium passivation (TCP) coatings; 3) electrolytically deposited cerium based coatings (EDCeCC); and 4) spray deposited cerium based coatings (SPCeCC). After application of the primer, the panels were then scribed to produce two scribe lines ~0.4mm wide, crossing in the center of the panels. Next, the back (non-painted) sides of the panels, the edges, and ~5mm of the front were covered with non-conducting tape to limit salt spray exposure to only the coated area. The prepared panels were labeled and exposed to salt spray for the times summarized in Table 23. After the specified salt spray exposure panels were rinsed with deionized water to remove salt and dried using compressed nitrogen. The panels were then scanned to provide a permanent image of the panel prior to subsequent testing.

Table 23. Panel labeling designations and salt spray exposure times for alternate pretreatment study

Panel Label	Salt Spray Exposure Time (hrs)
CrCC-084-0, TCP-084-0, EDCeCC-084-0, SPCeCC-084-0	0 (No exposure)
CrCC-084-1, TCP-084-1, EDCeCC-084-1, SPCeCC-084-1	150
CrCC-084-2, TCP-084-2, EDCeCC-084-2, SPCeCC-084-2	300
CrCC-084-3, TCP-084-3, EDCeCC-084-3, SPCeCC-084-3	500
CrCC-084-4, TCP-084-4, EDCeCC-084-4, SPCeCC-084-4	1000
CrCC-084-5, TCP-084-5, EDCeCC-084-5, SPCeCC-084-5	1500
CrCC-084-6, TCP-084-6, EDCeCC-084-6, SPCeCC-084-6	2000
CrCC-084-7, TCP-084-7, EDCeCC-084-7, SPCeCC-084-7	2500
CrCC-084-8, TCP-084-8, EDCeCC-084-8, SPCeCC-084-8	3000

Electrochemical testing was performed on all of the panels listed in Table 23 after introducing an artificial defect through the coatings down to bare metal. A schematic of the setup is shown in Figure 135. A Sherline Model 5400 CNC was used to drill holes ~1.6mm diameter and 50 μm (2 mil) into the panels to simulate a pitting type defect. Each drilled pit was exposed in a 1-cm^2 area flat cell for electrochemical testing. Test sequencing was controlled by CorrWare software in three stages: 1) 1000sec open circuit potential (OCP) stabilization; 2) Electrochemical impedance spectroscopy (EIS) from 0.01-100,000Hz with an AC amplitude of 10 mV; and 3) Cyclic potentiodynamic spectroscopy (CPDS) in the range of -0.3V to +0.8V and reversing to -0.35V, with respect to OCP. The reference electrode in each case was a saturated calomel electrode (SCE). The equipment used was a Princeton Applied Research 273A Potentiostat/Galvanostat coupled with a Solartron SI1255 HF Frequency Response Analyzer. The electrolyte typically used was comprised of 0.35 wt% NaCl and 0.7 wt% $(NH_4)_2SO_4$ in 18 MΩ deionized water.

Panels were tested at the natural pH of the electrolyte, which was ~5.6. The pH of the electrolyte was also varied by adding either sulfuric acid or sodium hydroxide to produce solutions with pH

values of 4, 5, 6, 8, or 10. Panels were also tested at these pH values to compare the performance.
In the final set of experiments OCP & EIS were performed without drilled pits on both 0hr panels and those that had been exposed to salt spray for 3000 hrs. Cyclic potentiodynamic measurements were also performed on the 3000hr panels to investigate electrochemical response of the films after salt spray exposure.

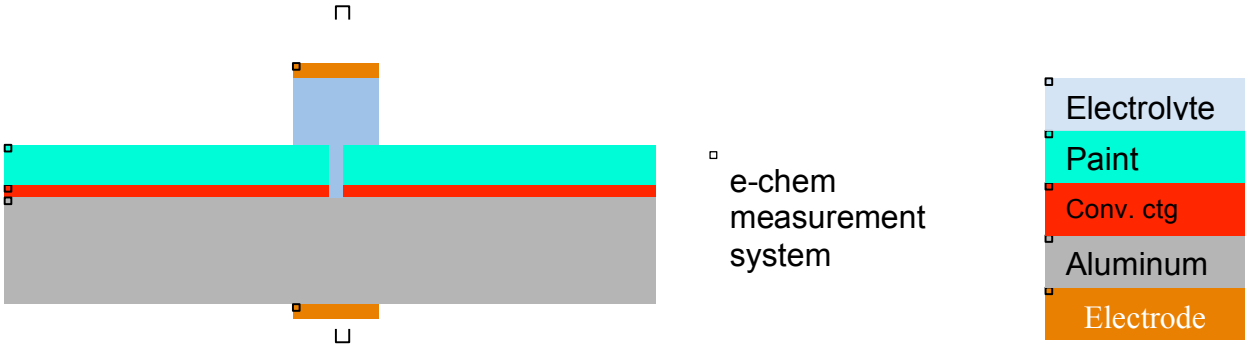

Figure 135. Electrochemical measurement setup for testing with drilled pits.

Panels were cut to produce test specimens that were ~1 cm^2 in area with no scribe lines or other visible film defects. XRD patterns were obtained using a PANalytical X'Pert Multipurpose Diffractometer utilizing Cu K-α radiation (λ = 0.15418 nm) and a PIXcel detector. Phases were identified and quantified utilizing PANalytical X'Pert High Score software (version 2.2e). Panels were cut to produce test specimens that were ~1 cm^2 in area with a scribe line present. Images and EDS were obtained using a Hitachi S570 LaB_6 SEM and analyzed using Revolution software. Panels that had been exposed to salt spray for 0 hr or 3000 hr panels were cut to ~1 cm^2 in area with a scribe line present. Areas were selectively milled away using a Helios Nanolab 600 Focused ion beam (FIB) system to expose cross-sections of the paint coatings to determine the change in porosity of the coating after exposure to salt spray.

Images of the panels after salt spray testing are shown in Figure 136-Figure 143 and are summarized in Table 24. Examination of the panels showed that the only conversion coating-primer combination that was able to provide long term corrosion protection during salt spray testing was the GN084 primer deposited on panels with CrCCs. Both electrodeposited and spray CeCCs showed significant salting in the scribe at 150 hrs. The salting appeared to increase with time, and with blistering of the paint film on the panels apparent after 150 hours for the primer on the EDCeCC and 500 hours for the primer on the SPCeCC. The primers deposited on TCP showed considerably less corrosion protection than primers on CrCCs, but more than primers on either type of CeCC.

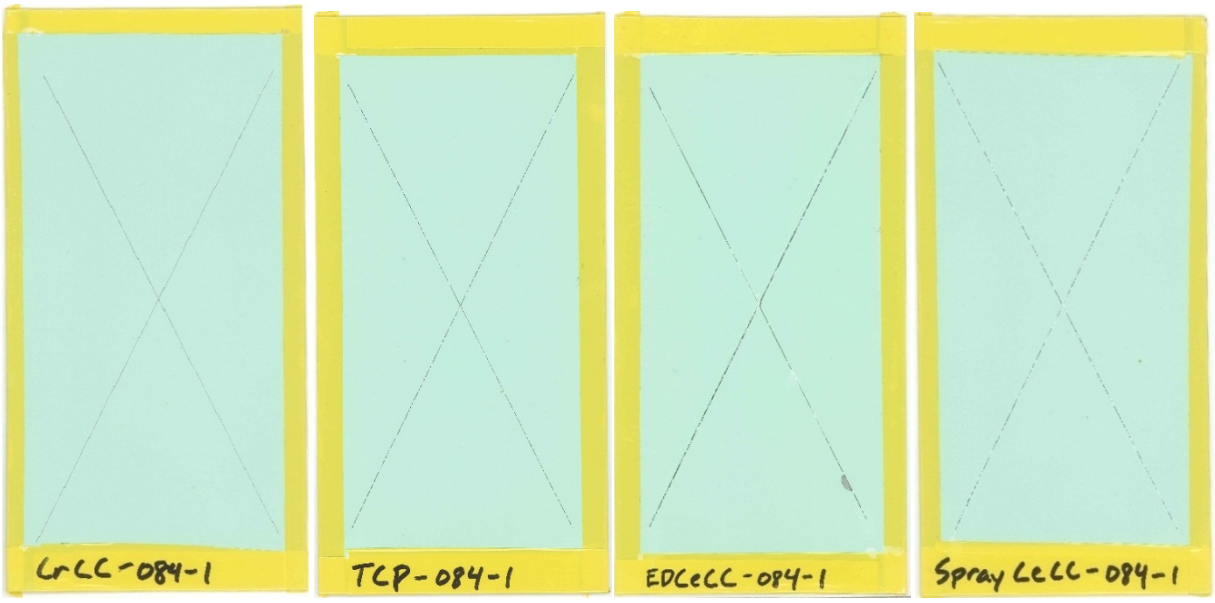

Figure 136. Primer coated panels after 150 hrs of salt spray exposure.

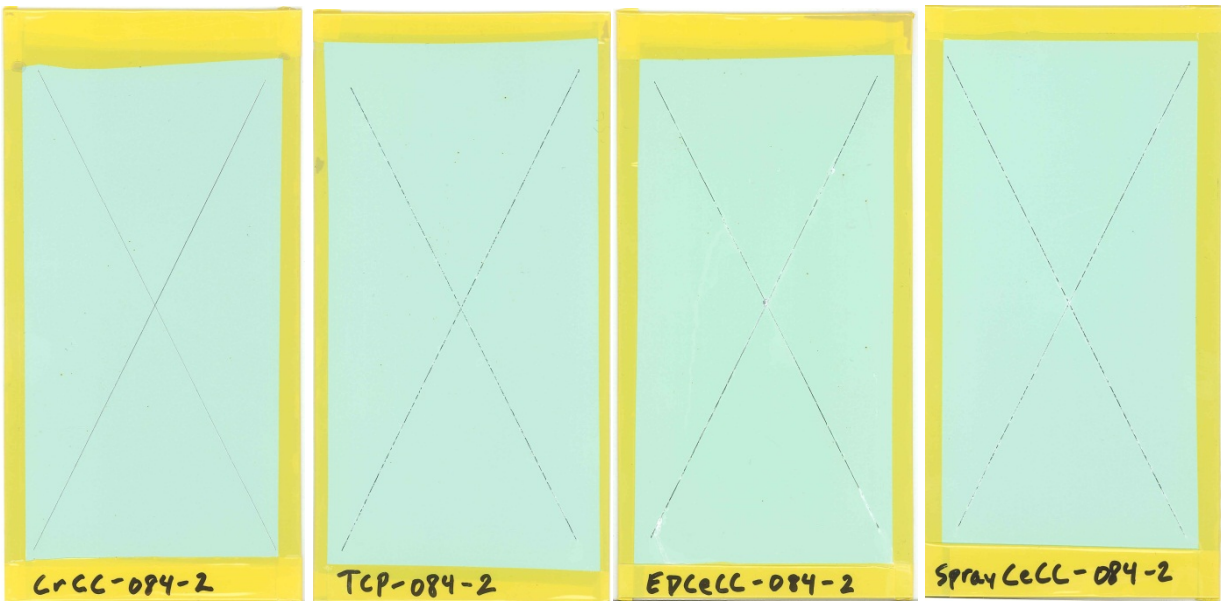

Figure 137. Primer coated panels after 300 hrs of salt spray exposure.

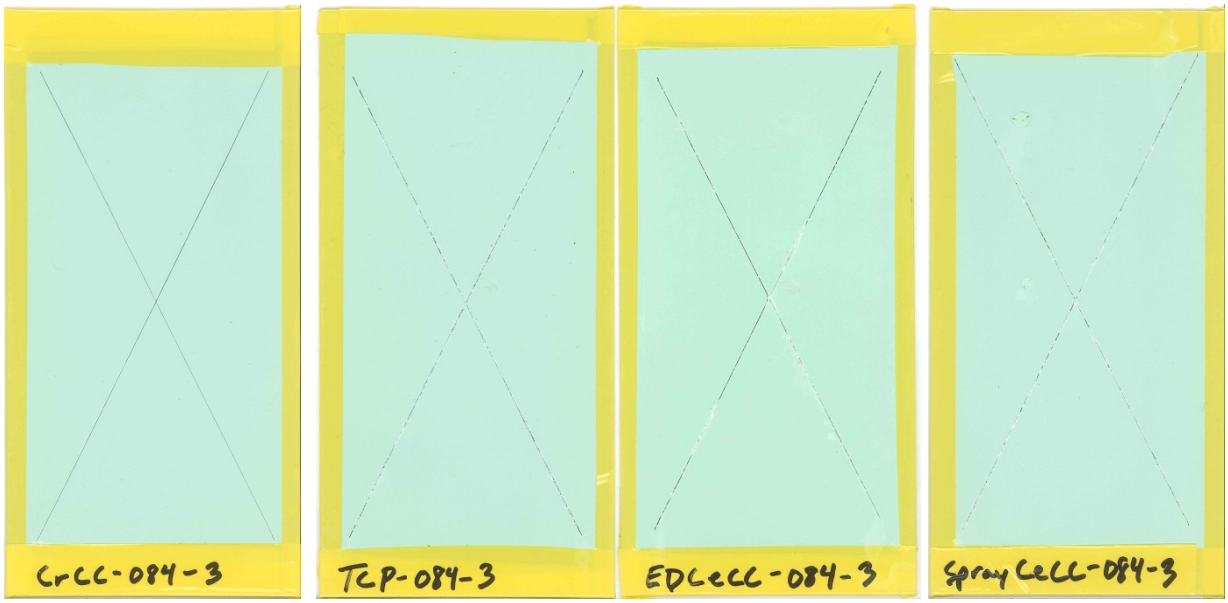

Figure 138. Primer coated panels after 500 hrs of salt spray exposure.

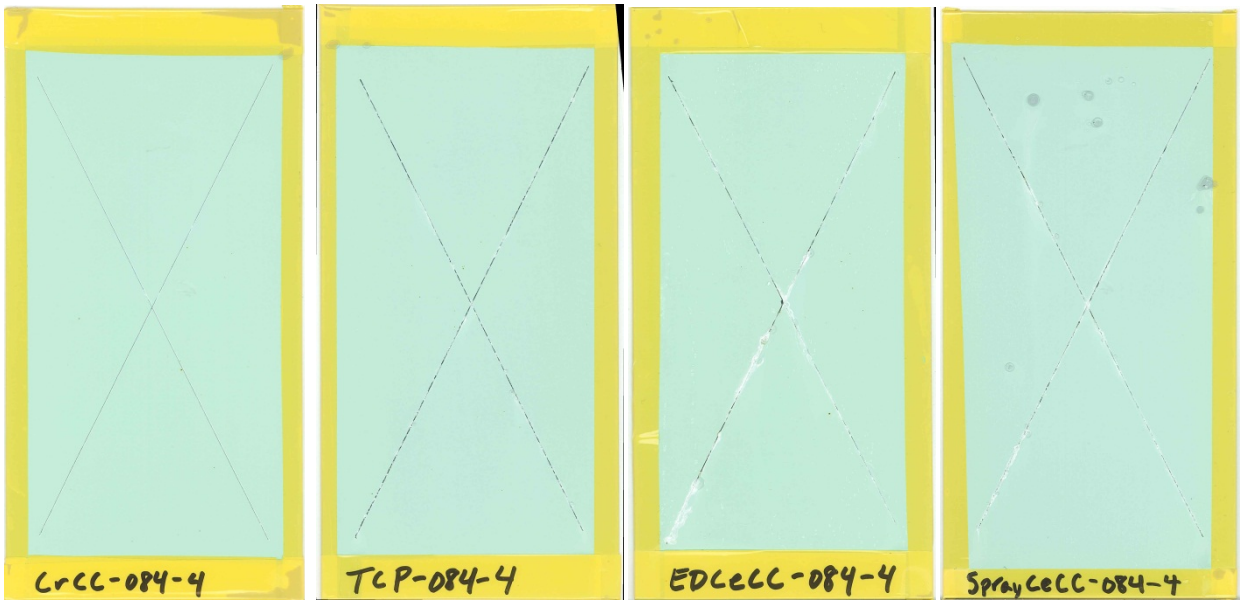

Figure 139. Primer coated panels after 1000 hrs of salt spray exposure.

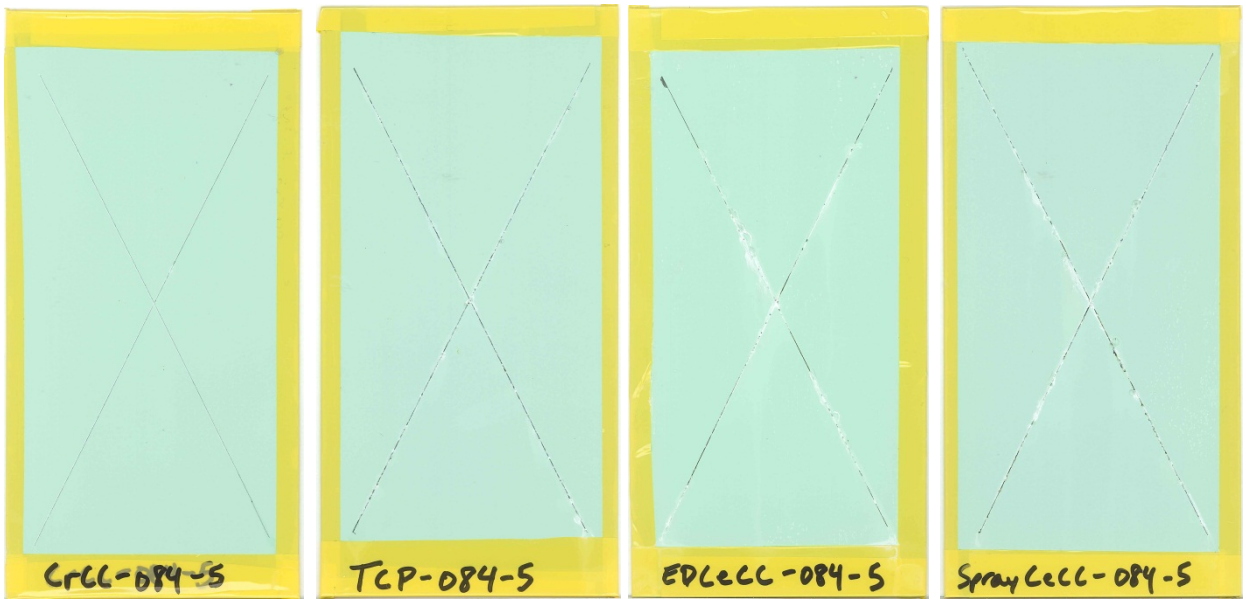

Figure 140. Primer coated panels after 1500 hrs of salt spray exposure.

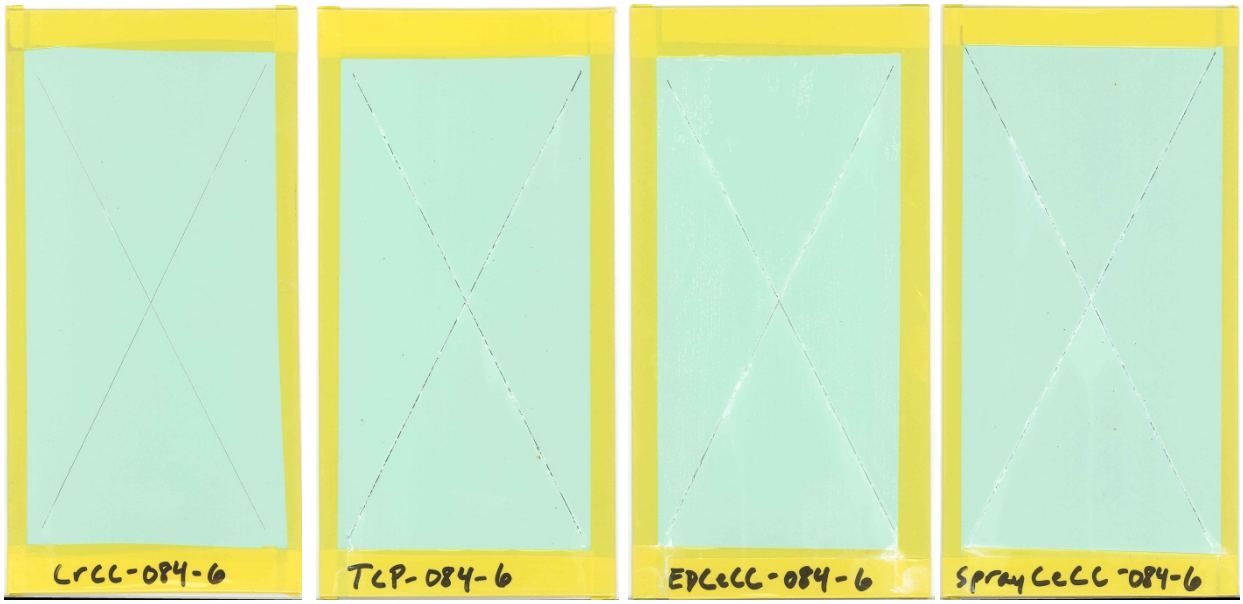

Figure 141. Primer coated panels after 2000 hrs of salt spray exposure.

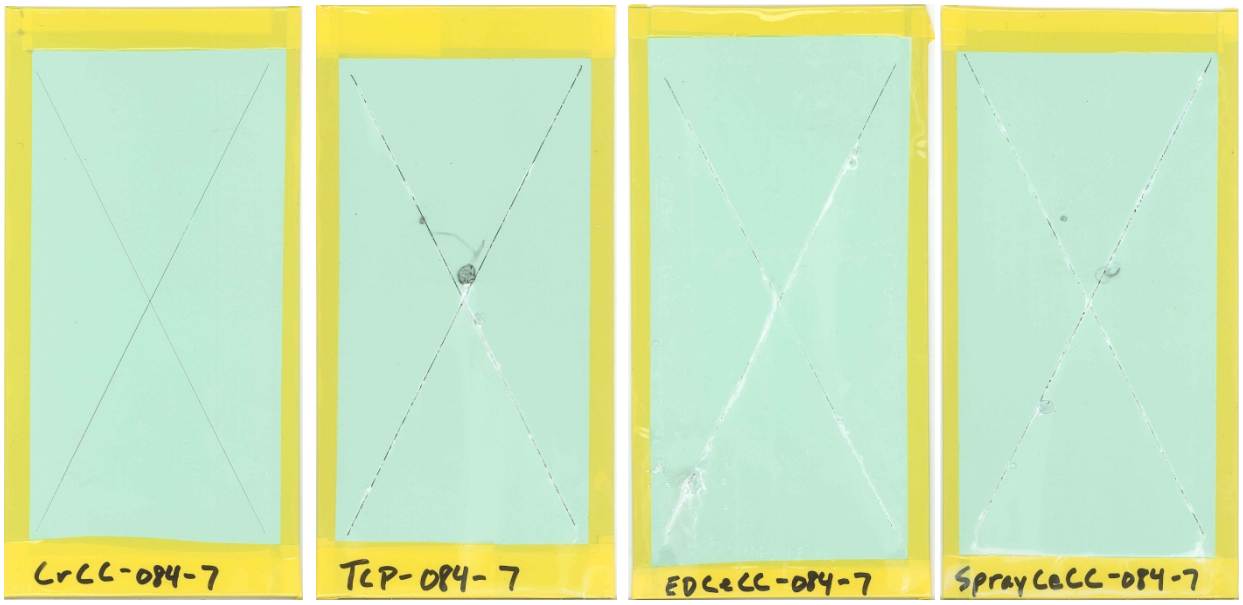

Figure 142. Primer coated panels after 2500 hrs of salt spray exposure.

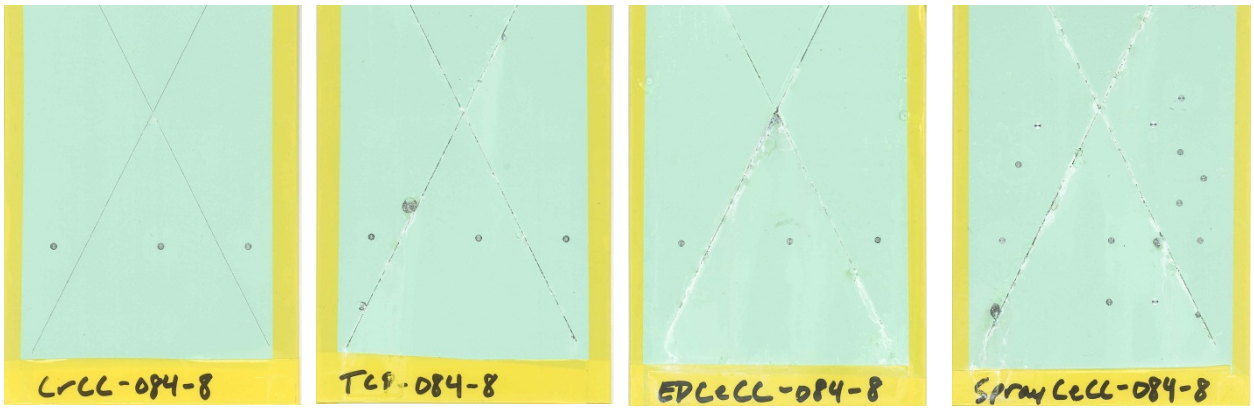

Figure 143. Primer coated panels after 3000 hrs of salt spray exposure.

Table 24. Summary of Salt Spray Results for Primers on Non-Chromate Conversion Coatings.

Conversion Coating	Salting Begins	Salting Increasing?	Runoff?	Blistering?
CrCC	2500 hrs	No	2500 hrs	No
EDCeCC	150 hrs	Yes—severe by 1000 hrs	150 hrs	150-3000 hrs
SPCeCC	150 hrs	Yes—severe by 1000 hrs	150 hrs	500-3000 hrs
TCP	300 hrs	Yes—severe by 3000 hrs	500 hrs	2500-3000 hrs

Electrochemical Analysis with Drilled Pits

The type of conversion coating affected the measured impedance of drilled pits on primer coated panels prior to salt spray testing. As shown in Figure 144, the highest impedance was measured for the combination of primer and the EDCeCC, which was just over 500 MΩ•cm^2. The impedance of the primer on either SPCeCC or TCP was ~350 MΩ•cm^2, while the primer on the CrCC had the lowest impedance at about 200 MΩ•cm^2. Based only on the initial impedance, any of the other the combinations should have had higher resistance to corrosion than the chromate based coatings.

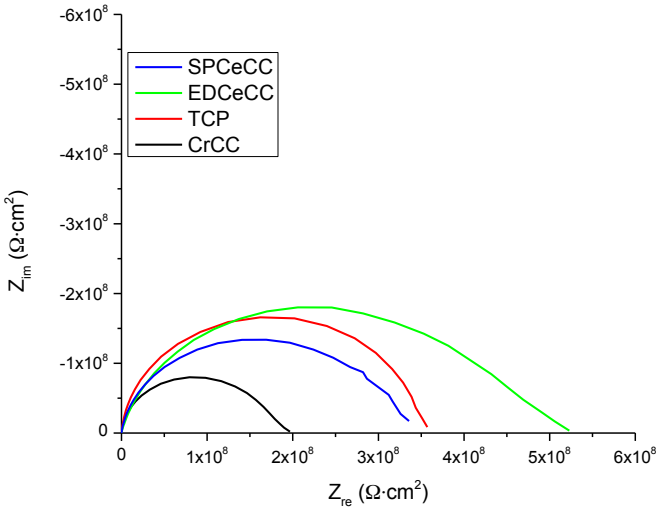

Figure 144. Impedance spectra for primers on panels with different pretreatments after 0 hrs in salt spray testing.

The data summarized in Table 25 reveal that the impedance of primer-coated panels decreases rapidly with exposure to salt spray. All panels show an initial drop of 50-95% in impedance after 150hrs salt spray exposure. This is followed by a period of relative stability through 2000 hrs of exposure. At 2500 hrs all the samples drop in impedance by more than 95%, relative to the values at 2000 hrs. Additionally, the complexity of the double layer increases with time: before salt spray exposure the EIS spectra can be fit to a model with a single RC time constant; after 2000 hours of exposure, the equivalent circuit has ~3 RC time constants; and at 2500 hours, the behavior can be described using 2 RC time constants. Table 25 and Table 26 summarize these changes in impedance and double layer complexity. This increase in complexity is likely due to an increase in porosity of the paint after exposure to salt spray and the accompanying permeation of the electrolyte into the paint.

Table 25. Impedance changes as a function of time in salt spray for primers on panels with different pretreatments

	Impedance (MΩ•cm^2)			
Time in salt spray (hrs)	CrCC	EDCeCC	SPCeCC	TCP
0	200	500	340	350
150	100	60	20	75
300	80	30	23	50
500	75	30	25	50
1000	80	25	10	50
1500	50	13	12	50
2000	50	15	13	45
2500	0.75	0.75	0.5	0.5
3000	1.5	0.17	0.3	0.8

Table 26. Double layer complexity vs. time in salt spray for primers on panels with different pretreatments

	Avg. # of RC time constants			
Time in salt spray (hrs)	CrCC	EDCeCC	SPCeCC	TCP
0	1	1	1	1.3
150	2	1.3	1.3	2
300	2	1.3	1	2
500	1.7	1.7	2.3	2
1000	2.3	2.7	2.3	2
1500	2.7	1.7	2.3	2.7
2000	2.7	2.7	3	3.3
2500	2	3	3	2
3000	2.5	2	2	2

The type of conversion coating also affected the potentiodynamic response of the primer coated panels. Figure 145 shows representative cyclic potentiodynamic spectroscopy results for panels prior to salt spray exposure. These results are summarized in Table 27. Based on passivation range, the CrCC panels should provide the best corrosion resistance, followed by TCP, then SPCeCC, and finally EDCeCC. Additionally, only the combination of the primer and the CrCC showed self-healing properties, which is shown by a re-passivation voltage that is more cathodic than the initial corrosion voltage. Combining these results with those from salt spray testing reveals that the relative performance of the coatings in salt spray testing can be predicted from passivation ranges and repassivation potentials measured prior to salt spray exposure using the drilled pit method.

Table 27. Summary of potentiodynamic data for primers on panels with drilled pits.

Conversion Coating	E_{corr} (V_{SCE})	I_{corr} (Amps/cm^2)	E_{pit} (V_{SCE})	Passivation Range (V)	E_{rp}-E_{corr} (V)
CrCC	-1.00	9.39 x 10^{-9}	-0.44	0.56	+0.15
TCP	-0.76	1.82 x 10^{-9}	-0.53	0.23	-0.06
SPCeCC	-0.61	3.64 x 10^{-9}	-0.40	0.21	-0.20
EDCeCC	-0.42	1.68 x 10^{-9}	-0.32	0.10	-0.30

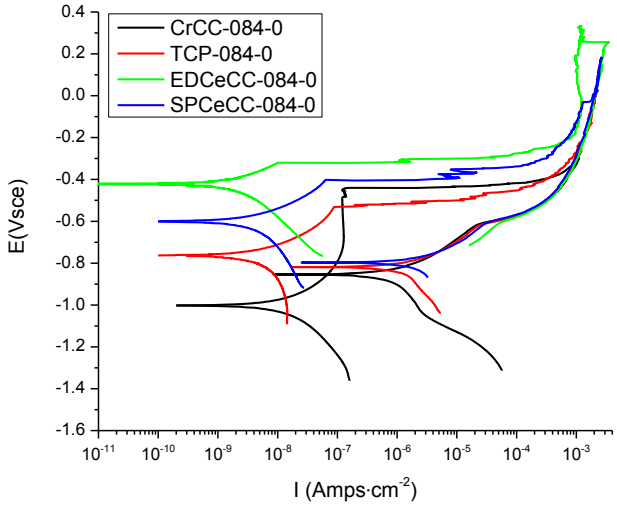

Figure 145. CPDS spectra for primers on panels with different pretreatments after 0 hrs in salt spray

Figure 146 summarizes the mean values for passivation range and re-passivation voltage relative to OCP for each of the coating combinations as a function of exposure time in salt spray. The panel with the CrCC conversion coating beneath the primer stands out as the only one exhibiting a good passivation range (generally >200mV) and self-healing through 500 hrs.

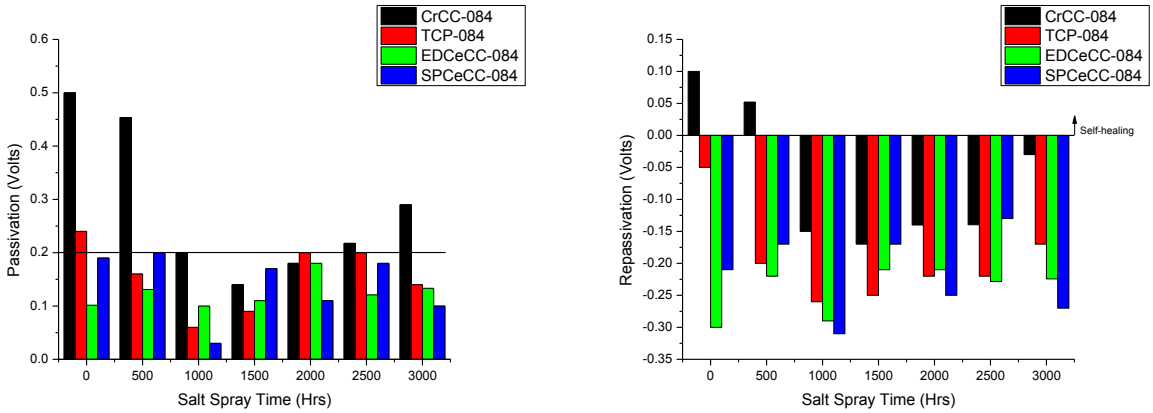

Figure 146. Mean passivation and re-passivation voltages for primers on panels with different pretreatments as a function of time in salt spray testing

The mean corrosion voltage (Figure 147) as judged by the OCP for three of the coating combinations tended toward -0.6V_{SCE}, which is the open circuit potential of aluminum. This may indicate there was no electrochemical protection during salt spray testing for all of the samples except for the panel with the CrCC. In general corrosion currents are low, less than 100 nAmp·cm^{-2} for all the materials throughout the duration of salt spray testing. This indicates that corrosion rates should be below 1.25MPY. The CrCC coated panels show a slight downward trend in corrosion current as opposed to the general upward trends of the other materials.

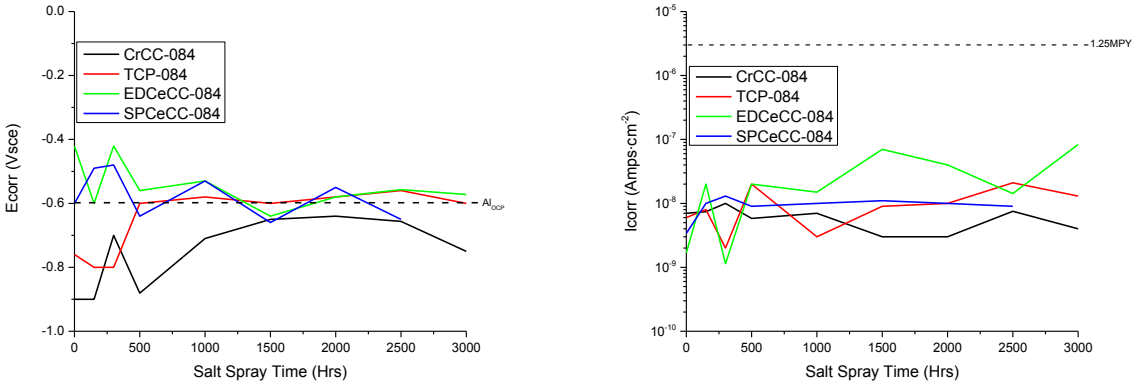

Figure 147. Mean corrosion voltages and currents for primers on panels with different pretreatments as a function of time in salt spray testing

Pitting potentials all trended to the same value regardless of which conversion coating was used with the primer. Pitting corrosion rate is often used to compare aluminum alloys and can be calculated using Equation VI.

$$MPY_{pit} \approx kI_{pit}\Lambda\frac{\varepsilon}{\rho} \qquad \text{(VI)}$$

Where k is a proportionality constant based on material and conditions, I_{pit} is the current at which the re-passivation voltage (E_{rp}) crosses the forward CPDS scan, Λ is $1.29x10^5$

(equivalents·sec·mils)/(Coulombs·cm·years), ε is the metal equivalent weight, and ρ is the metal density. Figure 148 shows three thresholds for k where pitting corrosion is less than 1.25MPY. For the most conservative value of k=100 none of the materials would pass with a pitting corrosion rate of <1.25MPY. It is likely that k falls in a range of 20-40 which indicates that the chromate materials would effectively mitigate pitting corrosion, but none of the other coating combinations would.

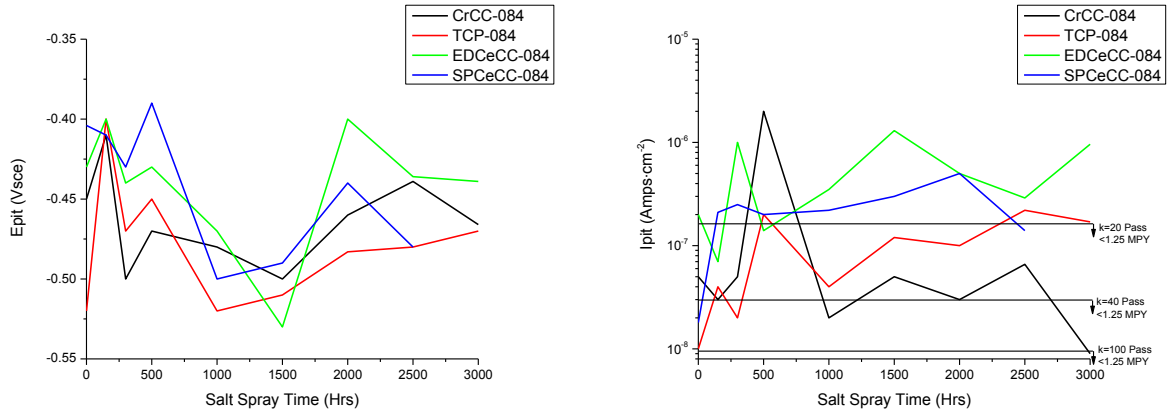

Figure 148. Mean pitting potentials and currents for primers on panels with different pretreatments as a function of time in salt spray testing

Figure 149 shows that primers deposited over CrCCs provided good passivation (>200mV) over a wide range of electrolyte pH values. In addition, examination of the re-passivation characteristics showed that primers deposited on CrCCs generally exhibited self-healing over the same pH range. Interestingly, primers deposited on cerium based conversion coatings also provided good passivation when the electrolyte pH was 8 or higher, which was well above the natural electrolyte pH of ~5.6. However, primers on cerium-based conversion coatings only exhibited self-healing at a pH of 10. Primers deposited on TCP coated panels were the worst performers by these measures, with lower passivation ranges and no re-passivation, indicating that TCP coatings are predominantly barriers with minimal electrochemical activity.

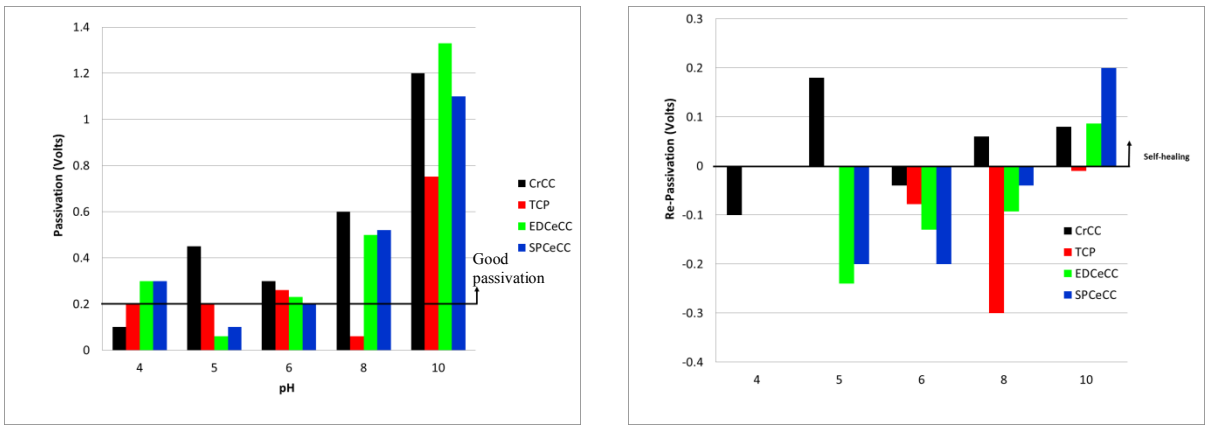

Figure 149. Mean passivation and re-passivation for primers on panels with different pretreatments as a function of electrolyte pH

The corrosion voltages (E_{corr}) and corrosion currents (I_{corr}) were similar for primers on all of the conversion coatings. As shown in Figure 150, the corrosion voltages were all about -0.8 V at a pH of 4 and remained in the range of about -0.6 to -1.0 for pH values up to 8. At a pH value of 10 the corrosion voltages converged to a value of -1.2 V, which indicates that highly alkaline electrolytes produce general corrosion leaving a relatively uniform underlying substrate. Likewise, corrosion currents were similar across the pH range. For the electrolyte pH range of 4 to 8, primers on all of the different types of conversion coatings had corrosion currents of about 10^{-8} A/cm^2. The corrosion current results indicate that unless the electrolyte is highly alkaline the corrosion rate should be less than 1.25MPY.

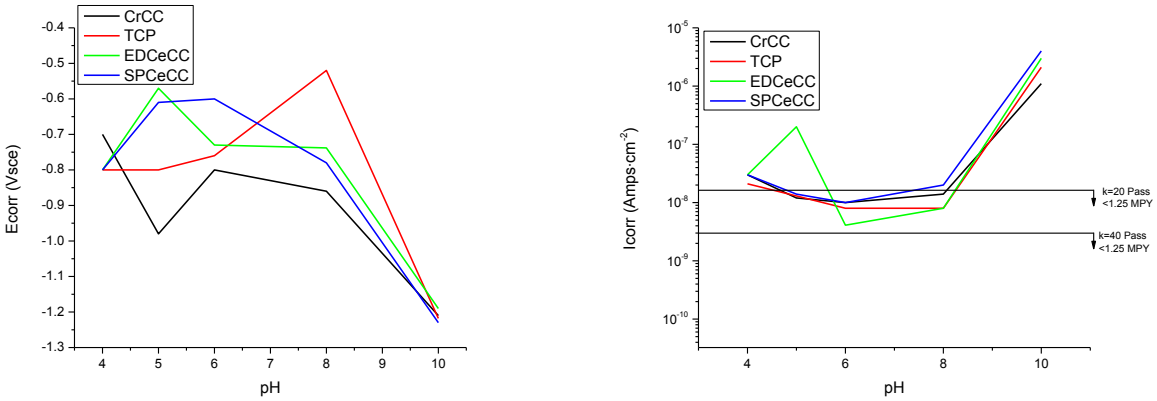

Figure 150. Mean corrosion voltages and currents for primers on panels with different pretreatments as a function of electrolyte pH

The pitting potentials (E_{pit}) and pitting currents (I_{pit}) revealed good performance of primers on all four types of conversion coatings under acidic conditions. Figure 151 showed that pitting potential was about -0.55 V for primers on all of the different conversion coatings at pH 4. Interestingly, the pitting potential was relatively constant with increasing electrolyte pH for primers on TCP panels while it increased to about 0 V for primers with the three other pretreatments, another indication the TCP coatings are not electrochemically active. Likewise, pitting currents equated to corrosion rates of less than 1.25 MPY at electrolyte pH values of less than 8, but increased for higher electrolyte pH values for all types of pretreatments. The results show that pitting corrosion should only be a concern if the electrolyte becomes highly alkaline.

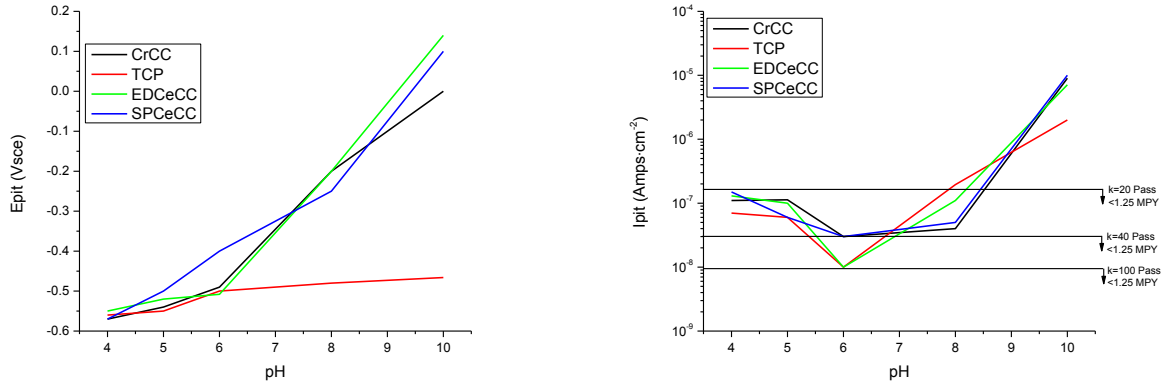

Figure 151. Mean pitting potential and current for primers on panels with different pretreatments as a function of electrolyte pH

The re-passivation voltage was very uniform (particularly across a pH of 4-8, see Figure 152) regardless of conversion coating. However, the surfaces became significantly more active at a pH of 10—again indicating general corrosion with highly alkaline electrolytes. These results are consistent with statements by the Army Corp of Engineers: *"Aluminum has excellent corrosion resistance in a wide range of water and soil conditions because of the tough oxide film that forms its surface… the oxide film is generally stable in the pH range of 4.5 to 8.5, but the nature of the dissolved compounds causing the pH reading is crucial."*[121]

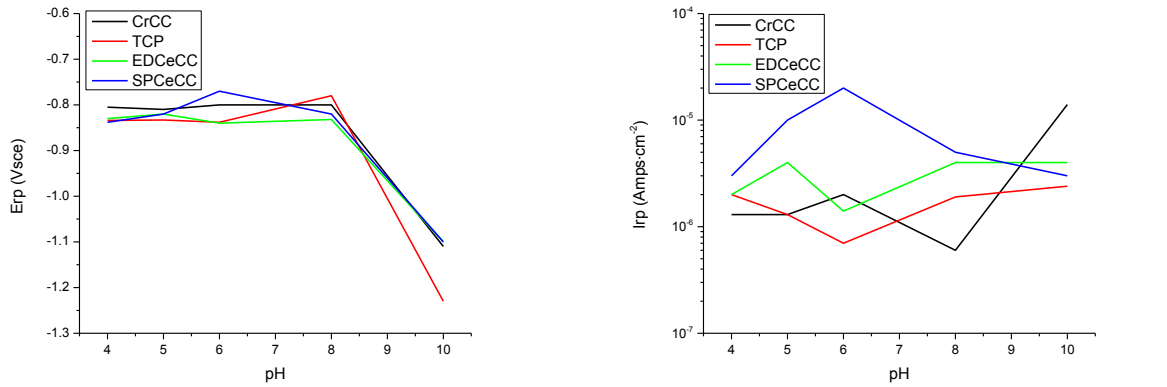

Figure 152. Mean re-passivation voltages and currents for primers on panels with different pretreatments as a function of electrolyte pH

Electrochemical Analysis of Primers without Drilled Pits

Figure 153 and Figure 154 shows the results of electrochemical testing of primers deposited on CrCCs with and without artificial defects (i.e., drilled pits). Impedance was ~25 times higher prior to salt spray exposure when tested without a drilled pit, although the spectra had significant noise when the frequency was <1Hz, which was especially obvious in specimen CrCC-084-0 EIS-1. After 3000 hours in salt spray testing, panels had nearly identical impedance values with

and without drilled pits, which indicates that most of the conduction was through the paint rather than through the drilled pit (see Table 28).

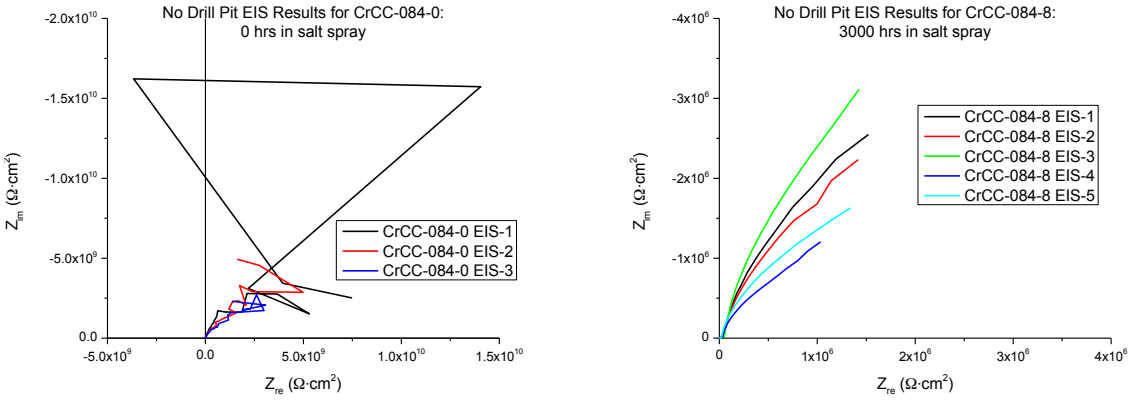

Figure 153. EIS Results for CrCC-084 after 0 hrs and 3000 hrs of salt spray testing without drilled pits

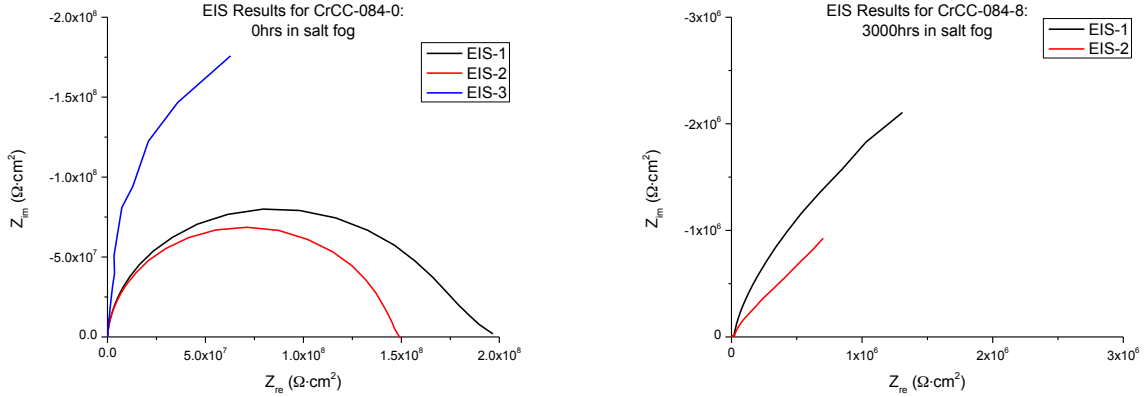

Figure 154. EIS Results for CrCC-084 after 0 hrs and 3000 hrs of salt spray testing with drilled pits

Table 28. Comparison of EIS results with and without drilled pit

	With Drilled Pit		Without Drilled Pit	
	$Z_{re\text{-}0hr}$ (MΩ•cm^2)	$Z_{re\text{-}3000hr}$ (MΩ•cm^2)	$Z_{re\text{-}0hr}$ (MΩ•cm^2)	$Z_{re\text{-}3000hr}$ (MΩ•cm^2)
CrCC	200	1.5	5000	2
EDCeCC	500	0.17	7500	0.8
SPCeCC	340	0.3	5000	0.4
TCP	350	0.8	5000	1

CPDS results for primers deposited on panels with CrCCs after 3000 hr of salt spray testing showed similar behavior with and without drilled pits (Figure 155). Corrosion voltage was about -0.75 V for panels with drilled pits and between -0.7 V and -0.6 V for panels without drilled pits. In addition, panels without drilled pits appeared to show some self-healing. The pitting potential was about -0.4V_{SCE} for panels with drilled pits test.

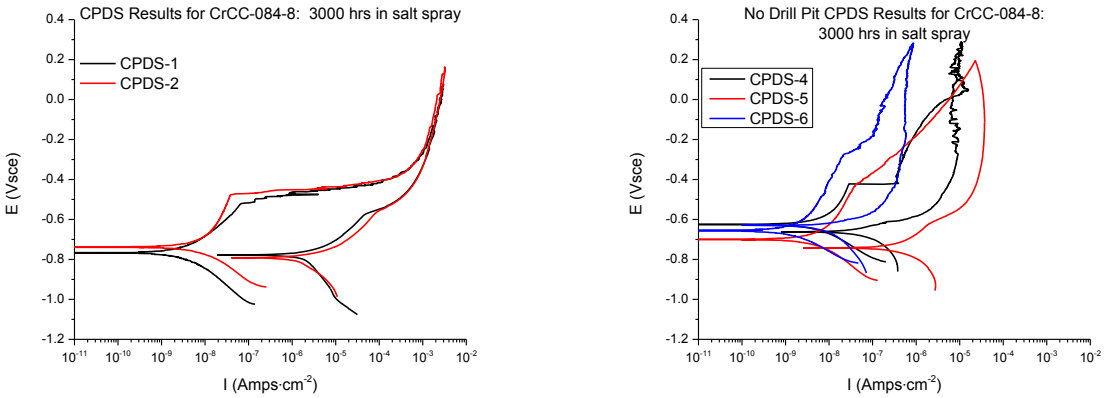

Figure 155. CPDS Results for CrCC-084 after 3000 hrs of salt spray testing with and without drilled pits

Results for primers deposited on panels treated with the TCP material (Figure 156 and Figure 157) again show an increase in impedance of ~15 times when tested without drilled pits compared to panels with drilled pits prior to salt spray testing. After 3000 hr in salt spray, the primers on panels without drilled pits had the same impedance as panels with drilled pits.

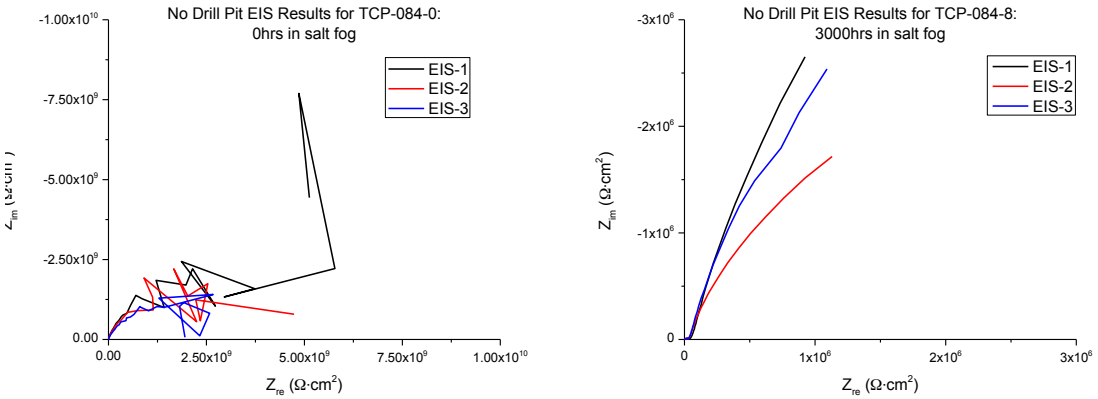

Figure 156. EIS results for primers on panels with TCP after 0 hrs and 3000 hrs of salt spray testing without drilled pits

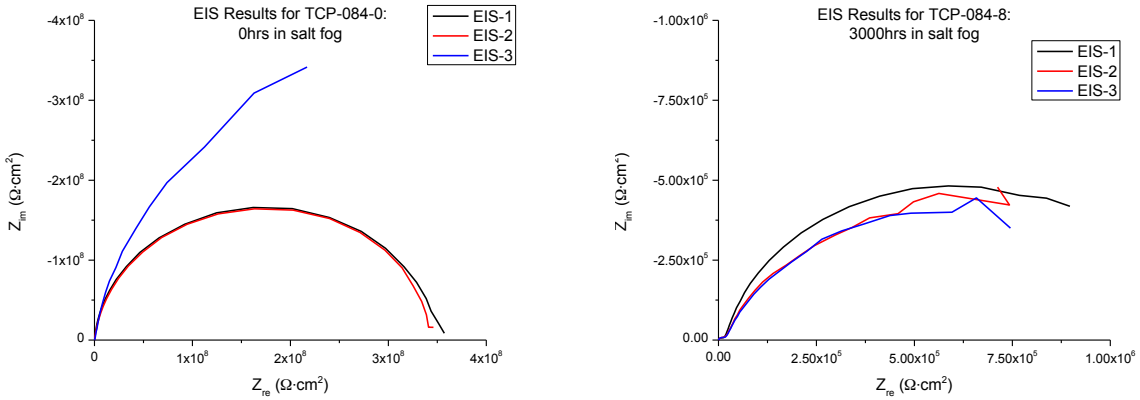

Figure 157. EIS results for primers on panels with TCP after 0 hrs and 3000 hrs of salt spray testing with drilled pits

CPDS results at 3000 hrs are similar for non-drilled pit and drilled pit specimens, but no pitting potential was observed in the non-drilled pit panels (Figure 158). The primers deposited on panels treated with TCP showed no self-healing properties as the re-passivation potentials were below the pitting potentials. As shown in Table 28 above, TCP coated panels have higher impedance than CrCCs before salt spray exposure with drilled pits and the same impedance as CrCCs before salt spray exposure without drilled pits. After 3000 hrs of salt spray, primers on panels pretreated with TCP had an impedance value that was about half that of primers deposited on panels with CrCCs.

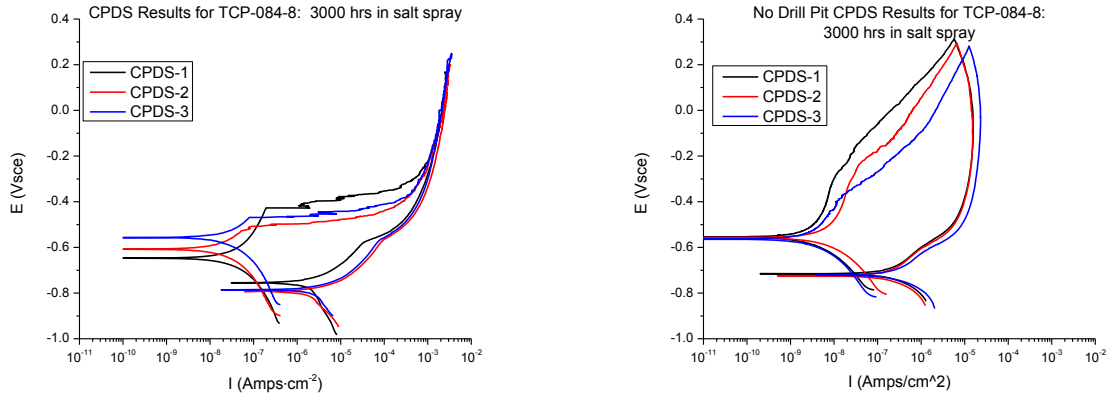

Figure 158. CPDS results for primers on panels with TCP after 0 hrs and 3000 hrs of salt spray testing with and without drilled pits

Primers deposited on panels with electrolytically deposited CeCCs (Figure 159 and Figure 160) had impedances that were higher by a factor of ~15 before salt spray testing when tested without a drilled pit as compared to panels with a drilled pit. After 3000 hr of salt spray testing, the impedance was ~5 times higher for panels without a drill pit. Compared to primers deposited on panels with CrCCs, primers deposited on panels with EDCeCCs show considerably higher

impedance before salt spray exposure with or without a drilled pit. After salt spray exposure the impedance of primers on panels with EDCeCCs drops to 0.1-0.5x relative to primers on panels with CrCCs (Table 28).

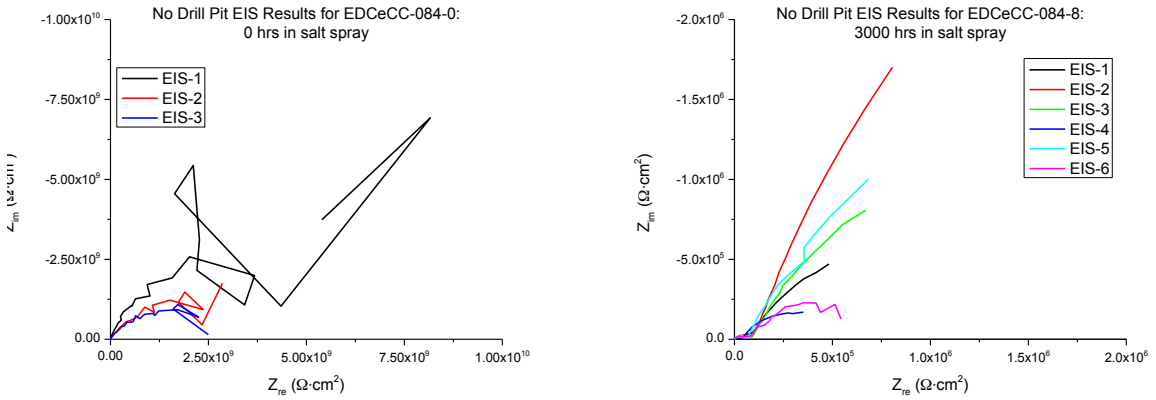

Figure 159. EIS results for primers deposited on panels with EDCeCC after 0 hrs and 3000 hrs of salt spray testing without drilled pits

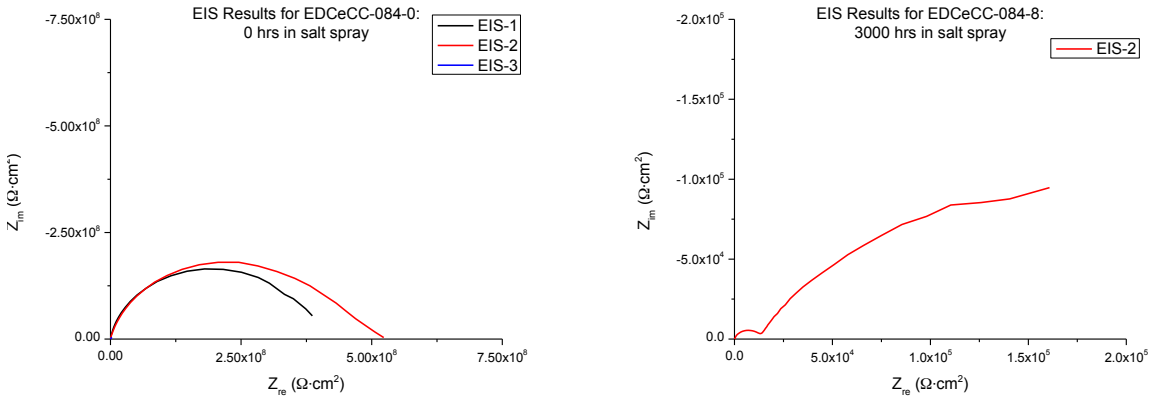

Figure 160. EIS results for primers deposited on panels with EDCeCC after 0 hrs and 3000 hrs of salt spray testing with drilled pits

Pitting potentials were similar for primers on all of the different pretreatments at about -0.4 V_{SCE} for panels with and without drilled pits after 3000 hr in salt spray testing (Figure 161). However, corrosion currents and re-passivation currents were ~10 and ~100 times lower, respectively, for the non-drilled pit panels. The non-drilled pit panels also showed the potential for self-healing based on the re-passivation voltage averaging ~0.1V higher than the corrosion voltage.

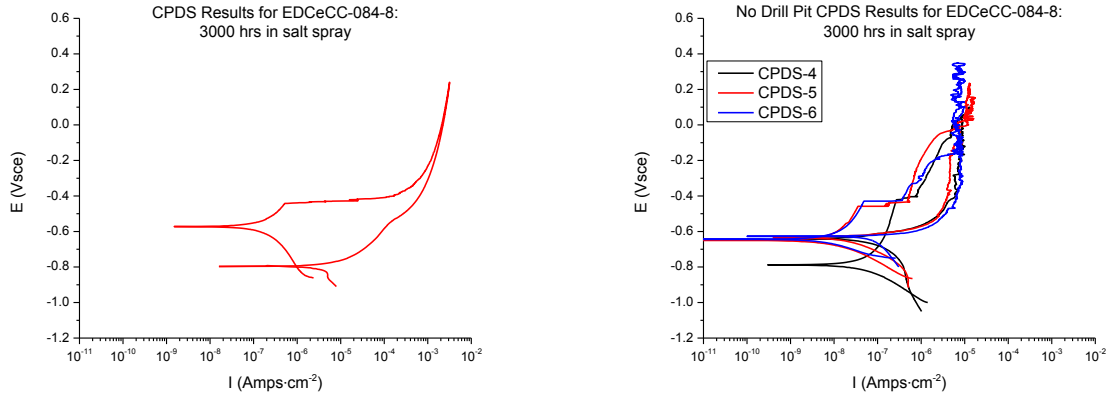

Figure 161. CPDS results for primers deposited on panels with EDCeCC after 0 hrs and 3000 hrs of salt spray testing with and without drilled pits

Primers on spray deposited CeCCs (Figure 162 and Figure 163) had about 15 times higher impedance before salt spray testing without drilled pits compared to primers with drilled pits. After 3000 hrs in salt spray testing, the impedance was roughly equal to panels without drilled pits (Table 28). Impedance of primers on SPCeCC coated panels with drilled pits was about double that of primers on CrCC coated panels before exposure to salt spray. Impedance of primers on panels with CeCCs without drilled pits was the same as primers on CrCC coated panels. After 3000 hrs of exposure to salt spray, the impedance of primers on SPCeCC coated panels was about 50% less than primers on CrCC coated panels.

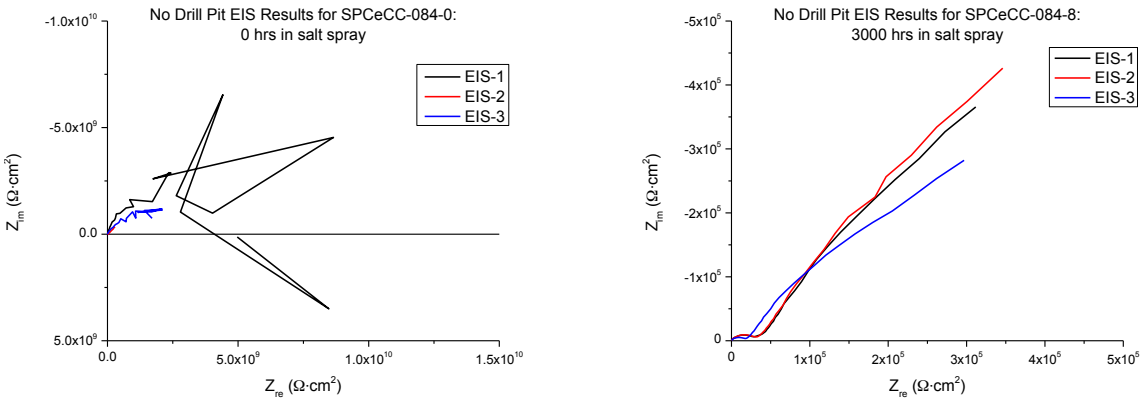

Figure 162. EIS results for primers deposited on panels with SPCeCCs after 0 hrs and 3000 hrs in salt spray testing without drilled pits

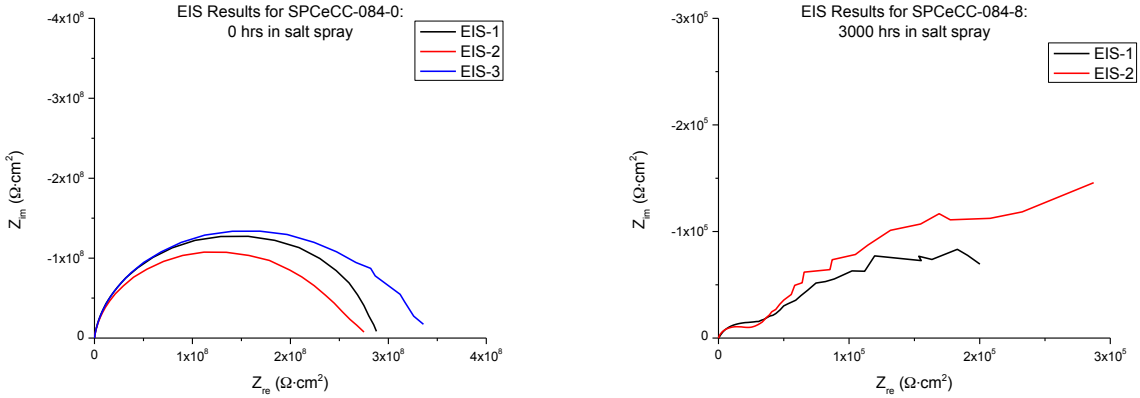

Figure 163. EIS results primers deposited on panels with SPCeCCs after 0 hrs in salt spray testing with drilled pits

Pitting potential (Figure 164) was slightly lower for primers on panels without drilled pits compared to those with drilled pits after 3000 hr in salt spray. However, corrosion current and re-passivation currents were about 20 times lower for primers on panels without drilled pits. Primers on panels without drilled pits also showed self-healing properties with a re-passivation voltage that averaged ~50mV higher than the corrosion voltage.

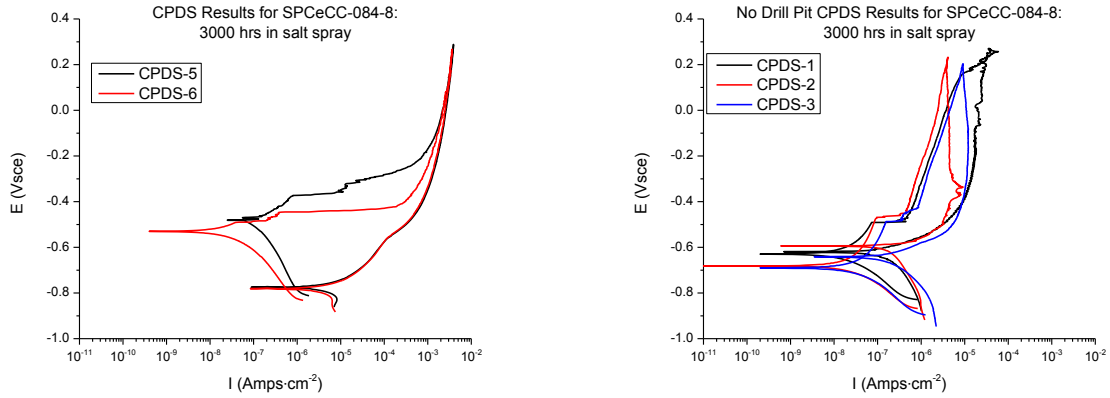

Figure 164. CPDS results for primers on panels with SPCeCCs after 3000 hrs in salt spray testing with and without drilled pits

The average results for OCP for primers without drilled pits on each pretreatment are shown in Figure 165 after 0 hr and 3000 hr in salt spray testing. Results showed a high OCP (about -0.2 V_{SCE}) for all of the primers before salt spray testing. The primer on the CrCC stabilized to this value the fastest. The highest OCP values were for primers on CrCCs and EDCeCCs at ~-0.1V_{SCE}. After 3000 hr in salt spray testing, all of the OCP values were closer to that of aluminum—again indicating that the electrolyte had permeated the primer and reached the substrate. In this test, the primer deposited on the panel pretreated with TCP material was anomalous: this combination showed a continual rise in the OCP value throughout the entire

stabilization time of 1000 s. This possibly indicates the formation of a passivation layer, such as an oxide, on the aluminum surface beneath the primer.

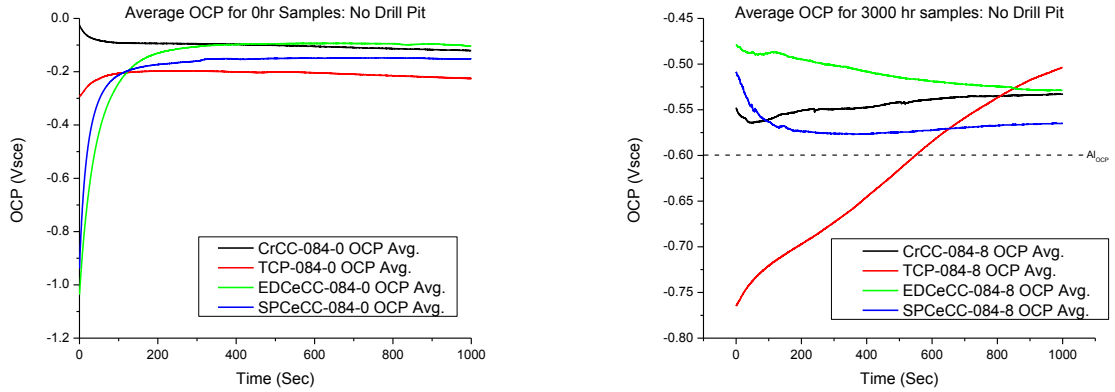

Figure 165. Mean OCP values for primers on different pretreatments after 0 hrs and 3000 hrs in salt spray testing without drilled pits

Characterization as a Function of Salt Spray Exposure Time

X-ray diffraction analysis was used to determine the relative amounts of crystalline phases in the primers as a function of exposure time in salt spray testing. The amounts of gypsum and $Pr(OH)_3$ were normalized to the amount of TiO_2, which was presumably inert and not removed from the primer during salt spray testing. Results indicated that gypsum depleted over time from the paint during salt spray exposure (Figure 166). About 50 wt% of the gypsum was lost in the first 300 hrs of salt spray exposure. The depletion continued until ~60 wt% of the gypsum was depleted after 3000 hr of salt spray testing. The relative amount of praseodymium (present as $Pr(OH)_3$) was roughly constant over the same time in salt spray testing (Figure 166). No significant variations in the relative amounts of gypsum or praseodymium were observed for the different types of conversion coatings in these ratios.

Particles that were rich in praseodymium were observed in the scribed areas for primers deposited on panels with CrCC starting at 500 hrs of salt spray exposure (Figure 167 and Figure 168) and for other conversion coatings starting at around 1500-2000hrs (Figure 169, Figure 170, and Figure 171). These particles were on the order of 5μm-10μm long for scribes on panels with primers deposited on CrCCs. Smaller particles (~100nm long) were observed in the scribes of panels with the primers that were deposited on the other pretreatments. In addition, Pr-rich particles were observed on the surface of panels that had not been exposed to salt spray after ~16 weeks in the ambient laboratory environment (Figure 172). Taken together, the results indicate that praseodymium was being transported from the primer matrix to the scribed areas of panels during salt spray exposure. Primers on CrCCs that exhibited the best corrosion resistance also had the largest particles that formed after the shortest amount of salt spray exposure, indicating that the relative amount of protection may be related to the size of the particles that form during exposure or the time required for the particles to form during exposure. In addition, Pr-rich crystals were observed on panels that were aged in the ambient laboratory environment, indicating that Pr species were mobile under a variety of conditions.

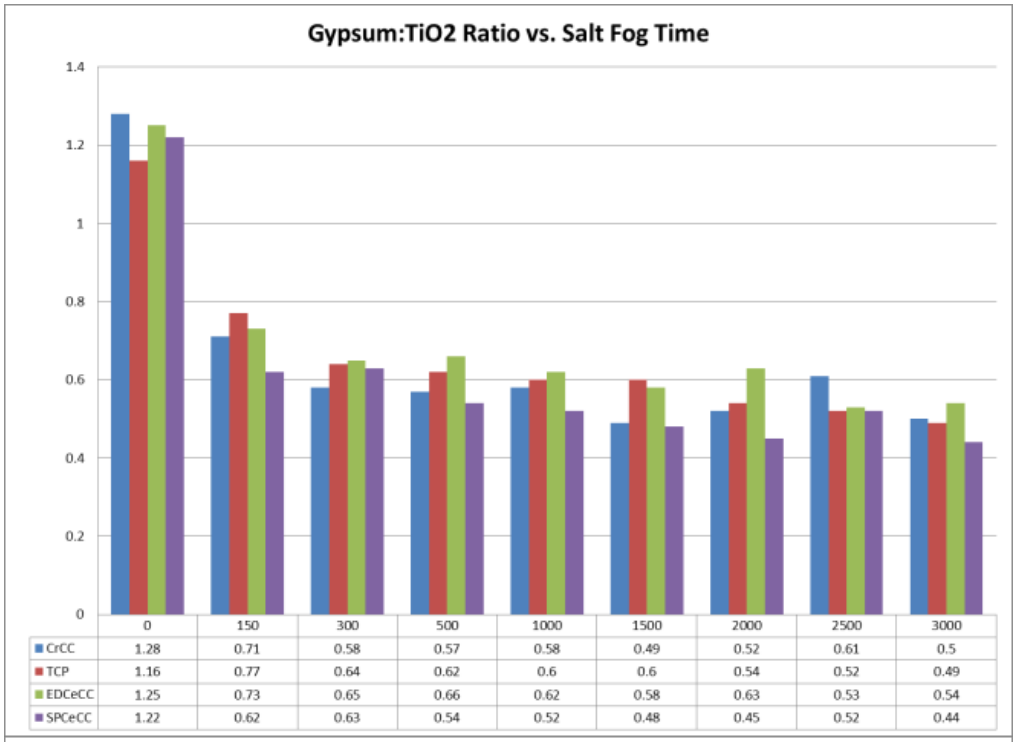

	0	150	300	500	1000	1500	2000	2500	3000
CrCC	1.28	0.71	0.58	0.57	0.58	0.49	0.52	0.61	0.5
TCP	1.16	0.77	0.64	0.62	0.6	0.6	0.54	0.52	0.49
EDCeCC	1.25	0.73	0.65	0.66	0.62	0.58	0.63	0.53	0.54
SPCeCC	1.22	0.62	0.63	0.54	0.52	0.48	0.45	0.52	0.44

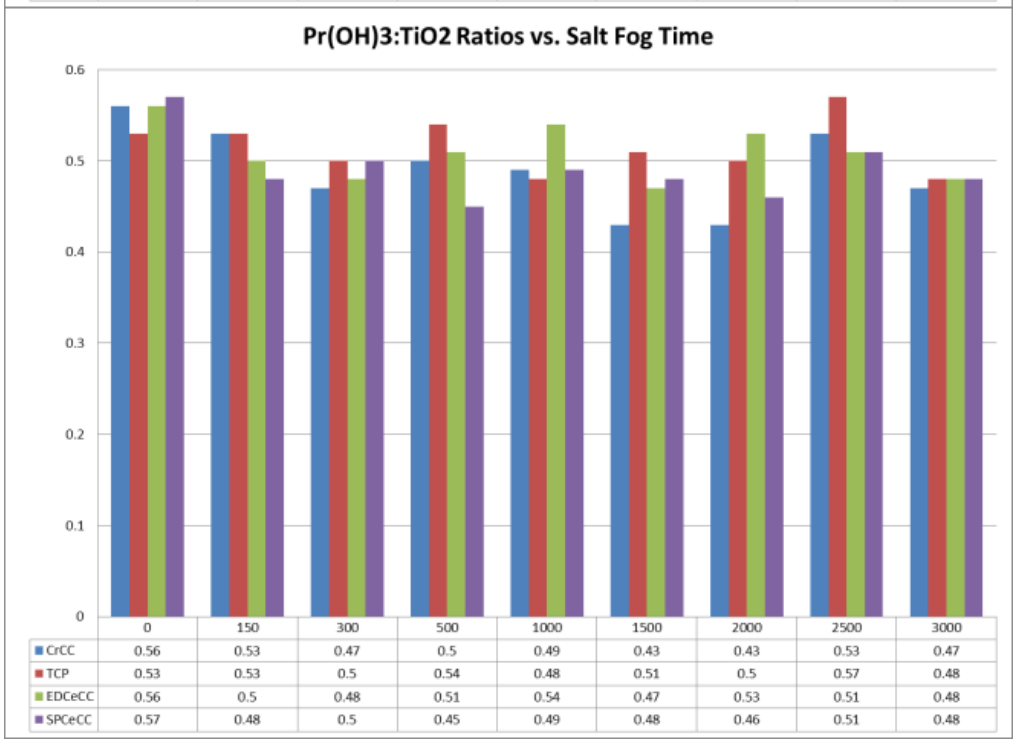

	0	150	300	500	1000	1500	2000	2500	3000
CrCC	0.56	0.53	0.47	0.5	0.49	0.43	0.43	0.53	0.47
TCP	0.53	0.53	0.5	0.54	0.48	0.51	0.5	0.57	0.48
EDCeCC	0.56	0.5	0.48	0.51	0.54	0.47	0.53	0.51	0.48
SPCeCC	0.57	0.48	0.5	0.45	0.49	0.48	0.46	0.51	0.48

Figure 166. XRD peak area ratios as a function of salt spray exposure time

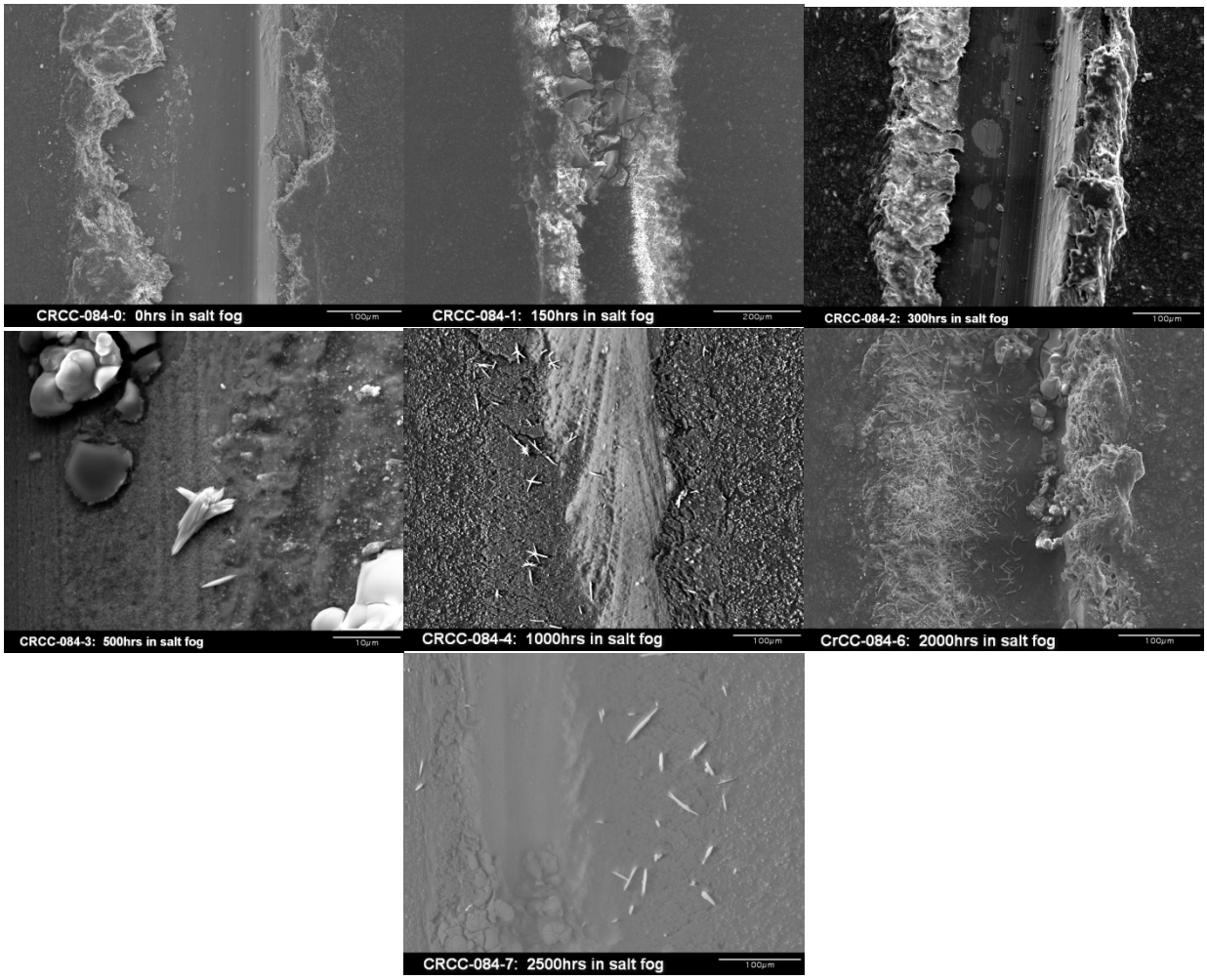

Figure 167. SEM images of Pr-rich particles as a function of salt spray exposure time for primers deposited on CrCCs

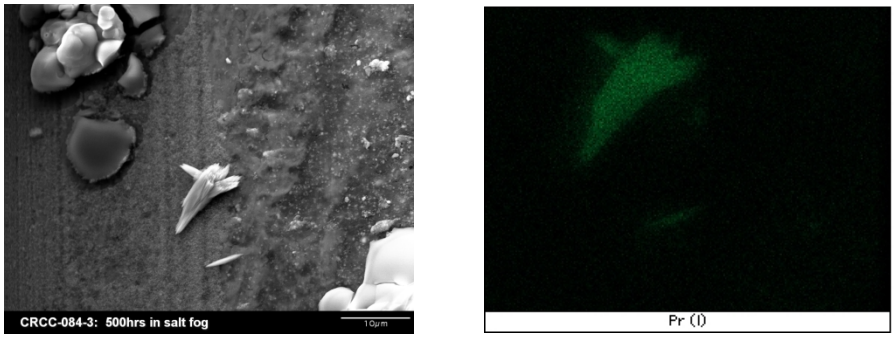

Figure 168. EDS mapping of Pr for a primer deposited on a CrCC after 500 hrs in salt spray showing Pr rich particles.

Pr-rich particles were first observed after 2000 hrs of salt spray exposure for primers deposited on panels with TCP (Figure 169). The appearance of large crystals coincided with the length of salt spray exposure at which salting was no longer increased as salt spray exposure time

increased. This observation supports the assertion that the formation of large (5-10 μm long) crystals is indicative of ability of the primer to inhibit corrosion.

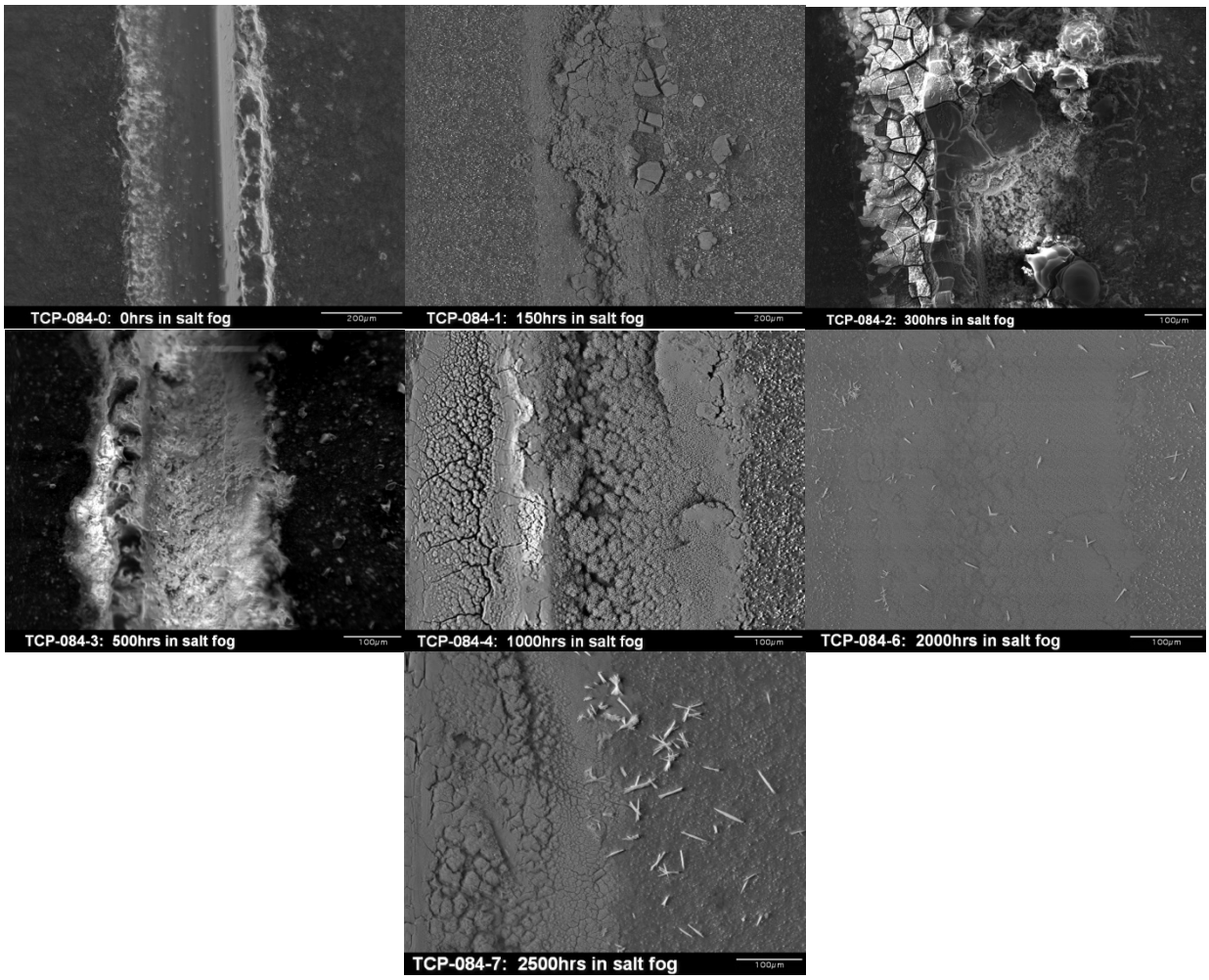

Figure 169. SEM images of Pr-rich particles as a function of salt spray exposure time for primers deposited on TCP.

Similar to primers deposited on panels pretreated with TCP, large (5-10 μm long) Pr-rich particles were observed on primers deposited on panels with EDCeCCs after ~1000 hrs of salt spray exposure (Figure 170). This again corresponds the approximate salt spray exposure time after which salting no longer increased with increased salt spray exposure time. The reason for the longer salt spray exposure time required for the large Pr-rich particles to form is not known, but may be influenced by the higher impedance or lower repassivation capabilities of the primers deposited on panels with TCP, EDCeCCs, or SPCeCCs.

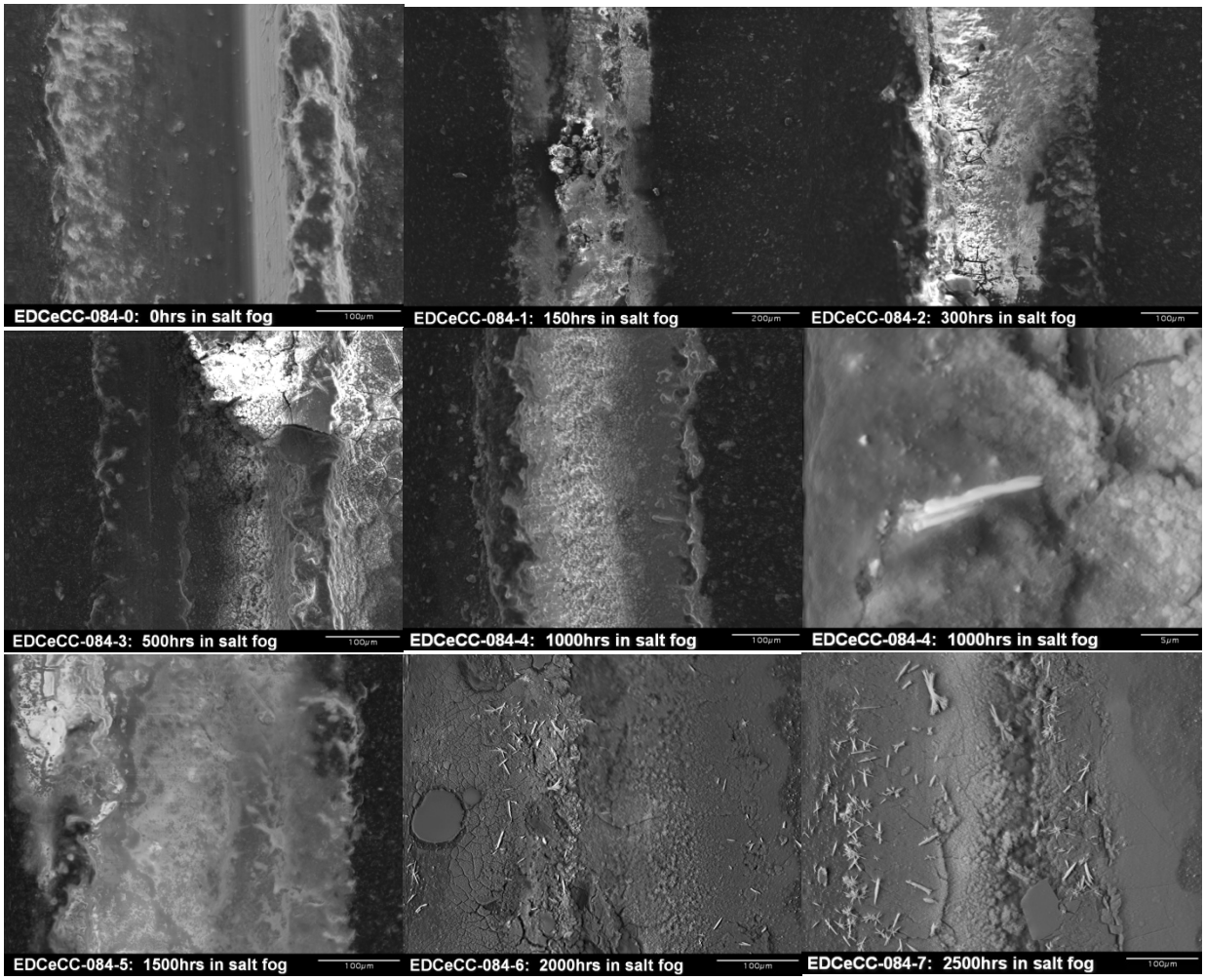

Figure 170. SEM images of Pr-rich particles as a function of salt spray exposure time for primers deposited on EDCeCCs.

Pr-rich particles 5-10μm long were observed as well on primers deposited on panels with SPCeCCs after ~1500 hrs of salt spray exposure (Figure 171). This again corresponds the approximate salt spray exposure time after which salting no longer increases with increased salt spray exposure time.

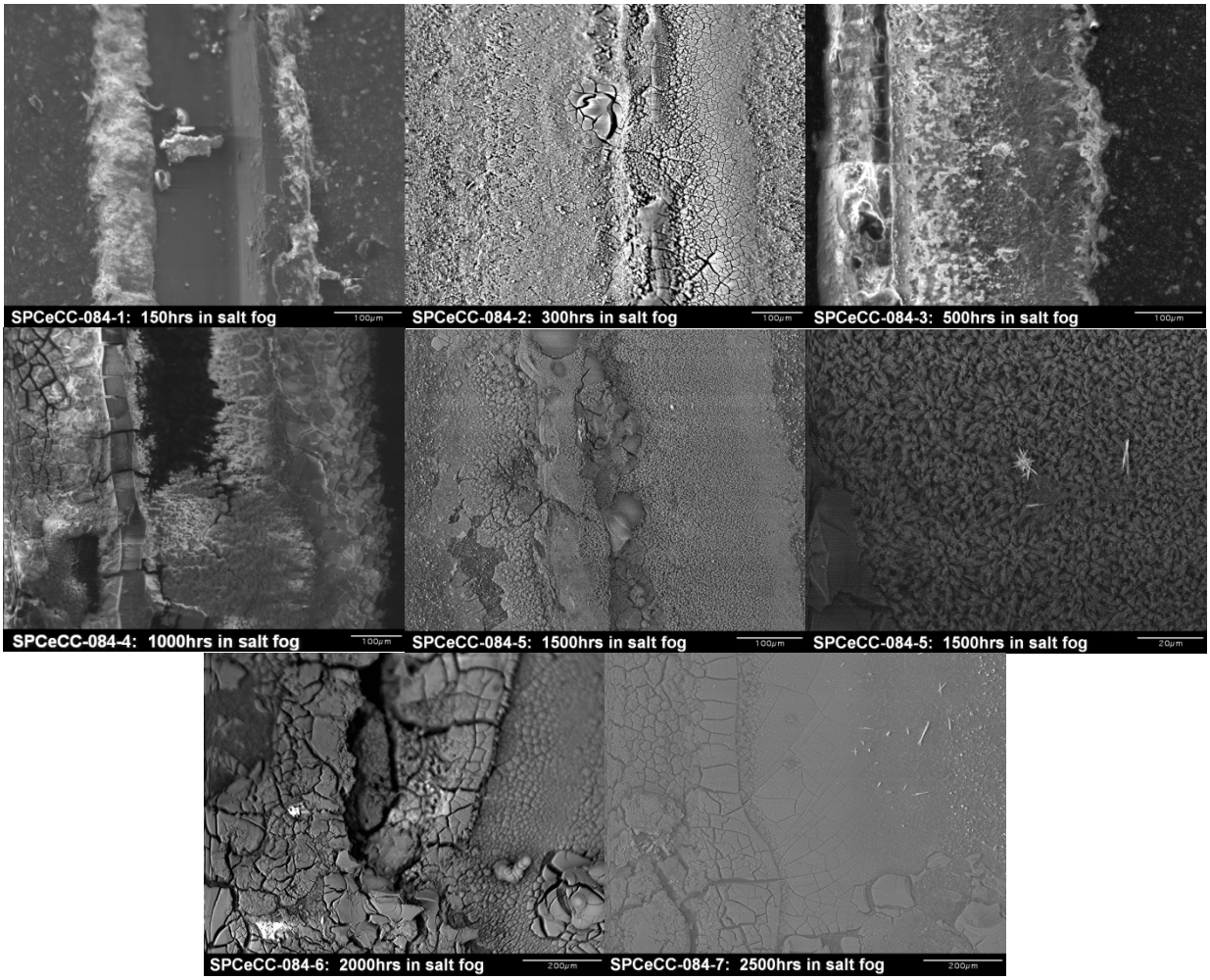

Figure 171. SEM images of Pr-rich particles as a function of salt spray exposure time for primers deposited on SPCeCCs

Figure 172 shows a typical SEM image of small (~100nm) praseodymium-rich particles in the scribed area of a primer deposited on a panel coated with a CrCC. This image was taken prior to salt spray exposure. Some of the crystals are highlighted for EDS in the areas labeled Spectra 1, 2, and 3. Additional crystals can be seen in the lower left corner of the image. Similar crystals can be seen in panels coated with either type of CeCC and TCP. Analysis by EDS indicates that praseodymium is present in these crystals although signal strength at the detector was low. The high chromium content in the EDS results is probably the result of the interaction volume of the beam, which is likely more than 1 μm into the underlying substrate. Nonetheless, this result shows that Pr-containing crystals are present on all the panels, regardless of conversion coating. It is the *early growth* (i.e., for salt spray exposure times of 500 hours or less) of these crystals that must be promoted for effective mitigation of corrosion.

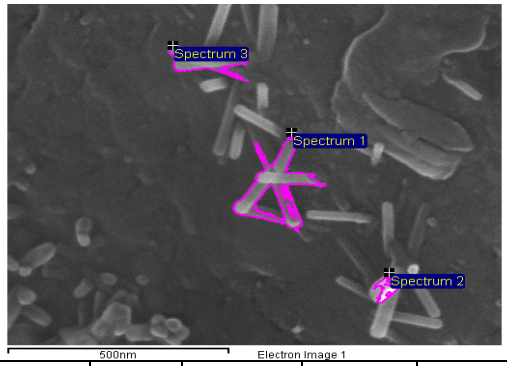

Point	In stats.	C	O	Al	S	Ca	Ti	Cr	Pr	Total
Spectrum 1	Yes	31.53	15	8.65	5.61	6.53	7.19	20.39	5.09	100.00
Spectrum 2	Yes	30.05	21.42	7.76	6.01	7.72	5.33	19.03	2.68	100.00
Spectrum 3	Yes	30.46	14.93	8.85	3.97	5.50	6.34	24.77	5.17	100.00
Best Estimate		**30.7±0.7**	**17±4**	**8.4±0.5**	**5±1**	**7±1**	**6.3±0.9**	**21±3**	**4±1**	

Figure 172. SEM and EDS analysis of Pr-rich particles on a primer deposited on a CrCC after 0 hrs in salt spray

Figure 173 and Figure 174 compares FIB cross-sections and subsequent EDS for primers deposited on panels with CrCCs before salt spray testing and after 3000 hr in salt spray testing. The depletion of calcium in the top half of the cross-section after 3000 hr of salt spray testing was apparent. This indicates the dissolution of the calcium sulfate out of the top surface of the primer, which supports the XRD analysis.

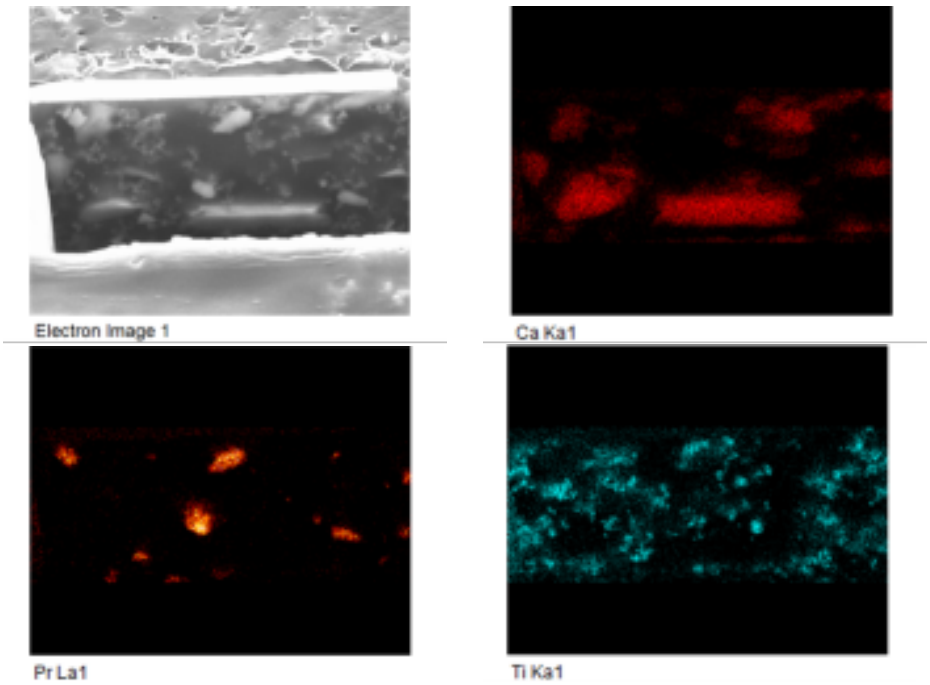

Figure 173. FIB cross section and EDS of primers deposited on CrCC before salt spray (0 hrs)

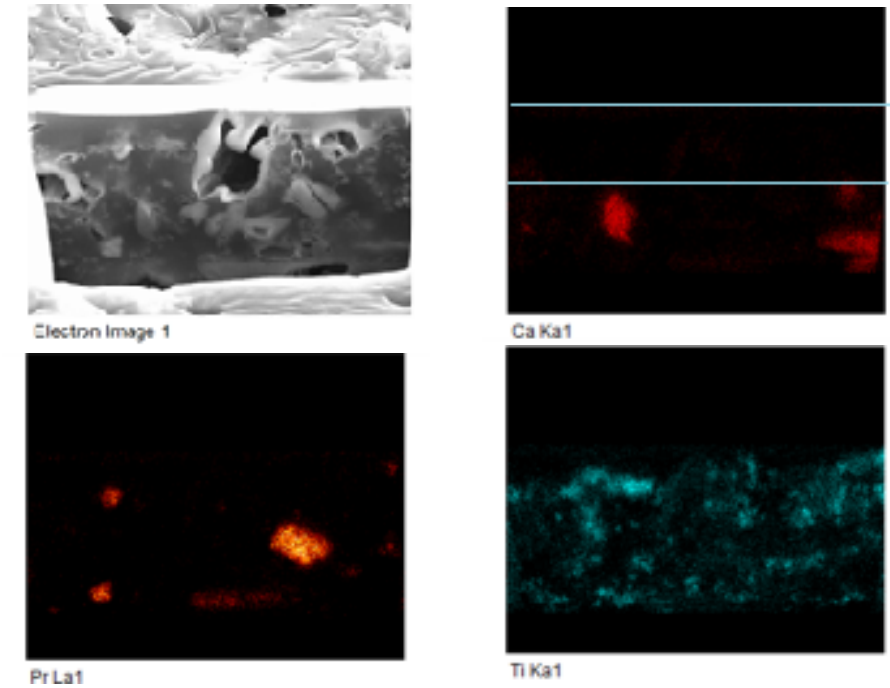

Figure 174. FIB cross section and EDS of primers deposited on CrCCs after 3000 hours in salt spray.

Figure 175 and Figure 176 show FIB cross-sections and subsequent EDS for primers on TCP before salt spray testing and after 3000 hr in salt spray testing. Calcium is again depleted in the

top portion of the primer after 3000 hrs in salt spray, as seen in the highlighted area. The depletion region appears to be thinner for primers deposited on TCP compared to primers on CrCCs or EDCeCCs.

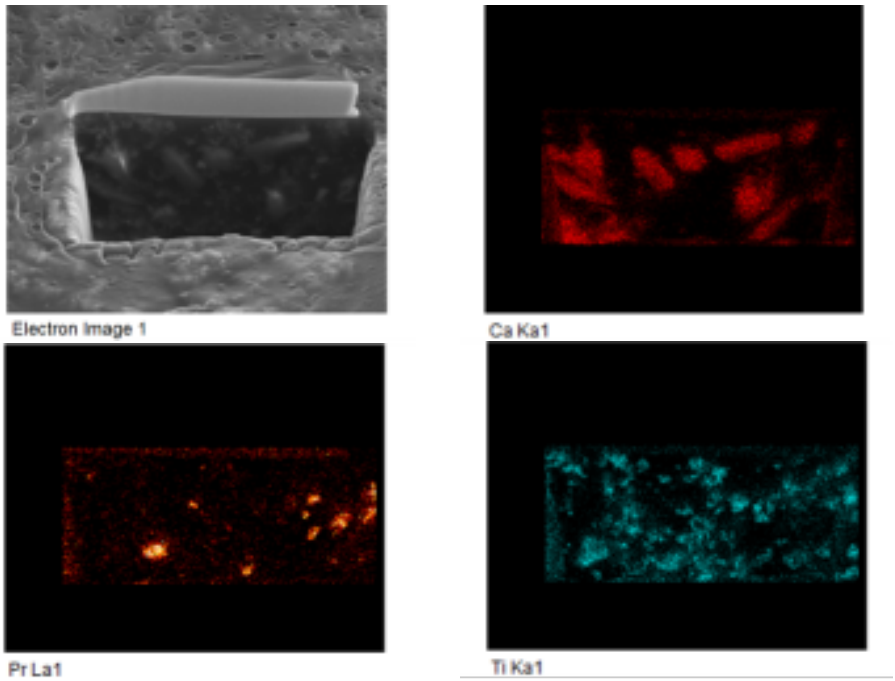

Figure 175. FIB Cross-Section and EDS on TCP-084-0 (0 hrs)

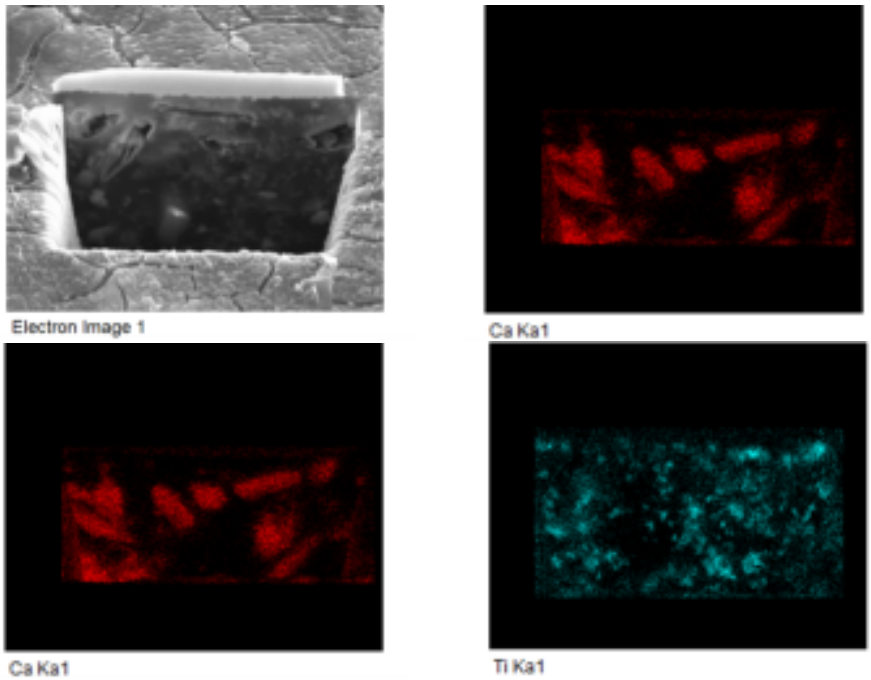

Figure 176 FIB Cross-Section and EDS on TCP-084-8 (3000 hrs)

Figure 177 and Figure 178 show FIB cross-sections and subsequent EDS for primers on EDCeCCs before salt spray testing and after 3000 hr in salt spray testing. The EDS results for the panel exposed to 3000 hrs of salt spray again show depletion of calcium in the top portion of the primer, as shown in the highlighted area.

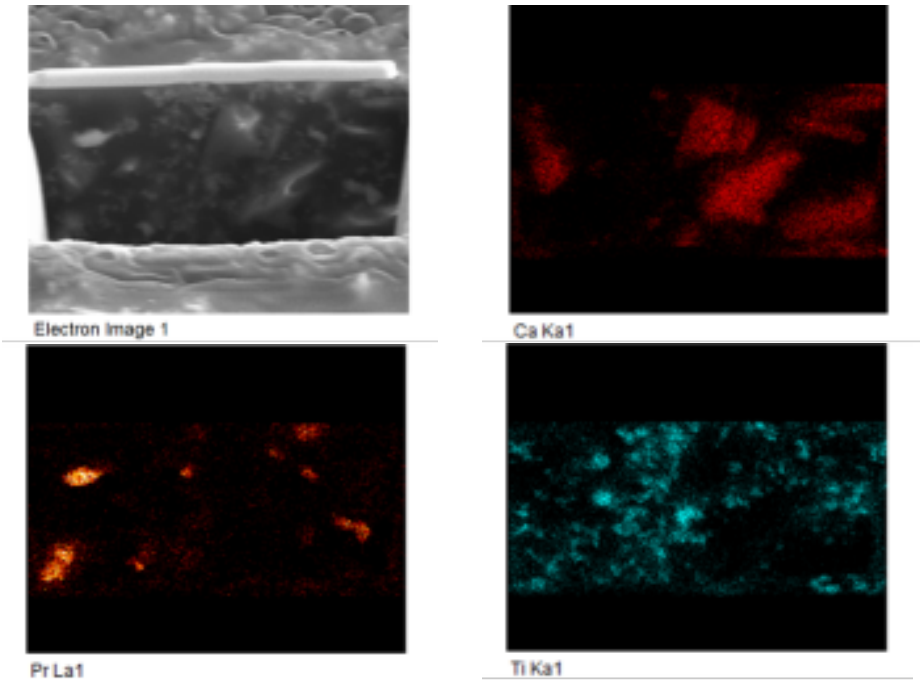

Figure 177. FIB Cross-Section and EDS on EDCeCC-084-0 (0 hrs)

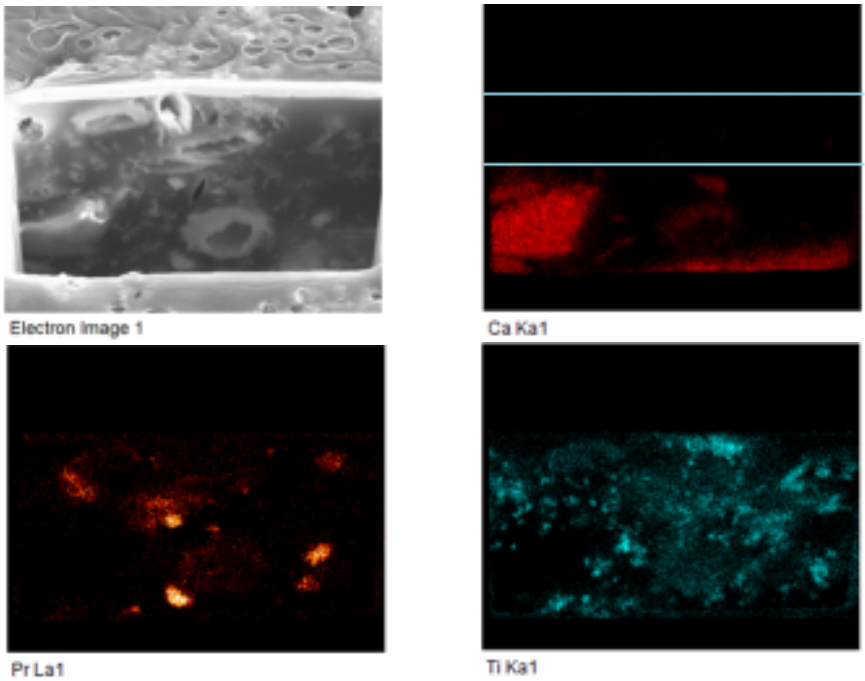

Figure 178. FIB Cross-Section and EDS on EDCeCC-084-8 (3000 hrs)

Task 5: Protection Mechanism Analysis

A combination of a knowledge of phase stability in rare-earth systems and results from the characterization of coatings after various stages of exposure to salt spray testing was used to devise protection mechanisms for both CeCCs and Pr-primer. Knowledge of phase stability in Ce and Pr systems were combined with information from solubility studies and observations from analytical and electrochemical characterization to propose models that define the initial phases present in the coatings, the conditions required for dissolution or activation of the inhibitors, the species that are transported, and the reactions that lead to passivation.

Corrosion Protection of Cerium-Based Conversion Coatings

Electrodeposited CeCCs do no contain sub-surface crevices as deposited because of the negative electrode potential and lack of chloride ions in the deposition solution (cerium nitrate is used). However, subsurface crevices can be introduced after deposition by exposing the electrodeposited coatings to a spray solution containing NaCl-H_2O_2-gelatin. Visually, exposure to the NaCl-H_2O_2-gelatin solution did not appear to alter the morphology or thickness of the coatings. However, to confirm that exposure to this solution resulted in the formation of subsurface crevices, FIB/SEM analysis was employed.

Coatings, whether they were exposed to the NaCl-H_2O_2-gelatin solution or not, had surfaces which were dominated by a nodular morphology. About 95% of the area of the coating surfaces had small cracks that did not exceed ~0.5 μm in width. FIB cross sections of areas of coatings that had small cracks (Figure 179) showed similar thicknesses (400-500 nm) regardless of whether they were treated with the NaCl-H_2O_2-gelatin solution or not. The small cracks extended through the coatings to the substrate, but did not appear to alter the underlying alloy at the small cracks. Some "curtaining" of the substrate was observed, but this was an artifact of the FIB milling. Complementary EDS analysis revealed no significant differences in the compositions of the coatings or substrate with and without treatment in the NaCl-H_2O_2-gelatin solution. No residual chloride or increased oxygen content was detected in the coating exposed to the NaCl-H_2O_2-gelatin solutions.

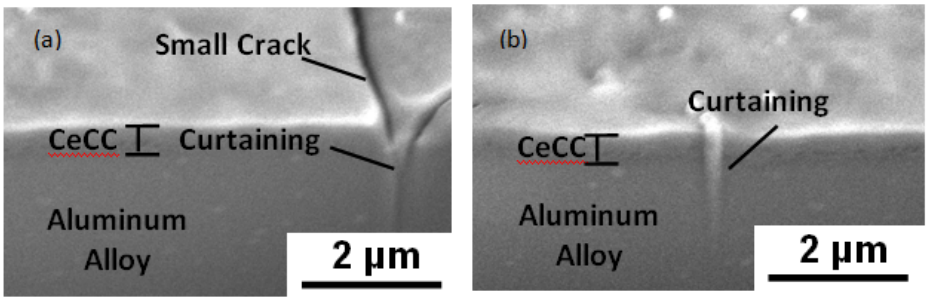

Figure 179. FIB cross section of areas with small cracks in CeCCs that were a) electrodeposited and b) electrodeposited then sprayed with a NaCl-H_2O_2-gelatin solution.

In addition to areas that had small cracks in the coating, about ~5% of the surface on the CeCCs that had been sprayed with the NaCl-H_2O_2-gelatin solution exhibited large cracks that were more than 1 µm in width (Figure 180). These areas had a similar appearance to the areas with large cracks that were reported for the spray deposited coatings in previous studies [53,77,102] which were found to be associated with the presence of subsurface crevices. FIB milling revealed that subsurface crevices were also present underneath coated areas of the electrodeposited coatings that exhibited large cracks after exposure to the NaCl-H_2O_2-gelatin solution. The crevices extended ~10 µm into the substrate (Figure 181). Many of the features observed previously in the crevices of spray deposited CeCCs were also noted in the crevices produced by the NaCl-H_2O_2-gelatin solution in this study. One consistently observed feature was a dark, oxygen-rich phase surrounding a large portion of the crevice. In addition, the crevices were connected to the surface of the coating through the large cracks in the CeCCs. Thus, this analysis showed that spraying the surface of electrodeposited coatings with a NaCl-H_2O_2-gelatin solution resulted in the formation of subsurface crevices. Further, these crevices were similar in size, morphology, and penetration depth to crevices that formed during spray deposition. Finally, formation of the crevices in the electrodeposited coatings appeared to have minimal impact on thickness, morphology, or composition of the coatings in areas away from the large cracks.

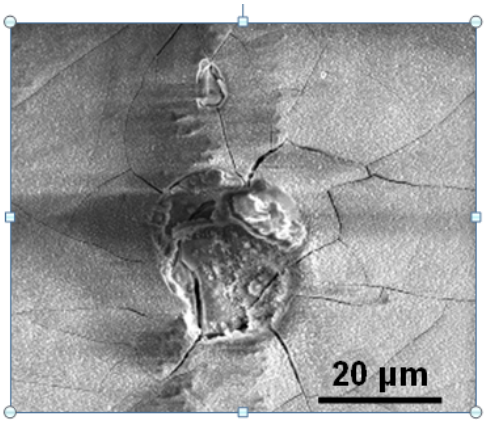

Figure 180. An area of an electrodeposited CeCC with large cracks after exposure to the NaCl-H_2O_2-gelatin solution.

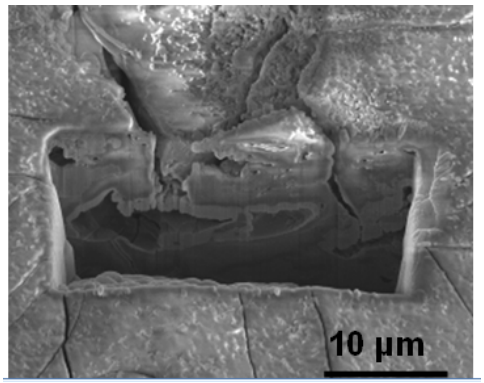

Figure 181. FIB cross section of an area with large cracks in an electrodeposited coating showing that exposure to the NaCl-H_2O_2-gelatin solution produced subsurface crevices.

Corrosion testing was performed on electrodeposited coatings with and without exposure to the NaCl-H_2O_2-gelatin solution to study the effects of the presence of subsurface crevices on the corrosion protection of otherwise identical coatings. Salt spray results showed the corrosion resistance was comparable for coatings with and without crevices, as long as a second post-treatment was employed after exposure to the NaCl-H_2O_2-gelatin solution. After 14 days salt spray testing, both the crevice-free and crevice-containing coatings exhibited no visible pitting or salt tailing on the surface. In contrast, crevice-containing coatings that were not post-treated a second time exhibited significant salt tailing after salt spray exposure. EIS testing of the three different types of coatings (Figure 182) mirrored the salt spray testing results. Crevice-free coatings and crevice-containing coatings that underwent a second post-treatment both had impedances of ~55 kΩ-cm^2 before salt spray exposure. Without the second post-treatment, the crevice-containing coatings had impedance values that were significantly lower, about 30 kΩ-cm^2. It can be concluded from the corrosion testing data that the presence of subsurface crevices had no significant effect on the corrosion protection of CeCCs when the coatings were post-treated after crevice formation.

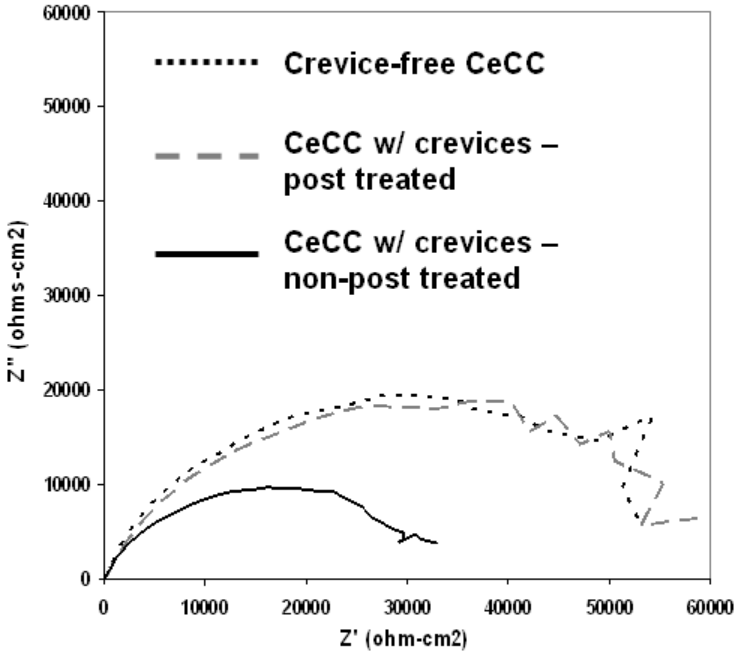

Figure 182. Nyquist plots of electrodeposited CeCCs with and without subsurface crevices.

The comparable corrosion testing results for electrodeposited coatings with or without crevices (assuming a post-treatment was employed after crevice formation) indicated that subsurface crevices were not required for CeCCs to exhibit significant corrosion protection. Conversely, the presence of crevices did not inhibit the ability of electrodeposited CeCCs to provide corrosion protection. Additionally, the poor corrosion protection of crevice-containing coatings that had not undergone a second post-treatment showed that the CeCCs alone were not fully responsible for the corrosion protection of panels that contained crevices. Although the second post-treatment did not alter the morphology, thickness, or composition of the CeCCs, the improved corrosion protection observed after the second post-treatment was likely associated with changes

to the composition or structure of features in the crevices, such as oxides or hydroxides. Thus the corrosion of subsurface crevices is associated with the formation of protective oxides / hydroxides. However, partial protection of the crevices by the coating through electrochemical means is also a possibility.

Corrosion testing showed that electrodeposited coatings with and without crevices had similar impedances (~55 kΩ-cm^2), which indicated similar abilities to provide corrosion protection. However, it is not clear if the presence of subsurface crevices altered the mechanism by which the CeCCs provided corrosion protection. To investigate this, EIS testing was performed on coatings with and without crevices after various salt spray exposure times. It should be noted here that due to the poor corrosion protection of CeCCs with crevices that were not post-treated a second time, all subsequent analysis of electrodeposited coatings with crevices is focused on coatings that were post-treated after exposure to the NaCl-H_2O_2-gelatin solution.

A Nyquist plot of the EIS data for crevice-free electrodeposited coatings as a function of salt spray exposure (Figure 183) showed the impedance of coatings without crevices varied during corrosion testing. During the first 24 hours of exposure, the impedance dropped to ~40 kΩ-cm^2 from an initial value of ~55 kΩ-cm^2 prior to salt spray exposure. After 96 hours and through 168 hours of exposure, the impedance increased to ~60 kΩ-cm^2, slightly higher than the initial coating.

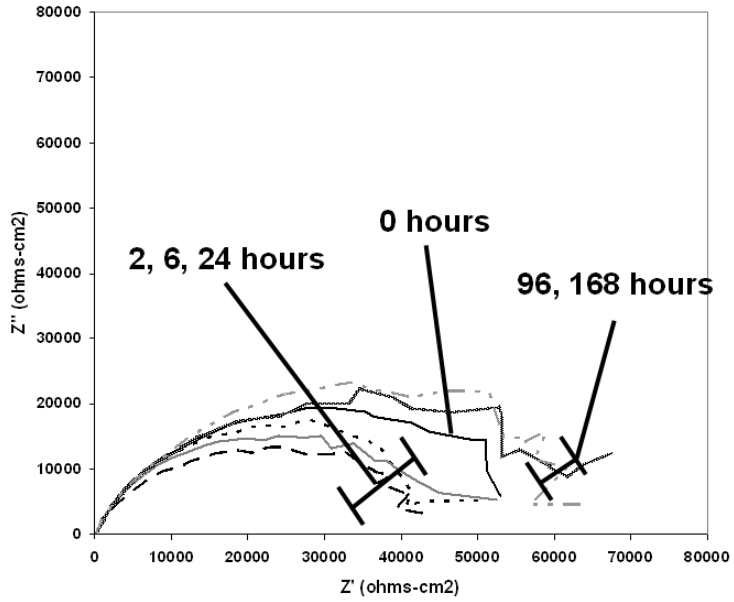

Figure 183. Nyquist plot of crevice-free electrodeposited CeCCs after various salt spray exposure times.

The initial decrease in impedance upon exposure to salt spray indicated a decrease in corrosion protection. It is likely that during the first few hours of salt spray exposure that protective features of the coating were broken down. For example, aluminum oxide exposed to salt spray would be expected to dissolve, which could decrease the impedance. Interestingly, after 24 hours of salt spray exposure, the impedance increased to ~60 kΩ-cm^2, which was greater than the pre-

salt spray values. This indicated healing of the protection that had been broken down during the initial phase of testing and/or formation of additional protective features during corrosion testing. As these processes occurred, no corrosion products were observed on the outer surfaces of the coatings.

Crevice-containing CeCCs exhibited significantly larger changes in impedance during corrosion testing, as shown in the Nyquist plot of the EIS data (Figure 184). During the first 96 hours of salt spray exposure, the impedance nearly doubled from an initial value of ~55 kΩ-cm^2 to ~100 kΩ-cm^2. After this initial increase, the impedance remained constant up to 168 hours for crevice-containing coatings. This same trend was observed in previous studies for post-treated, spray deposited CeCCs on substrates with crevices in which the impedance doubled after 24 hours of exposure [110]. Because higher impedance is associated with increased corrosion protection, it is evident that during corrosion testing the corrosion resistance of electrodeposited coatings with crevices increased. The EIS data does not, however, provide insight into whether the increased impedance was due to alteration of the coating, the crevices, or a combination of the two. It is clear though, from the electrochemical data, that CeCCs are not solely inert barriers to corrosion but rather exhibit some degree of active protection during corrosion testing, regardless of the presence of crevices based on the changes in impedance.

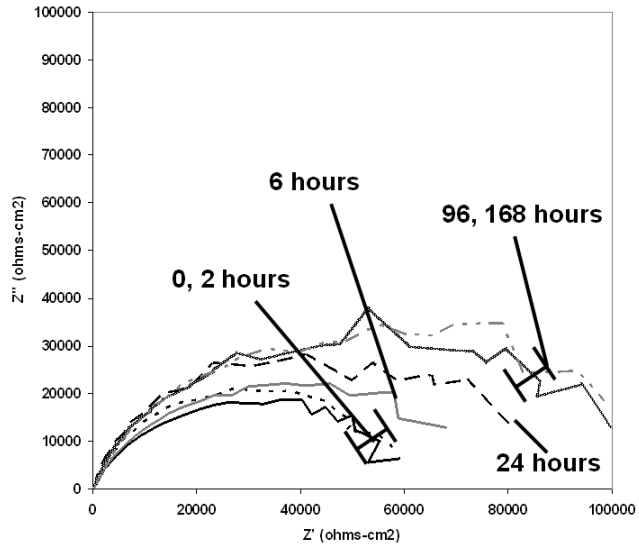

Figure 184. Nyquist plots of crevice-containing electrodeposited CeCCs after various salt spray exposure times.

To identify changes in the coatings or crevices that were impacting corrosion resistance, SEM/EDS analysis was performed after various salt-spray exposure times. After seven days of salt spray exposure, the surface of crevice-free coatings (Figure 185a), exhibited a nodular morphology with small cracks that were less than 0.5 μm wide. This appearance was very similar to the appearance prior to salt spray testing. Additionally, EDS data showed the composition of the surface was similar to concentrations detected prior to corrosion testing. In contrast, coatings with crevices exhibited significant changes in surface morphologies and compositions during salt spray exposure. After 7 days of salt spray testing, (Figure 185b) a fibrous morphology was observed and EDS analysis showed higher concentrations of aluminum

and oxygen, indicating a layer rich in Al and O had formed on the surface. The formation of a surface layer of Al-O on electrodeposited CeCCs with crevices is similar to previous observations of the formation of layers rich in Al and O on the surfaces of spray deposited CeCCs during salt spray testing [110]. The formation of the surface layer was associated with an increase in impedance. Since the layer rich in Al and O only formed on coatings with crevices, it is evident that the source of Al is the crevices in the subsurface.

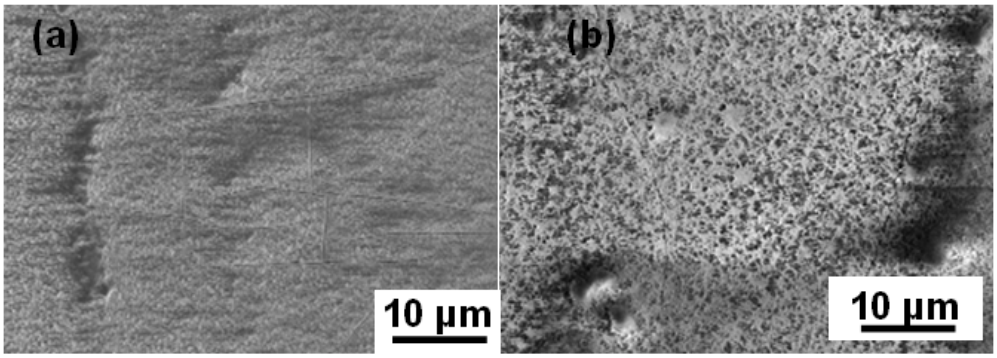

Figure 185. Surface morphologies after 7 days salt spray testing of electrodeposited CeCCs a) without and b) with subsurface crevices.

FIB cross sections of areas of electrodeposited CeCCs with small cracks showed the cross sectional structure of coatings with and without crevices were similar after 7 days salt spray testing (Figure 186). Coating thicknesses were the same as before salt spray testing (400-500 nm). No visible corrosion of the substrate was observed, including in areas where the small cracks extended to the substrate. Some of the small cracks in the electrodeposited CeCCs were observed to extend down to large intermetallic particles in the substrate (Figure 186a), yet the substrate did not visually appear to be corroded. Additionally, an interfacial layer ~10 nm thick was observed between the CeCC and substrate after salt spray exposure. The growth of an interfacial layer may be responsible for some of the increase in impedance noted after salt spray exposure.

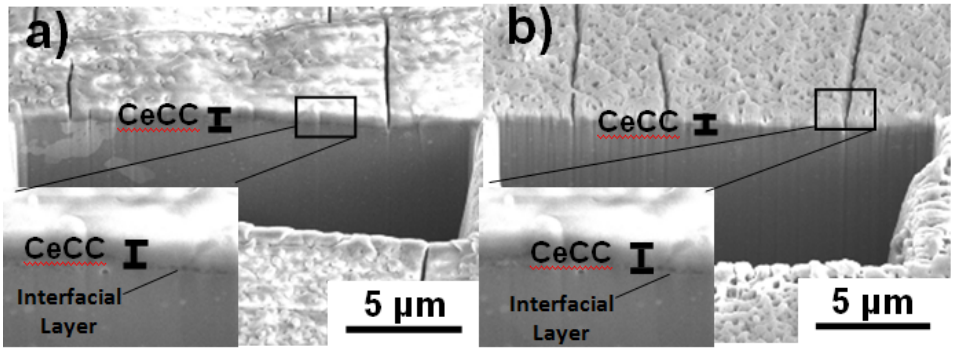

Figure 186. FIB cross sections of areas of electrodeposited CeCCs with small cracks a) with and b) without subsurface crevices after 7 days of salt spray exposure.

No significant differences were observed in the structure or composition of electrodeposited CeCCs with or without crevices after corrosion testing. Thus, the large difference in the change in impedance was likely due to changes in subsurface crevices during salt spray exposure. FIB cross sections of subsurface crevices after 7 days of salt spray testing (Figure 187) revealed that much of the volume that had been open prior to salt spray testing had been filled by a dark, oxygen-rich phase. As a result of the dark oxide formation, only a minimal fraction of the area of the alloy around the crevice was exposed as the dark oxide appeared to cover most of the inner surface of the crevice.

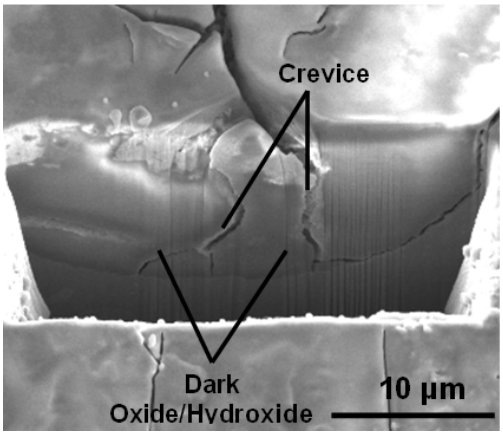

Figure 187. FIB cross section of a subsurface crevice after 7 days salt spray testing.

Cross Sectional Analysis of CeCCs

As-deposited CeCCs were comprised of cerium hydroxide and peroxide species that transformed into $Ce(OH)_4$ and $CeO_2 \cdot 2H_2O$ as the coating aged. These coatings exhibited regions of large cracks (>1 µm wide) on approximately 50 % of the substrate and showed visible corrosion pits and tails after one day of ASTM B117 salt spray exposure. A cross sectional TEM micrograph of the interface between an as-deposited CeCC and the alloy substrate before salt spray exposure is shown in Figure 188a. The average thickness of the interface was measured to be 10 – 20 nm. Chemical analysis performed by energy dispersive spectroscopy (EDS) revealed that the interface consisted predominately of Al and O both before and after salt spray exposure, consistent with the expected presence of native oxide/hydroxide layer on the metal surface. In each case, electron diffraction patterns collected from the interfacial region confirmed its crystallinity, but the patterns could not be indexed to a specific phase.

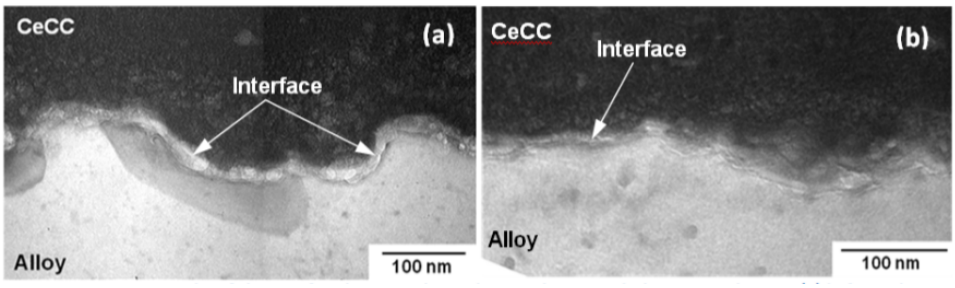

Figure 188. TEM micrographs of the interface between the as-deposited CeCC and Al 2024-T3 substrate, (a) before salt spray exposure (montage), (b) after 6 days salt spray exposure.

Prior to salt spray exposure, the lower half of the as-deposited CeCC (points 3 and 4 in Figure 189) contained Al concentrations in the range of 5 – 6 at. %, which was roughly double the concentrations of 2 – 3 at. % that were measured in the top half of the coating (points 1 and 2 in Figure 189). The increase in aluminum concentration near the coating/substrate interface is believed to be a result of the deposition process in which the combination of dissolved chloride ions and hydrogen peroxide etch the alloy substrate during coating deposition, resulting in the incorporation of aluminum into the CeCC near the substrate. Due to dissolution of aluminum from the substrate, the formation of crevices that can extend up to 10 µm into the alloy has been observed on approximately 10 % of the substrate.

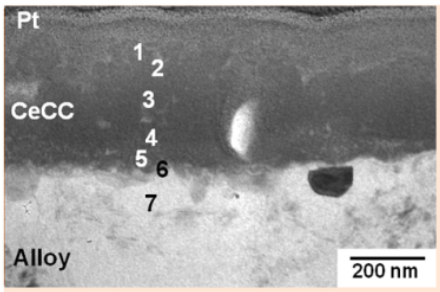

EDS Data (at. %)

Spot	Ce	Al	O	Cl	Pt
1	15	2.5	22	-	5.7
2	16	2.2	27	-	3.9
3	18	4.8	39	-	-
4	19	5.9	36	-	-
5	6.7	48	26	0.6	-
6	-	64	22	0.3	-
7	-	91	2.0	-	-

Figure 189. Cross section TEM with corresponding EDS analysis for as -deposited CeCCs prior to salt spray exposure (balance Cu).

The composition of the interface did not change after 6 days of salt spray exposure but was less uniform and not as well defined. The Al-O layer on the metal surface appeared to have been altered and now contained regions that were 20 – 50 nm thick and distributed unevenly across the interface. Point EDS analysis revealed a higher concentration of Al throughout the entire thickness of the coating after salt spray exposure. Aluminum concentrations near the top and bottom of the CeCC were ≈20 at. %, with concentrations near 8 at. % throughout the middle part of the CeCC. These concentrations were three times higher than those measured prior to salt spray exposure and suggest that Al could migrate through the cerium oxide/hydroxide coating during corrosion testing. Oxygen concentrations in excess of 70 at. % were measured in the bulk of the CeCC, approximately two times higher than values measured before salt spray exposure and may be partly explained by increased coating hydration and/or the formation of aluminum hydroxide within the CeCC. If aluminum dissolution occurred at the interface during salt spray

exposure, Al^{3+} ions could be introduced into the CeCC (and/or be transported to the surface via cracks), causing increased aluminum concentrations. The most likely way for this to occur is by chloride attack of aluminum oxides/hydroxides. EDS analysis consistently confirmed the presence of 1 – 2 at. % chlorine at interfacial regions, but did not detect chlorine in the upper half of the CeCC. These result suggest that the CeCCs were effective barriers to the penetration of chloride ions, but were potentially vulnerable where the substrate was exposed by defects in the coating (i.e., cracks and subsurface crevices).

The as-deposited CeCCs accumulated corrosion product during salt spray testing on more than 50 % of the panel surface. As viewed in cross section by SEM, an Al-O containing corrosion product was seen as a fibrous layer > 1 µm thick on the CeCC surface (Figure 190). Recent work previously discussed in this report has shown that an Al-O containing layer is formed on the surface of CeCCs only when subsurface crevices are present. These crevices, along with the formation of stable pits during salt spray exposure, introduce Al ions to the coating surface where they react to form the Al-O containing regions. Explanation of the migration of aluminum ions from the substrate into the coating is more complex. Potential mechanisms for this to occur include dissolution of aluminum hydroxides by reaction with chlorides at the interface and/or aluminum oxidation enabled by the generation of local pH changes during corrosion. While EDS point analyses shown in Figure 190 do not indicate the presence of chlorine, concentrations up to 2 at. % were intermittently detected along the coating/substrate interface of each specimen examined in this study.

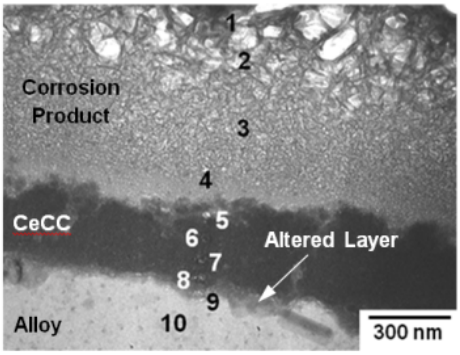

EDS Data (at. %)					
Spot	Ce	Al	O	Cl	Pt
1	-	7.6	?	-	64
2	-	54	22	1.1	12
3	-	62	26	0.6	5.1
4	-	64	26	0.9	4.6
5	8.0	20	50	-	-
6	9.0	8.0	76	-	-
7	8.8	8.2	74	-	-
8	6.1	27	62	-	-
9	0	88	10	-	-
10	-	95	1.5	-	-

Figure 190. Cross sectional TEM with corresponding EDS analysis for as-deposited CeCCs after 6 days of salt spray exposure (quant. analysis in progress) (balance Cu).

Electron diffraction was used to collect structural data from the substrate, the coating/substrate interface, and within the CeCC. Diffuse ring patterns observed from the CeCC are consistent with crystallites less than 10 nm in size, in agreement with previous analyses of similar CeCCs [75].

The diffraction patterns collected from as-deposited CeCCs prior to salt spray exposure revealed several different structures and demonstrated heterogeneity within the as-deposited coating. While some of the patterns could be confidently indexed to stoichiometric cerium oxide ($CeO_2 \cdot 2H_2O$), other patterns most closely corresponded to Ce-O compounds with stoichiometries

between those of Ce(III) and Ce(IV) oxides (e.g., Ce_2O_3 and CeO_2) and could include cerium hydroxy and/or peroxy species for which structural reference data are unavailable, Figure 191 and Table 29. This result is consistent with previously reported XPS analysis that indicated the presence of both Ce^{3+} and Ce^{4+} oxidation states in as-deposited coatings [119-120]. In addition, previously reported grazing incidence XRD of analogous CeCCs showed a single, broad peak centered near 29 degrees two theta that was attributed to nanocrystalline $CeO_2 \cdot 2H_2O$ or $Ce(OH)_4$ [53,83,119]. Heterogeneity within the CeCC could be explained by localized non-uniformity of the deposition process [70,102,108]. Cerium species deposited by a spontaneous process have been shown to first deposit at local cathodes (i.e., intermetallic compounds) on the alloy surface and then deposit on the remainder of the exposed substrate [61]. It is probable that local chemistry gradients are present during coating deposition near these sites, causing local fluctuations in the composition and rate of CeCC formation.

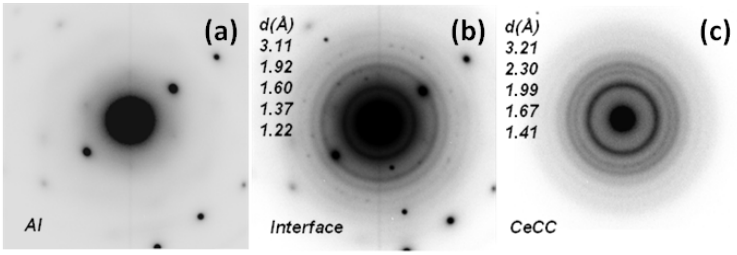

Figure 191. Electron diffraction patterns from as-deposited CeCCs before salt spray exposure, (a) aluminum matrix, (b) interface, (c) bottom of CeCC, and (d) top of CeCC (L = 500 mm).

Table 29. Measured d-spacings (Å) from electron diffraction ring patterns of as-deposited CeCCs before and after salt spray exposure.

Ce_2O_3 PDF 78-0484	CeO_2 PDF 81-0792	As-dep. Before	As-dep. After
3.37	3.12	3.21	3.15
3.03	2.70	2.30	2.71
2.25	1.91	1.99	1.92
1.95	1.63	1.67	1.63
1.68	1.56	1.41	
	1.35		

After 6 days of salt spray exposure, electron diffraction of the as-deposited CeCC indicated the coating had structurally changed. One of the d-spacings measured from as-deposited CeCCs, near 2.7 Å, corresponds to the (200) of CeO_2 and was only observed in coatings that were exposed to the salt spray environment. A summary of the measured interplanar spacings for as-deposited CeCCs before and after salt spray exposure is shown in Table 29. After salt spray, the coatings had become structurally more uniform and $CeO_2 \cdot 2H_2O$ was identified throughout the coating thickness. The more uniform CeCC structure may be a response to the aqueous environment and elevated temperatures encountered during salt spray testing, promoting the transition of cerium hydroxy and peroxy species to the more stable $CeO_2 \cdot 2H_2O$. Grazing

incidence XRD did not provide conclusive evidence of structural changes because peak broadening caused by the coating's nanocrystalline structure obscured subtle changes in Figure 192diffraction angle. Data from EDS analyses showed increased concentrations of aluminum and oxygen within the conversion coating after salt spray testing. The incorporation of aluminum atoms in the cerium oxide structure during deposition (or during salt spray exposure) should affect the crystalline structure and the resulting diffraction patterns. If this process had occurred, the resulting d-spacings should be shifted uniformly, corresponding to the decreased interplanar spacing caused by substitution of smaller aluminum atoms in place of larger cerium atoms. Such evidence could not be confirmed, nor could patterns collected from the CeCC be indexed to known cerium aluminate or aluminum hydroxide species.

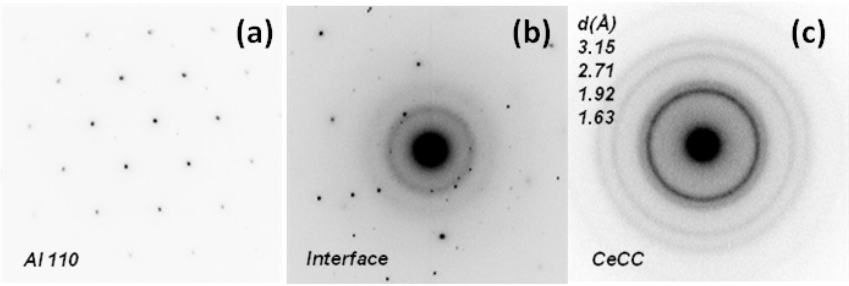

Figure 192. Electron diffraction patterns from as-deposited CeCCs after 6 days salt spray exposure, (a) aluminum matrix, (b) coating/substrate interface, (c) bottom of CeCC, and (d) top of CeCC.

Post-treated CeCCs provide significantly improved corrosion protection compared to as-deposited CeCCs and consistently withstood at least 7 days of salt spray exposure without exhibiting corrosion pits or salt tails. The improved corrosion resistance has previously been attributed to the improved barrier properties brought about by minimizing cracking in the coating as well as the formation of hydrated $CePO_4$ [102].

Analysis of the interface between the post-treated CeCCs and the underlying aluminum alloy substrate before salt spray exposure revealed no differences compared to the as-deposited coatings; the interfacial layer measured 10 – 20 nm in thickness and was predominately comprised of Al, Ce, and O (Figure 193). As shown in Figure 194, EDS analyses across the thickness of the post-treated CeCC revealed a phosphorus concentration gradient through the coating thickness, ranging from 22 at. % at the CeCC surface to 12 at. % at the coating-substrate interface. Consistent with analysis of as-deposited CeCCs, the aluminum concentration in the post-treated specimen was found to increase to ≈6 at. % near the interface whereas the Al value in the center of the coating measured ≈3 at. %.

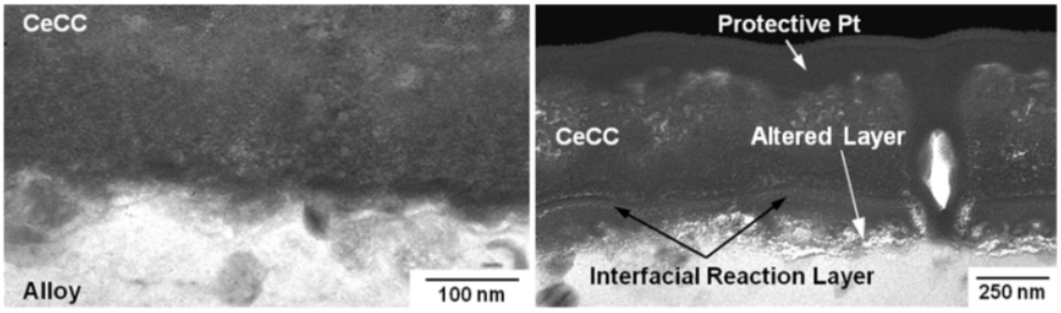

(a) (b)

Figure 193. TEM micrographs of the interface between post-treated CeCCs and Al 2024-T3 substrate, (a) before salt spray exposure (montage), (b) after 7 days salt spray exposure.

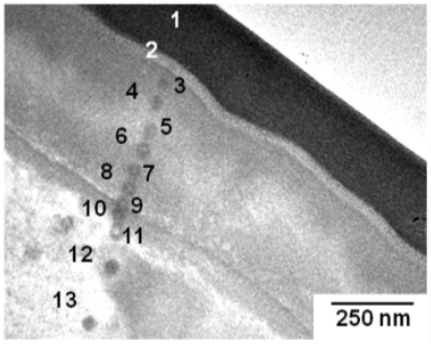

EDS Data (at. %)

Spot	Ce	P	Al	O	Cl	Pt
1	-	-	-	-	-	37
2	-	-	-	-	-	42
3	-	-	-	-	-	51
4	5.1	-	-	-	-	49
5	13	15	4.0	41	-	9.7
6	13	22	2.0	47	0.6	2.3
7	12	19	3.6	46	0.5	-
8	11	15	5.6	46	1.1	-
9	10	11	11	46	1.0	-
10	8.9	0.9	23	47	1.9	-
11	2.7	-	32	42	2.1	-
12	-	-	60	10	-	-
13	-	-	92	2.4	-	-

Figure 194. Cross section TEM with corresponding EDS analysis for post-treated CeCCs prior to salt spray exposure (balance Cu).

Post-treated specimens that did not have visible corrosion pits and tails after 7 days of neutral salt spray exposure responded to the corrosive environment. An interfacial reaction layer measuring 60 – 100 nm thick and comprised of Al, Ce, and O was located between the post-treated CeCC and alloy substrate as seen in Figure 193b and Figure 195. No phosphorous was detected in the interfacial layer, indicating that it was not a phosphate phase. Electron diffraction patterns confirmed the crystallinity of the layer, but the patterns could not be indexed to $CeAlO_3$, or any other Ce-Al containing phases. The layer could also be multiphase, potentially containing a mixture of cerium and aluminum oxides and/or hydroxides. The measured Al concentration in the top and bottom 50 – 100 nm of the post-treated coating was ≈6 at. %, which was about one fourth of the ≈25 at. % that was measured in the as-deposited CeCC after 6 days salt spray exposure. Oxygen concentration within post-treated CeCCs was determined to be independent of salt spray exposure, with concentrations ranging from 42 – 47 at. % in each case. These results suggest that the post-treated $CePO_4 \cdot H_2O$ coating is either a more effective barrier to the movement of Al^{3+} ions through the coating during corrosion or acts in such a way as to limit aluminum dissolution.

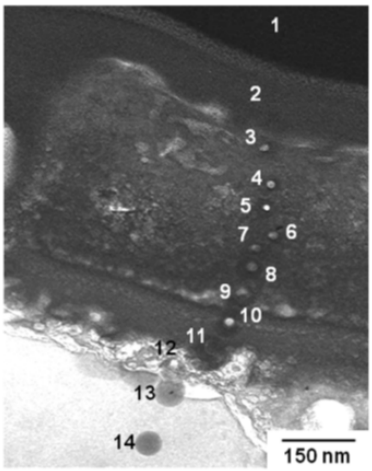

EDS Data (at. %)						
Spot	Ce	P	Al	O	Cl	Pt
1	-	-	-	-	-	40
2	-	-	-	-	-	43
3	6.4	-	14	21	-	21
4	9.4	14	5.6	38	-	6.0
5	9.1	23	0.9	42	-	-
6	10	19	0.8	44	-	-
7	11	19	1.7	42	-	-
8	11	14	5.8	44	-	-
9	9.4	16	5.8	46	-	-
10	8.2	-	19	51	0.8	-
11	9.0	-	25	45	2.1	-
12	-	-	57	29	-	-
13	-	-	87	5.7	-	-
14	-	-	91	1.8	-	-

Figure 195. Cross section TEM with corresponding EDS analysis for post-treated CeCCs after 7 days salt spray exposure (balance Cu).

The d-spacings calculated from diffraction patterns of the post-treated CeCCs before salt spray exposure did not correspond to the rhabdophane phase ($CePO_4 \cdot H_2O$). Similar to as-deposited CeCCs, post-treated coatings were not structurally uniform. Prior to salt spray, some ring patterns had d-spacings comparable to those collected from as-deposited CeCCs not exposed to salt spray, providing evidence that some of the species present in as-deposited coatings may have been unaffected by the post-treatment process (Table 29 and Table 30). In other instances, the d-spacings from post-treated CeCCs were similar to a combination of species such as hydrated cerium hydrogen phosphates or phosphites (i.e., $Ce_2(PO_4)_2HPO_4H_2O$, $CeH(HPO_3)_2(H_2O)_2$) (Figure 196). Patterns were collected throughout the thickness of the CeCC and coating structure did not appear to vary predictably with depth.

Table 30. Measured d-spacings (Å) from electron diffraction ring patterns of post-treated CeCCs before and after salt spray exposure.

$CePO_4 \cdot H_2O$ PDF 35-0614	Post-treated Before	Post-treated After
3.01	3.24	3.05
2.82	2.32	2.80
2.19	2.00	2.22
1.85	1.42	1.82
1.36	1.20	1.36
1.16		1.16

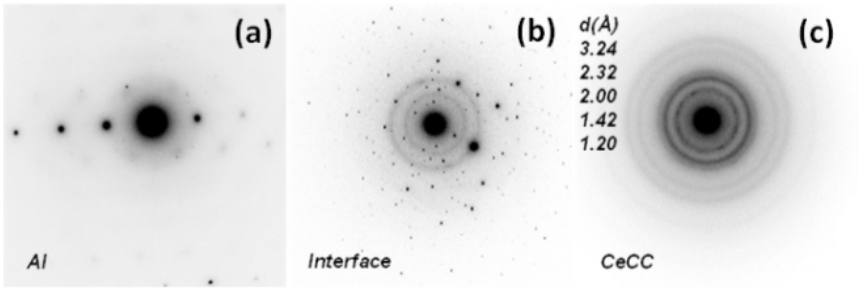

Figure 196. Electron diffraction patterns from post-treated CeCCs before salt spray exposure, (a) aluminum matrix, (b) coating/substrate interface, (c) CeCC (L = 360 mm).

Similar to as-deposited coatings, post-treated CeCCs changed structurally during salt spray exposure. The ring patterns produced by electron diffraction in the coatings were indexed to $CePO_4 \cdot H_2O$, indicating that less stable phosphate species had transitioned to the favored rhabdophane phase during salt spray exposure (Figure 197 and Table 30). In particular, the ring patterns from post-treated CeCCs exposed to salt spray included d-spacings that were not observed for other conditions, most notably those near 2.8 Å and 2.2 Å and are in agreement with standard diffraction files for hydrated $CePO_4$ (Table 30).

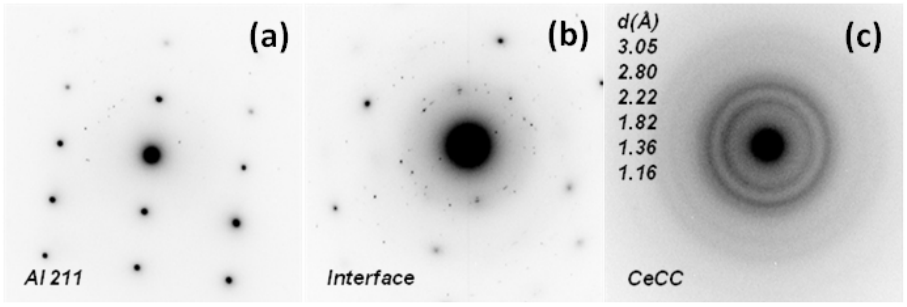

Figure 197. Electron diffraction patterns from post-treated CeCCs after 7 days exposure to neutral salt spray, (a) aluminum matrix, (b) coating/substrate interface, (c) bottom of CeCC, and (d) top of CeCC (L = 500mm).

Solubility of Cerium Species

Solubility studies were conducted to determine if dissolution of cerium species from conversion coatings could play a part in the corrosion protection provided by CeCCs. Standard UV-vis spectra for 1 mM $CeCl_3$ and 1 mM $Ce(ClO_4)_4$ in 0.1 M NaCl are shown in Figure 198. Characteristic peaks were observed for Ce(III) at wavelengths of 252 nm, 240 nm, and 220 nm. Because the highest peak was obtained at 252 nm, all spectra were analyzed at that wavelength for Ce(III) content. Although the UV-vis scan was performed from 3000 to 175 nm, no distinct characteristic peaks were detected above 275 nm. In addition, peaks below a wavelength of 200 nm could not be analyzed due to noise. UV-vis scans were also performed for standard solutions of 1mM $AlCl_3$, 1 mM $CuSO_4$, and 1mM NaH_2PO_4 to identify peaks that could possibly interfere

with analysis of the Ce peaks. No peaks were observed for these solutions in the 240-260 nm wavelength range.

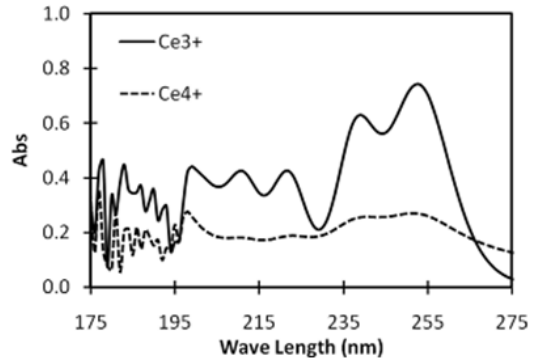

Figure 198. Standard UV-vis spectra obtained for 1 mM $CeCl_3 \cdot 7H_2O$ and 1mM $Ce(ClO_4)_4$ in 0.1 M NaCl solutions.

The UV-vis spectra of the 0.1 M NaCl solution in which as-deposited and sealed CeCCs were immersed at various pH values for 7 hours showed cerium peaks at 252 nm wavelength only when the solution pH was 2.0 (Figure 199). When the solution pH was 3.0, only a small cerium absorbance peak of 0.01 was detected and at pH ≥ 4, no cerium absorbance peaks were detected. Immersion for 250 hours produced peaks at 252 nm wavelength only when the solution pH was 2.0 (Figure 200). Some higher pH solutions showed background absorption; however, no cerium characteristic peaks were observed at 252 nm suggesting that the absorbance was not due to cerium. The absorbance at 252 nm for CeCCs placed in the solution with a pH of 2.0 solution increased from 0.21 after 7 hours to 0.33 after 250 hours for as-deposited panels and from 0.25 after 7 hours to 0.37 after 250 hours for sealed panels. This increase in absorbance over time indicated that either cerium was released during that period or the background absorbance level increased, similar to that observed for CeCCs immersed in higher pH solutions. Therefore, the results indicated cerium was only released from the coatings in NaCl solutions at a pH of 2.0.

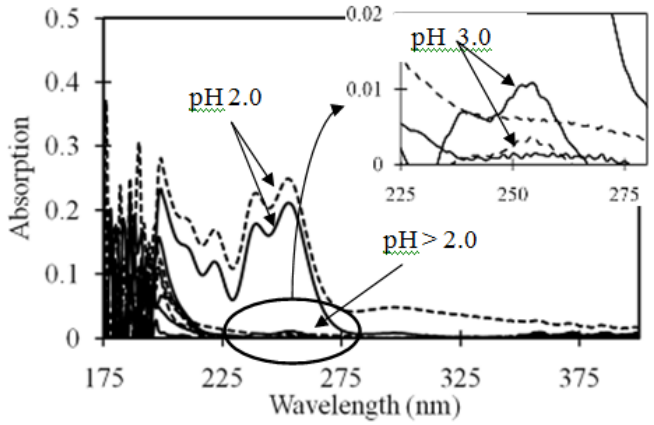

Figure 199. UV-vis spectra of 0.1 M NaCl solutions after immersion of CeCCs for 7 hours. Note: solid lines represent sealed panels and dashed lines represent as-deposited panels.

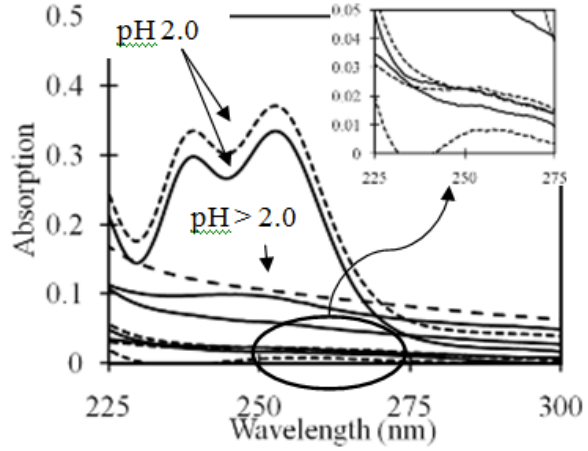

Figure 200. UV-vis spectra of 0.1 M NaCl solution after immersion of CeCCs for 250 hours. Note: solid lines represents sealed panels and dashed lines represent as-deposited panels.

The concentration of cerium released into the solution from the coating was calculated using Beer's law $A = \varepsilon BC$, where A is the absorbance, ε is molar absorbtivity with units of $L\ mol^{-1}\ cm^{-1}$, B is length of the cuvette in which the sample is contained, and C is concentration of the elements in the solution, expressed in mol L^{-1}. Comparing the absorbance of a set of known Ce(III) concentrations to the absorbance of the unknown test sample, an unknown concentration of the test sample can be calculated.

The time study of cerium species released from the coatings into the 0.1 M NaCl solution at pH 2.0 for 250 hours immersion is shown in Figure 201. The S/V ratio was 0.4. The absorbance values were converted to concentration using Beer's law. The time study showed most of the cerium was released during the initial 24 hours of immersion. Another set of experiments with

S/V = 0.25 for pH 2.0 solution was also performed for 500 hours and showed a similar release curve. The sealed panels for the S/V = 0.25 experiment released ~0.40 mM and as-deposited panels released ~0.27 mM at 500 hours. Higher pH solutions did not show characteristic cerium peaks for 500 hours of exposure, even at larger S/V ratio of 1.3. Thus, the time study at pH 2 showed cerium is released mainly during the initial 24 hours.

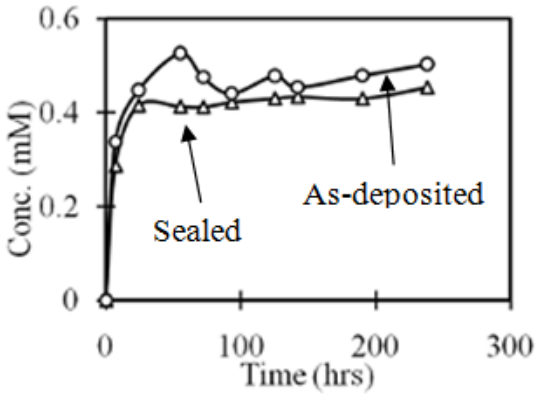

Figure 201. Concentration of cerium species released from CeCCs into 0.1 M NaCl solutions at a pH of 2.0 with a surface to volume ratio of 0.25/cm as a function of immersion time.

The pH of the test solution was measured after 500 hours immersion and showed an increase in pH of ~3 pH units (Table 31). The increase in pH was slightly higher by about ~0.5 pH units for the solutions in which sealed panels were immersed than as-deposited panels. The increase in pH indicates that during immersion the reactions that occurred produced basic species such as hydroxide ions or consumed protons. Release of cerium was only detected at low pH value of 2.0 and the increase in pH after prolonged immersion indicated the release of cerium will stop or decrease to an undetectable value by UV-vis spectroscopy.

Table 31. pH change of 0.1 M NaCl solution before and after immersion of CeCCs in 0.1 M NaCl solution with a surface to volume ratio of 0.25/cm. (Note: 1 indicates an adjusted NaCl solution pH to 2.0 and 2 indicates the natural pH of NaCl)

	Sealed1	As-dep1	Sealed 2	As-dep 2
Initial pH	2	2	~5.7	~5.7
Final pH	5.4	4.6	8.1	7.8

The increase in pH and no detection of cerium at pH ≥ 3 after immersion of the panels in 0.1 M NaCl solution suggests the overall reactions that occur during corrosion generate basic species. After the experiment, dark spots (not shown here) were visible on the coated panels suggesting pitting corrosion had occurred during immersion. One possible reaction that may occur at an anodic site is given in Equation VII:

$$2Al + 6H_2O \rightarrow 2Al^{3+} + 6OH^- + 3H_{2\,(g)} \qquad \text{(VII)}$$

Another reaction that may occur during corrosion that again increases the pH is oxygen reduction at cathodic sites, which is given by Equation (VIII):

$$O_{2\,(g)} + 2H_2O + 4e^- \rightarrow 4OH^- \qquad \text{(VIII)}$$

Combined, these two reactions would increase the pH, which would impede dissolution of cerium.

Solubility diagrams were constructed for $Ce(OH)_3$, $Ce(OH)_4$, and CeO_2 and showed that $Ce(OH)_3$ is the most soluble while CeO_2 is the least soluble (Figure 202). The solubility diagrams were constructed using total cerium species in Equations IX and X obtained from the standard formation constants tabulated in Table 32 [122-124]. Equation X is used for determining the total cerium species obtained from both the dissociation of $Ce(OH)_{4(s)}$ and $CeO_{2(s)}$.

$$\left[Ce(III)\right]_T \rightarrow \left[Ce^{3+}\right] + \left[Ce(OH)^{2+}\right] + \left[Ce(OH)_2^+\right] \qquad \text{(IX)}$$

$$\left[Ce(IV)\right]_T \rightarrow \left[Ce^{4+}\right] + \left[Ce(OH)^{3+}\right] + \left[Ce(OH)_2^{2+}\right] + \left[Ce(OH)_3^+\right] \qquad \text{(X)}$$

Table 32. The water ionization constant and formation constants of cerium (III) and cerium (IV) complexes with hydroxide at 25 °C [68,123-125].

Reaction	Constant
$H_2O = H^+ + OH^-$	$Kw = 10^{-14}$
$Ce(OH)^{2+} \rightarrow Ce^{3+} + OH^-$	$\beta = 10^{-4.8}$
$Ce(OH)_2^+ \rightarrow Ce^{3+} + 2OH^-$	$\beta = 10^{-10.4}$
$Ce(OH)_{3(S)} \rightarrow Ce^{3+} + 3OH^-$	$K_{sp} = 10^{-26.15}$
$Ce(OH)^{3+} + H^+ \rightarrow Ce^{4+} + H_2O$	$\beta = 10^{-14.76}$
$Ce(OH)_2^{2+} + 2H^+ \rightarrow Ce^{4+} + 2\,H_2O$	$\beta = 10^{-28.04}$
$Ce(OH)_3^+ + 3H^+ \rightarrow Ce^{4+} + 3H_2O$	$\beta = 10^{-40.53}$
$Ce(OH)_{4(s)} + 4H^+ \rightarrow Ce^{4+} + 4H_2O$	$K_{sp} = 10^{-51.86}$
$CeO_{2(s)} + 2H_2O \rightarrow Ce^{4+} + 4HO^-$	$K_{sp} = 10^{-63.1}$

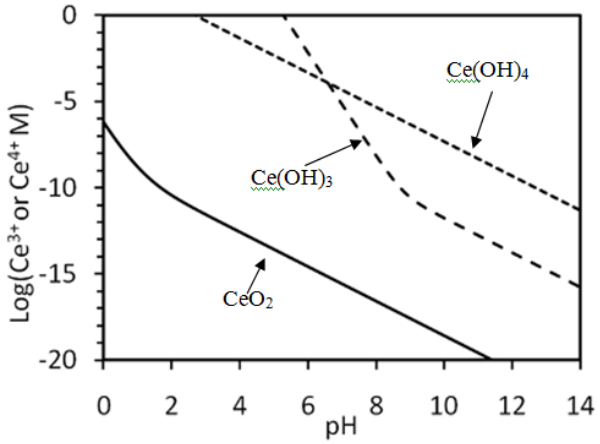

Figure 202. Solubility as a function of pH for $Ce(OH)_3$, $Ce(OH)_4$, and CeO_2.

The solubility diagram showed that $Ce(OH)_3$ exhibited a solubility of 1M at ~pH 5 (Figure 202). The UV-vis experiments did not detect release of cerium at pH ≥ 3 suggesting the coatings do not have significant amount of $Ce(OH)_3$. The solubility diagram in Figure 202 shows the solubility of $Ce(OH)_4$ is significantly lower than $Ce(OH)_3$. At ~pH 4, the amount of total cerium that dissociated was ~0.05M. Part of the coatings may be composed of $Ce(OH)_4$; however, the UV-vis results of 0.4 mM in Figure 201 suggest $Ce(OH)_4$ to be a minimal component of the coating. Based on the detected cerium from the UV-vis results, the majority of the coatings in the as-deposited condition are most probably CeO_2, which is consistent with previous results [120,122]. The limited cerium concentration indicates that the as-deposited coatings are not likely to be able to dissolve and migrate in a manner similar to CrCCs.

The solubility diagram shows that $CePO_4$ has higher solubility than CeO_2 (Figure 202). The solubility diagram was constructed using total cerium species in Equation XI and total phosphate species in Equation XII obtained from the standard dissociation and formation constants tabulated in Table 33.[12,13,16]

$$\left[\mathrm{Ce(III)}\right]_T \rightarrow \left[Ce^{3+}\right] + \left[CeH_2(PO_4)^{2+}\right] + \left[Ce(PO_4)\right] \qquad \text{(XI)}$$

$$\left[PO_4^{3-}\right] \rightarrow \left[PO_4^{3-}\right] + \left[HPO_4^{3+}\right] + \left[H_2PO_4^{3-}\right] + \left[H_3PO_4\right] \qquad \text{(XII)}$$

Where the phosophate ions are given by Equations XIII-XVI.

$$PO_4^{3-} \rightarrow \left(1 + K_1[H^+] + K_1K_2[H^+]^2 + K_1K_2K_3[H^+]^3\right)^{-1} \qquad \text{(XIII)}$$

$$HPO_4^{2-} \rightarrow \frac{\left[PO_4^{3-}\right]\left[H^+\right]}{K_3} \qquad \text{(XIV)}$$

$$H_2PO_4^{2-} \rightarrow \frac{\left[HPO_4^{2-}\right]\left[H^+\right]}{K_2} \quad \text{(XV)}$$

$$H_3PO_4 \rightarrow \frac{\left[H_2PO_4^-\right]\left[H^+\right]}{K_1} \quad \text{(XVI)}$$

Table 33. Dissociation constants for phosphate species and formation constant of cerium (III) complexes with phosphate at 25 °C [68,126-128].

Reaction	Constant
$H_3PO_4 \rightarrow H_2PO_4^- + H^+$	$K_1 = 10^{-2.12}$
$H_2PO_4^- \rightarrow HPO_4^{2-} + H^+$	$K_2 = 10^{-7.21}$
$HPO_4^{2-} \rightarrow PO_4^{3-} + H^+$	$K_3 = 10^{-12.35}$
$Ce(PO_4)_{(s)} \rightarrow Ce^{3+} + PO_4^{3-}$	$K_{sp} = 10^{-26.0}$
$Ce(PO_4) \rightarrow Ce^{3+} + PO_4^{3-}$	$\beta = 10^{-11.73}$
$CeH(PO_4)^+ \rightarrow Ce^{3+} + HPO_4^{2-}$	$\beta = 10^{-4.32}$
$CeH_2(PO_4)^{+2} \rightarrow Ce^{3+} + H_2PO_4^-$	$\beta = 10^{-1.92}$
$Ce(HPO_4)_2^- \rightarrow Ce^{3+} + 2HPO_4^{2-}$	$\beta = 10^{-8.34}$

During immersion in 0.1 M NaCl solution, the only source of phosphate was from the coatings. $CePO_4$ dissociates into Ce^{3+} and PO_4^{3-}. In order to construct the solubility diagram as a function of pH, a fixed concentration of 10^{-13} M total phosphate was used. If a higher concentration of total phosphate such as 10^{-3} M had been used, the solubility of cerium species would have driven to a lower values (Figure 203). The solubility diagram shows even though the solubility product of $CePO_4$ (pK_{sp} = -26) was very similar to that of $Ce(OH)_3$ (pK_{sp} = -26.15), $CePO_4$ was less soluble as the solubility lines were below that of $Ce(OH)_4$. This limited solubility suggests that the release of cerium from sealed coatings is not likely to occur at the pH values typically encounter by high strength aluminum alloys. Therefore, the ability of phosphate sealed CeCCs to protect aluminum alloys against corrosion in NaCl solutions must rely on some mechanism other than dissolution and migration of cerium species. Based on previous analysis, the corrosion protection exhibited by CeCCs may be due to the formation of a Ce-Al-O interfacial layer between the CeCC and the aluminum alloy substrate [75].

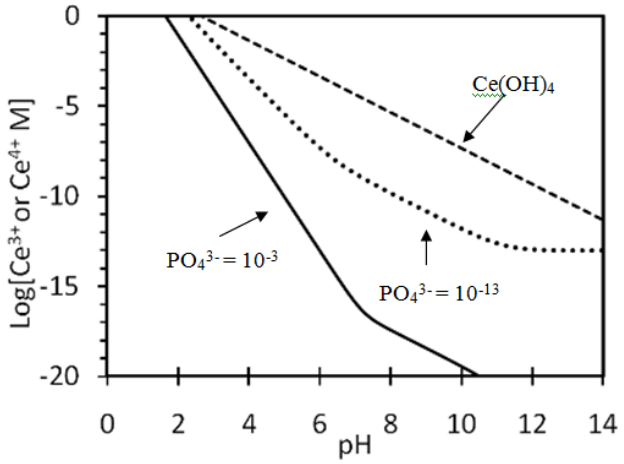

Figure 203. Solubility of $CePO_4$ as a function of pH at two different PO_4^{3-} concentrations. The solubility curve of $Ce(OH)_4$ from Figure 202 was also inserted for comparison.

Solubility of Praseodymium Species

Colormetric UV-VIS assays were performed to study the role of pH and phases present on Pr^{3+} solubility within the primer matrix, which has been determined to be a key factor in corrosion protection. Test panels were prepared using Al 2024-T3 panels with CrCCs and primers formulated with 1) Pr_2O_3 or 2) Pr_6O_{11} as well as the control primer, which was the standard Deft 084 series primer. Small samples (~1 cm^2) were cut from larger test panels and soaked for 2 weeks in ~10 mL of electrolyte with the pH values ranging from 5 to 8. The absorbance of each sample solution was recorded at 650 nm using a colormetric reagent and the concentration of Pr^{3+} leached from the panels was calculated from a calibration curve (Table 34).

Table 34. The concentration of Pr^{3+} leached from (A) Pr_2O_3 primers, (B) Pr_6O_{11} primers, and (C) 084 series primers as detected by UV-VIS spectroscopy and calculated from a calibration curve.

A Pr_2O_3 primer

Initial pH	Concentration Pr^{3+} (mM)
5	4.0±0.97
6	3.0±0.55
7	~1
8	---

B Pr_6O_{11} primer

Initial pH	Concentration Pr^{3+} (mM)
5	~1
6	---
7	---
8	---

C 084 primer

Initial pH	Concentration Pr^{3+} (mM)
5	~1
6	---
7	---
8	---

At a pH of 5, the concentration of Pr^{3+} was ~1 mM from Pr_6O_{11} primer and control specimen (084 primer) while no Pr^{3+} was detected at pH 6, 7, or 8 from these samples (Table 34B and Table 34C). In contrast, for the Pr_2O_3 primer, the Pr^{3+} concentrations range from ~4 mM for the panel soaked at pH of 5 to ~1 mM for the primer soaked at a pH of 7, with no Pr^{3+} detected for the primer soaked at pH of 8 (Table 34A). The results indicate that Pr_2O_3 is more soluble over a

wider range of pH values compared to Pr_6O_{11}. In addition, the presence of gypsum in the 084 primer decreases the solubility of Pr^{3+} at all pH values. This data supports both salt spray exposure results and electrochemical results which showed the primer formulated with Pr_2O_3 to be the most "rapidly" reacting in providing corrosion protection.

A collaborative effort between Ohio State University and the coatings group at Missouri S&T examined the speciation of Pr in various environments. Speciation studies were conducted using a computational approach (OLI Software) for $Pr(OH)_3$ in water at pH=0 to 12 with atmospheric CO_2 present (Figure 204). Multiple Pr hydroxide ions were computed, but at virtually 0 mol concentrations across all pH regimes. At ambient concentrations, CO_2, the predominant Pr species in water is the Pr^{3+} ion in the acid neutral range and $Pr(OH)_3$ precipitates out in the neutral-alkaline regime. Predictions for the precipitation of $Pr(OH)_3$ correlate well with experimental precipitation results showing Pr^{3+} is solubilized at low pHs and precipitation occurs at ~pH=7.

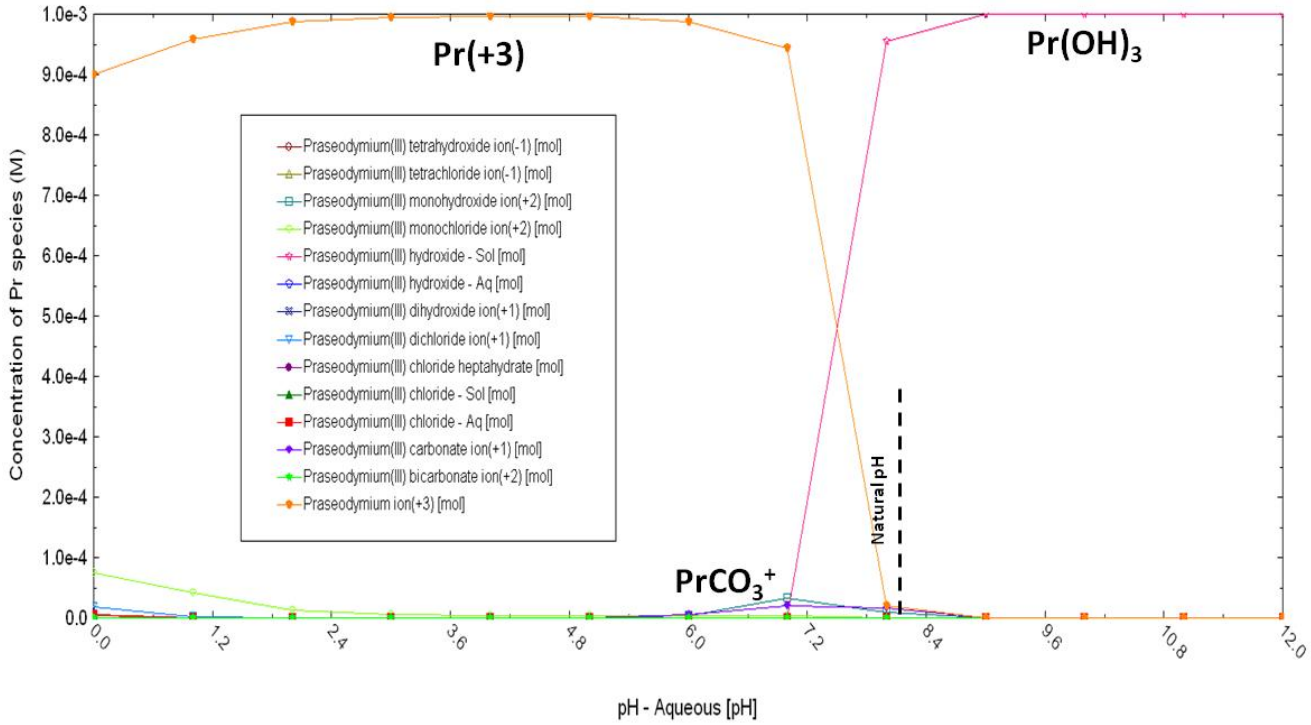

Figure 204. Speciation diagrams as a function of pH generated by OLI software compliments of OmarLopez-Garrity/Rudy Buchheit Fontana Corrosion Center Department of Materials Science and EngineeringThe Ohio State University.

Corrosion Protection of Primers on Non-Chromate Conversion Coatings

Salt spray testing has traditionally been used to evaluate the ability of coatings to provide corrosion protection. As summarized in Table 24, primers deposited on chromate based conversion coatings provided excellent protection through 3000 hrs of salt spray testing. SEM-EDS results (Figure 167 through Figure 171) showed that elongated particles containing praseodymium were prevalent in the scribed areas of primers after salt spray testing. The

elongated particles were typically on the order of 100 nm long. However, only the primers deposited on CrCCs had crystals form during the first 500 hrs of salt spray exposure. The primers provided significant corrosion protection during this time and throughout the entire 3000 hrs of salt spray testing. In contrast, primers deposited on panels pretreated with TCP or cerium based conversion coatings showed significant corrosion during the first 150 hrs of exposure and no Pr-rich particles were detected by SEM-EDS in the scribed areas. For these panels, the degree of salting appeared to increase through ~1500-2000 hrs of exposure. After 1500-2000 hrs of salt spray exposure, praseodymium-rich particles were seen in the scribed areas of primers deposited on panels pretreated with TCP or cerium-based conversion coatings. At the same time, the extent of salting seemed to stabilize for these samples. Coupled with results from other studies, the results of this study suggest that pretreatments affect the transport and formation of praseodymium-rich particles. In addition, the appearance of the praseodymium-rich particles coincides with a decrease or cessation of corrosive activity in scribed areas of test panels. For primers on CrCCs, the Pr-rich particles form during the initial stages of salt spray and the primers provide significant corrosion protection throughout the duration of testing. For panels on other pretreatments, Pr-rich particles do not form until after 1500 to 2000 hrs of testing. Prior to particle formation, the scribes continue to salt, which is evidence of corrosive activity. After the Pr-rich particles appear, corrosive activity decreases.

An aspect of the present study has been correlating the salt spray results to electrochemical testing. Figure 135 shows the electrochemical measurement setup when the drilled pit method is used. The direct electrical connection is assumed to be electrode-electrolyte-aluminum-electrode with no permeation of the electrolyte into either the paint or the conversion coating. It is also assumed that transport of inhibitors may occur from the paint to the site of corrosion in the drilled pit. This model could also allow for transport of inhibitors from the pretreatments to the site of corrosion.

Figure 205 shows the experimental setup employed when no drilled pits were used. This set up was used for testing before salt spray exposure. If the electrolyte has little or no permeation into the paint, then the electrical double layer will be located at the electrolyte-paint interface. The three electrical interfaces of interest in this analysis are: electrolyte-EDL-paint; paint-conversion coating; and conversion coating-aluminum. The presence of these interfaces affects the phase angle for panels analyzed before salt spray testing as shown in the example below (Figure 206).

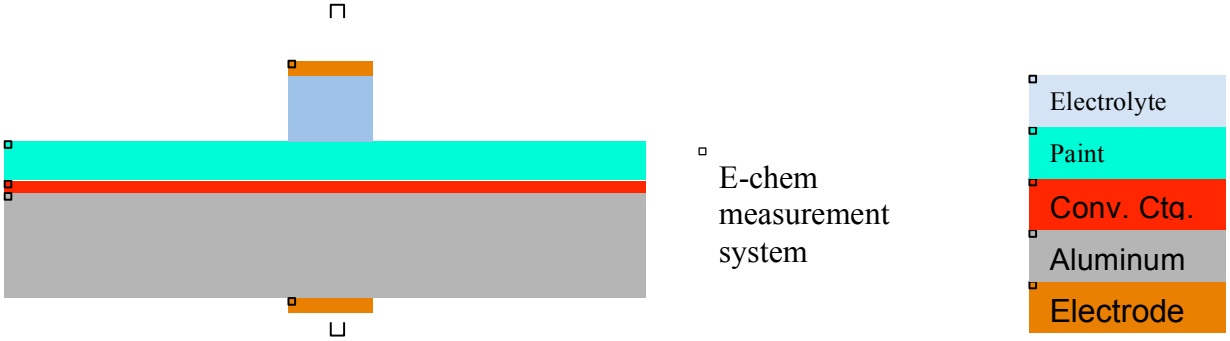

Figure 205. Electrochemical measurement setup without drilled pits used at testing before salt spray exposure.

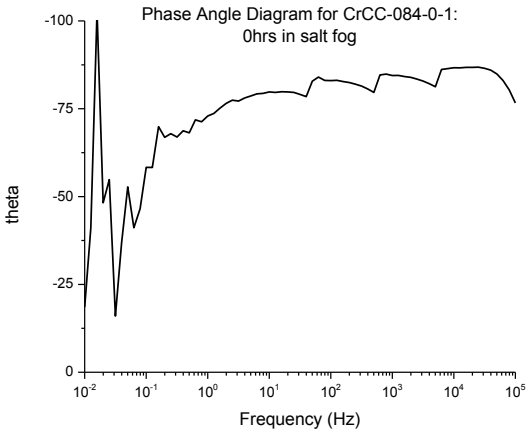

Figure 206. Example phase angle diagram showing high frequency features due to interfaces in the coating system.

When a sample has been in salt spray for 3000 hrs, about 60 wt% of the calcium sulfate is lost from the paint film by dissolution, which leaves a porous structure. The conversion coating material may also be lost. At this point, the electrolyte can permeate the paint and possibly the conversion coating, thereby making direct contact with the substrate and allowing ionic species to contact the substrate. In tests done without drilled pits (Figure 207), no phase angle drop is expected, although one is possible due to the conversion coating-aluminum interface. Because of the increased porosity of the paint after salt spray testing, which allows permeation of the electrolyte into the paint, a reduction in impedance is expected as well as an increase in capacitance. Also expected is an increase in the number of time constants since electrical double layers can form at the surface of the paint, the paint-conversion coating interface, and possibly the conversion coating-aluminum interface.

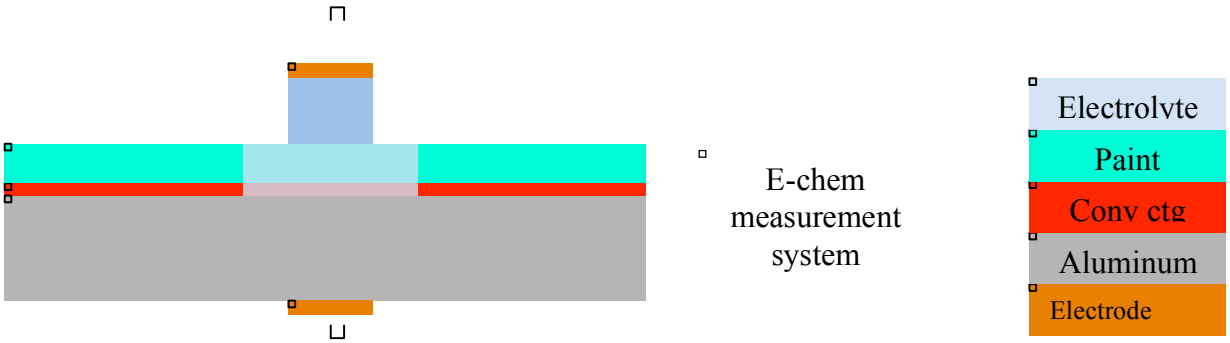

Figure 207. Electrochemical measurement setup used for primers without drilled pits for panels examined after 3000hrs of salt spray testing

Figure 208 shows the case of a drilled pit being used on a panel with permeable films. Ionic conduction takes place directly in the pit from electrolyte to the substrate. In parallel, ionic conduction through the paint is also possible. The two different conduction paths are likely

responsible for the very complex behavior seen for panels after exposure to salt spray where 2-4 time constants were seen. These time constants would correlate to the following interfaces (double layers): electrolyte-paint; paint-conversion coating; conversion coating-aluminum; and electrolyte-aluminum. While the electrolyte-aluminum conduit presumably has the lowest resistivity it also has a surface area that is a factor of about 50 smaller than the paint conduit based on the relative sizes of the drilled pits and the cell used for electrochemical testing.

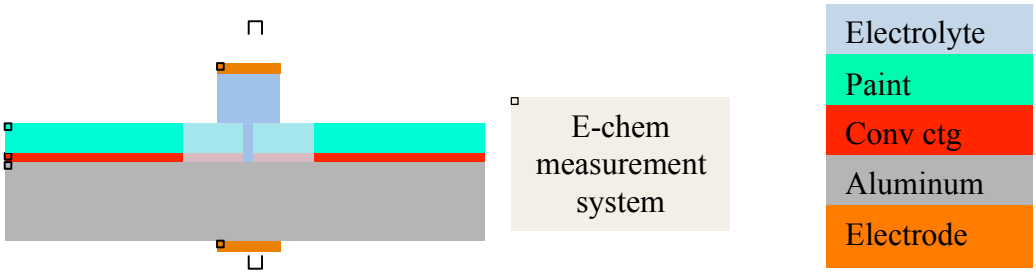

Figure 208. Electrochemical measurement setup for testing with drilled pits after 3000hrs of salt spray testing

Task 6: Final Model Development and Application

The overall goal of this project was to determine the mechanisms by which rare-earth based compounds provide corrosion protection to high strength aluminum alloys. The research focused on two specific coating systems, cerium-based conversion coatings and an epoxy-polyamide primer containing a praseodymium-based inhibitor package. These coatings were selected based on demonstrated corrosion protection. The approach taken in the research was to characterize the phases present before and after corrosion and changes in electrochemical response during corrosion to elucidate, which, if any, species that dissolved from the coating during corrosive attack, were transported from the coating to the site of damage/attack, and then reacted to passivate corrosion. As described below, significant progress was made toward understanding the critical steps in the corrosion protection mechanisms of both types of coatings.

Cerium-Based Conversion Coatings

Based on the results for Task 5 described above, it is proposed that the growth of the dark oxide / hydroxide in crevices during corrosion testing was responsible for at least part of the impedance increase that was observed in crevice-containing coatings during salt spray exposure. The proposed mechanism by which crevices were passivated by oxide / hydroxide formation is illustrated in Figure 209. Prior to salt spray exposure, the subsurface crevices are connected to the external environment through the large cracks observed in the coating (Figure 209a). A relatively thick (~1 μm) oxide / hydroxide that was present after crevice formation surrounds most of the inner surface of crevices, although some areas of the substrate are exposed. Processing after crevice formation, particularly post-treatment, altered the structure and composition of the oxide / hydroxide such that it became more resistant to corrosion, preventing these areas from corroding during the initial stages of salt spray exposure.

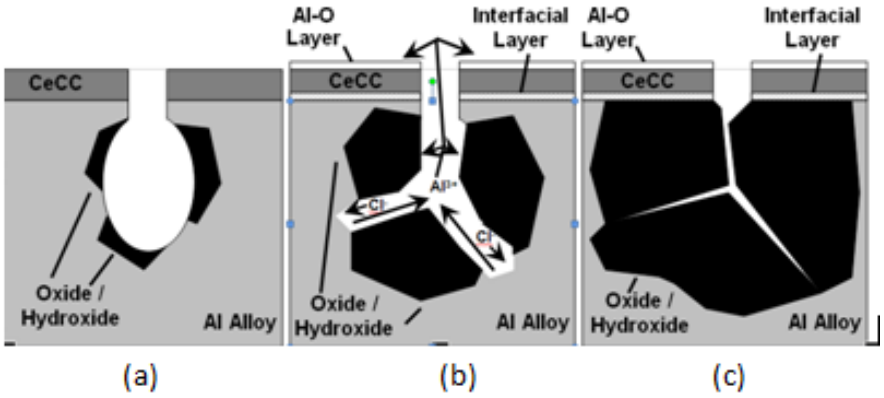

Figure 209. Proposed mechanism of the passivation of subsurface crevices.

Some corrosion occurred in the crevices during salt spray exposure as was evident by the layer rich in Al and O that was observed on the surface of the CeCCs after salt spray testing. During early stages of salt spray exposure (Figure 209b), it is likely that electrolyte solution penetrated into the crevices, causing limited corrosion in areas where the crevices were not protected by a thick oxide layer. Exposure to salt spray testing appears to lead to aluminum dissolution from exposed areas and the aluminum could then be transported out of the crevice to the surface where it forms the surface layer that has been observed. Although limited dissolution continues inside the crevices, it does not result in the formation of salt tails on the surface of the coating.

In addition to the aluminum that is presumably produced by substrate dissolution and transported out of the crevices, some of the aluminum appears to deposit on the inner surface of the crevices, effectively restricting transport of electrolyte into or aluminum out of the crevices (Figure 209c). Dissolution of aluminum will increase the size of the crevices. However, due to the volume increase associated with conversion of aluminum metal to aluminum hydroxide (200 - 320% increase in volume depending on whether boehmite or gibbsite is formed), limited aluminum dissolution could result in formation of both a layer rich in Al and O on the CeCC surface and additional aluminum oxide / hydroxide in the crevices. The increase in impedance would not require the entire network of crevices to be filled, but could be limited to the most active areas. Once hydroxide fills the crevice to the extent that the electrolyte is prevented from reaching the substrate, corrosion would be inhibited. The passivation of crevices by hydroxide growth appears to be consistent with both the increase in impedance and the enhanced corrosion protection of coatings with crevices.

Although coatings with subsurface crevices offer significant corrosion protection, subsurface crevices are not necessary for CeCCs to exhibit corrosion inhibition. Crevice-free coatings, which had cracks that extended through the CeCCs to the Al alloy substrates, did not exhibit growth of a layer rich in Al and O on the surface nor did they have subsurface crevices that would allow for controlled corrosion in select areas. Yet, crevice-free coatings still exhibited significant protection, as indicated by the increase in the impedance of the coating after 24 hours of salt spray exposure and the suppression of pitting/tailing for up to 336 hours of salt spray testing. Hence, development of the interfacial layer between the coating and substrate appears to play a critical role in corrosion protection. Further, the formation of an interfacial layer coupled

with the build up of protective oxides / hydroxides on CeCC surfaces and/or in subsurface crevices indicate that CeCCs are not simply barriers that prevent contact of corrosive species with the Al alloy substrate, but provide active corrosion protection.

The structure of as-deposited and post-treated CeCCs changed during salt spray exposure, with each coating becoming structurally more uniform. These changes may be caused by the transition of species present after coating deposition (i.e., cerium hydroxy/peroxy compounds for as-deposited coatings, cerium hydrogen phosphate compounds and/or unreacted hydroxy/peroxy species for post-treated coatings) to favored $CeO_2 \cdot 2H_2O$ or $CePO_4 \cdot H_2O$ phases respectively. The change in coating structure and formation of an interfacial reaction layer during salt spray exposure suggests that the protection mechanism of CeCCs extends beyond that of a static barrier coating and demonstrates that CeCCs can exhibit an active response to the salt spray environment.

The growth of an interfacial reaction layer in post-treated specimens (Figure 193), and its corresponding absence in as-deposited specimens, has important implications for the processes that may be responsible for the improved corrosion performance observed from post-treated CeCCs and may help explain their improved electrochemical properties (i.e., more anodic pitting potentials and larger charge transfer resistances). Pinc et al. used electrochemical impedance spectroscopy to evaluate the electrochemical response of CeCCs as a function of salt spray exposure time and reported an increase in charge transfer resistance with salt spray exposure time up to 336 hours of exposure for post-treated specimens [118]. Upon reaching 336 hours, the charge transfer resistance of post-treated CeCCs was found to decrease, corresponding to the observed formation of corrosion pits. The increased resistance before 336 hours was attributed to the development of a surface layer on top of the CeCC that was rich in aluminum and oxygen. The surface layer was detected by Auger electron spectroscopy (AES) depth profiles. As-deposited specimens were also found to exhibit an increased aluminum concentration near the surface during salt spray testing, but did not exhibit an impedance increase. As a result, it was hypothesized that the $CePO_4 \cdot H_2O$ phase facilitated the formation of a protective alumina layer on the outer surface of the CeCC. The present study confirmed the higher aluminum concentrations near the surface of as-deposited and post-treated CeCCs after salt spray exposure, but, in contrast, proposes the increased impedance is a result of the interfacial reaction layer that forms between the CeCC and the aluminum alloy substrate.

Analysis after salt spray provided no evidence that chloride ions had migrated through either as-deposited or post-treated CeCCs. The EDS analyses performed on as-deposited or post-treated CeCCs did not reveal the presence of chlorine in the top half of the CeCC after one week of salt spray exposure and indicated that the coating was an effective barrier to chloride ions. Chlorine was only detected in the corrosion product on the surface of as-deposited CeCCs and intermittently detected at the coating/substrate interface in both as-deposited and post-treated CeCCs. This analysis also supports the hypothesis that pitting corrosion initiates from sites that are presumably more electrochemically active (i.e., regions containing subsurface crevices) and not by attack/penetration of the CeCC by chloride ions. Prior to salt spray exposure, the presence of chlorine at the interface is believed to be a result of the deposition process in which chloride ions were trapped at or near the interface during the initial rapid formation of the coating. However, additional chloride ions may be introduced to the interface during salt spray

exposure (where cracks in the CeCC extend to the substrate). An altered region consisting of aluminum, oxygen, and ≈1 at. % chlorine was detected just above the alloy substrate in as-deposited and post-treated specimens after salt spray exposure (labeled in Figure 188 and Figure 193). This layer is believed to be a form of aluminum hydroxide, which may not be stable in the presence of chloride ions. The presence of cracks and other defects enable chloride ions to react with the aluminum hydroxide or hydrated oxides at the coating/substrate interface and take up positions on oxygen vacancy sites and/or lead to formation of soluble aluminum chloride species [113]. Such a reaction could produce additional oxygen vacancies at the interface, potentially allowing for the migration of chloride ions along the interface, leading to the formation of the altered layer, shown schematically in Figure 210a. Attack of the aluminum hydroxide could facilitate a reaction with neighboring Ce species, potentially forming a non-stoichiometric cerium aluminate at the interface. A change in pH near the interface may also influence the stability of cerium or aluminum species, potentially facilitating species migration and the formation of a more stable phase(s) (Figure 210b). Continued introduction of chloride ions would increase aluminum dissolution, providing a mechanism by which aluminum ions are continually generated and either incorporated into the interfacial reaction layer (for post-treated CeCCs), transported into the CeCC, or released to the surface via cracks. The formation of corrosion pits was not observed at crack/substrate interfaces, nor was the interfacial layer determined to bridge this gap, indicating that post-treated CeCCs provided limited electrochemical protection of the alloy substrate exposed by coating defects.

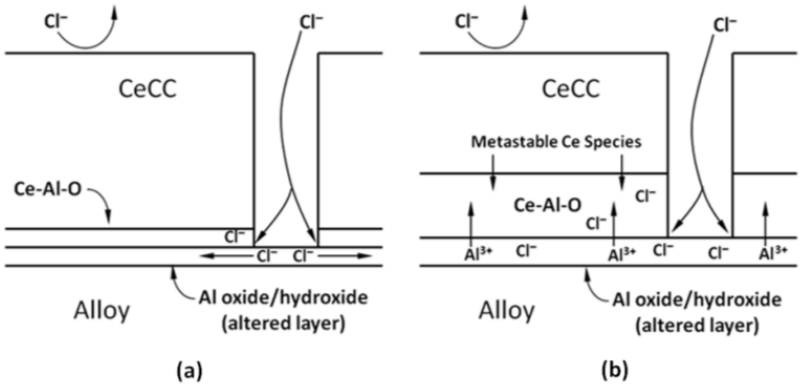

Figure 210. Potential mechanism of interfacial reaction layer formation for post-treated CeCCs during (a) initial formation of altered layer by chloride ion attack and migration at the interface, and (b) after continued chloride exposure, chloride facilitates aluminum dissolution from the altered layer, releasing it towards the CeCC where it reacts with metastable cerium compounds to form the interfacial phase(s).

Praseodymium-Based Inhibitor in Epoxy-Polyamide Primer

With knowledge gained from salt spray exposure, XRD, SEM-EDS, phase stability, and LA ICP-MS, a schematic outlining a proposed corrosion protection mechanism of Pr-primers on CrCC was developed (Figure 211). Gypsum is an acidic extender, which controls the pH in the primer matrix. The presence of gypsum apparently stabilizes the matrix pH between 2 and 7, since that is the range in which Pr^{3+} is soluble. Once outside the primer matrix, the dissolved Pr^{3+} ions precipitate out of solution, presumably at around pH of 7 as $Pr(OH)_3$, which then reacts with CO_2

in the air to form the hydroxycarbonate species that are detected after exposure to a corrosive environment. Post-mortem analysis of corroded specimens has identified Pr-rich clusters in areas of the scribe prone to salting. Further analysis by SEM-EDS revealed that the substrate beneath the precipitates was rich in Cu and Fe compared to the alloy matrix. Hence, the activity of the exposed metal may influence the response of the primer, most likely due to variations in local pH during salt spray exposure. In addition to the local pH, the presence of CrCCs must influence re-precipitation of Pr-species, since panels with other pre-treatments do not perform as well in salt spray testing.

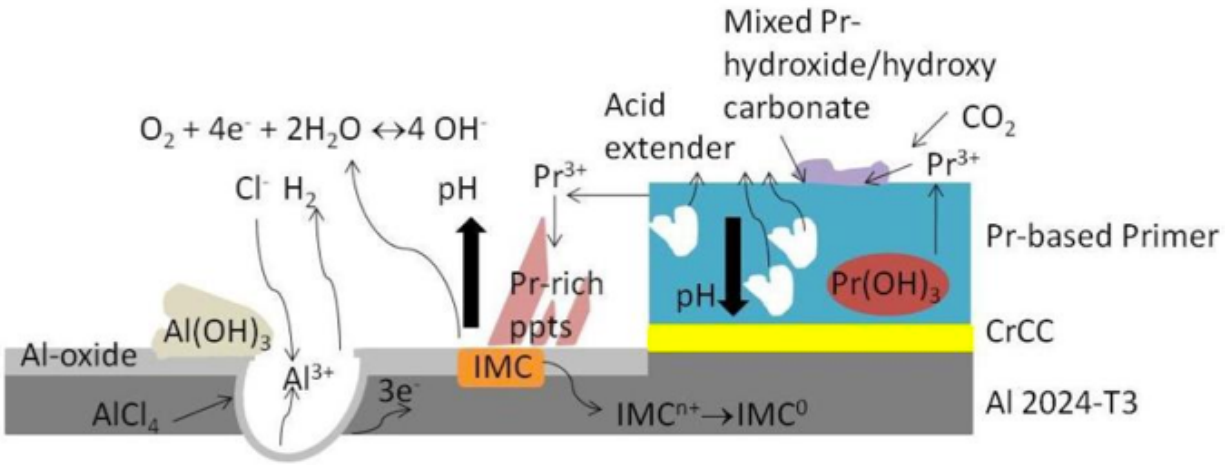

Figure 211. Schematic outlining a proposed corrosion protection mechanism of Pr-primers with CrCC on Al 2024-T3.

Figure 211 shows the mechanistic model developed previously[4] for Pr-containing primers deposited on aluminum alloy substrates with Cr conversion coatings. Pr-species dissolve in the relatively low pH environment of the primer, which is buffered by the use of an acid extender in the primer matrix. The dissolved Pr-species then transport out of the primer. Some of the Pr-species precipitate at electrochemically active sites on the alloy surface due to the higher pH environment. The Pr-rich precipitates then inhibit further corrosion of the alloy surface. This model explains the efficacy of the Pr-primer system when used with Cr conversion coatings. However, the model does not explain the difference observed when the same primer is deposited on non-Cr surface pretreatments such as TCP or cerium-based conversion coatings.

Several possible explanations exist to explain the differences in protection between substrates with CrCCs and those with other pretreatments. The differences could occur due to changes in any of the main steps involved in the corrosion protection mechanism (dissolution of Pr-species from the primer, transport, precipitation at electrochemically active sites), but changes to the precipitation process were deemed more likely than the other two due to the differences in the timing of the appearance of large Pr-rich precipitates during corrosion testing of the primers on the different types of pretreatments. Some of the possible changes that could affect the precipitation of Pr-rich particles include: 1) the pH at the electrochemically active sites is too low for precipitation to occur for other pretreatments; 2) precipitation occurs, but the crystals do not bond to the site and are washed off in the salt spray; 3) migration of Cr^{6+} species may facilitate transport of Pr species to the scribe whereas Ce only migrates at high pH and TCP not

at all, so Cr^{6+} transport may significantly influence Pr transport; and 4) other (heretofore unidentified) electrochemical processes may interfere with precipitation. The first possibility seems unlikely since electrochemical testing conducted as part of other research has revealed that CeCCs perform well when the pH of the test electrolyte is ~4 and greater than or equal to 8. Further, other research has shown that CeCCs exhibit no migration of species in corrosive environments. So, in the case of CeCCs, it seems unlikely that their use under Pr-containing primers would interfere with precipitation in scribed areas where the primer and pretreatment have been removed. The second possibility also seems unlikely since Ce species are unlikely to transport to the scribed areas. For the final suggestion, it may be possible that the pretreatment impacts electrochemical processes that are occurring in the scribed areas and/or at the primer-pretreatment or pretreatment-substrate interfaces that impact the protection mechanism. Further research is needed to identify possible processes and to determine which ones interfere with precipitation of Pr-rich particles during corrosion.

Summary of Technical Accomplishments

A number of technical accomplishments were achieved during the course of this project. The philosophy that guided the project throughout its course was that rare earth compounds were not inherently protective, but protection required that the appropriate rare-earth compound was present in an appropriate phase in the right type of coating. The results throughout the project reinforced this initial hypothesis and helped elucidate corrosion protection mechanisms. The significant progress made in each year of the projects is summarized.

Year 1

The phase stability of Pr-O species (Task 2) was investigated. Initially, the phase changes that occur spontaneously under atmospheric conditions leading to the hydration and/or carbonation of Pr_2O_3, Pr_6O_{11}, $Pr(OH)_3$, and $Pr_2(CO_3)_3 \bullet 8H_2O$ were studied. Later, precipitation studies were used to study the effects of varying conditions on the solubility of precipitation products generated. Progress was also made toward the goals of the other tasks. Both CeCCs and primer coatings were deposited using standard procedures. Preliminary characterization of test panels identified species present in the field as $Ca_2SO_4 \bullet 2H_2O$, $Pr(OH)_3$, and TiO_2 along with Ca and Pr species formed in the scribe in response to corrosion. Using FIB machining, the presence of sub-surface damage was identified for CeCC-coated Al 2024-T3 and Al 7075-T6. Based on this discovery, the project team proposed to change the scope of the studies to focus additional effort on understanding the role of the sub-surface damage during corrosion. New electrochemical techniques were developed to add the capability of site-specific analysis of specific areas of test panels (e.g., inside scribes, near corrosion pits, etc.). The physical characterization, electrochemical characterization, and performance evaluation of test panels continued throughout. The results from Year 1 provided information about the phase stability of rare-earth systems that was necessary to understand and interpret characterization and electrochemical test results.

Year 2

An on-going review of the technical literature was used to gather information related to phase stability of rare-earth species, the deposition of CeCCs, and microelectrochemical testing. The

phase stability of Pr compounds was explored, with emphasis on species relevant to the corrosion inhibitor used in the Deft primer. Two deposition methods were investigated to produce CeCCs without developing sub-surface voids. In the first, immersion deposition was used to deposit coatings without sub-surface voids using a deposition solution in which some of the oxidizer (H_2O_2) was replaced by an alternate compound. The second approach replaced some or all of the chloride ions with nitrates. Although coatings could be deposited using each approach, none of these coatings provided significant corrosion protection. The evolution of composition and structure were characterized for CeCCs and primers as they were exposed to corrosive environments. Analytical methods and electrochemical tests provided complementary information about changes in coatings during corrosive attack. Overall, the results provide the necessary background to begin formulating and testing hypotheses related to the corrosion protection mechanisms of coatings based on rare-earth compounds.

Year 3

During Year 3, models for corrosion protection mechanisms were established for CeCCs and experiments designed to evaluate the role of each component of an epoxy-polyamide primer were designed and conducted. The toxicity of rare-earth elements was investigated in the technical literature. Phase stability studies were finalized. Research continued on deposition of CeCCs without developing sub-surface crevices, which provided valuable insight into the corrosion protection mechanisms of these coatings. Results showed that using less aggressive activation solutions (Na_2CO_3) for the surface pre-treatment of Al7075-T6 not only led to deposition of uniform coatings with fewer cracks and craters, but also produced coatings with the best corrosion performance with fewer subsurface crevices. Electrodeposited CeCCs without subsurface crevices had similar thicknesses, compositions, morphologies, and corrosion response compared to spray deposited CeCCs with subsurface crevices. The evolution of composition and structure were examined for CeCCs and primers with Pr-based corrosion inhibitors was completed as a function of time in corrosive environments. Analytical methods and electrochemical tests provided complementary information about changes in coatings during corrosive attack. Results from these tasks were combined to develop hypotheses for the corrosion protection mechanisms. Work has shown that corrosion protection afforded by CeCCs occurs through the generation of an interfacial layer between the surface of CeCCs and the substrate. Protection was also dependent upon the growth of hydrated aluminum oxide in sub-surface crevices that were connected to the external environment through cracks in the coatings. Although the protection mechanism model for the primer was not finalized, preliminary results indicated the corrosion response of Pr-primers was affected by pH and atmospheric conditions resulting in re-precipitation of Pr-rich species at sites prone to attack.

Year 4

In the final year of the project, progress was made in two main areas. One area was in the deposition of CeCCs on aluminum alloys used for casting including AA 380 and AA 413. This work was motivated by industrial interest in developing environmentally-friendly and energy conscious methods for corrosion protection. Although the silicon content of the alloys was anticipated to cause problems with deposition, CeCCs that were able to provide significant corrosion protection were deposited on AA 380 by adding a high temperature water rinsing step to the standard surface preparation process. The other area of progress was in examining the corrosion protection offered by an epoxy-polyamide primer containing a Pr-based corrosion

inhibitor package on alternative surface pretreatments. Specifically, Deft's GN084 primer was deposited on AA 2024-T3 substrates that had been treated with either a chromate conversion coating, an electrodeposited CeCC, a spray-deposited CeCC, or trivalent chromium passivation (TCP). The primer demonstrated the ability to provide at least some corrosion protection for all four cases. However, the appearance of Pr-rich crystals in scribes, which was correlated to the ability to provide protection, was delayed in the three alternative pretreatments compared to panels with chromate conversion coatings. Whereas primers on chromate conversion coatings could protect scribes from corrosion for the duration of testing in salt spray for at least 2000 hours, primers on the other pretreatments only began to inhibit corrosion after an induction period of somewhere between 1000 and 1500 hours.

Accomplishments

Throughout the course of the project, steady progress was made toward the overall goal of devising corrosion protection mechanisms for rare-earth based coatings. The most significant contributions of this project were:

- An increased fundamental understanding of the phase stability of praseodymium compounds. At the outset of the project, technical literature was available on the phase stability of cerium compounds, the composition and structure of cerium-based conversion coatings, and the corrosion response of cerium-based conversion coatings whereas very limited information had been published regarding similar subjects for praseodymium. Information on thermal decomposition, precipitation studies, and solubility was generated and disseminated.
- Discovery of sub-surface crevices along with development of methods to mitigate their formation during CeCC deposition. Sub-surface crevices are caused by the combination of chloride ions and oxidizers such as hydrogen peroxide in the cerium coating bath. Although this combination of compounds promotes rapid coating deposition, it also attacks the substrate leading to crevice formation. Spontaneous and current driven methods were developed to produce coatings without damaging the underlying substrate.
- Modified microelectrochemical test methods to characterize cerium-based conversion coatings. Microelectrochemical test methods had been used by others to study the behavior of intermetallic compound precipitates in aluminum alloy matrices. In this project, the methods were modified and extended to study the corrosion behavior of cerium-based conversion coatings. Coating surface features were examined and correlated to areas that provided strong protection or that were susceptible to corrosion. Specific surface features that could be identified from optical microscope observations were shown to be the likely sights of the initiation of corrosion pits.
- Developed electrochemical methods to characterize the protective behavior of primer coatings. During the course of the project, artificial defects (i.e., holes milled through the primer to the underlying aluminum substrate) were employed to study the corrosion response of the praseodymium-based inhibitor. Primer-coated panels were examined as a function of exposure time in ASTM B117 salt spray and as a function of electrolyte pH to understand the coating response. Using this method, coatings were found to passivate corrosion at elevated electrolyte pH values (e.g., pH = 8), but not at lower pH values (e.g., pH = 5). These methods could be used to quickly (i.e., in a few minutes) assess the

ability of coatings to provide corrosion protection as compared to weeks for conventional methods such as salt spray testing.

- Devised a corrosion protection mechanism for cerium-based conversion coatings. Initially, cerium-based conversion coatings were thought to protect the underlying high strength aluminum alloy substrates primarily as barrier coatings with some ability to protect damaged areas or other flaws in the coatings. The discovery of sub-surface crevices meant that the coatings were not only protecting areas of undamaged substrate beneath the coatings, but also sub-surface crevices with relatively high surface areas that were exposed to the external environment by cracks through the coatings. Cerium-based conversion coatings protect the underlying substrate by developing an altered layer at the coating-substrate interface and promote protection of sub-surface crevices by allowing for formation of a protective hydrated aluminum oxide inside the crevices. Both mechanisms are needed when coating deposition leads to the formation of sub-surface crevices while only the former seems to be active for coatings deposited without forming sub-surface crevices.
- Elucidation of the corrosion protection mechanism of praseodymium-based inhibitors in epoxy-polyamide primers. Phase stability studies showed that the praseodymium species that was incorporated into the primer, namely Pr_2O_3, reacted with water and carbon dioxide in the ambient environment to form hydroxycarbonate species. In addition, solubility and precipitation studies showed that praseodymium species were soluble under acidic conditions, but precipitated at higher pH values. Studies of using model primers revealed that either the praseodymium species or the acid extender (gypsum) provided corrosion protection when incorporated into the polymer matrix alone. In both cases, the individual species were quickly depleted from the coating. However, the combination of the praseodymium species and the acid extender had a synergistic effect that provided long term (up to 3000 hours in ASTM B117 salt spray) corrosion protection. The acid extender moderated the pH in the coating matrix, allowing praseodymium species to dissolve from the coating, transport the site of attack, and precipitate to passivate the substrate.

Technical Summary

Corrosion protection mechanisms were studied for cerium-based conversion coatings and epoxy-polyamide primers containing a praseodymium-based inhibitor package. The rare-earth based inhibitors in these coatings are not inherently protective, but require that specific phases be incorporated into the appropriate type of coating.

Cerium-based conversion coatings are capable of providing significant corrosion protection to high strength aluminum alloys (i.e., no salt tails after two weeks of ASTM B117 salt spray testing). Coatings that provide protection require appropriate surface preparation, coating deposition solution formulation, and post-treatment. For AA 2024-T3, surface preparation by acid activation has been shown to remove the Al-rich surface oxide layer, which exposes intermetallic particles and facilitates coating deposition. Immersion for 5 min in a 1 wt% solution of sulfuric acid that has been heated to 50°C is an example of an effective activation process. For 7075-T6, the Mg-rich surface oxide can be removed by alkaline activation in

solutions containing NaOH or Na_2CO_3. Once the surface oxide is removed from the Al alloy, the coating deposition solution is the next critical factor that affects corrosion protection. The most effective coating solutions contain a combination of chloride ions, hydrogen peroxide, and gelatin. The presence of gelatin in the coating solution moderated the deposition rate and led to the formation of coatings that were thinner, but more resistant to crack formation during processing. The combination of chloride ions and hydrogen peroxide in the coating solution led to the formation of sub-surface crevices during coating deposition. Crevices were typically present over about 10% of the surface area of the coating, but produced large cracks (>1 μm wide) that were visible on the surface of CeCCs. The crevices extended up to about 10 μm into the substrate and appeared to form in areas with high concentrations of intermetallic particles. Cerium-based conversion coatings were able to provide corrosion protection despite the presence of the sub-surface crevices. The replacement of chloride ions with nitrates or decreasing the concentration of hydrogen peroxide decreased the deposition rate and resulted in coatings that did not provide significant corrosion protection. Solubility studies revealed that cerium species from conversion coatings were virtually insoluble above pH values of 2. Hence, the corrosion protection of cerium-based conversion coatings was not due to dissolution and transport of cerium ions. However, cerium-based conversion coatings appeared to be a robust barrier to attack of aluminum alloys by chloride ions. In addition, an interfacial reaction layer formed between cerium-based conversion coatings and the underlying substrates, which indicated that the coatings were more than simply an inert barrier. Due to their active response, cerium-based conversion coatings were able to provide corrosion protection despite the presence of cracks, pinholes, and other defects.

Epoxy-polyamide primers containing a praseodymium-based inhibitor package provide corrosion protection to high strength aluminum alloys that have been pre-treated with chromate conversion coatings. Electrochemical testing of panels with artificial defects milled through primers in electrolytes with different pH values revealed that praseodymium species were most effective at pH values of 8 or higher. Examination of scribed areas confirmed that praseodymium species were dissolving from the coating, transporting to the scribed areas and precipitating in the form of praseodymium-rich crystals. The formation of the praseodymium-rich particles has only been observed in coatings that inhibit salt formation in scribed areas. Precipitation studies and other analyses of the phase stability of praseodymium compounds indicated that the crystals were likely to be praseodymium hydroxycarbonate. Formulation of control primers in which the praseodymium-based inhibitor package was replaced with only Pr_2O_3, gypsum, or talc showed that either Pr_2O_3 or gypsum provided some protection for a limited amount of time (500 hours or less) during salt spray testing, but only the combination of Pr_2O_3 and gypsum provided corrosion protection for extended (2000 hours or longer) times in salt spray testing. During corrosion testing, gypsum was depleted from the coating within about 500 hours of salt spray testing, but praseodymium levels were relatively unchanged throughout the duration of testing. Taken together, the results showed that praseodymium-based corrosion inhibitors were able to dissolve from an epoxy-polyamide primer when the acidity of the environment in the primer was moderated by the presence of gypsum. The dissolved praseodymium species then migrated to damaged areas and precipitated to mitigate corrosive attack. The primers were less effective on non-chromate conversion coatings such as trivalent chromium passivation or cerium-based conversion coatings, but still showed the ability to inhibit salt formation after initial salting during the first 1500 to 2000 hours of salt spray testing. In contrast, epoxy-polyamide primers

on aluminum alloys with chromate conversion coatings were able to inhibit corrosion as soon as the panels were exposed to salt spray testing. Hence, praseodymium species are able to dissolve from a primer matrix, transport to the site of corrosion, and precipitate to inhibit corrosion when Pr_2O_3 is added to the primer and gypsum is present to control the chemical environment in the primer matrix.

References

1. M. Costa, "Toxicity and Carcinogenicity of Cr(VI) in Animal Models and Humans" *Critical Reviews in Toxicology,* **27** 431-442 (1997).
2. http://www.osha.gov/SLTC/hexavalentchromium/standards.html.
3. R.G. Buchheit and A.E. Hughes, "Chromate and Chromate-Free Conversion Coatings" pp. 720-735 in Corrosion ASM International Handbook Vol. 9 (2003).
4. J.O. Stoffer, T.J. O'Keefe, E.L. Morris, P. Yu, and S.A. Hayes, "Corrosion Resistant Coatings ," U.S. Patent 7,759,419, Issued July 20, 2010.
5. R.S. Mikhail and S. Brunauer, "Surface Area Measurements by Nitrogen and Argon Adsorption," Journal of Colloid and Interface Science, 52 (1975) 527-577.
6. T.J. Haley, "Pharmacology and Toxicology of the Rare Earth Elements" *Journal of Pharmaceutical Sciences*, 54 (1965) 663-670.
7. S. Hirano, K.T. Suzuki, "Exposure, Metabolism, and Toxicity of Rare Earths and Related Compounds" *Environmental Health Perspectives*, 104 (1996) 85-95.
8. Y. Nakamura, Y. Tsumura, Y. Tonogai, T. Shibata, Y. Ito**, "**Differences in Behavior Among the Chlorides of Seven Rare Earth Elements Administered Intravenously to Rats" *Fundamental and Applied Toxicology*, 37 (1997) 106-111.
9. W. Lin, Y. Huang, X. Zhou, and Y. Ma, **"**Toxicity of Cerium Oxide Nanoparticles in Human Lung Cancer Cells" *International Journal of Toxicology*, **25** (2006) 451-457.
10. G. Adachi, N. Imanaka, and Z.C. Kang. Binary Rare Earth Oxides. Kluwer Academic Publishers 2004 Dordrecht.
11. D. A. Burnham and L. Eyring. "Phase Transformations in the Praseodymium-Oxide System: High Temperature X-Ray Diffraction Studies" *Journal of Physical Chemistry,* 72 (1968) 4415-4424.
12. R.E. Ferguson, E.D. Guth, and L. Eyring. "Praseodymium Oxides. I. Phase Study by Dissociation Pressure Measurements" *Journal of the American Chemical Society,* 76 (1953) 3890-3894.
13. M. Gasgnier, G. Schiffmacher, L. Albert, and P.E. Caro. "Preparation, Crystalline Properties and X-Ray Absorption Spectra of Rare Earth Oxides RO_x (R=Ce, Pr, and Tb; $1.5 \leq x \leq 2$)" *Journal of the Less-Common Metals* 156 (1989) 59-73.
14. R. Sharma, H. Hinode, and L. Eyring. "A Study of the Decomposition of Praseodymium Hydroxy Carbonate and Praseodymium Carbonate Hydrate"*Journal of Solid State Chemistry* 92 (1991) 401-419.
15. M. Zinkevich. "Thermodynamics of Rare Earth Sesquioxides" *Progress in Materials Science* 52 (2007) 597-647.
16. E.C. Shears and L.I. Ceram. "A Study of Praseodymium Oxides by D.T.A. and Dilatometer." *Transactions of the British Ceramics Society* 60 (1961) 773-782.
17. S. Bernal, F.J. Botana, R. Garcia, and J.M. Rodriquez-Izquierdo. "Chemistry of the Rare-earth-metal Sesquioxides. Comparative Study Hexagonal and Cubic Neodymia Samples" *Journal of the Chemical Society Dalton Transactions* 7 (1988) 1765-1771.
18. M.P. Rosynek and D.T. Magnuson. "Preparation and Characterization of Catalytic Lanthanum Oxide" *Journal of Catalysis* 46 (1977) 402-413.
19. P.E. Caro, J.O. Sawyer, and L. Eyring. "The Infrared Spectra of Rare Earth Carbonates". *Spectrochimica Acta* 28A 1167-1173 (1972).

20. S. Bernal, F.J. Botana, R. Garcia, J.M. Rodriquez-Izquierdo. "Behavior of Rare Earth Sesquioxides Exposed to Atmospheric Carbon Dioxide and Water." *Reactivity of Solids* 4 23-40 (1987).
21. L.R. Morss, Handbook on the Physics and Chemistry of Rare Earths Vol. 18, Amsterdam:North Holland, p. 239 (1994).
22. E.R. Birnbaum, Gmelin Handbook of Inorganic Chemistry, 8th Ed. System No. 39, Part D5, Berlin: Springer, p. 1, (1984).
23. G. Adachi, G. and N. Imanaka, "The Binary Rare Earth Oxides", *Chem. Rev.* 98 (1998), 1479-1514.
24. L. Erying, Synthesis of Lanthanide and Actinide Compound, Netherland:Kluwer Academic Publisher, p.187 (1991).
25. E. Schweda, "Diffusionless Phase Transiton and Related Structures in Oxide", *Key Eng. Mater.* 68 (1992) 187-215.
26. E.D. Guth, J.R. Holden, N.C. Baenziger, and L. Eyring, "Praseodymium Oxides II. X-Ray and Differential Thermal Analysis", *J. Am. Chem. Soc.*, 76 (1954) 5239-5242.
27. P.X. Huang, F. Wu, B.L. Zhu, G.R. Li, Y.L. Wang, X.P. Gao, H.Y. Zhu, T.Y. Yan, W.P. Huang, S.M. Zhang, and D.Y. Song, "Praseodymium Hydroxide and Oxide Nanorods and Au/Pr_6O_{11} Nanorod Catalysts for CO Oxidation", *J. Phys. Chem. B.*, 110 (2006) 1614-1620.
28. J. Mikulova′, S. Rossignol, J. Barbier Jr.,D. Duprez, and C. Kappenstein, "Characterizations of Platinum Catalysts Supported on Ce, Zr, Pr-oxides and Formation of Carbonate Species in Catalytic Wet Air Oxidation of Acetic Acid", *Catal. Today*, 124 (2007) 185-190.
29. Y. Borchert, P. Sonström, W. Michaela, H. Borchert, and M. Bäumer, "Nanostructured Praseodymium Oxide: Preperation, Structure, and Catalytic Properties" *J. Phys. Chem C*, 112 (2008) 3054-3063.
30. S. Shrestha, C.M.Y. Yeung, F. Marken, C.E. Mills, and S.C. Tsang, "Layer-by-layer Deposition of Praseodymium Oxide on Tin-doped Indium Oxide (ITO)Surface", *Sens. Actuators B*, 123 (2007) 100-406.
31. S. Shrestha, F. Marken, J. Elliot, C.M.Y. Yeung, C.E. Mills, and S.C. Tang, "Electrochemical Deposition of Praseodymium Oxide on Tin-Doped Indium Tin Oxide as a Thin Sensing Film", *J. Electrochem. Soc*. 153 (2006) C517-C520.
32. M. Gasgnier, G. Schiffmacher, L. Albert, and P.E. Caro, "Preparation, Crystalline Properties and X-Ray Absorption Spectra of Rare Earth Oxides RO_x (R=Ce, Pr, and Tb; $1.5 \leq x \leq 2$)", *J. Less-Common Met.*, 156 (1989) 59-73.
33. L. Eyring, Science and Technolgy of Rare Eath Materials, New York: Academic Press Inc.,p. 99 (1980).
34. R. Sharma, H. Hinode, and L. Eyring, "A Study of the Decomposition of Praseodymium Hydroxy Carbonate and Praseodymium Carbonate Hydrate", *J. Solid State Chem.,* 92 (1991) 401-419.
35. M. Zinkevich, "Thermodynamics of Rare Earth Sesquioxides", *Prog. Mater. Sci.*, 52 (2007) 597-647.
36. E.C. Shears, and L.I. Ceram, "A Study of Praseodymium Oxides by D.T.A. and Dilatometer", *Brit. Ceram. Trans. J.*, 60 (1961) 773-782.
37. M. Foex, and J.P. Traverse, "Investigations About Crystalline Transformation in Rare Earths Sesquioxides at High Temperatures", *Rev. Int. Hautes Temp. Refract.*, 3 (1966) 429-453.

38. T.D. Chikalla, C.E. McNeilly, and F.P. Roberts, "Polymorphic Modifications of Promethium Oxide (Pm_2O_3)", *J. Am. Ceram. Soc.* 55 (1972) 428-429.
39. S. Bernal, F.J. Botana, G. Cifredo, J.J. Calvino, A. Jobacho, and J.M. Rodriquez-Izquierdo, "Preperation and Characterization of Praseodymium Oxide to be Used as a Catalytic Support", *J. Alloys Compd.* 180 (1992) 271-279.
40. M.P. Rosynek and D.T. Magnuson, "Preparation and Characterization of Catalytic Lanthanum Oxide", *J. Catal.*, 46 (1977) 402-413.
41. P.E. Caro, J.O. Sawyer, and L. Eyring, "The Infrared Spectra of Rare Earth Carbonates", *Spectrochim. Acta* 28A (1978) 1167-1173.
42. S. Bernal, F.J. Botana, R. Garcia, and J.M. Rodriquez-Izquierdo, "Behavior of Rare Earth Sesquioxides Exposed to Atmospheric Carbon Dioxide and Water", *React. Solids*, 4 (1987) 23-40.
43. M.P. Rosynek, "Catalytic Properties of Rare Earth Oxides", *Catal. Rev*., 16 (1977) 111-154.
44. R. Alvero, J.A. Odriozola, J.M. Trillo, and S.J. Bernal, "Lanthanide Oxides: Preparation and Aging", *J. Chem.*, *Soc. Dalton Trans.*, 87 (1984) 87-91.
45. S. Bernal, J.A. Diaz, R. Garcia, and J.M. Rodriguez-Izquierdo, "Study of Some Aspects of the Reactivity of Lanthanum Oxide with Carbon Dioxide and Water", *J. Mater. Sci.*, 20 (1985) 537-541.
46. S. Bernal, F.J. Botana, R. Garcia, J.M. Pintado, and J.M. Rodriguez-Izquierdo, "Study of the Aging in Air of a Cubic Sample of Samaria", *Mater. Res. Bull.*, 22 (1987) 131-138.
47. S. Bernal, F.J. Botanta, R. Garcia, and J.M. Rodriguez-Izquierdo, "Study of the Interaction of Two Hexagonal Neodymium Oxides with Atmospheric CO_2 and H_2O", *J. Mater. Sci.*, 23 (1988) 1474-1480.
48. R. Alvero, J.A. Odriozola, and J.M. Trillo, "Influence of the Method of Preparation on Ytterbia Hydration", *J. Mater. Sci.*, 20 (1985) 1828-1834.
49. R. Alvero, I. Bernal, J.A. Carrizosa, and J.M. Trillo, "Lanthanide oxides: Lutetium Sesquioxide Hydration". *J. Less-Common Met.*, 110 (1985) 425-432.
50. R. Alvero, S. Bernal, I. Carrizosa, J.A. Odriozola, and J.M. Trillo, "The Kinetics of Ln_2O_3 Hydration Under Mild Conditions", *Thermal Anal.*, 32 (1987) 635-643.
51. H. Dexpert, M. Lamaitre-Blaise, and P. Caro, "Chemistry and Reactivity of Compounds with Layered Structures in the Ternary Heterogeneous Systems Rare Earth Oxides - Carbon Dioxide – Water", *Reactiv. Solids*, 7th Proc. Int. Symp. (1972) 758-765.
52. A. Tareen and T.R.N. Kutty, "Hydrothermal Phase Equilibria in Ln_2O_3-H_2O Systems" J. Chem. Sci., 89 (1980) 277-282.
53. W.G. Fahrenholtz, H. Zhou, and M.J. O'Keefe, "Characterization of Spontaneously Formed Cerium-based Conversion Coatings on Aluminum," *Cer. Eng. and Sci. Proc.,* 23 (2002) 469-476.
54. W. Pinc, S. Geng, M.J. O'Keefe, W.G. Fahrenholtz, and T.J. Keefe, "Effects of acid and alkaline based surface preparations on spray deposited cerium based conversion coatings on Al 2024-T3. *Appl. Surf. Sci.*, 255 (2009) 406-4065.
55. F.H. Scholes, C. Soste, A.E. Hughes, S.G. Hardin, and P.R. Curtis, "The Role of Hydrogen Peroxide in the Deposition of Cerium-based Conversion Coatings", *App. Surf. Sci.*, 253 (2006) 1770-1780.

56. P. Campestrini. H. Terryn, A. Hovestad, and J. H. W. de Wit, "Formation of Cerium-based Conversion Coatings on AA2024: Relationship with the Microstructure" *Surface and Coatings Technology*, 176 (2004) 365-384.
57. S. A. Kulinich, A. S. Akhtar, D. Susac, P. C. Wong, K. C. Wong, K. A. R. Mitchell, "On the Growth of Conversion Chromate Coatings on 2024-Al Alloy" *Applied Surface Science***,** 253 (2007) 3144-3153.
58. S.M. Cohen, "Replacements for Chromium Pretreatments on Aluminum" *Corrosion,* 51 (1995) 71-78.
59. R. L. Twite and G. P. Bierwagen, **"**Review of Alternatives to Chromate for Corrosion Protection of Aluminum Aerospace Alloys" *Progress in Organic Coatings***, 33** (1998) 91-100.
60. J. R. Waldrop and M. W. Kendig, Nucleation of Chromate Conversion Coating on Aluminum 2024-T3 Investigated by Atomic Force Microscopy" *Journal of the Electrochemical Society,* 145 (1998) L11-L13.
61. C.M. Rangel, T.I. Paiva, and P.P. da Luz, "Conversion Coating Growth on 2024-T3 Al Alloy. The Effect of Pre-treatments," *Surf. and Coat. Tech.*, 202 (2008) 3396-3402.
62. J. Zhao, L. Xia, A. Sehgal, D. Lu, R. L. McCreery, and G. S. Frankel," Effects of Chromate and Chromate Conversion Coatings on Corrosion of Aluminum Alloy 2024-T3" *Surface and Coatings Technology*, 140 (2001) 51-57.
63. B.R.W. Hinton, D.R. Arnott, and N.E. Ryan, "Cerium Conversion Coatings for the Corrosion Protection of Aluminum", *Mater. Forum*, 9 (1986) 162-173.
64. L.E.M. Palomino, I.V. Aoki, H.G. de Melo, "Microstructural and Electrochemical Characterization of Ce Conversion Layers Formed on Al Alloy 2024-T3 Covered with Cu-Rich Smut" *Electrochimica Acta*, 51 (2006) 5943-5953.
65. A. Decroly and J-P. Petitjean, "Study of the Deposition of Cerium Oxide by Conversion on Aluminum Alloys" *Surface Coatings Technology,* 194 (2005) 1-9.
66. S. Joshi, W.G. Fahrenholtz, and M.J. O'Keefe, "Effect of Alkaline Cleaning and Activation on Aluminum Alloy 7075-T6 for Deposition of Cerium-based Conversion Coatings," Applied Surface Science, 257 (2011) 1859-1863.
67. A.E. Hughes, J.D. Gorman, P.R. Miller, B.A. Sexton, P.J.K. Paterson, and R.J. Taylor, "Development of Cerium-based Conversion Coatings on 2024-T3 Al Alloy After Rare-Earth Desmutting", *Surf. Interface Anal.*, 36 (2004) 290-303.
68. S.A. Hayes, P. Yu, T.J. O'Keefe, M.J. O'Keefe, and J.O. Stoffer, "The Phase Stability of Cerium Species in Aqueous Systems", *J. Electrochem. Soc.*, 149 (2002) C623-C630.
69. A. de Frutos, M.A. Arenas, Y. Liu, P. Skeldon, G.E. Thompson, J. De Damborenea, and A. Conde, "Influence of Pre-treatments in Cerium Conversion Treatment of AA2024-T3 and 7075-T6 Alloys," *Surf. Coat. Tech.*, 202 (2008) 3797-3807.
70. W. Pinc, P. Yu, M.J. O'Keefe, and W.G. Fahrenholtz, "Effect of gelatin additions on the corrosion resistance of cerium based conversion coatings spray deposited on Al 2024-T3. *Surf. Coat. Tech.*, 203 (2009) 3533-3540.
71. S. Geng, P. Yu, M.J. O'Keefe, W.G. Fahrenholtz, and T.J. O'Keefe, *J. App. Electrochem.*, 40 (2010) 551-559.
72. C. Wang, F. Jiang, and F. Wang, "Cerium Chemical Conversion Coating for Aluminum Alloy 2024-T3 and its Corrosion Resistance", *Corrosion*, 60 (2004) 237-243.

73. B.F. Rivera, B.Y. Johnson, M.J. O'Keefe, and W.G. Fahrenholtz, "Deposition and Characterization of Cerium Oxide Conversion Coatings on Aluminum Alloy 7075-T6," *Surf. and Coat. Tech.*, 176 (2004) 349-356.
74. H. Zhang, and Y. Zuo, "The Improvement of Corrosion Resistance of Ce Conversion Films on Aluminum Alloy by Phosphate Post-treatment," *Applied Surface Science*, 254 (16) (2008), 4930-4935.
75. B.Y. Johnson, A. Williams, and M.J. O'Keefe, "Microstructural Characteristics of Cerium Oxide Conversion Coatings Obtained by Various Aqueous Deposition Methods," *Mater. Character.*, 54 (2005), 41-48.
76. A.E. Hughes, F.H. Scholes, A.M. Glenn, D. Lau, T.H. Muster, and S.G. Hardin, "Factors Influencing the Deposition of Ce-based Conversion Coatings, Part I: The Role of Al^{3+} Ions," *Surf. and Coat. Tech.*, 203 (2009), 2927-2936.
77. B.L. Treu, S. Joshi, S., W. Pinc, M.J. O'Keefe, and W.G. Fahrenholtz, "Sub-Surface Electrochemical Effects on the Spontaneous Deposition of Cerium Conversion Coatings on Aluminum Alloys", *ECS Trans.* 19 (2009) 101-112.
78. T. Suter, and H. Bohni, "Microelectrodes for Studies of Localized Corrosion Processes," *Electrochim. Acta*, 43 (1998) 2843-2848.
79. M.M. Lohrengel, A. Moehring, and M. Pilaski, "Capillary-based Droplet Cells: Limits and New Aspects," *Electrochim. Acta*, 47 (2001) 137-141.
80. R.G. Buchheit, R.K. Boger, M.C. Carroll, R.M. Leard, C. Paglia, and J.L. Searles, "The Electrochemistry of Intermetallic Particles and Localized Corrosion in Al alloys", *JOM* 53 (2001) 29-33.
81. T. Suter, and H. Bohni, "Microelectrodes for Corrosion Studies in Microsystems," *Electrochim. Acta,* 47 (2001) 191-199.
82. B.W.R. Hinton, D.R. Arnott, and N.E. Ryan, "The Inhibition of Aluminum Alloy Corrosion by Cerous Cations" *Materials Forum*, **7** 211-217 (1984).
83. M. Dabala, L. Armelao, A. Buchberger, and I. Calliari, "Cerium-based Conversion Layers on Aluminum Alloys" *Journal of Applied Surface Science,* 172 (2001) 312-322.
84. H. Dextpert, and P. Caro, "Crystal Structure of Neodymium Hydroxycarbonate $NdOHCO_3$", *Mater. Res. Bull*., 9 (1974) 1577-1585.
85. N.V. Zubova, V.M. Makarov, V.D. Nikolskii, P.N. Petrov, E.G. Teterin, and N.T> Chebotarev, "Phase Equilibriums in a Lanthanum Oxide-Uranium Trioxide-Water System at 270°", *Russ. J. Inorg. Chem.* (English Transl.),13 (1968) 2284-2289.
86. B. Klingenberg, and M.A. Vannice, "Influence of Pretreatment on Lanthanum Nitrate, Carbonate, and Oxide Powders", *Chem. Mater.*, 8 (1996) 2755-2768.
87. R.L.N. Sastry, S.R. Yoganarasimhan, P.N. Mehrotra, and C.N.R. Rao, "Preperation, Characterization, and Thermal Decomposition of Praseodymium, Terbium, and Neodymium Carbonates, *J. Inorg. Nucl. Chem.,* 28 (1966) 1165-1177.
88. D.L. Moscardini M. Ionashiro, D.E. Rasera, and I Giolito, I. Thermal Decomposition of the Hydrated Basic Carbonates of Lanthanides and Yttrium in CO_2 Atmosphere, *Thermochim. Acta,* 219 (1993) 225-233.
89. J.M. Haschek, and L. Eyring, "Hydrothermal Equilibria and Crystal Growth of Rare Earth Oxides, Hydroxides, Hydroxynitrates, and Hydroxycarbonates," *Inorg. Chem.* 10 (1971) 2267-2270.

90. M. Popa, and M. Kakihana, "Praseodymium Oxide Formation by Thermal Decomposition of a Praseodymium Complex Solid State Ionics," 141-142 (2001) 265-272.
91. G.A.M. Hussein, "Formation of Praseodymium Oxide From the Thermal Decomposition of Hydrated Praseodymium Acetate and Oxalate," *J. Anal. Appl. Pyrolysis*, 29 (1994) 89-102.
92. H.E. Swanson, and R.K. Fuyat, Standard x-ray Diffraction Powder Patterns Vol. II", *National Bureau of Standards Circular (U. S.),* p. 65 (1953).
93. O. Greis, R. Ziel, B. Breidenstein, A. Haase, and T. Petzel, "Crystal Structures of cubic α -PrOF and Rhombohedral β -PrOF from x-ray Powder diffraction", *Mater. Sci. Forum*, 166-169(Pt. 2) (1994) 677-682.
94. V. Savin, A. Elyutin, N. Mikhailova, and Z. Eremenko, "Thermochemical Study of the Process of Decomposition of Dysprosium, Lanthanum, and Neodymium Carbonates", Zhurnal Fizicheskoi Khimii' 62 (1988) 1180-1187.
95. J. Sawyer, P. Caro, and L. Eyring, "Hydroxycarbonates of the Lanthanide Elements", *Rev. Chim. Miner.,* 10 (1973) 93-104.
96. http://www.serdp.org/content/search?cqp=Standard&SearchText=WP-1519&x=0&y=0
97. D.J. Piron, The Electrochemistry of Corrosion National Association of Corrosion Engineers Houston TX p. 186 (1991).
98. S.I. Pyun and S.M. Moon, "The Inhibition Mechanism of Pitting Corrosion of Pure Aluminum by Nitrate and Sulfate Ions in Neutral Chloride Solution" *J. Solid State Electrochem.*, 3 (1999) 331-336
99. S. Joshi, W.G. Fahrenholtz, and M.J. O'Keefe, "Alkaline Activation of Al 7075-T6 for Deposition of Cerium-Based Conversion Coatings, Surface and Coatings Technology, 205 (2011) 4312-4319.
100. M.E. Orazem, N.E. Pebere, and B. Tribollet, "Enhanced Graphical Representation of Electrochemical Impedance Data", *J. Electrochem. Soc.*, 153 (2006) B129-B136.
101. R. Cottis, and S. Turgoose, NACE International Series 7, Houston TX (1999).
102. D.K. Heller, W.G. Fahrenholtz, and M.J. O'Keefe, "The Effect of Phosphate Source on the Post-treatment of Cerium Based Conversion Coatings on Al 2024-T3 and its Correlation to Corrosion Perfomance", *J. Electrochem. Soc.*, 156 (2009) C400-C406.
103. I. Miller, and J.E. Freund, Freund, Miller & Freund's Probability and Statistics for Engineers (7th Edition) Prentice Hall Englewood Cliffs NJ (1993).
104. S. Siegel, and N.J. Castellan, Nonparametric Statistics, Mc-Graw Hill Book Company, p. 45, New York, NY (1988).
105. F. Mansfeld and J. C. S Fernandes, "Impedance Spectra for Aluminum 7075 During the Early Stages of Immersion in Sodium Chloride" *Corrosion. Science*, 34 (1993) 2105-2108.
106. T.J. O'Keefe, P. Yu, Pourbaix Diagrams, Encyclopedia of Materials: Science and Technology, Elsevier Science, 7774-7781 (2001).
107. J. R. Scully, D. C. Silverman, M. W. Kendig, Electrochemical Impedance: Analysis and interpretation, STP ASTM, p11 (1993).
108. B.R.W. Hinton, "Corrosion Inhibition with Rare Earth Metals Salts," *Journal of Alloys and Compounds*, 180 (1992) 15-25.
109. J. O. Park, C. H. Paik, Y. H. Huang, and R. C. Alkire, D. A. Jones, *Journal of Electrochemical Society*, 146 (1999) 517-523.

110. W. Pinc, S. Maddela, M. O'Keefe, W. Fahrenholtz, "Formation of Subsurface Voids in Aluminum Alloy 2024-T3 During Deposition of Cerium-based Conversion Coatings" *Surface and Coatings Technology,* **204** 4095-4100 (2010).
111. D.K. Heller, W.G. Fahrenholtz, and M.J. O'Keefe, "Chemical and Structural Analysis of Subsurface Crevices Formed During Spontaneous Spray Deposition of Cerium-Based Conversion Coatings," accepted for publication in Materials Characterization, July 30, 2011
112. S. You, P. Jones, A. Padwal, P. Yu, M. O'Keefe, W. Fahrenholtz, and T. O'Keefe, **"**Response of Nanocrystalline Cerium-based Conversion Coatings on Al 2024-T3 to Chloride Environments" *Materials Letters* 61 (2007) 3778-3782.
113. R.K. Hart, "The Formation of Films on Aluminium Immersed in Water," *Transactions of the Faraday Society*, 53 1020-1027 (1957).
114. B.C. Bunker, G.C. Nelson, K.R. Zavadil, J.C. Barbour, F.D. Wall, J.P. Sullivan, C.F. Windisch Jr., M.H. Engelhardt, D.R. Baer, "Hydration of Passive Oxide Films on Aluminum" *Journal of Physical Chemistry B*, 106 4705-4713 (2002).
115. G.E. Fair, R.S. Hay, and E.E. Boakye, "Precipitation Coating of Rare-earth Orthophosphates on Woven Ceramic Fibers - Effect of Rare-earth Cation on Coating Morphology and Coated Fiber Strength" *Journal of the American Ceramic Society*, **91** 2117-2123 (2008).
116. D. K. Heller, W. G. Fahrenholtz, and M. J. O'Keefe**, "**The Effect of Post-treatment Time and Temperature on Cerium-based Conversion Coatings on Al 2024-T3," *Corrosion Science***,** 52 (2010) 360-368.
117. S. Joshi, W.G. Fahrenholtz, and M.J. O'Keefe, "Effect of Humidity on Cerium Based Conversion Coatings," ECS Transactions, 28 (2011) 217-228.
118. W. Pinc, D. Heller, W. Fahrenholtz, M. O'Keefe, "Electrochemical and Structural Changes in Cerium Based Conversion Coatings During Exposure to Salt Spray," ECS Trans., 25 (2010) 3-17.
119. X. Yu, G. Li, "XPS Study of Cerium Conversion Coating on the Anodized 2024 Aluminum Alloy," *Journal of Alloys and Compounds*, 364 (2004) 193-198.
120. M. A. Jakab and J. R. Scully, "Effect of pH and Chloride Ion Concentration on Inhibitor Storage in Amorphous Al-Co-Ce Alloys" *Corrosion,* 64 (2008) 198-210.
121. Engineer manual EM1110-2-1614 design of coastal revetments, seawalls and bulkheads. 30-june-1995 page d-1. U.S. Army Corps of Engineers, Washington, DC.
122. P. Yu, S. A. Hayes, T. J. O'Keefe, M. J. O'Keefe, and J. O. Stoffer, "The Phase Stability of Cerium Species in Aqueous Systems. II. The Ce(III/IV)-H2O-H2O2/O2 Systems. Equilibrium Considerations and Pourbaix Diagram Calculations" *Journal of the Electrochemical Society*, 153 (2006) C74-C79.
123. F. J. Presuel-Moreno, M. A. Jakab, and J. R. Scully, "Inhibition of the Oxygen Reduction Reaction on Copper with Cobalt, Cerium, and Molybdate Ions**"** *Journal of the Electrochemical Society***,** 152 (2005) B376-B387.
124. K. A. Yasakau, M. L. Zheludkevich, S. V. Lamaka, and M. G. S. Ferreira, "Mechanism of Corrosion Inhibition of AA2024 by Rare-Earth Compounds" *Journal of Physical Chemistry B* 110 (2006) 5515-5528 (2006).
125. F. J. Presuel-Moreno, H. Wang, M. A. Jakab, R. G. Kelly, and J. R. Scully, "Computational Modeling of Active Corrosion Inhibitor Release from an Al-Co-Ce Metallic Coating. Protection of exposed AA 2024-T3" *Journal of the Electrochemical Society*, 153 (2006) B486-B498.

126. A. J. Bard, R. Parsons, J. Jordan, Standard Potentials in Aqueous Solution, IUPAC, (1985) p616.
127. R. H. Byrne, J. H. Lee and L. S. Bingler, "Rare Earth Element Complexation by PO_4^{3-} Ions in Aqueous Solution" *Geochimica et Cosmochimica Acta*, 55 (1991) 2729-2733.
128. X. Liu and R. H. Byrne, "Rare Earth and Yttrium Phosphate Solubilities in Aqueous Solution" *Geochimica et Cosmochimica Acta***,** 61 (1997) 1625-1633.

Appendix 1. Publications and Presentations

List of Conference Presentations

1. J. Claypool, W.G. Fahrenholtz, M.J. O'Keefe, E. Morris, and R. Albers, "Corrosion Protection Mechanisms of Rare-Earth Compounds Based on Ce and Pr," Partners in Environmental Technology Technical Symposium and Workshop, November 28-December 1, 2011, Washington, DC.
2. C. Lin, S. Maddela, M.J. O'Keefe, and W.G. Fahrenholtz, "Deposition of Cerium-Based Conversion Coatings on Aluminum Alloy 380," Materials Science and Technology Conference and Exhibition, October 16-20, 2011, Columbus, OH.
3. B.L. Treu, W.G. Fahrenholtz, M.J. O'Keefe, E.L. Morris, and R. Albers, "Corrosion Protection Mechanism of Praseodymium-Based Inhibitors," DoD Corrosion Conference, August 1-5, 2011, Palm Springs, CA.
4. W.R. Pinc, S. Joshi, D.K. Heller, W.G. Fahrenholtz, and M.J. O'Keefe, "Corrosion Protection Mechanisms of Cerium-Based Conversion Coatings," Partners in Environmental Technology Technical Symposium and Workshop, November 29-December 2, 2010, Washington, DC.
5. B.L. Treu, W.G. Fahrenholtz, M.J. O'Keefe, E. Morris, and R. Albers, "Characterization of Pr-Based Inhibitors and Corrosion Response of a Pr-Containing Primer," Partners in Environmental Technology Technical Symposium and Workshop, November 29-December 2, 2010, Washington, DC.
6. S. Joshi, M. O'Keefe, and W. Fahrenholtz, "Characterization of Cerium-based Conversion Coatings Deposited on Alkaline Activated Al 7075-T6," Materials Science and Technology 2010, October 17-21, 2010, Houston, TX.
7. D. Heller, W. Fahrenholtz, M. O'Keefe, "Interfacial Analyses of Cerium Based Conversion Coatings on Al 2024-T3," Materials Science and Technology 2010, October 17-21, 2010, Houston, TX.
8. E.A. Kulp, W.G. Fahrenholtz, and M.J. O'Keefe, "The Effects of Peroxide Stabilizers on the Performance of Cerium-Based Conversion Coatings on Al 2024-T3," Materials Science and Technology 2010, October 17-21, 2010, Houston, TX.
9. B.L. Treu, W.R. Pinc, W.G. Fahrenholtz, M.J. O'Keefe, E.L. Morris, and R.A. Albers, "Effect of Phase on the Electrochemical and Morphological Properties of Praseodymium-based Coatings," 218th Meeting of the Electrochemical Society, October 10-15, 2010, Las Vegas, NV.
10. E.A. Kulp, S. Maddela, W.G. Fahrenholtz, and M.J. O'Keefe, "The effect of peroxide stabilizers on the corrosion protection of sprayed and electrodeposited cerium-based conversion coatings on Al 2024-T3," 218th Meeting of the Electrochemical Society, October 10-15, 2010, Las Vegas, NV.
11. S. Joshi, W.G. Fahrenholtz, and M.J. O'Keefe, "Effect of Humidity on Cerium-Based Conversion Coatings," 217th Meeting of the Electrochemical Society, April 25-30, 2010, Vancouver, BC, Canada
12. D. Heller, W.G. Fahrenholtz, M.J. O'Keefe, and G. Fair, "Directly Deposited $CePO_4$ Coatings for the Corrosion Protection of Al 2024-T3," 217th Meeting of the Electrochemical Society, April 25-30, 2010, Vancouver, BC, Canada

13. W. Pinc, S. Maddela, W.G. Fahrenholtz, and M.J. O'Keefe, "Corrosion Protection Mechanisms of Cerium-Based Conversion Coatings on Aluminum Alloys," 217th Meeting of the Electrochemical Society, April 25-30, 2010, Vancouver, BC, Canada
14. B.L. Treu, W. Pinc, W.G. Fahrenholtz, M.J. O'Keefe, E. Morris, and R. Albers, "Characterization of Transport Processes in a Praseodymium-Based Coating," 217th Meeting of the Electrochemical Society, April 25-30, 2010, Vancouver, BC, Canada.
15. M.J. O'Keefe, W.G. Fahrenholtz, E. Morris, and R. Albers, "Influence of Phase and pH on the Corrosion Protection of Rare Earth Inhibitors Coatings," NACE Annual Conference, March 14-18, 2010, Houston, TX.
16. B.L. Treu, S. Joshi, S. Maddela, M. Zhang, E.A. Kulp, W.G. Fahrenholtz, and M.J. O'Keefe, "Characterization of Surface and Sub-Surface Morphology of Cerium-Based Conversion Coatings on Aluminum Alloys," Central States Microscopy and Microanalysis Meeting, November 10-11, 2009, Rolla, MO.
17. S. Joshi, D. Heller, W. Pinc, W.G. Fahrenholtz, and M.J. O'Keefe*, "Microelectrochemical Testing of Cerium Based Conversion Coatings," 216th Meeting of the Electrochemical Society, October 4-9, 2009, Vienna, Austria.
18. W. Pinc, W.G. Fahrenholtz, and M.J. O'Keefe, "Electrochemical and Structural Changes in Cerium-Based Conversion Coatings During Exposure to Salt Spray," 216th Meeting of the Electrochemical Society, October 4-9, 2009, Vienna, Austria.
19. W. Pinc, S. Joshi, M. O'Keefe, and W. Fahrenholtz, "Effect of an Artificial Defect on the Corrosion Behavior of a Cerium-Based Conversion Coating," Proceedings of the DoD Corrosion Conference, August 10-14, 2009, Washington DC.
20. B.L. Treu, W.R. Pinc, S. Joshi, W.G. Fahrenholtz, and M.J. O'Keefe, "Sub-Surface Electrochemical Effects on the Spontaneous Deposition of Cerium Conversion Coatings on Aluminum Alloys," 215th Meeting of the Electrochemical Society, May 24-29, 2009, San Francisco, CA.
21. W. Fahrenholtz, M. O'Keefe, W. Pinc, B. Treu, S. Joshi, E. Morris, and R. Albers, "Characterization of Species and Coating Morphology Involved in the Corrosion Protection of Rare-Earth Coatings," The Partners in Environmental Technology Technical Symposium and Workshop, December 2-4, 2008, Washington DC.

List of Theses and Dissertations

1. S. Joshi, "Electrochemical Characterization of Cerium-based Conversion Coatings on Al 7075-T6," PhD Dissertation, Missouri University of Science and Technology, Rolla, MO June 2010.
2. William R. Pinc, "Characterization of the Corrosion Protection Mechanism of Cerium-Based Conversion Coatings on High Strength Aluminum Alloys" PhD Dissertation, Missouri University of Science and Technology, Rolla, MO June 2010.
3. Daimon K. Heller, "Phosphate Post-Treatment of Cerium-Based Conversion Coatings on Al 2024-T3," PhD Dissertation, Missouri University of Science and Technology, Rolla, MO June 2010.
4. Ci Lin, "Deposition and Characterization of Cerium-Based Conversion Coatings on Aluminum Alloys 380 and 413" MS Thesis, Missouri University of Science and Technology, Rolla, MO December 2011.

List of Journal Publications

1. S. Joshi, W.G. Fahrenholtz, and M.J. O'Keefe, "Dissolution of Cerium from Cerium-based Conversion Coatings in 0.1 M NaCl Solutions," accepted for publication in Corrosion Science, March 15, 2012.
2. B.L. Treu, W.R. Pinc, W.G. Fahrenholtz, M.J. O'Keefe, E. Morris, and R. Albers, "Electrochemical Response and Transport Processes in a Praseodymium-Containing Primer Coating, submitted to the Journal of the Electrochemical Society, October 19, 2010.
3. D.K. Heller, W.G. Fahrenholtz, and M.J. O'Keefe, "Chemical and Structural Analysis of Subsurface Crevices Formed During Spontaneous Spray Deposition of Cerium-Based Conversion Coatings," Materials Characterization, 62(11) 1071-1075 (2011).
4. S. Joshi, W.G. Fahrenholtz, and M.J. O'Keefe, "Electrochemical Characterization of Al 7075-T6 Surface Oxide after Alkaline Treatments," Journal of the Electrochemical Society, 158(9) C296-C301 (2011).
5. B.L. Treu, W.G. Fahrenholtz, and M.J. O'Keefe, "Characterization of the Thermal Decomposition Products of Praseodymium and Oxygen Based Oxides, Hydroxides, and Carbonates," Inorganic Materials, 47(9) 974-978 (2011).
6. S. Joshi, W.G. Fahrenholtz, and M.J. O'Keefe, "Alkaline Activation of Al 7075-T6 for Deposition of Cerium-Based Conversion Coatings, Surface and Coatings Technology, 205(17-18) 4312-4319 (2011).
7. S. Joshi, W.G. Fahrenholtz, and M.J. O'Keefe, "Effect of Alkaline Cleaning and Activation on Aluminum Alloy 7075-T6 for Deposition of Cerium-based Conversion Coatings," Applied Surface Science, 257(6) 1859-1863 (2011).
8. W.R. Pinc, S. Maddela, M.J. O'Keefe, and W.G. Fahrenholtz, "Formation of subsurface voids in aluminum alloy 2024-T3 during deposition of cerium-based conversion coatings," Surface and Coatings Technology, 204(24) 4095-4100 (2010).
9. B.L. Treu, S. Joshi, W. R. Pinc, M.J. O'Keefe, and W.G. Fahrenholtz, "Characterization of Localized Surface States of Al 7075-T6 During Deposition of Cerium-Based Conversion Coatings," Journal of the Electrochemical Society, 157(8) C282-C287 (2010).

List of Conference Proceedings Papers

1. B.L. Treu, W.G. Fahrenholtz, and M.J. O'Keefe, "Corrosion Protection Mechanisms of Praseodymium-Based Inhibitors," Proceedings of the DoD Corrosion Conference, August 1-5, 2011, Palm Springs, CA.
2. B.L. Treu, W.G. Fahrenholtz, and M.J. O'Keefe, "Effect of Phase on Electrochemical and Morphological Properties of Praseodymium-Based Coatings," ECS Transactions, 33(35) 53-56 (2011).
3. B.L. Treu, W.R. Pinc, W.G. Fahrenholtz, M.J. O'Keefe, E.L. Morris, and R.A. Albers, "Characterization of Transport Processes in a Praseodymium-Containing Coating," ECS Transactions, 28(24) 229-237 (2011).
4. D.K. Heller, W.G. Fahrenholtz, G.E. Fair, and M.J. O'Keefe, "Directly Deposited Cerium Phosphate Coatings for the Corrosion Protection of Al 2024-T3," ECS Transactions, 28(24) 203-215 (2011).

5. W.R. Pinc, S. Maddela, W.G. Fahrenholtz, and M.J. O'Keefe, "Corrosion Protection of Cerium-based Conversion Coatings With Subsurface Crevices," ECS Transactions, 28(24) 187-201 (2011).
6. S. Joshi, W.G. Fahrenholtz, and M.J. O'Keefe, "Effect of Humidity on Cerium Based Conversion Coatings," ECS Transactions, 28(24) 217-228 (2011).
7. W. Pinc, D. Heller, W. Fahrenholtz, and M. O'Keefe, "Electrochemical and Structural Changes in Cerium-Based Conversion Coatings During Exposure to Salt Spray Testing," Coatings for Corrosion Protection, ECS Transactions, 25(29) 3-17 (2010).
8. S. Joshi, W.G. Fahrenholtz, and M.J. O'Keefe, "Microelectrochemical Testing of Cerium-Based Conversion Coatings," Coatings for Corrosion Protection, ECS Transactions, 25(29) 19-30 (2010).
9. B.L. Treu, S. Joshi, W.R. Pinc, M.J. O'Keefe, and W.G. Fahrenholtz, "Sub-Surface Electrochemical Effects on the Spontaneous Deposition of Cerium Conversion Coatings on Aluminum Alloys," Corrosion (General), ECS Transactions, 19(29) 101-113 (2009).

List of Book Chapters

1. M.J. O'Keefe, W.G. Fahrenholtz, E.L. Morris, and J.O. Stoffer, "Ch. 9: Corrosion Resistant Polymer Coatings Containing Rare Earth Compounds," submitted to *Rare Earth-Based Corrosion Inhibitors*, edited by M. Forsyth and B. Hinton, Woodhead Publishing, tentative publication date in 2012.